



Experimental and Numerical Study of Triply Periodic Minimal Surface Structures

By
Hao Fu

A thesis submitted to the University of Birmingham
for the degree of DOCTOR OF PHILOSOPHY

School of Engineering
Department of Civil Engineering
University of Birmingham

March 2024

UNIVERSITY OF
BIRMINGHAM

University of Birmingham Research Archive

e-theses repository

This unpublished thesis/dissertation is copyright of the author and/or third parties. The intellectual property rights of the author or third parties in respect of this work are as defined by The Copyright Designs and Patents Act 1988 or as modified by any successor legislation.

Any use made of information contained in this thesis/dissertation must be in accordance with that legislation and must be properly acknowledged. Further distribution or reproduction in any format is prohibited without the permission of the copyright holder.

ABSTRACT

3D printing is an emerging additive manufacturing technology that has revolutionised the development of new materials and structures across various industries. Its ability to produce complex shapes with ease has notably contributed to many fields. Among these innovations, Triply Periodic Minimal Surface (TPMS) structures stand out as a novel type of porous structures, characterised by their particular features such as high specific strength and stiffness. These structures, resembling forms found in biological systems, have become a focal point in materials research over the last decade.

In the last few years, civil engineering practitioners started exploring applying TPMSs in their field. Previous studies on TPMS, however, have largely focused on small-scale material properties, limiting their direct applicability in civil engineering contexts. The structural properties of large-scale TPMS structures, including their static and dynamic characteristics, remain largely undefined. This gap signifies a crucial need for further exploration of large-scale TPMS structures, especially for applications in civil engineering, like railway engineering.

This thesis investigates the suitability of TPMS structures for civil engineering (specifically railways), undertaking a series of static and dynamic studies. The research begins by establishing simplified models of several TPMSs and proceeds to design corresponding solid models. Several TPMS structures have been 3D printed to create large-scale samples for compressive testing. Based on these tests, Finite Element Method (FEM) models of individual unit cells are developed and validated, allowing for the generation of complex structures and their subsequent numerical

analysis.

To examine the effect of unit arrangement on the mechanical and cracking behaviours of specific TPMS structures, the Discrete Element Method (DEM) has been employed. This approach utilises the compressive test data of individual units to validate the DEM models. The study then numerically simulates various TPMS configurations, performing a mesoscopic analysis of their behaviour.

To assess the dynamic properties of these structures, multiple TPMS units have been 3D printed and subjected to impact hammer tests. This testing analyses the frequency, dynamic stiffness, and damping characteristics of the structures. A combined DEM and FEM approach conceptualises the TPMS structure as a support layer in railway applications, examining its mechanical performance under sleeper displacement. Finally, the thesis explores the applicability of concrete TPMS structures by modelling concrete TPMS structures under combined compressive and torsional loads via DEM.

ACKNOWLEDGMENTS

Firstly, I want to express my profound gratitude to Dr Sakdirat Kaewunruen for his invaluable guidance throughout my PhD study. His expertise and mentorship in various aspects, including experimental tests, numerical simulations, and thesis writing, have been pivotal in my academic and personal growth. I am also grateful to my second supervisor, Dr Mayorkinos Papaelias, for his invaluable support during my doctoral studies.

I extend my sincere gratitude to my examiners, Prof Charalampos Baniotopoulos and Prof Chayut Ngamkhanong, for their insightful suggestions to improve the quality of this thesis.

My heartfelt thanks are extended to all the members of the Track Engineering and Operations for Future Uncertainties (TOFU) group at the University of Birmingham. Working alongside such knowledgeable and supportive colleagues, including but not limited to Mr Xu Huang, Mr Junhui Huang, Rucheng Liu, Dr Dan Li, Dr Jessada Sresagunchai, Dr Pasakorn Sengsri and Mr Xia Qin, has been an enriching and invaluable experience.

I am also grateful to the visiting doctoral researchers in our group, such as Dr Yang Li, Dr Ruihua Liang, Dr Zhichao Huang, Dr Ting Li, among others, for their insightful guidance and support during my PhD studies.

Special appreciation goes to my colleagues at the Birmingham Centre for Railway Research and Education (BCRRE), particularly Dr Huayu Duan, Dr Linxiao Li, Dr Jingyuan Yang, for their assistance and collaboration in my experimental work.

I am deeply thankful to the China Scholarship Council for their financial support. My gratitude also goes to the research project S-CODE (Switch and Crossing Optimal Design and Evaluation) for funding my tuition, and to the Rail Infrastructure Systems Engineering Network (RISEN) for their support in my exchange project and financial assistance during my secondment in Portugal.

I owe a world of thanks to my family for their unwavering support and understanding throughout my PhD life. A special mention to my wife, Dr Xiaotong Jian, for being my rock and providing endless emotional support during my PhD.

Lastly, I extend my sincerest thanks to all my family members, friends, and others who have offered me continuous support, patience, time, encouragement, and advice throughout my doctoral studies.

LIST OF PUBLICATION

This doctoral thesis is written in the format of a collection of articles. This doctoral thesis is predominantly constituted of the following significant scientific articles:

Journal Papers:

- 1 **Fu, Hao**, and Sakdirat Kaewunruen. "The axially-loaded behaviours of Schwarz Primitive (SP)-based structures: an experimental and DEM study." *Thin-Walled Structures* (2024): 111973. DOI: <https://doi.org/10.1016/j.tws.2024.111973>
- 2 **Fu, Hao**, Xu Huang, and Sakdirat Kaewunruen. " Nonlinear Instabilities of TPMS Cellular Units Under Axially Loaded Conditions." *International Journal of Structural Stability and Dynamics* (2024): 2450261. DOI: <https://doi.org/10.1142/S0219455424502614>
- 3 **Fu, Hao**, Xu Huang, and Sakdirat Kaewunruen. "Experimental investigations into nonlinear dynamic behaviours of triply periodical minimal surface structures." *Composite Structures* 323 (2023): 117510. DOI: <https://doi.org/10.1016/j.compstruct.2023.117510>
- 4 **Fu, Hao**, Junhui Huang, and Sakdirat Kaewunruen. "Mechanical performance of Bio-Inspired Gyroid and Primitive concrete structures under combined compression and torsion Loads: A discrete element method study." *Engineering Structures* 291 (2023): 116429. DOI: <https://doi.org/10.1016/j.engstruct.2023.116429>
- 5 **Fu, Hao**, Yushi Yang, and Sakdirat Kaewunruen. "Multi-hazard effects of crosswinds on cascading failures of conventional and interspersed railway tracks exposed to ballast washaway and moving train loads." *Sensors* 23.4 (2023): 1786. DOI: <https://doi.org/10.3390/s23041786>

- 6 **Fu, Hao**, and Sakdirat Kaewunruen. "Experimental and DEM investigation of axially-loaded behaviours of IWP-based structures." *International Journal of Mechanical Sciences* 235 (2022): 107738. DOI: <https://doi.org/10.1016/j.ijmecsci.2022.107738>
- 7 **Fu, Hao**, and Sakdirat Kaewunruen. "Numerical investigation of porous composite honeycomb track slab under point load." *Materials Today: Proceedings* 65 (2022): 1628-1633. DOI: <https://doi.org/10.1016/j.matpr.2022.04.691>
- 8 **Fu, Hao**, and Sakdirat Kaewunruen. "State-of-the-art review on additive manufacturing technology in railway infrastructure systems." *Journal of Composites Science* 6, no. 1 (2021): 7. DOI: <https://doi.org/10.3390/jcs6010007>

In addition, during the period of postgraduate study, the following papers were published:

- 9 Kaewunruen, Sakdirat, **Hao Fu**, and Caizhi Ye. "Numerical studies to evaluate crack propagation behaviour of prestressed concrete railway sleepers." *Engineering Failure Analysis* 131 (2022): 105888. DOI: <https://doi.org/10.1016/j.engfailanal.2021.105888>
- 10 Sengsri, Pasakorn, **Hao Fu**, and Sakdirat Kaewunruen. "Mechanical properties and energy-absorption capability of a 3D-printed TPMS sandwich lattice model for meta-functional composite bridge bearing applications." *Journal of Composites Science* 6, no. 3 (2022): 71. DOI: <https://doi.org/10.3390/jcs6030071>

Chapter 2 is mainly based on Paper 8. Chapter 3 uses the information from Paper 1 to 4 and Paper 6, 8 and 10. Chapter 4 is mainly based on Paper 2 and uses some parameters from Paper 10. Chapter 5 is mainly based on Paper 1 and Paper 6. Chapter 6 is mainly based on Paper 3. Chapter 7 uses some parameter from Paper 5, 7 and 9. Chapter 8 is mainly based on Paper 4.

CONTENTS

ABSTRACT	1
ACKNOWLEDGMENTS	3
LIST OF PUBLICATION	5
CONTENTS	7
LIST OF FIGURES	13
LIST OF TABLES	29
 CHAPTER 1 INTRODUCTION	 1
1.1 INTRODUCTION	2
1.2 GENERAL BACKGROUND.....	3
1.3 RESEARCH PROBLEMS	5
1.4 SCOPE OF STUDY	7
1.5 AIM AND OBJECTIVES	10

1.6	NOVELTY AND ORIGINALITY OF WORK	11
1.7	THESIS STRUCTURE	12
CHAPTER 2	REVIEW OF ADDITIVE MANUFACTURING IN RAILWAY	
	SYSTEM AND TPMS STRUCTURES	15
2.1	INTRODUCTION	16
2.2	ADDITIVE MANUFACTURING IN FASTENER SYSTEM	23
2.3	ADDITIVE MANUFACTURING IN SUPPORTING LAYERS	26
2.4	ADDITIVE MANUFACTURING IN TPMS STRUCTURES	29
2.5	RESEARCH GAPS.....	35
CHAPTER 3	TPMS SURFACES AND STRUCTURES GENERATION	39
3.1	INTRODUCTION	40
3.2	PROPERTIES OF TPMS	41
3.3	MATHEMATICAL EXPRESSION OF TPMS	44
3.4	GENERATION OF TPMS.....	51
3.5	SOLID TPMS STRUCTURES	55

3.6	FABRICATION OF TPMS STRUCTURES	61
3.7	CONCLUSION	65
CHAPTER 4	MECHANICAL BEHAVIOURS OF TPMS CELLULAR UNITS UNDER VARIOUS LOADS	66
4.1	INTRODUCTION	67
4.2	DETAILS FOR COMPRESSIVE TESTS	68
4.3	TEST RESULTS FOR COMPRESSION	71
4.4	FEM SIMULATIONS FOR COMPRESSION.....	74
4.5	FEM RESULTS FOR COMPRESSION.....	84
4.6	CONCLUSION OF COMPRESSIVE BEHAVIOURS	89
4.7	FEM SIMULATION FOR TORSION AND SHEAR.....	90
4.8	FEM RESULTS FOR TORSION AND SHEAR.....	100
4.9	CONCLUSION OF TORSION AND SHEAR BEHAVIOURS	107
CHAPTER 5	MECHANICAL PERFORMANCE AND CRACKING PATTERNS OF SP AND IWP STRUCTURES	109

5.1	INTRODUCTION	110
5.2	COMPRESSIVE TESTS.....	111
5.3	DEM MODELLING OF IWP AND SP BASED STRUCTURES.....	116
5.4	COMPRESSIVE STRENGTH	137
5.5	FORCE DISTRIBUTION	143
5.6	CRACK PATTERN.....	151
5.7	LOAD-DISPLACEMENT CURVE AND ENERGY ABSORPTION	158
5.8	CONCLUSION	163

CHAPTER 6 DYNAMIC PROPERTIES OF TPMS BASED **STRUCTURES 168**

6.1	INTRODUCTION	169
6.2	TPMS STRUCTURES.....	170
6.3	IMPACT HAMMER TEST	175
6.4	NATURAL FREQUENCY	183
6.5	DYNAMIC STIFFNESS	185

6.6	DAMPING RATIOS.....	190
6.7	CONCLUSION	194
CHAPTER 7	FEASIBILITY OF TPMS STRUCTURES AS RAILWAY	
	SUPPORT LAYERS	197
7.1	INTRODUCTION	198
7.2	COUPLED DEM AND FEM MODELS	199
7.3	RESULT AND DISCUSSION.....	207
7.4	CONCLUSION	216
CHAPTER 8	STRUCTURAL PERFORMANCE OF CONCRETE TPMS	
	STRUCTURES UNDER VARIOUS LOADS	218
8.1	INTRODUCTION	219
8.2	CONCRETE DEM TPMS MODELS	220
8.3	DISCUSS OF SIMULATION RESULTS	233
8.4	CONCLUSION	242

CHAPTER 9	CONCLUSION.....	244
9.1	INTRODUCTION	245
9.2	RESEARCH FINDINGS.....	246
9.3	RECOMMENDATIONS FOR FUTURE RESEARCH	248
References	251

LIST OF FIGURES

Figure 1.1 Workflow of this research.	9
Figure 2.1 The components of (a) ballasted track; (b) concrete slab track, also known as ballastless track (remade from [4]).	17
Figure 2.2 Percentage of additive manufacturing applications in different industries (Data collected from [7]).	19
Figure 2.3 EU INFRASTAR project for enhancing the rails. (a) The reinforced railhead [16]; (b) Field test in Malmaban [17].	21
Figure 2.4 Moulds for making railway components, produced by 3D printing: (a) Mould for the fastener pad; (b) smart moulds with complex cooling channels. Retrieved from [55].	24
Figure 2.5 Optimization of railway fastener components: (a) Railway clips optimized according to stress conditions; (b) 3D printed spikes. Retrieved from [55].	25
Figure 2.6 Porous structures that are potentially useful in rail pads: (a) honeycomb structure; (b) lattice structure [64] ; (c) A gradient IWP-TPMS structure.	25
Figure 2.7 3D printed composite bearers with multi-layers, reproduced from [65].	26
Figure 2.8 Sleepers of optimized shapes; (a) India FRP sleeper[66]; (b) frictional sleeper[67];	

(c) winged sleeper[68, 69].	27
Figure 2.9 Schematic diagram of a smart ballast particle containing sensors inside: (a) geometry obtained from real ballast particle, (b) 3D printed particle with the simplified shape, (c) install sensor inside and (d) Smart sensor ballast particles and real ballast particles. Remade from [74, 75].	28
Figure 2.10 Geogrids and geocells produced by 3D printing: (a) 3D printed reduced size (one-tenth size) geogrid [72], (b) 3D printed geogrid with honeycomb holes [76] and (c) 3D printed geocell [77].	28
Figure 2.11 Value ranges of specific energy absorption (SEA) and specific strength of various popular porous structures.	30
Figure 2.12 Schematic representation of the three most widely studied TPMS surfaces. (a) IWP, (b) Gyroid and (c) Primitive	32
Figure 3.1 <i>Polyommatus icarus</i> butterfly and the elaborate microarchitecture of its wing scales: (a) displays the underside of the <i>Polyommatus icarus</i> , (b) reveals a plethora of verdant scales affixed to the wing, each embedding gyroid configurations, (c) offers a SEM (Scanning Electron Microscopy) depiction of the gyroid formations on the ventral scale surface, and (d) demonstrates a conceptual model of the anticipated gyroid structure viewed along axes $\langle 001 \rangle$ (left) and $\langle 111 \rangle$ (right)[105].	42
Figure 3.2 An examination of the weevil and its microstructural features: (a) captures an image	

of the weevil, (b) and (c) provide, respectively, an optical microscopy image and a Scanning Electron Microscopy (SEM) image showcasing the scales affixed to the exoskeleton, (d) a cross-sectional SEM picture and (e) a schematic illustration of a Diamond frame [106]..... 42

Figure 3.3 Simplified polygonal IWP surface. The facets and points are plotted with different colours according to value of Z-coordinates. (a) beneath view with lines only, (b) perspective view with lines and triangular meshes..... 53

Figure 3.4 Several simplified TPMSs with their facets and points are plotted using different colours according to value of Z-coordinates. (a) IWP, (b) Gyroid and (c) Primitive..... 54

Figure 3.5 Three typical TPMSs and their Main Solid (Skeletal) and Sheetal unit cells 55

Figure 3.6 Design of the sheetal type and two solid types of Primitive based unit cells..... 57

Figure 3.7 The two types of Skeletal-IWP units and their main frames..... 58

Figure 3.8 A Comparison of Sheetal SP Structures: the left image illustrates the structure produced by the 'shell' function, highlighting its unidirectional thickening, whereas the right image showcases the structure formed through the 'thicken' function, demonstrating uniform thickening in two directions..... 59

Figure 3.9 Fabrication Process of Solid Types (Skeletal Types) SP Structures. This sequence illustrates the transformation from surface to solid SP structures: (a) demonstrates sealing

the SP surface using the 'Fill' command in Geomagic software; (b) presents the DXF file of the SP surface in AutoCAD; (c) depicts the conversion to a planar domain within AutoCAD; (d) shows the creation of the solid model for the Main Solid SP unit cell in AutoCAD; and (e) the generation of the Secondary Solid SP unit cell.	60
Figure 3.10 Schematic Diagram of SLA 3D printing process	62
Figure 3.11 (a) Process flow diagram of stereolithography beginning with an STL file and concluding with model completion; (b) Detailed breakdown of the STL file structure showing the format of triangular facets with their vertices and normal vectors.....	63
Figure 3.12 Schematic diagrams and examples of printed units	64
Figure 4.1 Schematic of compressive tests	70
Figure 4.2 Five tested samples before and after the test	70
Figure 4.3 Load-displacement curves of experimental compression assessments	71
Figure 4.4 Compressive strength of CB-R, IWP-1, IWP-2, SP-1 and SP-2 units from tests ...	73
Figure 4.5 Stiffness of CB-R, IWP-1, IWP-2, SP-1 and SP-2 units from tests	73
Figure 4.6 Various types of units based on SP surface.....	75
Figure 4.7 Various IWP unit cells and IWP surface.....	76
Figure 4.8 Full-sized and quarter-scaled FEM models for CB-R and IWP-4 units.....	77

Figure 4.9 Stress path of Linear Drucker-Prager Model in both compression and tension.....	79
Figure 4.10 Boundary and loading conditions of FEM models.....	81
Figure 4.11 Schematic diagrams and examples of printed units	82
Figure 4.12 Comparison of load-displacement curves between FEM simulation and experiments for (a) CB-R unit, (b) IWP unit cells and (c) SP unit cells.....	83
Figure 4.13 Load-displacement curves of all TPMS unit cells from FEM. (a) SP unit cells compared with CB-R unit and (b) IWP unit cells compared with CB-R unit	85
Figure 4.14 Compressive strength of all types of units from FEM	87
Figure 4.15 Stiffness assessed from FEM simulations for all TPMS units and CB-R	87
Figure 4.16 Stress at the maximum load in quarter-scale TPMS units in Ansys.....	88
Figure 4.17 Comparison between the cracking area in experiments and stress concentration area in quarter-scale TPMS units in Ansys.....	89
Figure 4.18 Hybrid surfaces of W and P TPMSs (H-WP surfaces) with various λ_1 and λ_2 ...	92
Figure 4.19 The visual surfaces of new types TPMSs (a) H-DX, (b) H-DW, (c) H-XX and (d) H-RWP.....	92
Figure 4.20 Skeletal-TPMS unit cells. (a) and (b) are the primary and complementary type of Primitive (SP) and IWP units, (c) and (d) are the primary and complementary type of H-	

DX, H-DW, H-XX and H-RWP units, (e) cubic amalgamation of Primitive (SP) unit; (f) excise dispersed element to form H-XX-P units.....	94
Figure 4.21 The boundary conditions: (a) Supporting condition , (b) Loading condition for compressive research, (c) Loading condition for shear research, (d) Loading condition for torsional research	97
Figure 4.22 (a) to (e) The 3D printed samples;(f) Tensile FEM model.....	99
Figure 4.23 Load-displacement curves of skeletal SP and IWP unit cells from compressive tests and FEM simulation.....	99
Figure 4.24 Specific Load-displacement curves of skeletal hybrid TPMS structures from compressive FEM simulation.	102
Figure 4.25 Specific Load-displacement curves of skeletal hybrid TPMS structures from shear FEM simulation.	103
Figure 4.26 Specific torque-rotation angle curves of skeletal hybrid TPMS structures from torsion FEM simulation.	105
Figure 5.1 Experimental load-displacement curves of the two IWP based designs.	112
Figure 5.2 Fractured IWP specimens, annotated with crimson lines, identify the crack-susceptible regions from tests.	113
Figure 5.3 Experimental load-displacement curves of the two SP based designs.....	114

Figure 5.4. Post-compressive test fractured specimens, with Main SP depicted on the left and Secondary SP on the right. Red demarcation lines at the lower section of the image indicate the zones of failure.	116
Figure 5.5 Modelling of the two IWP designs in DEM (a) Wall elements for cellular contour (b) breakable Clusters models.....	118
Figure 5.6 The Volumetric Domains of the main and secondary SP unit cells.....	118
Figure 5.7 DEM representations of (a) Main SP unit cell and (b) Secondary SP unit cell. To the left, the Wall component comprising numerous facets elements; to the right, the cluster embodying the SP unit cell configuration.	120
Figure 5.8 Illustration of contact mechanisms Linear contact model for Wall-Ball contacts.	123
Figure 5.9 Illustration of contact mechanisms Linear parallel model for Ball-Ball contacts.	123
Figure 5.10 Illustration of surface gaps for the linear-based models in PFC 6.0.	125
Figure 5.11 DEM analysis of IWP designed structures: (a) main type for case M555 and (b) secondary type for case S555.....	131
Figure 5.12 DEM analysis of IWP designed structures: (a) Main SP structure adopting a “557” unit cell alignment and (b) Secondary SP structure with a “332” unit cell pattern.	133
Figure 5.13 Comparison of outcomes from experiments and DEM calculations for IWP designs (a) main type and (b) secondary type.....	135

Figure 5.14 Post-compression visualisation of fragmented DEM representations for IWP units	135
Figure 5.15 Comparison of outcomes from experiments and DEM calculations for SP designs	
(a) main type and (b) secondary type.....	137
Figure 5.16 Post-compression visualisation of fragmented DEM representations for SP units.....	137
Figure 5.17 Engineering strength outcomes from sole layered DEM models of various unit cell configurations. (a) Main IWP variant designs and (b) Secondary IWP variant designs.	139
Figure 5.18 Engineering strength outcomes from multi-layered DEM models of various unit cell configurations. (a) Main IWP variant designs and (b) Secondary IWP variant designs.	140
Figure 5.19. Engineering strength outcomes from Main SP DEM models of various unit cell configurations. (a) sole-layer in z direction and (b) multi-layer in z direction.....	142
Figure 5.20. Axial load advancement in DEM models M114, M115, and M116, underscoring the instability preceding fracture initiation.	142
Figure 5.21. Engineering strength outcomes from Secondary SP DEM models of various unit cell configurations. (a) sole-layer in z direction and (b) multi-layer in z direction.	143
Figure 5.22 Analysis of contact force chains inside main IWP designs for various cases	146

Figure 5.23 Analysis of contact force chains inside secondary IWP designs for various cases 147

Figure 5.24 Depiction of contact force chains within the core unit cell of Primary SP frameworks across variable unit cell arrangements. Rows (a) to (d) delineate the contact force chains for configurations M111, M151, M551, and M555, correspondingly. Column (1) visualises both compressive and tensile force chains via uniformly sized cylinders; Column (2) displays these chains with cylinders scaled to the force magnitude; Column (3) is dedicated to the compressive force chain with uniform cylinder sizes; and Column (4) focuses on the tensile force chain, similarly utilising cylinders of a consistent diameter. 149

Figure 5.25 Illustration of contact force chains within the central unit cell of Secondary SP structures for varied unit cell configurations. Rows (a) through (d) illustrate the contact force chains for setups S111, S151, S551, and S555, respectively. Column (1) shows both compression and tension force chains represented by uniformly sized cylinders; Column (2) portrays these chains with cylinders sized according to contact force magnitude; Column (3) exclusively features the compression force chain with uniform cylinder diameters; and Column (4) exclusively presents the tension force chain, also with uniform cylinder diameters. 150

Figure 5.26 Illustration of fracture manifestations identified via contact elements upon model failure with fracture zones for case M551, denoted by red marks. (a) Main IWP design

and (b) Secondary IWP design. 151

Figure 5.27 Trends of sphere movements inside the main IWP unit. (a) isotropic perspective with spheres and speed vectors, (b) isotropic perspective focusing solely on speed vectors, (c) frontal perspective of speed vectors, (d) overhead perspective of speed vectors, (e) sectional planes, (f) speed vectors in sectional plane 1, and (g) speed vectors in sectional plane 2. 153

Figure 5.28 Trends of sphere movements inside the secondary IWP unit. (a) isotropic perspective with spheres and speed vectors, (b) isotropic perspective focusing solely on speed vectors, (c) frontal perspective of speed vectors, (d) overhead perspective of speed vectors, (e) sectional planes, (f) speed vectors in sectional plane 1 and 2, and (g) speed vectors in sectional plane 3. 154

Figure 5.29 Fractures in main and secondary IWP designs..... 154

Figure 5.30 Comparison of '444' unit cell configuration SP samples following axial compression tests, presented from the front, both sides, and the rear. (a) the 3D printed Main SP structure; (b) the DEM-simulated Main SP model; (c) the 3D printed Secondary SP structure; and (d) the DEM-simulated Secondary SP model..... 156

Figure 5.31 Contact force chain coloured by the magnitude of contact forces at a strain of 2%: (a) Main SP structure for the '555' configuration, and (b) Secondary SP structure for the '555' configuration..... 157

Figure 5.32 Contact force chain coloured and scaled by the magnitude of contact forces at a strain of 2%, within (a) Main SP structure and (b) Secondary SP structure, with ‘551’ unit cell configuration.	157
Figure 5.33 The average load versus displacement curves of the two IWP designs of different cases. (a) Main IWP designs and (b) Secondary IWP designs.	159
Figure 5.34 The average energy absorption versus displacement curves of the two IWP designs of different cases. (a) Main IWP designs and (b) Secondary IWP designs.	160
Figure 5.35 The average load versus displacement curves of the two IWP designs of different cases. (a) Main SP designs and (b) Secondary SP designs..	162
Figure 5.36. The average energy absorption versus displacement curves of the two IWP designs of different cases. (a) Main SP designs and (b) Secondary SP designs.	163
Figure 6.1 Simplified polygonal (a) IWP, (b) Gyroid and (c) Primitive surfaces. The facets and points are plotted with different colours according to value of Z-coordinates.	171
Figure 6.2 Three classes of TPMS based cellular unit of IWP, Gyroid and Primitive designs. (a) sheetal type, (b) main solid type and (c) secondary solid type.	172
Figure 6.3 3D printed specimens of three classes of TPMS structures in a 4×4×4 arrangement of IWP, Gyroid and Primitive designs. (a) sheetal type, (b) main solid type and (c) secondary solid type.	174

Figure 6.4 Impact hammer tests of TPMS structures. (a) a potential TPMS support in railway tracks; (b) schematic illustration test setup, (c) conceptual illustration of the test setup and (d) an actual test image.	176
Figure 6.5 Instruments for impact hammer testing from PROSIG ltd.....	177
Figure 6.6 Illustration of data from an impact hammer test on the MS-IWP structure (a) impulse load in the time domain and (b) acceleration response in the time domain.....	179
Figure 6.7 Acceleration responses in frequency domain from a set of four evaluations on the MS-IWP structure	180
Figure 6.8 Employing the half-power bandwidth technique to deduce damping ratios.	183
Figure 6.9 Natural frequencies and linear fits all TPMS designs. (a) IWP, (b) Primitive and (c) Gyroid and (d) all TPMS structures.....	185
Figure 6.10 Scatter diagram of dynamic stiffness and parabolic fitting three classes of (a) IWP, (b) Primitive, (c) Gyroid and (d) all TPMS structures.....	187
Figure 6.11 Frequency response functions in nondimensional form for the three classes of (a) IWP, (b) Primitive and (c) the Gyroid structures.....	190
Figure 6.12 Evaluation of damping ratios for IWP designs by different methods for(a) main solid type, (b) secondary solid type and (c) sheetal type	192
Figure 6.13 Evaluation of damping ratios and linear fit for all three classes of TPMS designs	

by different methods. (a) IWP, (b) Primitive, (c) Gyroid structures and (d) all nine variants.	193
Figure 7.1 An example of track model with TPMS supporting layer.....	200
Figure 7.2 DEM modelling of TPMS unit cells used for main (1) and secondary (2) TPMS track supporting layers. (a) IWP (b) Primitive and (c) Gyroid.	202
Figure 7.3 Force transfer from DEM elements to FEM elements.	203
Figure 7.4 Introduction of the DEM and FEM coupling in a contact between a discrete element and triangle vertexes.	204
Figure 7.5 Load-Displacement curves of sleeper in the DEM simulation of TPMS tracks ...	208
Figure 7.6 Linear fit of Load-Displacement curves for the DEM simulations of TPMS tracks.....	208
Figure 7.7 Energy absorption-displacement curves for the DEM simulations of TPMS tracks.....	210
Figure 7.8 The Von Mises Equivalent stress distribution inside the subgrade in DEM modelling of TPMS tracks. (a) Main skeletal IWP type, (b) Secondary skeletal IWP type, (c) Main skeletal Primitive type, (d) Secondary skeletal Primitive type, (e) Main skeletal Gyroid type and (f) Secondary skeletal Gyroid type.....	211
Figure 7.9 The contact force distribution inside the MS-IWP support layer beneath the center	

of the sleeper. (a) both the compression and tension force are plotted, (b) only the compression contacts are plotted and (c) on the tension contacts are plotted. All the contacted are scaled according to the force.	212
Figure 7.10 The contact force chain of the area beneath the center of the sleeper. (a) Main skeletal IWP type, (b) Secondary skeletal IWP type, (c) Main skeletal Primitive type, (d) Secondary skeletal Primitive type, (e) Main skeletal Gyroid type and (f) Secondary skeletal Gyroid type.	214
Figure 7.11 The contact force chain inside the TPMS layer from the top view and the front view. (a) Main skeletal IWP type, (b) Secondary skeletal IWP type, (c) Main skeletal Primitive type, (d) Secondary skeletal Primitive type, (e) Main skeletal Gyroid type and (f) Secondary skeletal Gyroid type.	215
Figure 8.1 Concrete Primitive and Gyroid TPMS structures from [197].	222
Figure 8.2 Cellular units for the Gyroid (1) and Primitive (2) TPMS. (a) the main skeletal design and (b) the secondary skeletal design.	222
Figure 8.3 DEM cellular units by sphere elements (Balls) for the Gyroid (1) and Primitive (2) TPMS. (a) the main skeletal design and (b) the secondary skeletal design.	224
Figure 8.4 A depiction of an active contact mechanism among two spherical bodies.	226
Figure 8.5 The viscoelastic elements of the Soft-bond constitutive model.	226

Figure 8.6 The DEM models, and the tested specimens from [197] for validation purpose. (a) main Gyroid design and (b) secondary Primitive design.....	228
Figure 8.7 Load-displacement curves for concrete TPMS structures under compressive loads from tests (rest results from [197]) and numerical simulation for (a) main Gyroid variant and (b) secondary Primitive variant.	230
Figure 8.8 Cracked concrete TPMS structures. Images are from test and DEM numerical simulations.	231
Figure 8.9 Illustration of applying compression and torsion loads in DEM modelling for concrete TPMS structures subjected, secondary Primitive design as an example.....	233
Figure 8.10 load-displacement response to only compression load for Gyroid and Primitive-based structures.	234
Figure 8.11 Cracking patterns in TPMS specimens subjected to compressive load only.	235
Figure 8.12 Torsion moment versus rotation angle curves under torsion condition of upper cap for main (1) and secondary (2) TPMS designs. (a) Primitive and (d) Gyroid.	236
Figure 8.13 Cracking patterns in the four Gyroid and Primitive designs under a rotation speed of twenty degrees per minute.	237
Figure 8.14 Compressive load-displacement response under mixed loading conditions for main (1) and secondary (2) TPMS designs. (a) Primitive and (d) Gyroid.....	238

Figure 8.15 Torsion-load against rotation-angle graphs under mixed loading conditions for main (1) and secondary (2) TPMS designs. (a) Primitive and (d) Gyroid.....	240
Figure 8.16 Peak compression forces and torsion moments for the main and secondary skeletal Primitive and Gyroid variants under various mixed loading conditions.	241
Figure 8.17 Cracking patterns in the main and secondary skeletal Primitive and Gyroid variants under mixed loading condition at 20°/min rotation speed.	241

LIST OF TABLES

Table 2.1 Materials used by different researchers to strengthen rail.	23
Table 3.1 Mathematic expressions and images of several common TPMSs.....	49
Table 3.2 Nodal expressions and images of some complex TPMSs.	50
Table 3.3 The calculation of x_i , y_i and z_i . ($C_p=17$ and $l=1$).....	51
Table 3.4 Mechanical properties of 3D printed “photosensitive resin 8200”.....	65
Table 4.1 Comparison of geometric properties and relative density of SP unit cells to the cube block.....	75
Table 4.2 Comparison of geometric properties and relative density of IWP unit cells to the cube block	76
Table 4.3 Material properties of the two steel plates in FEM simualtion.....	77
Table 4.4 Parameters of the 3D printed samples in FEM simulations using Ansys.....	79
Table 4.5 FEM modelling results of all TPMS unit cells compared to CB-R.....	86
Table 4.6 The specific density of the TPMS units compared to cube block	95
Table 4.7 Compressive load and stress distribution of the hybrid TPMS structures at a displacement of 2.5 mm.....	101

Table 4.8 Shear load and stress distribution of the hybrid TPMS structures at a displacement of 2.5 mm	104
Table 4.9 Torque and stress distribution of the hybrid TPMS structures at average rotation angle of 5°	106
Table 5.1 Parameters for DEM IWP and IWP unit cell models.	128
Table 5.2 The introduction of case abbreviation of IWP and SP designs with numerous units.....	129
Table 5.3 Contact characteristics for main and secondary IWP designs for various cases	145
Table 5.4 Specification of contact elements within Main and Secondary SP models for cases ‘111’, ‘151’, ‘551’ and ‘555’.....	148
Table 5.5 Energy absorption capacity and displacement at their peak loads for the IWP variant designs.....	160
Table 6.1 Details of the 3D printing material	173
Table 6.2 Regression analysis specifics for the linear fit of natural frequencies.....	184
Table 6.3 Regression analysis specifics for Parabola fit of dynamic stiffness	187
Table 6.4 Regression analysis specifics for the linear fit of damping ratios	194
Table 7.1 Parameters for sleeper and subgrade	201

Table 7.2 Parameters for DEM TPMS supporting layers.	202
Table 7.3 Linear fit details of Load-Displacement curves for the DEM simulations of TPMS tracks	209
Table 7.4 Specification of contact elements within coupled DEM and FEM TPMS track models at the sleeper displacement of 2 cm.	212
Table 8.1 DEM parameters for Balls and Walls	228
Table 8.2 DEM parameters for linear and soft-bond constitutive behaviours	229

CHAPTER 1

INTRODUCTION

1.1 INTRODUCTION

The additive manufacturing technology, also known as 3D printing, has experienced a remarkable surge in development in recent years, profoundly impacting a variety of industries. This technological evolution has not gone unnoticed in the realm of civil engineering and railway construction, where it offers promising new avenues for innovation. The ability of additive manufacturing to create structures with intricate and complex designs is particularly advantageous. One notable example is the application of Triply Periodic Minimal Surface (TPMS) structures. These structures are a specific type of porous architecture, celebrated for their unique combination of lightweight characteristics and high strength, making them ideal for various engineering applications.

However, the development towards integrating these advanced structures into civil engineering has faced significant challenges. Most notably, previous research has predominantly focused on the fabrication and testing of small-scale TPMS prototypes. This limitation has been a major hurdle in demonstrating the feasibility of these structures for large-scale civil engineering projects, where factors such as load-bearing capacity and structural integrity are paramount. Therefore, expanding research to include larger-scale structures is not just beneficial but essential to truly harness the potential of 3D printing in this field.

Moreover, understanding the dynamic behaviour of TPMS structures under various conditions is crucial, especially in civil engineering where structures are subject to diverse forces and stresses. This chapter delves into both quasi-static and dynamic analyses of TPMS structures. The quasi-static study focuses on the bearing capabilities and the resilience of the structures

under compressive forces, while the dynamic research investigates how these structures respond to impact loads, reflecting those loads in railway engineering due to the movement of trains. The findings of this research are expected to provide meaningful findings into the applicability and mechanical behaviour of TPMS structures in real-world civil engineering and railway scenarios, marking a significant step forward in the practical application of additive manufacturing technology in these fields.

1.2 GENERAL BACKGROUND

The advent of 3D printing, or additive manufacturing, represents a significant leap forward in industrial fabrication. This technology, which operates on the principles of layered manufacturing and material overlaying, has revolutionized the way objects are created from digital models. It's a synthesis of machinery, material science, and information technology, marking a pivotal point in the new industrial revolution. The applications of additive manufacturing span various sectors, from aerospace, where it's used for creating complex parts that withstand extreme conditions, to medical biology for bespoke prosthetics and implants. In engineering construction, this technology facilitates the creation of intricate designs that were previously unfeasible, and in the automotive industry, it allows for rapid prototyping and customisation of parts. Additionally, 3D printing has found its way into niche areas like cultural heritage preservation, where it aids in restoring and replicating ancient artifacts, and even in the fashion industry for innovative garment design. These diverse applications underscore the versatility and growing importance of 3D printing in contemporary industry and research.

TPMS based structures, a product of additive manufacturing innovation, have garnered attention for their mechanical superiority and architectural potential. Characterized by their minimal surface features, TPMS structures offer a unique combination of lightweight and strength, making them highly advantageous in various fields. The good properties of TPMS, including high energy absorption capacity and stiffness-to-weight ratio, are particularly beneficial in fields requiring robust yet lightweight materials. Already, TPMS structures have been employed in areas such as artificial bone scaffolds, where their porous nature facilitates cell growth and nutrient delivery. In the realm of aerospace, TPMS structures can contribute to reducing the weight and mass of components without losing structural integrity.

The railway industry, a cornerstone of public transportation and goods transit, is actively incorporating innovative technologies and materials to enhance efficiency and safety. As trains evolve to be faster and heavier, the demand for more resilient and reliable infrastructure grows.

This drive for innovation has led to the exploration of new structural designs and materials, with an emphasis on improving the mechanical performance of critical components like railway turnouts. In this context, the railway industry is exploring the use of advanced materials and structures to meet the stringent demands of modern rail systems. The integration of new technologies is not only aimed at enhancing the physical properties of railway components but also at extending their service life and reducing maintenance requirements.

The probable application of TPMS structures in civil and railway engineering is a promising area of exploration. Given their exceptional mechanical properties, TPMS structures could

significantly contribute to the development of more resilient and efficient infrastructure. In civil engineering, the use of TPMS could revolutionize the design and construction of load-bearing elements, offering new solutions for challenging engineering problems. In railway engineering, the integration of TPMS structures into components like sleepers and turnouts could lead to improvements in vibration reduction, energy absorption, and overall track stability. This is particularly relevant in the context of high-speed and heavy-duty railway systems, where the dynamic loads are significantly greater. The application of TPMS structures in these fields could not only enhance the performance and safety of railway systems but also pave the way for more sustainable and cost-effective infrastructure solutions.

1.3 RESEARCH PROBLEMS

The exploration of TPMS structures in civil and railway engineering is a burgeoning field, marked by promising potential but also by significant research challenges that need to be addressed to fully leverage their capabilities in these domains.

One of the most critical aspects that require further investigation is the effect of the quantity and arrangement of TPMS unit cells on their overall mechanical performance. In the realm of materials science, where TPMS structures have been predominantly studied, the focus has been on small-scale unit cells with numerous layers. This abundance of layers and the small size have been integral to achieving desired mechanical properties in applications like biomedical implants. However, in civil and railway engineering applications, the scenario is markedly different. In railway engineering, structures are subjected to prolonged dynamic loads, necessitating substantial shock absorption and energy dissipation capabilities. Here, the

structures often feature fewer layers and unit cells due to larger overall dimensions and different functional requirements. This discrepancy in scale and structure raises questions about the transferability of findings from small-scale TPMS studies to large-scale engineering applications. Therefore, it is essential to conduct in-depth analyses of TPMS structures with fewer layers and unit cells to understand how these configurations influence strength, durability, and other critical mechanical properties in the context of civil and railway infrastructure.

Additionally, while existing studies have highlighted the superior energy absorption and mechanical strength of TPMS structures, there is a lack of consensus on the most effective TPMS configuration. This debate extends to the understanding of failure mechanisms under various load conditions. Current research often overlooks the real-world conditions that TPMS structures would encounter in civil and railway engineering, such as long-term dynamic loads, environmental variations, and the impact of these factors on the cracking and failure behaviours of the materials. Such understanding is crucial for ensuring the reliability and safety of TPMS-based solutions in large-scale infrastructure projects.

Moreover, the dynamic properties of TPMS structures, such as damping ratios, natural frequencies, and dynamic stiffness, remain underexplored, particularly under varied load amplitudes and real service conditions. This gap in research is significant given that civil engineering structures are often subjected to a range of dynamic forces, from vehicular movement to environmental stresses. The performance of TPMS structures under these dynamic conditions is critical for their application in areas such as vibration reduction and

foundational supports in civil infrastructure.

In light of these challenges, the research community needs to focus on developing a more comprehensive understanding of TPMS structures, considering the specific requirements and conditions of civil and railway engineering. This includes conducting studies on TPMS configurations with several layers and unit cells, exploring their failure mechanisms under practical load conditions, and thoroughly investigating their dynamic properties. Such research efforts will not only contribute to the theoretical understanding of TPMS structures but will also pave the way for their practical application in enhancing the safety, efficiency, and sustainability of large-scale engineering projects.

1.4 SCOPE OF STUDY

The scope of this thesis encompasses both experimental studies and numerical simulations aimed at enhancing our understanding of the static and dynamic properties of large-scale TPMS structures. This comprehensive approach is designed to address the various research challenges and gaps identified in the field, particularly in the context of civil and railway engineering applications.

The thesis begins with an extensive review of additive manufactured components in railway infrastructure. This includes a discussion on the prospects and challenges of implementing 3D printing technology into railway engineering. Furthermore, the properties and existing research on TPMS structures are thoroughly reviewed for subsequent study in the thesis.

To design suitable TPMS structures, a bespoke algorithm has been developed for generating Triply Periodic Minimal Surfaces (TPMSs) based on their mathematical expressions. This algorithm

simplifies the TPMS surfaces into polygonal surfaces that have numerous triangular mesh. Based on this approach, SP and IWP surfaces, which are currently at the forefront of research, were printed as structural units. These units were then subjected to cubic compression tests.

Following the experimental phase, Ansys software has been employed to perform FEM simulations on various TPMS units. This included an extended analysis incorporating torsional FEM simulations, offering a more inclusive insight into the mechanical performance under different loading conditions.

To research the impact of the quantity and arrangement of unit cells on the mechanical performance and cracks of SP and IWP structures, the DEM is utilized. This involved constructing and validating multi-unit cell models of SP and IWP structures, based on the initial compression tests. DEM simulations are carried out to study the distribution of internal force chains and microscopic mechanical behaviours, such as cracking patterns, under compression.

For the investigation of the dynamic properties of these structures, 4x4x4 models of IWP, SP, and Gyroid TPMS structures were printed and subjected to impact hammer tests. These tests provided valuable data on natural frequencies and damping ratios, key indicators of dynamic performance.

Building on previous research on TPMS-concrete structures, the thesis explores the bearing capacity and cracking profiles of TPMS structures subject to torsional and combined compressive-torsional forces using discrete element analysis. This analysis is crucial for understanding the performance of TPMS structures under more complex loading scenarios typical in civil engineering applications.

The research also delves into a preliminary study combining both DEM and FEM to assess the dynamic characteristics of TPMS structures when used as railway track supporting layers. This part of the study is particularly focused on assessing the viability of TPMS structures in practical railway engineering scenarios.

In total, the thesis discusses with an emphasis on the establishment, simplification, and analysis of TPMS unit cells, the influence of unit cell arrangement, dynamic performance of TPMS structures, and a preliminary exploration of their application in civil and railway engineering. The research findings are then summarized, illustrating a comprehensive approach to understanding and applying TPMS structures in large-scale engineering projects.

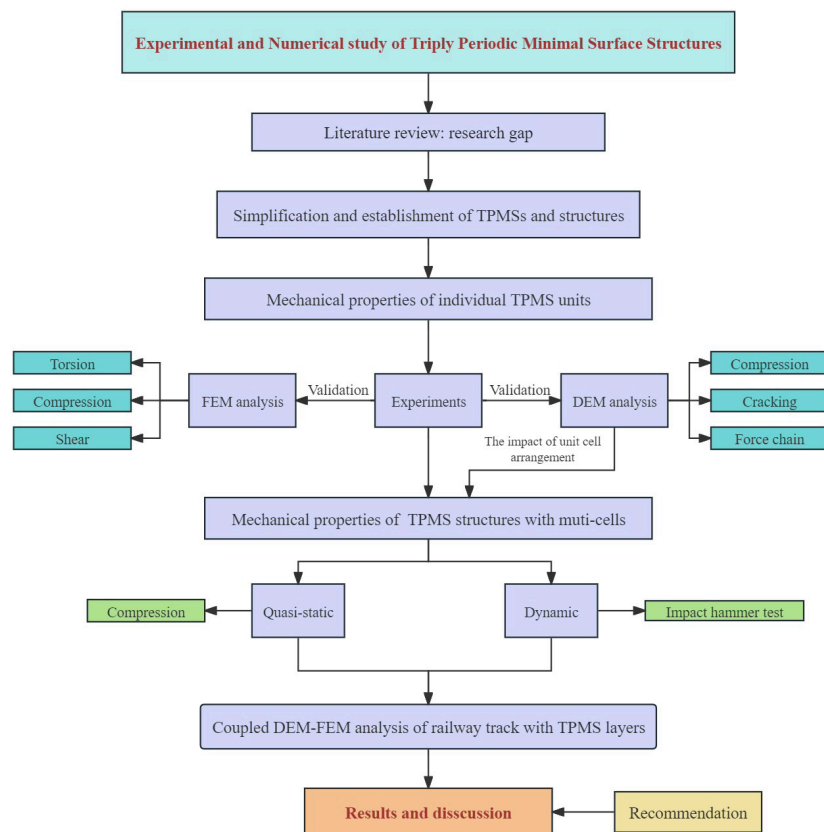


Figure 1.1 Workflow of this research.

1.5 AIM AND OBJECTIVES

The thesis aims to investigate the performance of TPMS structures with large-sized unit cells and study the feasibility of utilising TPMS structures as supporting layers in railway infrastructures. Experiments and simulations of TPMS structures using DEM and FEM are carried out. The aims of the thesis are achieved by completing the following objectives.

- Review studies on 3D printing in the railway system and TPMS structures, and define the gap of TPMS structures in civil engineering and railway engineering.
- Simplify TPMSs and build printable TPMS digital models.
- Investigate the mechanical performance of individual TPMS unit cells subjected to compression, shear, and torsion loads using FEM methods.
- Study the effects of unit cell configurations on the compressive behaviours, including strength, force distribution, and cracking patterns, of SP and IWP-based TPMS structures.
- Evaluate the natural frequency, dynamic stiffness, and damping properties of different types of TPMS structures using impact hammer tests.
- Compare the performance of TPMS structures as supporting layers in railway systems.
- Analyze the concrete structures of TPMS geometry subjected to compression and torsion loads.

1.6 NOVELTY AND ORIGINALITY OF WORK

This thesis presents several novel contributions to application and understanding of TPMS structures in the field of civil and railway engineering. The research conducted herein is pioneering in several aspects, which are detailed in the following chapters. The general contributions of the thesis can be summarised as follows:

1. **Innovative Application of Large-Scale TPMS in Civil Engineering:** This thesis extends the application of TPMS structures beyond their traditional use in small-scale applications, such as biomedical implants, to large-scale civil and railway engineering. This transition addresses a critical research gap in the scalability and application of TPMS structures.
2. **Development of a novel approach for TPMS Structure Design:** A unique algorithm is created to simplify TPMS surfaces into polygonal surfaces. This simplification facilitates the practical additive manufacturing of these structures and is a novel approach in the study of TPMS.
3. **Comprehensive Analysis of SP and IWP Structures:** The thesis provides an in-depth analysis of SP and IWP structures, two of the most promising TPMS configurations, through both experimental and numerical methods. This dual approach offers a holistic understanding of these structures' mechanical behaviours.
4. **Integration of DEM in TPMS Analysis:** Pioneering, the DEM is applied to study the mechanical performance and failure mechanisms of TPMS structures, providing new insights into their behaviour under various load conditions.
5. **Detailed Study of Dynamic Performance of TPMS Structures:** The research includes a novel

investigation into the dynamic properties of TPMS structures, including resonant frequency (natural frequency) and damping ratios, under different loading scenarios, addressing a significant gap in current TPMS research.

6. **Exploration of TPMS Structures Subject to Combined Loads:** The thesis explores the effect of torsional and compressive loads on the performance of TPMS structures, a scenario not extensively studied in existing literature, thus contributing to a deeper understanding of TPMS structures.
7. **Preliminary Investigation of TPMS Structures as Railway Support Layers:** The study pioneers the investigation of TPMS structures as potential support layers in railway infrastructure, combining discrete and finite element methods to assess their suitability, a novel approach in the field.

1.7 THESIS STRUCTURE

The thesis is structured into nine chapters, including the introduction and conclusion, adhering to the alternative format specified by the University of Birmingham (7.4.1). Below is an outline of each chapter, detailing its content and focus.

Chapter 1: Introduction: This chapter offers an overview of the research backdrop, content, innovations, and the structure of the thesis. It sets the stage for the detailed exploration of TPMS structures in civil and railway engineering.

Chapter 2: Literature Review: This chapter offers an exhaustive survey on the utilisation of additive manufacturing technologies within the realm of railway engineering. It also discusses the

current state of research on TPMS structures, identifying gaps and opportunities for further study.

Chapter 3: TPMS Surface Introduction and Modelling: This chapter delves into what TPMS surfaces are and the process of their simplification and modelling using a custom-developed program. It lays the foundation for understanding the complexities and potential of TPMS structures.

Chapter 4: Mechanical Properties of Single TPMS Units: Focusing on the mechanical performance of individual TPMS units, this chapter encompasses both experimental studies and finite element analysis, offering a detailed insight into the structural integrity and response of TPMS units under various conditions.

Chapter 5: Mechanical Performance and Cracking Patterns of SP and IWP Structures: This chapter explored the compressive behaviours and cracking modes of SP and IWP structures with different unit cell amounts. It also includes analyses of force chain distribution and microscopic contact information.

Chapter 6: Dynamic Properties of TPMS Structures: This chapter presents the dynamic properties of 4x4x4 TPMS structures, assessed using impact hammer tests. The focus is on understanding the behaviours of these structures under dynamic loading conditions.

Chapter 7: TPMS Structures as Railway Support Layers: Employing a combination of DEM and FEM, this chapter provides a fundamental analysis of TPMS structures when used as support layers in railway systems.

Chapter 8: Mechanical Performance of Concrete TPMS Structures under Various Loads: The

eighth chapter investigates the mechanical properties and cracking behaviour of concrete TPMS structures subject to compressive, torsional, and combined loading scenarios using discrete element analysis. This provides insights into the structural resilience and failure mechanisms of TPMS in more complex load conditions.

Chapter 9: Conclusions and Future Prospects: The final chapter synthesises main findings of this thesis, drawing conclusions on the overall research and suggesting directions for future research. It encapsulates the contributions of the thesis to the field and outlines potential areas for further exploration and application of TPMS structures.

The structure of this thesis is designed to systematically address the research questions, presenting a thorough investigation of TPMS structures from fundamental concepts to complex applications in railway and civil engineering. In terms of scientific impact and industry applications, this work pioneers the integration of TPMS structures with additive manufacturing technologies to enhance structural efficiencies in civil and railway engineering. The application of TPMS in these sectors could significantly reduce material costs and increase sustainability by optimising material distribution and strength. Academically, this thesis contributes to the fundamental understanding of TPMS behaviours under various loading conditions, bridging significant gaps in the literature and providing a robust framework for future research. In the industry, the findings could inform design standards and construction practices, potentially leading to more resilient and economically viable civil infrastructures. This could catalyse further research collaborations between academia and industry, driving innovation in construction methods and materials science.

CHAPTER 2

REVIEW OF ADDITIVE

MANUFACTURING IN

RAILWAY SYSTEM AND TPMS

STRUCTURES

2.1 INTRODUCTION

Tracing the lineage of the railway system back to its inception with the advent of the steam locomotive in the early 19th century, the United Kingdom laid the foundation for the modern railway transport system. Over the years, railways have emerged as a vital transportation mode globally, serving as the lifeline for national economies and societal development. The advent of high-speed rail has particularly underscored railways' advantages in terms of speed, capacity, energy efficiency, minimal pollution, land usage efficiency, and safety [1]. Countries such as Japan, France, and Germany have significantly invested in high-speed rail, showcasing its feasibility and advantages. In Europe, the railway became a cornerstone of industrial and economic expansion, facilitating unprecedented levels of connectivity and efficiency. The advent of high-speed rail further accentuated these benefits, offering a mode of transport that combines speed, capacity, and environmental efficiency [2]. Europe's investment in high-speed rail, led by countries such as France with its renowned TGV (Train à Grande Vitesse) and Germany with its ICE (InterCity Express), has significantly contributed to the region's transport infrastructure, making rail a preferred choice for intercity travel.

The railway system's infrastructure is a marvel of engineering, designed to accommodate the ever-increasing speeds and axle loads of modern trains. At the heart of this infrastructure are the track structures, which are pivotal in ensuring the smooth, efficient, and safe operation of rail services. These track structures have evolved significantly over time, adapting to the technological advancements and operational demands of the railway industry. They are broadly categorized into two main types: ballasted and slab tracks, each with distinct characteristics and components

tailored to meet specific operational requirements [3]. Figure 2.1 shows the components of typical ballasted track and slab track.

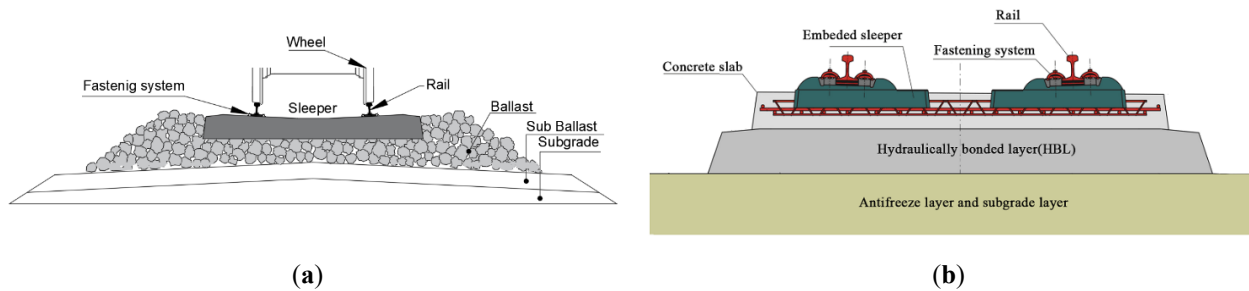


Figure 2.1 The components of (a) ballasted track; (b) concrete slab track, also known as ballastless track (remade from [4]).

Ballasted tracks are the traditional choice for railway infrastructure, consisting of a layered assembly that includes rails, fasteners, sleepers (ties), and a gravel bed (ballast) [5]. Each component plays an important role in the track's overall behaviour. Rails serve as the direct interface with train wheels, guiding them along the track. Made from high-strength steel, rails must resist wear and deformation under the weight of passing trains. Fasteners connect the rails securely to the sleepers, allowing for minor adjustments in rail alignment while transferring loads to the sleepers. Sleepers (ties) disperse the loads from the rails across a wider area of the ballast bed. Sleepers can be made from wood, concrete, or steel, each material offering different benefits in terms of durability, performance, and environmental impact. Gravel bed (ballast) comprises crushed stone that provides a stable base for the sleepers, facilitates drainage, and contributes to the overall elasticity of the track infrastructure. The ballast particles absorb and distribute the impact loads exerted by moving trains, mitigating the impact on the subgrade below. The flexibility and cost-effectiveness of ballasted tracks have made them a widespread choice. However, the dynamic forces generated by high-speed trains pose significant challenges to the integrity and longevity of these tracks, necessitating regular maintenance to prevent degradation and ensure

operational safety.

In contrast, slab tracks represent a modern alternative, designed to meet the demands of high-speed rail operations with an emphasis on stability, reduced noise, and minimal maintenance [4, 6]. The key components of slab tracks include concrete slab foundation, rails and fastener and sleepers. Concrete slab foundation replaces the traditional ballast bed, providing a rigid and stable base for the rails and sleepers. The slab foundation is typically made from reinforced concrete, offering enhanced durability and resistance to deformation. Rails and fasteners are similar to ballasted tracks, but the fasteners used in slab tracks are often designed to accommodate the reduced elasticity of the system, ensuring a secure attachment to the concrete slab. Sleepers are embedded directly into the concrete slab, these sleepers are usually made from concrete due to its compatibility with the slab foundation and its ability to withstand high loads. Slab tracks offer significant advantages in terms of longevity and reduced maintenance, particularly in high-speed rail applications. The rigid structure provides a high degree of track stability, lowers noise levels from train operations, and eliminates the need for regular ballast tamping and replacement. However, the initial construction costs are higher, and the system is more sensitive to substructure deformations, requiring careful consideration during the design and construction phases.

Both ballasted and slab tracks have unique components and functionalities tailored to meet the diverse requirements of railway operations. The choice between these two types of track structures depends on various factors, including operational speeds, maintenance capabilities, environmental conditions, and budget constraints. As the railway industry continues to evolve, the development of innovative materials and construction techniques is likely to further enhance the performance and efficiency of railway track structures.

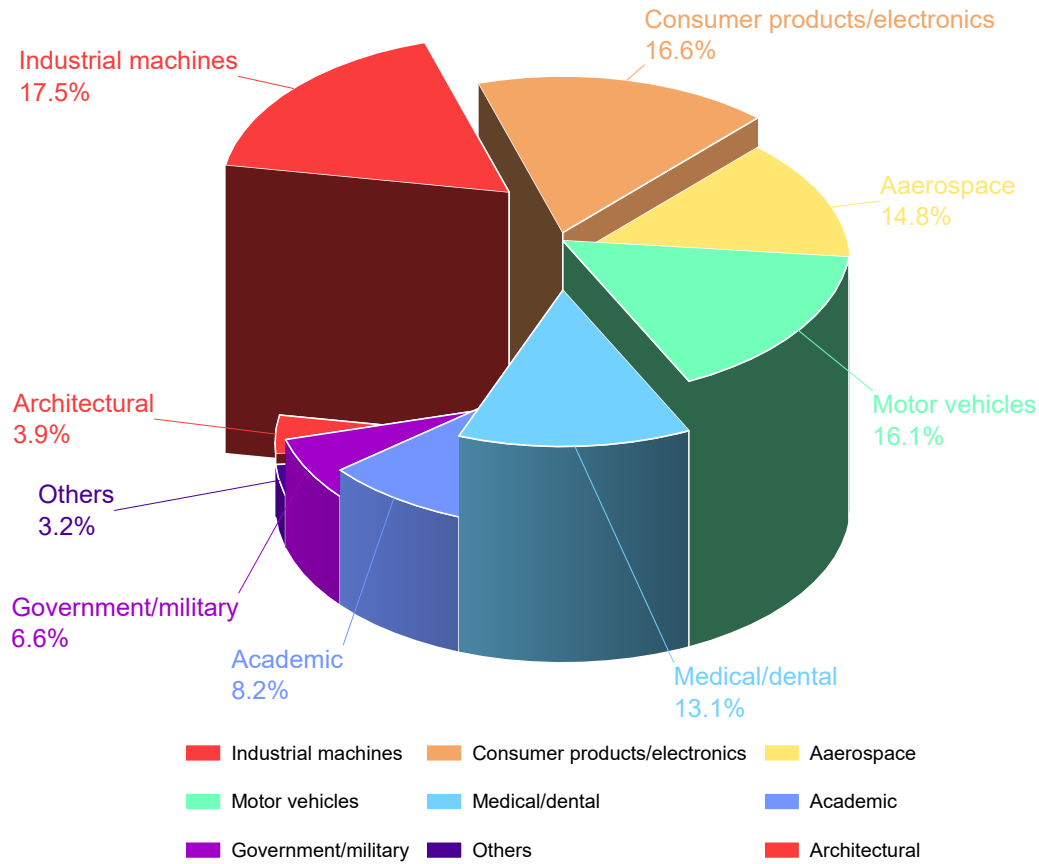


Figure 2.2 Percentage of additive manufacturing applications in different industries (Data collected from [7]).

The infusion of advanced technologies into railway engineering signifies a transformative leap towards modernizing and enhancing the railway infrastructure [8, 9]. 3D printing, or additive manufacturing, stands at the forefront of this revolution. By facilitating the layer-by-layer construction of objects from digital models, additive manufacturing introduces a level of versatility and efficiency previously unattainable. 3D printing technology has already commenced application across various sectors, as illustrated by Figure 2.2, indicating the usage of additive manufacturing in different industries up to the year 2017. In recent decades, a significant interest has emerged among numerous railway organizations and academics in integrating 3D printing technologies within the railway sector. For instance, Siemens Mobility in Germany has initiated

the Alliance for Availability programme, aiming to manufacture vehicle spare parts using 3D printing. Additionally, Mobility Goes Additive (MGA) achieved a milestone by producing the first 3D printed railway safety component. Moreover, the China Academy of Railway Sciences (CARS) launched a 3D printing office in 2016, aiming to utilise additive manufacturing technology in railway infrastructures. Its application in railway engineering spans from the production of custom parts and components to the potential creation of novel track structures, offering avenues to significantly reduce maintenance demands and enhance the overall resilience of track system.

In the context of the UK and Europe, the integration of additive manufacturing and other innovative technologies into the railway sector is increasingly recognized as a strategic imperative. From the development of spare parts for rolling stock to the exploration of 3D-printed track components, these technologies promise to address the longstanding challenges of railway maintenance and infrastructure development. Furthermore, the adoption of machine learning for predictive maintenance and the exploration of novel materials for track construction underscore the sector's move towards a more sustainable, efficient, and future-proofed railway system. This Chapter is mainly based on Paper 8 in the list of publication.

3D PRINTING IN RAILS

As a pivotal component of the railway system, directly interfacing with the wheels of rolling stock, rails play an indispensable role in load bearing, guidance, load transmission, and partial electrical circuit connections [10-12]. Typically fashioned from high-carbon and alloy steels, rails are renowned for their strength, wear resistance, and durability. The application of additive manufacturing technology, particularly through selective laser melting (SLM) additive manufacturing, has emerged as a revolutionary method for rail repair and reinforcement [13]. The SLM process encompasses a four-step methodology [14, 15]: initially, a high-energy laser melts the substrate material on the rail's surface to form a molten pool. Subsequently, a gas-assisted delivery system transports metal powder to the molten area. The third step involves the heating and melting of this powder, which then blends with the material in the molten pool before solidifying upon cooling. The final step repeats this printing process across the designated area, facilitated by the coordinated movement of the nozzle and laser according to preset parameters.



(a)



(b)

Figure 2.3 EU INFRASTAR project for enhancing the rails. (a) The reinforced railhead [16]; (b) Field test in Malmabanan [17].

The European INFRASTAR initiative marked a pioneering application of 3D printing for rail

enhancement, specifically targeting the improvement of wear and rolling contact fatigue (RCF) resistance in the railhead [16-19]. This involved the creation of a reinforced covering on the rail surface using the SLM method, with field tests conducted on the Malmaban line, as shown in Figure 2.3, demonstrating a significant extension in rail service life [20]. Subsequent research has extensively explored the repair and reinforcement of rails through 3D printing. Studies indicate that the mechanical behaviour and microstructure of treated rails are controlled by various factors within the 3D printing process [21, 22], including the type of material used, the granularity of the metal powder, printing speed, scanning pattern, and laser type. The SLM method is versatile, capable of reinforcing rails made from any material. In addition to research on Selective Laser Melting (SLM), only a single researcher has employed 3D printing technology for the fabrication of scale-model railway tracks. The material used was a composite polylactic acid (PLA), with a focus on examining its flexibility and compressive characteristics [23].

The reinforced layers produced via 3D printing can be segmented into several types according to material composition, such as Fe-based, Ni-based, Co-based, among others, as detailed in Table 2.1. Although comprehensive theoretical studies summarizing the full impact of laser melting reinforcement on rail performance are yet to be formulated, key observations from past studies include the formation of finer grains within the molten pool by high-energy lasers [24, 25], leading to more uniform overlay layers; the significant impact of powder transport speed during 3D printing on the dimensions and precision of the rail reinforcement layer [26, 27]; and the determination of grain size and shape within the reinforcement layer by the heating and cooling cycles [22, 28]. Moreover, reinforcement layers featuring angular microstructures provide higher hardness compared to those with leaf-like microstructures [29], although the hardness of the

overlay is minimally affected by slight variations in the 3D printing process [30]. The reinforcement layer can increase rail hardness internally along the surface, reaching a maximum at approximately 0.25mm thickness [31], thus enhancing wear resistance and crack resistance[32, 33]. However, thermal treatments involved in the reinforcement process, including laser heating and cooling solidification, can introduce residual stresses within the rail, potentially diminishing fatigue life and durability [34-36]. The incorporation of reinforcing materials within the overlay can further augment the rail mechanical performance [31, 37-39]. Improvements in the 3D printing process can enhance material yield strength and ultimate tensile strength, thereby offering a promising avenue for rail maintenance and longevity [40-43].

Table 2.1 Materials used by different researchers to strengthen rail.

Reference	Base material of powders	Powder type
Lai et al.(2019)[25]	Fe-based	410L, 420SS
	Co-based	Stellite 6, Stellite 21
Lu et al.(2019)[44]	Fe-based	martensitic stainless steel (MSS)
Roy et al. (2018-2020)[36, 45, 46]	Fe-based	410L, 420SS
	Co-based	Stellite 6
Fu et al.(2015)[28]	Fe-based	martensitic stainless steel (MSS)
Zhu et al.(2019)[47]	Fe-based	316L, 410L, 420L
Lewis et al. (2015-2017)[33, 48, 49]	Fe-based	Hadfield, martensitic stainless steel (MSS), 316 Stainless
	Co-based	Stellite 6
Narayanan et al. (2019)[50]	Fe-based	a premium martensitic stainless steel
Meng et al. (2019)[51, 52]	Ni-based	Not mentintoned
Wang et al.(2017-2018)[14, 15, 34]	Fe-based	AISI316L stainless steel produced by Höganäs
	Co-based	Stellite 21
Seo et al.(2019)[53]	Ni-based	Inconel 625, Hastelloy C
	Ni-based	Stellite 6
Clare et al. (2012)[29]	Ni-based	Stellite 6
Guo et al. (2015)[10]	Co-based	Not mentintoned
Wang et al. (2014)[31]	Co-based	Not mentintoned
Aladesanmi et al. (2019)[54]	Others	Ti, TiB2[54]

2.2 ADDITIVE MANUFACTURING IN FASTENER SYSTEM

The fastening system, an integral component of the railway infrastructure, predominantly consists of clips and baseplates. Its principal function is to secure the rails to the sleepers or foundations,

thereby preventing lateral movement of the rails and ensuring operational safety. Additionally, the elasticity of the fastening clips plays a pivotal role in mitigating the impact of high-speed trains on the rails, subsequently reducing rail wear. Therefore, the fastening system is imperative in keeping the safety and integrity of railway operations.

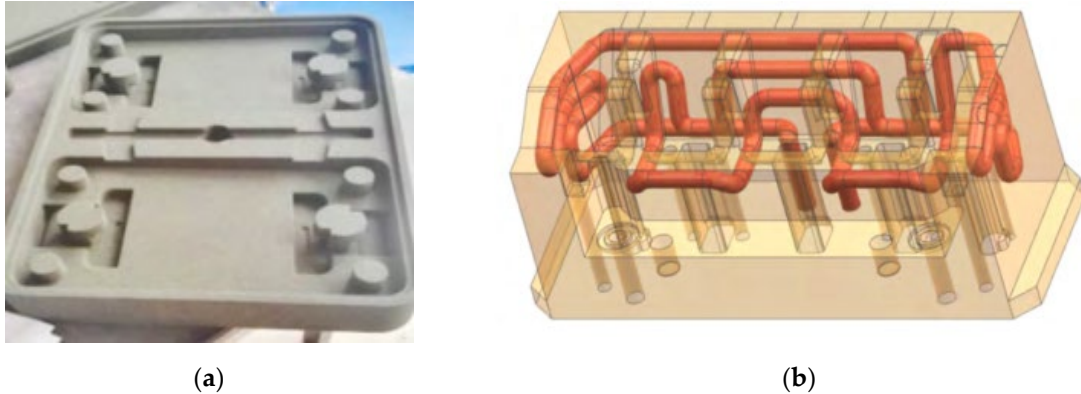


Figure 2.4 Moulds for making railway components, produced by 3D printing: (a) Mould for the fastener pad; (b) smart moulds with complex cooling channels. Retrieved from [55].

The China Academy of Railway Sciences (CARS) has explored the use of 3D printing technology to assist in the production of fastening clips [55]. Compared to the traditional casting methods typically employed in fastening clip manufacturing, the 3D printing-assisted sand casting technique significantly reduces the production time by approximately 25 days. The 3D-printed molds used in this process are illustrated in Figure 2.4. Furthermore, CARS has proposed using 3D printing technology combined with structural topology optimization to fabricate bespoke clip designs and spiral track spikes. The uniquely designed components manufactured through this method can reduce internal stress and material usage. The optimized clips and spikes are displayed in Figure 2.5.



Figure 2.5 Optimization of railway fastener components: (a) Railway clips optimized according to stress conditions; (b) 3D printed spikes. Retrieved from [55].

Currently, there is limited direct application research regarding the baseplates situated beneath the rails. However, the potential future application of 3D-printed elastic baseplates in railway systems seems promising, particularly those made from high-strength and high-stiffness cellular structures. Widely utilized in various sectors, structures such as honeycomb ([56-58]), lattice ([59-61]), and TPMS ([62, 63]) are notable for their lightweight yet high-strength characteristics. These structures, designed through appropriate structural configurations, can exhibit excellent dynamic energy absorption properties or achieve unique mechanical characteristics like a negative Poisson's ratio. Design methodologies may involve altering the size, type, and thickness of the cellular units, or implementing gradient designs. Examples of typical cellular structures are presented in Figure 2.6.

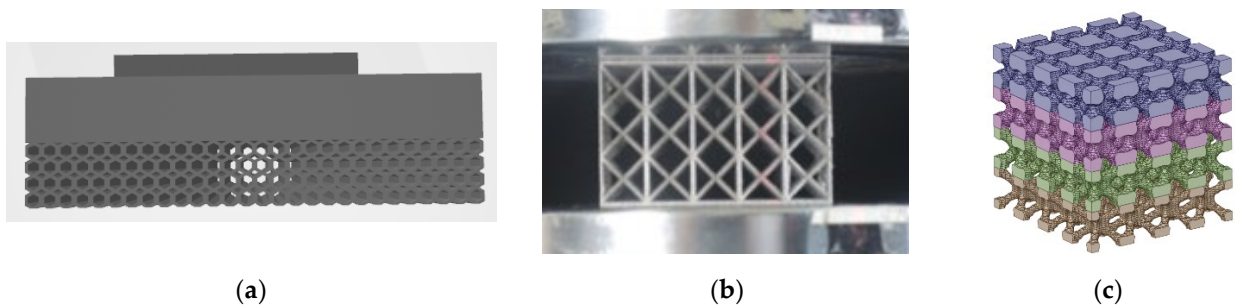


Figure 2.6 Porous structures that are potentially useful in rail pads: (a) honeycomb structure; (b) lattice structure [64] ; (c) A gradient IWP-TPMS structure.

In summary, the utilisation of 3D printing in the fastening system, particularly in the production

of clips and pads, marks a significant advancement in railway technology. The utilisation of 3D printing not only streamlines the manufacturing process but also enables the fabrication of optimized components that can enhance the overall efficiency and safety of railway operations. The exploration of innovative designs in fastening components, particularly through the use of advanced cellular structures, holds great promise for the future of railway infrastructure development.

2.3 ADDITIVE MANUFACTURING IN SUPPORTING LAYERS

This section delves into the employment of 3D print within the supporting layers of railway infrastructure. Railway track structures are fundamentally divided into ballasted tracks, comprising sleepers and a ballast bed, and ballastless tracks, which utilise concrete slabs. The discussion herein sequentially explores the utilisation of additive manufacturing technology in sleepers, ballast beds, and ballastless track slabs.



Figure 2.7 3D printed composite bearers with multi-layers, reproduced from [65].

Railway sleepers, classified by their material composition, include wooden, concrete, composite, and steel variants. Presently, composite materials are predominantly used in 3D-printed sleepers. The Shift2Rail initiative has undertaken efforts to fabricate sleepers featuring a tri-layered design with varying mechanical properties [65]. These are characterised by a gradual reduction in material density and rigidity from top to bottom, alongside a tapering thickness. The design of these

innovative 3D-printed sleepers is illustrated in Figure 2.7. Additionally, sleeper design innovations include India's FRP hollow sleepers [66], friction-type sleepers with textured undersides [67], and winged sleepers optimised for lateral stability [68, 69]. The advent of advanced composite materials and concrete 3D printing technology simplifies the manufacturing of these diverse sleeper types, as depicted in Figure 2.8. Currently, 3D printing technology facilitates the creation of scaled, intricate sleeper models for preliminary mechanical performance studies.

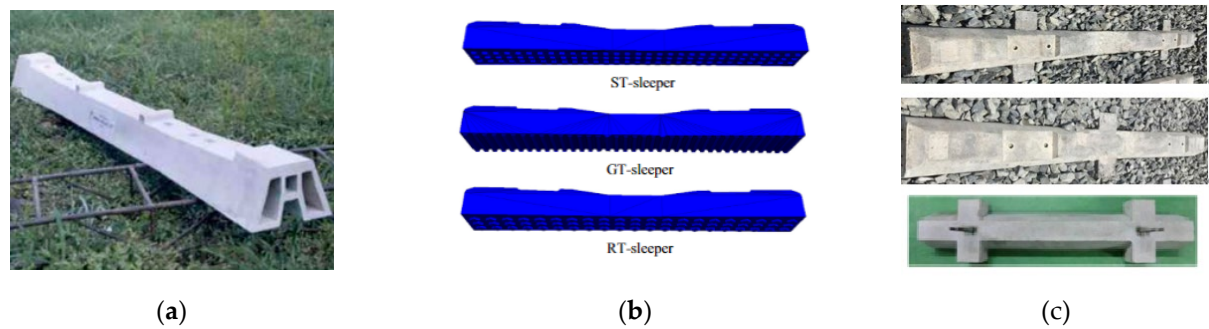


Figure 2.8 Sleepers of optimized shapes; (a) India FRP sleeper[66]; (b) frictional sleeper[67]; (c) winged sleeper[68, 69].

In the realm of railway ballast beds, 3D printing technology's application extends to the production of smart ballast particles. These are manufactured to mimic the shape of actual ballast particles, incorporating embedded wireless transmitters for six-axis (translation and rotation) acceleration sensing, enabling data transmission via Bluetooth or WiFi [70, 71]. This innovation allows for the real-time monitoring of ballast particle movement when trains pass. Furthermore, 3D-printed geogrids, as shown in Figure 2.9, can be integrated into ballasted track beds to enhance the interlocking strength between ballast particles, thereby improving the track structure's overall stability [72, 73].

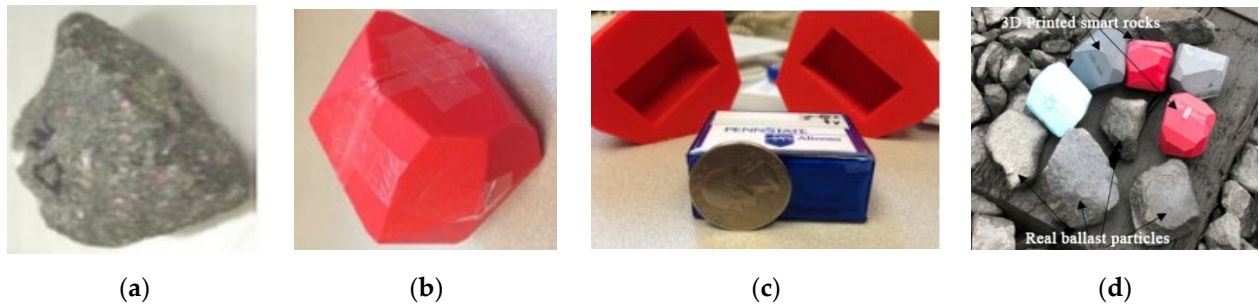


Figure 2.9 Schematic diagram of a smart ballast particle containing sensors inside: (a) geometry obtained from real ballast particle, (b) 3D printed particle with the simplified shape, (c) install sensor inside and (d) Smart sensor ballast particles and real ballast particles. Remade from [74, 75].

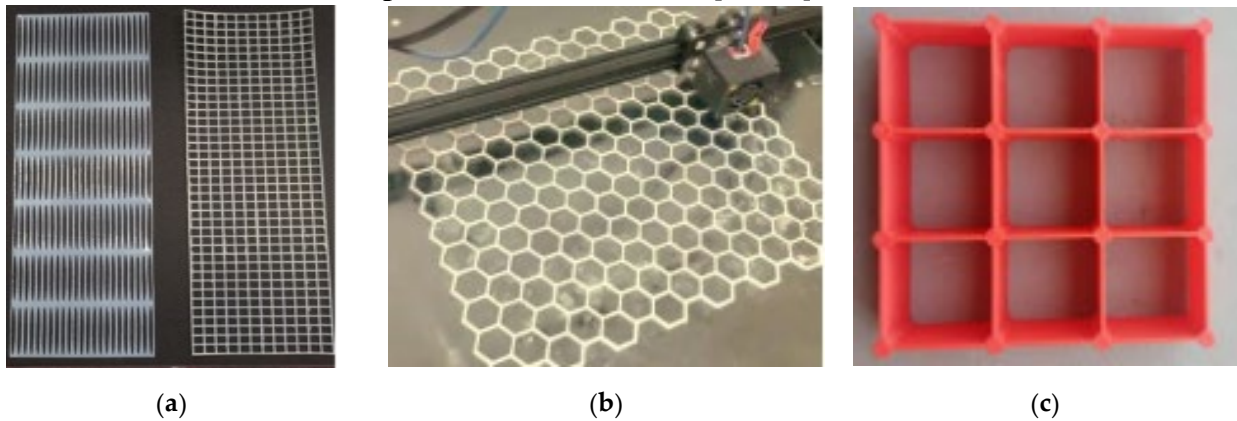


Figure 2.10 Geogrids and geocells produced by 3D printing: (a) 3D printed reduced size (one-tenth size) geogrid [72], (b) 3D printed geogrid with honeycomb holes [76] and (c) 3D printed geocell [77].

While direct applications of 3D printing in ballastless slab tracks are yet to be realised, the use of 3D-printed concrete structures has been prominent in bridge construction and architectural design. The UK's High Speed 2 (HS2) project has proclaimed the use of 3D-printed concrete slabs within its railway initiatives [78], asserting that 3D printing can significantly reduce material usage and carbon emissions.

In conclusion, the integration of 3D printing technology in railway infrastructure, from sleepers to ballast beds and potentially ballastless track slabs, represents a significant stride towards innovative, sustainable railway construction and maintenance practices. The advancements in material science and manufacturing technologies not only facilitate the creation of more durable,

efficient railway components but also underscore the potential for 3D printing to revolutionise the railway industry's approach to design, construction, and environmental responsibility.

2.4 ADDITIVE MANUFACTURING IN TPMS STRUCTURES

The development of additive manufacturing has catalyzed a paradigm shift towards lightweight designs, capitalizing on biomimicry and topological optimization to finely tune the interplay between a material's structure and its performance capabilities. Among the forefront of these innovations are TPMS structures, which are distinguished by their periodic cellular arrangement made up of interconnected rods and nodes [79]. Such structures offer the potential to meticulously adjust mechanical properties through alterations in the topology of the lattice nodes, thereby presenting a material with not only superior mechanical strengths but also the ability to dissipate energy under deformation [80-82]. This makes TPMS structures particularly advantageous for applications requiring vibration damping and impact resistance, such as in aerospace components [83, 84].

TPMS materials, defined by their minimal surface area under given constraints and characterized by a zero-mean curvature, effectively partition space into two separate regions without self-intersection, maintaining periodicity across all three spatial dimensions. The array of minimal surfaces forming TPMS has been identified in more than 17 known varieties, with particular attention paid to the Schoen Gyroid, Schwarz Diamond, and Schwarz Primitive surfaces. Discovered within cubic phases in strontium soap and lipid-water systems by Luzzati et al., and later mathematically defined by Schoen, the Gyroid minimal surface exemplifies the intricate beauty and complexity inherent in TPMS structures.

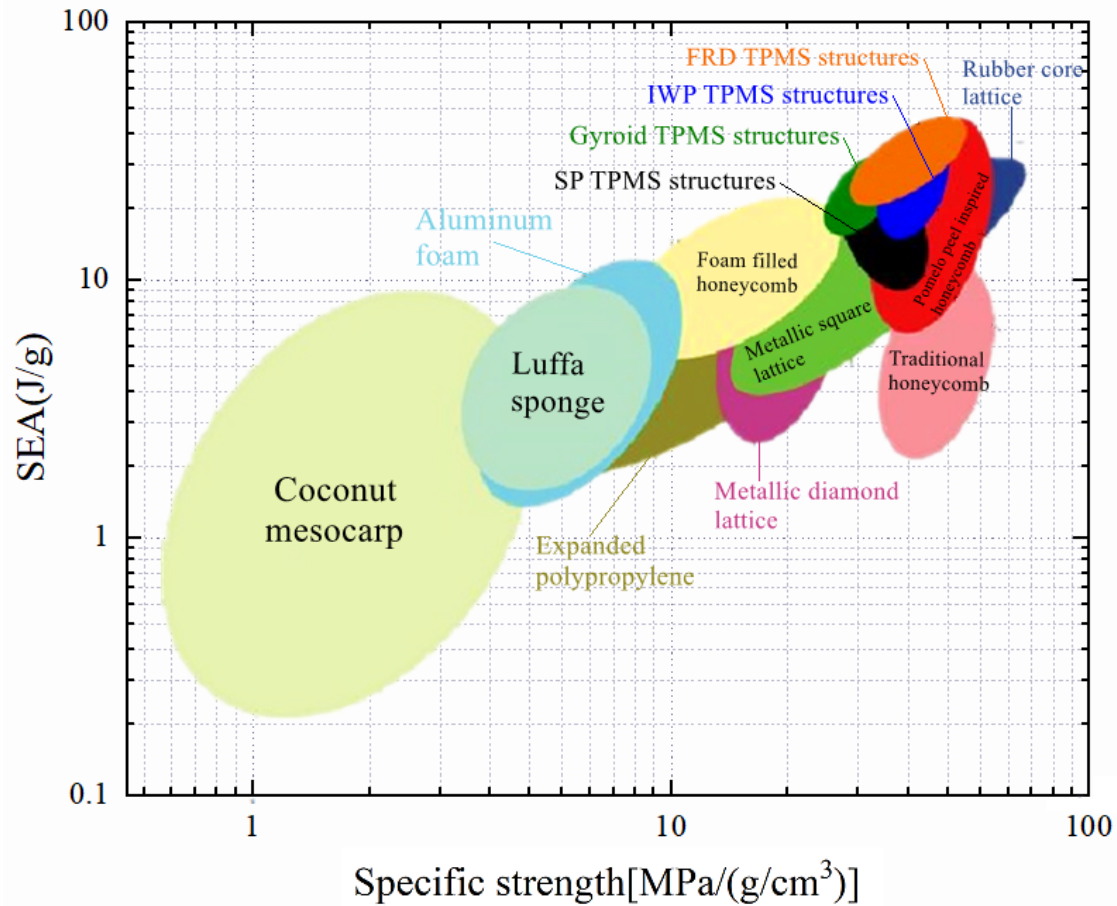


Figure 2.11 Value ranges of specific energy absorption (SEA) and specific strength of various popular porous structures.

TPMS structures not only match the high performance of truss lattice configurations, including light weight, high strength-to-weight ratios, and enhanced energy absorption but also inherit smooth surface qualities and uniform curvature radii from TPMS surfaces [85]. These characteristics facilitate even stress distribution under loads, thereby improving fatigue resistance and expanding the scope for applications. The complexity of fabricating TPMS lattice structures, traditionally challenging with conventional methods, has been addressed through advancements in additive manufacturing technologies. It is concluded that TPMS structures have competitive specific strength and SEA as indicated in Figure 2.11, showcasing the potentials of TPMS supports over other structures and highlighting their suitability for biomorphic scaffold designs due to their

smooth surfaces and uniform curvature radii. TPMS's unique properties have sparked interest across various disciplines, including mechanical, material, chemical, and biomedical engineering, with research focusing on their mechanical behaviour, heat and mass transfer capabilities, and their potential in tissue engineering and acoustics.

In tissue engineering, TPMS scaffolds meet the critical requirements of connectivity, porosity, and surface morphology for nutrient transport and waste removal, while microgeometry on TPMS surfaces promotes cell adhesion and proliferation. The revolutionary progress in additive manufacturing has eased the constraints on manufacturing complexity, enabling the digital fabrication of geometric microstructures with intricate topologies, pushing forward the creation of geometric microstructures across fields such as aerospace, architectural engineering, and biomedical devices. Inspired by natural structures, researchers have embarked on designing artificial biomimetic geometric microstructures for various applications, including lightweight corrugated panels and high-efficiency thermal exchangers. TPMS structures, embodying the principles of minimal surfaces with zero mean curvature, smooth connectivity, and an elevated surface-to-volume ratios, have found widespread application in cooling devices, implants, energy-absorbing structures, and lightweight architectural designs. This exploration into TPMS and its integration into additive manufacturing showcases the intersection of natural inspiration [62, 86-88] and technological innovation, highlighting TPMS's significant potential in advancing material science and engineering applications.

In the realm of TPMS structures, three variants currently dominate the field of research: the I-graph-wrapped package (IWP) surface, the Gyroid surface, and the Schwarz Primitive (Primitive) surface, as shown in Figure 2.12. Illustrations of these TPMS surfaces provide a visual

understanding of their intricate designs. Researchers have embarked on the fabrication of both skeletal and sheet-like structures based on these surfaces, employing a variety of materials for 3D printing and subjecting them to comprehensive testing to evaluate their strength, modulus, and energy absorption capabilities.

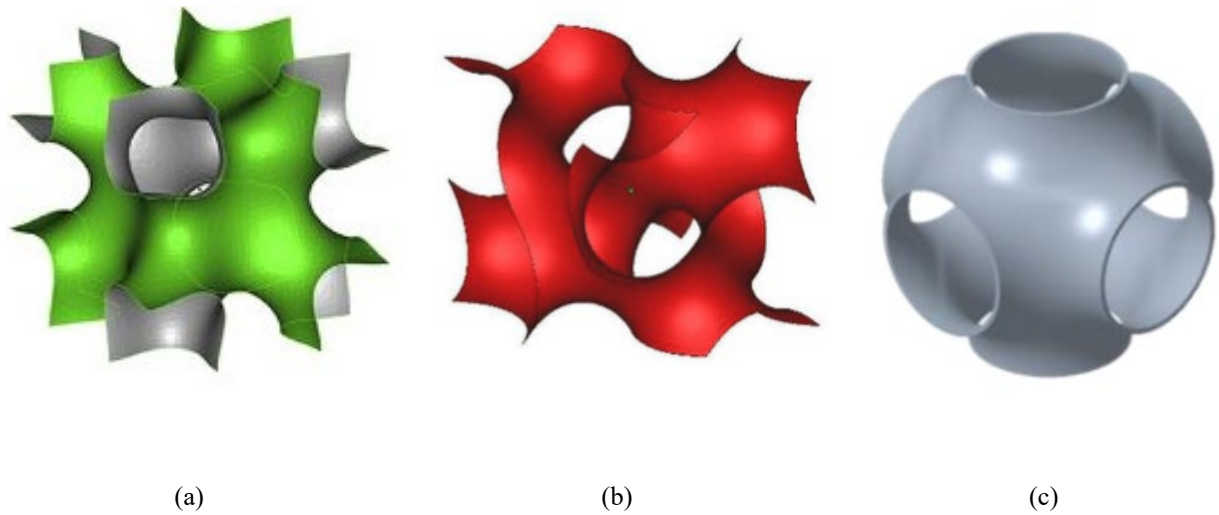


Figure 2.12 Schematic representation of the three most widely studied TPMS surfaces. (a) IWP, (b) Gyroid and (c) Primitive.

Xiaoyang Zheng undertook a research on the mechanical performance and structural relationships of four types of topological bicontinuous porous structures derived from TPMSs, including Gyroid, Diamond, SP, and IWP configurations, using a combination of numerical analysis, computational simulation, and experimental validation [89]. The study investigates how these structures' microarchitectures influence their macroscopic mechanical behaviours, particularly focusing on stiffness, strength, and deformation modes. Through FEM, Ahmed S. investigated the elastic behaviours of interpenetrating phase composites (IPCs) reinforced with seven distinct TPMS structures, revealing enhanced stiffness in all directions and unique deformation behaviours compared to traditional composites. Particularly, the IWP-IPC exhibits superior elastic characteristics and the capacity for deformation through stretching at low volume fractions,

offering new directions for future material design and applications [90]. Diab W. Abueidda introduced innovative cellular materials crafted from several TPMSs, demonstrating via FEM analysis that their electrical/thermal conductivities and mechanical properties correlate with density, with CLP-foam exhibiting distinct anisotropy. It underscores TPMS-based foams' engineering potential, particularly emphasizing the Gyroid-sheet's enhanced performance over traditional lattice configurations. [91].

Oraib Al-Ketan explored the mechanical performances of 3D printed IPCs with architectures based on TPMSs, revealing that these composites are dominated by bending deformation and are suited in damage tolerance and vibration damping applications. Employing computer-aided design and Polyjet 3D printing, it was demonstrated that TPMS-based IPCs, particularly those incorporating the IWP geometry, offer superior mechanical performance and stress distribution compared to traditional rod-connected architectures, highlighting the significant impact of phase topology on composite material properties [85]. Alya Alhammadi investigated the microstructure and mechanical behaviours of laser powder bed fusion (LPBF) fabricated AlSi10Mg IWP cellular structures, revealing that heat treatment enhances ductility due to grain growth, despite a reduction in tensile strength with rising test temperatures. It was found that the structural integrity and structural properties of these IWP metallic cellular structures are significantly influenced by thermal treatments, which modify grain structure and size, affecting the material's strength and ductility, particularly under varying testing temperatures and relative densities [92]. Biwei Deng introduced a novel class of mechanical metamaterials based on several types of sheetal TPMS structures, including IWP, SP, FRD, and SD, demonstrating superior mechanical properties and ease of production, particularly in 3D printing, across a broad range of densities [93]. Kamran A

researched the viscoelasticity in both time and frequency domain and elastic response of IWP structures [94]. Nejc Novak assessed the quasi-static behaviours of four types of sheetal TPMS structures under compressive loads, revealing enhanced mechanical properties and strain rate hardening, with the Diamond type showing the peak plateau stress level and specific energy absorption [95]. Mariam Ouda demonstrated TPMS-based static mixers with sheetal Gyroid, Diamond, SP, and IWP structures in energy efficiency with comparable or superior mixing efficiency, especially in single-element configurations [96]. Zahid Ahmed Qureshi highlighted the potential of TPMS cells (sheetal Gyroid, IWP, and SP) in improving latent heat thermal energy storage systems, demonstrating their superiority in energy efficiency and thermal management [97]. Minhao Shen fabricated and tested TPMS-based cellular ceramics of sheetal IWP, SP, and SP surfaces, demonstrating that compressive strength increases with relative density, with the s14 structure showing the highest strength. [98]. Xin Shi proposed a novel optimization method merging topology optimization with TPMS architectural design to enhance the stiffness of TPMS lattice structures, with effectiveness verified through finite element analysis and experiments [99]. Ugur Simsek compared the exactitude and efficiency of computation of five modelling processes for modal characterization of TPMS structures, finding super-element modelling notably effective [100]. Hanfeng Yin found researched the crashworthiness of sheetal TPMS structures under axial impact using nonlinear FEM and found that the FRD-sheet structure as having superior energy absorption capacity [80].

Altintas investigated the natural vibrational behaviour of beams formed from TPMS unit cells, revealing significant influences of material type, geometry, and wall thickness on their modal characteristics. It was found that variations in wall thickness notably affect the stiffness and mass

of TPMS-based structures, impacting their natural vibration modes, with thicker walls increasing rigidity more than mass, thereby affecting high vibration modes substantially [101]. Elmadih and colleagues demonstrated that TPMS lattice structures, particularly network and matrix gyroid lattices, exhibit mechanical bandgaps that can be tuned for vibration isolation by adjusting cell size and volume fraction. This ability to control bandgaps opens up new possibilities for designing lattice structures with inherent vibrational isolation properties, suitable for various engineering applications [102]. Simsek et al. focused on the modal parameters of Gyroid based structures fabricated from metal material HS188, revealing a strong correlation between simulation models and experimental modal testing. It highlighted the impact of wall thickness on modal parameters, suggesting that Gyroid-based structures offer promising dynamic performance for engineering applications and underscoring the potential of simulation and optimization in advancing additive manufacturing technologies [103]. Viet and his team built several FEM models to investigate the modal shapes and natural frequency of gradient TPMS beams, finding that cubic functions effectively express stiffness dependence on porosity, and various factors significantly influence vibrational and buckling behaviours. It was observed that the mass distribution, beam size and nature of the material have substantial effects on the performance of these beams, with specific tpms geometries and materials showing distinct advantages in terms of inherent vibrational frequency and critical load stress [104].

2.5 RESEARCH GAPS

The incorporation of additive manufacturing technologies in railway engineering is at the forefront of innovative exploration, emanating from its proven efficacy in facilitating lightweight constructions within the realms of civil construction and aerospace sectors. The unique capability

of additive manufacturing to realise structures of complex geometries facilitates the achievement of sophisticated mechanical properties and architecturally aesthetic designs. TPMS structures stand out for exceptional attributes, such as superior strength-to-weight ratios, stiffness-to-weight ratios, and remarkable energy absorption capacities. These characteristics position TPMS structures as a transformative solution across a broad spectrum of applications, notably within the demanding discipline of civil engineering and, specifically, in the enhancement and development of railway infrastructure.

The array of materials amenable to additive manufacturing spans polymers, including photo-sensitive resins, thermoplastic polymers, and hydrogels, to metals such as iron, titanium, cobalt, and copper alloys, and extends to ceramics encompassing cementitious materials, clays, and silicate glasses. This diversity enables the construction of structures with intricate shapes through various additive manufacturing processes. Notwithstanding these advancements, the mechanical performance of materials produced via 3D printing frequently falls short due to inherent inaccuracies in the printing process, leading to outcomes that may be inferior compared to those produced through traditional casting methods. Challenges such as uneven internal deformation, residual stresses, porosity, and the presence of micro-cracks can significantly compromise the strength and longevity of printed components. This predicament is exacerbated by the lack of universally recognised standards for the quality assurance of 3D printed materials, introducing a level of uncertainty that acts as a barrier to the widespread adoption of this technology within railway engineering. Moreover, the inherent dimensional limitations associated with current 3D printing technologies pose substantial challenges in fabricating large-scale components, such as railway sleepers or track supports, which exceed the size constraints of standard printers.

Historically, the body of research on TPMS structures has predominantly resided within the materials science domain, focusing on units of relatively minor scale. This focus contrasts sharply with the scale and complexity of challenges present in civil engineering applications, especially within the context of railway infrastructure, where structural units required are significantly larger and subject to a wide range of complex loading conditions. This discrepancy underscores a notable gap in the research, particularly in terms of understanding the mechanical behaviour and performance of large-scale TPMS structures under the dynamic and static loads characteristic of railway infrastructure.

Furthermore, the exploration of the impact of TPMS unit cell arrangement on the mechanical properties of structures within civil engineering is notably lacking. The promise of 3D printing technology to customise the geometry of TPMS structures offers a promising avenue for enhancing structural performance, specifically addressing engineering challenges such as optimising load distribution, improving vibration damping capabilities, and ensuring resilience under environmental stressors. Despite this potential, the strategic arrangement of TPMS units and their application on a large scale within civil engineering projects remain under-researched areas, necessitating focused scholarly inquiry. It is imperative to understand how various configurations of TPMS structures can be optimised for mechanical performance, considering the unique demands of railway engineering.

An immediate imperative for thorough research into the application of TPMS structures within railway engineering is paramount. A thorough exploration of the dynamic characteristics and comprehensive performance evaluation of TPMS structures under realistic operational conditions is essential to advance the adoption of 3D printing technologies in railway infrastructure. Such

scholarly endeavours should aim to bridge the current knowledge gaps regarding the scale-up process, arrangement optimisation, and overall implementation of TPMS structures for civil engineering applications. By leveraging the full potential of 3D printing to fabricate complex shapes, these efforts could significantly enhance the mechanical performance and aesthetic design of railway components. The successful integration of 3D printed TPMS structures into railway infrastructure not only promises to augment the durability and performance of these systems but also contributes towards the development of more efficient, sustainable, and robust railway infrastructure. This advancement has the potential to revolutionise the construction and maintenance of railway systems, aligning with broader objectives of innovation, sustainability, and enhanced performance within civil engineering projects. In summary, the current research into the application of TPMS within railway engineering uncovers significant gaps that demand focused scholarly attention. While additive manufacturing technologies have shown great promise in various sectors, their integration into railway infrastructure highlights specific challenges and opportunities for innovation. These applications pose unique challenges, including the need for structures that can withstand diverse and complex loading conditions. The research to date has concentrated on small-scale experiments within the materials science field, which do not adequately address the complexities faced in civil engineering contexts. There is a critical need to extend these studies to understand the behaviour and performance of TPMS structures under the dynamic and static loads typical of railway environments. Additionally, the impact of various TPMS unit cell configurations on structural integrity and performance remains poorly explored. Such investigations are essential to optimise load distribution, enhance vibration damping, and ensure resilience under environmental stressors in railway applications.

CHAPTER 3

TPMS SURFACES AND STRUCTURES GENERATION

3.1 INTRODUCTION

TPMSs are distinguished by their continuous minimal surface area within a given boundary, a concept derived from the mathematical discipline of differential geometry. These surfaces are increasingly utilised across a broad spectrum of fields, including materials science, architecture, and biomedical engineering, due to their optimal surface area to volume ratios and their intricate yet visually appealing geometrical characteristics. Such attributes make TPMS particularly appealing for innovative design and manufacturing applications requiring efficiency and aesthetic value.

The aim of this chapter is to explicate the processes involved in generating TPMS surfaces and structures. It begins with a concise historical and theoretical overview of TPMS, setting the stage for a deeper exploration of their unique properties. The discussion then shifts to the mathematical expressions that describe TPMS, establishing a foundation for appreciating their geometric complexity and the computational techniques used in their creation. The latter sections of the chapter address the practical aspects of fabricating solid TPMS structures, including the various methods employed in their 3D printing. This exploration not only reinforces the theoretical knowledge of TPMS but also bridges the gap to their practical application in cutting-edge technological domains. This chapter is essential for the subsequent chapters that focus on the testing and simulation of 3D printed TPMS structures. The foundational digital and 3D printed models developed in this chapter facilitate the further modelling and experimental work necessary for advancing this field of study. This Chapter uses the information from Paper 1 to 4 and Paper 6, 8 and 10 listed in the LIST OF PUBLICATION.

3.2 PROPERTIES OF TPMS

TPMS structures represent a fascinating type of structures identified by their geometric arrangement, which extends periodically in three dimensions without any self-intersections. The curvature κ of a point at any position on the TPMS is defined as inverse value of the radius pertaining to the circle of best fit along the curve where it crosses the perpendicular plane to the surface at a given point [40]. The κ_1 and κ_2 denote the peak and trough principal curvatures at a specific location. The Gaussian curvature K , defined as $K(p) = \kappa_1 \cdot \kappa_2$, is adopted as an inherent metric of curvature. The mean curvature, H , calculated as $H(p) = \frac{1}{2}(\kappa_1 + \kappa_2)$, is the average of the peak and trough principal curvatures. All the points on any TPMS are of $H(p) = 0$ and $K(p) \leq 0$, which means TPMSs are one group of minimal surfaces. These surfaces, notable for their minimal surface area under specific constraints and a mean curvature of zero across the entire structure, effectively divide space into two distinct regions. TPMS structures have been identified in various nature-inspired forms, such as the skeletal patterns of sea urchins, biological membranes, butterfly wing scales (Figure 3.1), and the exoskeletons of beetles (Figure 3.2), underscoring their significance in both natural and engineered systems.

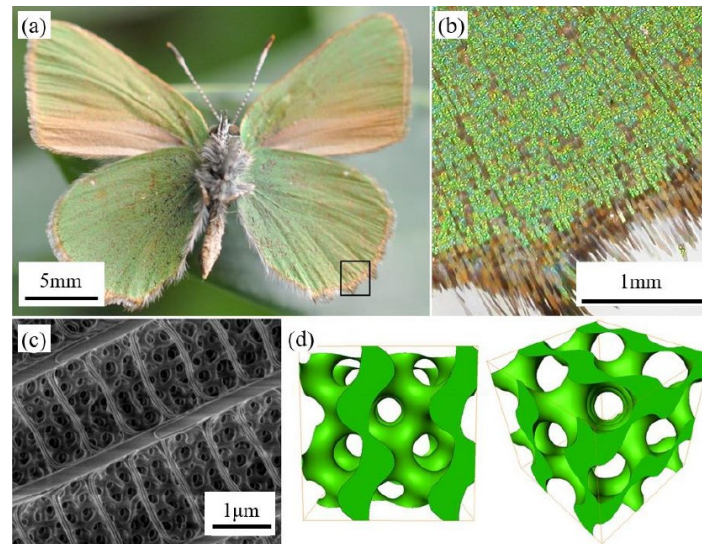


Figure 3.1 *Polyommatus icarus* butterfly and the elaborate microarchitecture of its wing scales: (a) displays the underside of the *Polyommatus icarus*, (b) reveals a plethora of verdant scales affixed to the wing, each embedding gyroid configurations, (c) offers a SEM (Scanning Electron Microscopy) depiction of the gyroid formations on the ventral scale surface, and (d) demonstrates a conceptual model of the anticipated gyroid structure viewed along axes $\langle 001 \rangle$ (left) and $\langle 111 \rangle$ (right)[105].

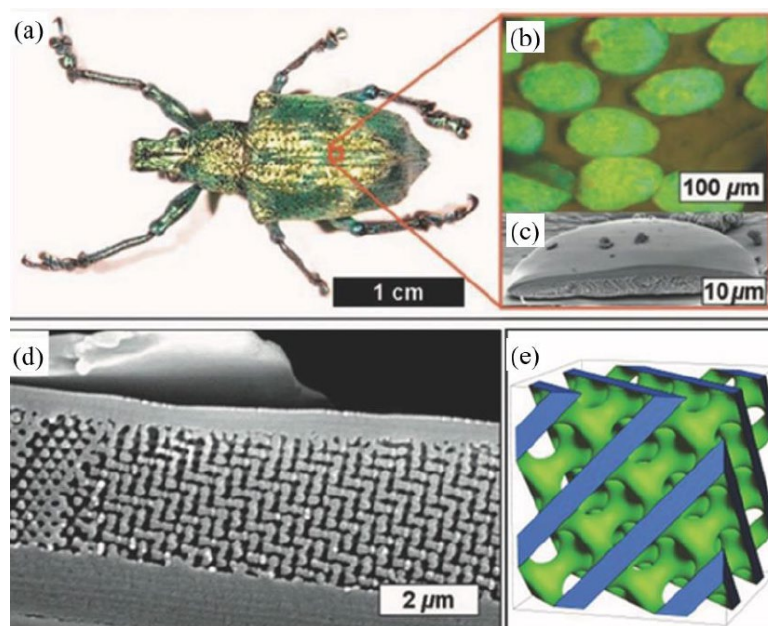


Figure 3.2 An examination of the weevil and its microstructural features: (a) captures an image of the weevil, (b) and (c) provide, respectively, an optical microscopy image and a Scanning Electron Microscopy (SEM) image showcasing the scales affixed to the exoskeleton, (d) a cross-sectional SEM picture and (e) a schematic illustration of a Diamond frame [106].

The unique properties of TPMS, including their smoothness and the uniform distribution of curvature, make TPMS based structures an optional candidate for a broad application across mechanical, material science, chemical, and biomedical disciplines [107, 108]. Their smooth surface minimizes stress concentrations, leading to structures with high specific strength and rigidity, suitable for creating supportive frameworks [109]. Moreover, the fully interconnected nature of these surfaces, without isolated voids, facilitates continuous passages for materials, making them particularly relevant for tissue engineering where nutrient transport and waste removal are critical.

The high surface area-to-volume ratio of TPMS enhances their efficiency in heat transfer applications, with their geometry significantly impacting fluid dynamics and thermal properties, such as Reynolds number and heat transfer efficiency [110, 111]. The smoothness of TPMS also contributes to reduced resistance in fluid flow, making them highly suitable for applications in thermal management.

In acoustics, the porous nature of TPMS can be tailored to create bandgap structures that impede the propagation of sound waves across various frequencies, offering potential solutions for sound absorption and noise reduction [112-114]. This adaptability extends to tissue engineering, where the connectivity, porosity, and surface morphology of scaffolds are crucial. TPMS naturally meets these requirements, supporting cell attachment and proliferation through easily adjustable parameters like frequency and wall thickness.

Recent research has highlighted the performance of TPMS structures in terms of mechanical properties, such as elasticity, shear modulus, yield strength, and anisotropy under varying

conditions of relative density [115-118]. These studies affirm that TPMS's uniform stress distribution contributes to superior fatigue performance and a broader range of applications. The complexity of TPMS structures, traditionally challenging to manufacture, is now being addressed through advanced additive manufacturing (AM) techniques, opening up possibilities in aerospace, biomedical, and optimization fields.

The growing interest in TPMS and related materials across various sectors is driven by their complex and highly symmetrical structures, along with emerging evidence of their exceptional physical, chemical, mechanical, and optical properties. As the understanding of these surfaces expands, so too does their potential for innovative applications, making TPMS a key area of focus for future research and development.

3.3 MATHEMATICAL EXPRESSION OF TPMS

The Weierstrass-Enneper representation is capable for describing TPMSs [119-121]. These surfaces find extensive applications in various scientific and engineering fields, including material science, architecture, and biology, due to their unique structural properties, as indicated in Equation 3.1 to Equation 3.3. In these equations, $X(u, v)$ is a point in three-dimensional space. $P(z)$ is a polynomial, often used to control the curvature. $f(z)$ and $g(z)$ are complex functions derived from the integral of $P(z)$. The parameters often vary according to the specific kind of TPMS in question (for example, SP, Schwarz D, Gyroid, etc.).

To describe a TPMS using the Weierstrass-Enneper representation, one must identify suitable meromorphic function $g(z)$ and holomorphic function $f(z)$ that satisfy the specific periodic conditions of the TPMS in question. A meromorphic function is analytic except at isolated points

where it may have poles, while a holomorphic function is analytic at every point within its domain. The choice of these functions is crucial as they determine the geometry and the periodicity of the resulting surface. The first step is choosing a meromorphic function $g(z)$ and a holomorphic function $f(z)$ such that their product $g(z)f(z)$ represents the desired geometric characteristics and periodicity of the TPMS. The functions must be defined on a domain in the complex plane that reflects the symmetry and periodicity of the target TPMS. These functions are integral to capturing the geometric characteristics and periodicity inherent to TPMS. The representation is founded on the computation of the real parts of complex integrals derived from these functions, encapsulated in Equation 3.1 to Equation 3.3. The procedure not only demands a thorough understanding of complex analysis and differential geometry but also necessitates an analytical approach to the selection of $g(z)$ and $f(z)$. This selection is paramount, as the characteristics of these functions directly influence the geometry and periodicity of the TPMS. Furthermore, the process may require iterative refinement of these functions to accurately model the TPMS's unique geometric features while adhering to the principles of minimal surfaces. This methodological approach underscores the complexity and analytical depth required in applying the Weierstrass-Enneper representation to TPMS. It exemplifies a blend of mathematical rigour and geometric intuition, aimed at achieving an accurate and periodic representation of TPMS through the precise manipulation of complex functions.

$$f(z) = \Re \int_0^z P(t)dt \quad 3.1$$

$$g(z) = \Im \int_0^z P(t)dt \quad 3.2$$

$$X(u, v) = \Re \int \left(\frac{1}{2}(1 - g^2)du + i \frac{1}{2}(1 + g^2)dv + (f - i\bar{f})dz \right) \quad 3.3$$

Another way to represent TPMSs mathematically is using Fourier series [122-124]. The representation of TPMSs through Fourier series is an insightful approach that captures the inherent periodicity and complex geometry of these surfaces. This method utilises the principle that every periodic function can be represented as a combination of sines and cosines multiplied by a factor that represents the amplitude of a particular frequency. In the context of TPMS, this translates to expressing the surface's geometry in terms of harmonic components that together delineate its periodic structure in three-dimensional space.

To embark on such a representation, one initially considers the surface's parametric equations, which define the spatial coordinates $X(u, v)$, $Y(u, v)$, and $Z(u, v)$ in terms of two factors u and v . The essence of employing a Fourier series in this scenario is to express each of these coordinates as an infinite sum of sinusoidal functions, with frequencies matching the surface's periodicity in different axial directions. The Fourier series representation of a TPMS are expressed in Equation 3.4 to Equation 3.6 for each coordinate.

$$X(u, v) = \sum_{n=-\infty}^{\infty} \sum_{m=-\infty}^{\infty} a_{nm} e^{i(n\alpha u + m\beta v)} \quad 3.4$$

$$Y(u, v) = \sum_{n=-\infty}^{\infty} \sum_{m=-\infty}^{\infty} b_{nm} e^{i(n\alpha u + m\beta v)} \quad 3.5$$

$$Z(u, v) = \sum_{n=-\infty}^{\infty} \sum_{m=-\infty}^{\infty} c_{nm} e^{i(n\alpha u + m\beta v)} \quad 3.6$$

Here a_{nm} , b_{nm} , and c_{nm} are the Fourier coefficients that need to be determined for each harmonic component, and α and β are constants that relate to the periodicity of the TPMS in the u and v parametric plane, respectively. The complex exponential function $e^{i(n\alpha u + m\beta v)}$ represents the harmonic basis functions, with i being the imaginary unit.

The determination of the Fourier coefficients is a critical step in this representation, requiring the application of Fourier analysis techniques to the surface's geometric data. These coefficients encapsulate the amplitude and phase of each harmonic component, thereby defining the surface's shape and periodicity.

This Fourier series approach offers a powerful tool for analysing and synthesising TPMS, enabling the examination of their properties in the frequency domain. It facilitates the study of the surface's structural characteristics, such as symmetry, smoothness, and the distribution of curvature, by inspecting the amplitude and distribution of its harmonic components. Furthermore, this representation is invaluable in computational modelling and simulation, providing a method for approximating the surface with a finite number of harmonic terms, thus making numerical calculations feasible.

The Fourier series representation of TPMS is a sophisticated mathematical framework that captures the essence of these surfaces through harmonic analysis. It not only provides a deeper understanding of their geometric and periodic properties but also offers practical benefits in computational modelling and the exploration of their physical and architectural applications.

The expression of TPMSs as implicit functions offers a different perspective from the parametric or Fourier series representations. An implicit function for a TPMS is a scalar function $F(x, y, z)$ defined in three axial directions, where the surface is represented when output equals zero ($F(x, y, z) = 0$). This form is particularly useful for identifying points on the surface without explicitly parameterising the surface in terms of two variables, as is done in parametric representations. To express a TPMS as an implicit function, one would define a function $F(x, y, z)$

such that for any point (x, y, z) on the TPMS, F evaluates to zero. The challenge lies in determining the precise form of F that captures the geometry and periodicity of the TPMS. The function F typically involves combinations of trigonometric, polynomial, or other mathematical functions that adhere to the surface's triply periodic nature.

The most employed implicit method to define TPMSs indeed utilises the function of a Fourier series. The approach succinctly captures the essence of TPMS by representing the surface as a sum of cosine terms, each modulated by amplitude factors and phase shifts, thereby encapsulating the surface's periodic nature in three dimensions. The formal expression provided in Equation 3.7.

$$\Phi(\mathbf{r}) = \sum_k F(k) \cos[2\pi \mathbf{k} \cdot \mathbf{r} - \alpha(k)] = 0 \quad 3.7$$

Here $F(k)$ denotes the amplitude factor associated with each vector \mathbf{k} , \mathbf{r} represents the vector of position in three axes, and $\alpha(k)$ is the phase shift corresponding to each vector, captures the mathematical foundation underlying TPMS representation in terms of Fourier series. The utilisation of a Fourier series for defining TPMS leverages the intrinsic periodicity of these surfaces across three independent spatial directions. The amplitude factor $F(k)$ and the phase shift $\alpha(k)$ play crucial roles in shaping the geometry and topology of the surface, allowing for a detailed characterisation of its features. By adjusting these parameters, one can model a wide range of TPMS with varying complexities and geometric properties. Table 3.1 lists the mathematic expressions and single-cell images of several common types of TPMSs. Table 3.2 lists the equations of several types of TPMSs of complex shapes. Herein, $X = 2\pi x, Y = 2\pi y, Z = 2\pi z$. The unit cell size is 1. Those mathematic functions are obtained from past research [125, 126], and the images are produced using matlab.

Table 3.1 Mathematic expressions and images of several common TPMSs

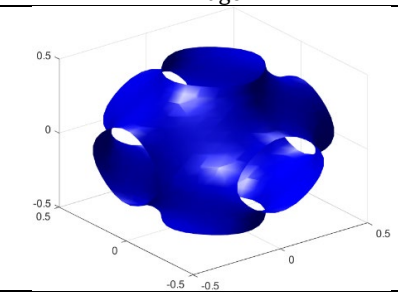
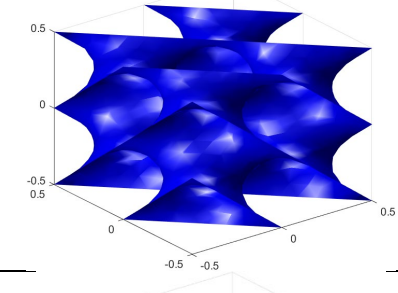
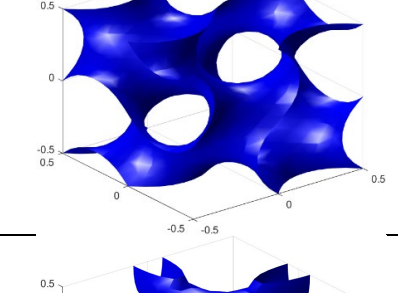
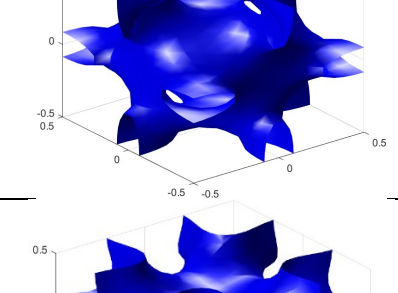
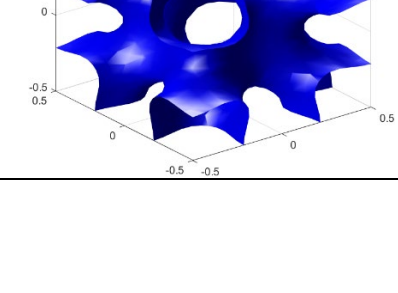
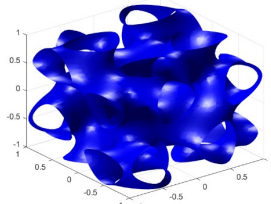
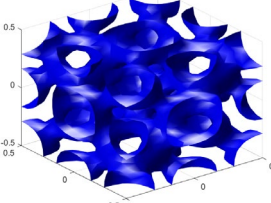
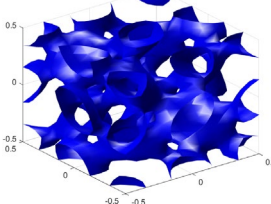
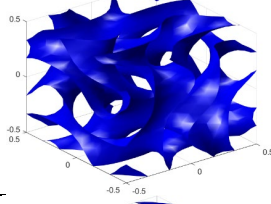
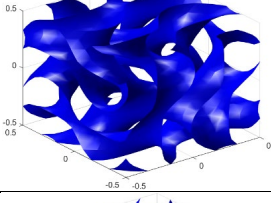
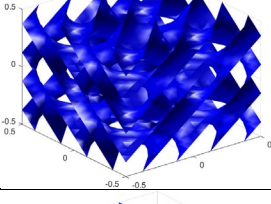
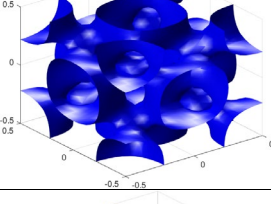
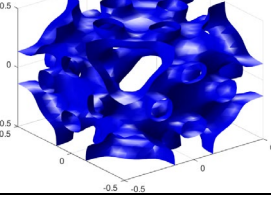
TPMS Type	Nodal approximation equation	Image
Schwarz P (SP)	$\Phi(\mathbf{r}) = \cos X + \cos Y + \cos Z = 0$	
Diamond (D)	$\Phi(\mathbf{r}) = \sin X \sin Y \sin Z + \sin X \cos Y \cos Z + \cos X \sin Y \cos Z + \cos X \cos Y \sin Z = 0$	
Gyroid (G)	$\Phi(\mathbf{r}) = \sin X \cos Y + \sin Y \cos Z + \sin Z \cos X = 0$	
Neovius	$\Phi(\mathbf{r}) = 3(\cos X + \cos Y + \cos Z) + 4\cos X \cos Y \cos Z = 0$	
IWP	$\Phi(\mathbf{r}) = 2(\cos X \cos Y + \cos Y \cos Z + \cos X \cos Z) - (\cos 2X + \cos 2Y + \cos 2Z) = 0$	

Table 3.2 Nodal expressions and images of some complex TPMSs.

TPMS Type	Nodal approximation equation	Image
The Split P Surface	$\Phi(\mathbf{r}) = 1.1(\sin 2X \cos Y \sin Z + \sin 2Y \cos Z \sin X + \sin 2Z \cos X \sin Y) - 0.2(\cos 2X \cos 2Y + \cos 2Y \cos 2Z + \cos 2X \cos 2Z) - 0.4(\cos 2X + \cos 2Y + \cos 2Z) = 0$	
The D prime Surface	$\Phi(\mathbf{r}) = 0.5(\sin X \sin Y \sin Z + \cos X \cos Y \cos Z) - 0.5(\cos 2X \cos 2Y + \cos 2Y \cos 2Z + \cos 2X \cos 2Z) - 0.2 = 0$	
The Lidinoid Surface	$\Phi(\mathbf{r}) = 0.5(\sin 2X \cos Y \sin Z + \sin 2Y \cos Z \sin X + \sin 2Z \cos X \sin Y) - 0.5(\cos 2X \cos 2Y + \cos 2Y \cos 2Z + \cos 2X \cos 2Z) + 0.15 = 0$	
Double Gyroid	$\Phi(\mathbf{r}) = 2.75(\sin 2X \cos Y \sin Z + \sin 2Y \cos Z \sin X + \sin 2Z \cos X \sin Y) - (\cos 2X \cos 2Y + \cos 2Y \cos 2Z + \cos 2X \cos 2Z) = 0$	
G Prime	$\Phi(\mathbf{r}) = 5(\sin 2X \cos Y \sin Z + \sin 2Y \cos Z \sin X + \sin 2Z \cos X \sin Y) + (\cos 2X \cos 2Y + \cos 2Y \cos 2Z + \cos 2X \cos 2Z) = 0$	
Double Diamond	$\Phi(\mathbf{r}) = (\sin 2X \sin 2Z + \sin 2Y \sin 2Z + \sin 2X \sin 2Y) + \cos 2X \cos 2Y \cos 2Z = 0$	
OCTO	$\Phi(\mathbf{r}) = 4(\cos X \cos Y + \cos Y \cos Z + \cos X \cos Z) - 2.8 \cos X \cos Y \cos Z + 1.2(\cos X + \cos Y + \cos Z) + 2.4 = 0$	
FRD	$\Phi(\mathbf{r}) = 8 \cos X \cos Y \cos Z + \cos 2X \cos 2Y \cos 2Z - (\cos 2X \cos 2Y + \cos 2Y \cos 2Z + \cos 2X \cos 2Z) = 0$	

3.4 GENERATION OF TPMS

On the surfaces of TPMSs, an infinite number of points exist. Employing the nodal approximation equations for various TPMSs outlined in Section 3.2, it is feasible to compute the coordinates of points on these surfaces. A higher number of points used in approximating the surface results in a smoother surface. However, an excessive number of points can lead to an increase in the size of digital files, which is detrimental to subsequent processes such as model generation, 3D printing, and numerical simulations. Consequently, there is a necessity for surface simplification. Taking the IWP surface as a case study, the simplification of TPMSs entails an approximation process utilising commercial software, such as Matlab.

To achieve a reduction in the number of elements and accelerate numerical calculations, references [127, 128] advocate for the replacement of the smooth IWP surface with a polygonal surface. This replacement strategy involves utilising a finite array of points, distributed at regular intervals along each axial direction. Such an arrangement not only significantly lessens the computational burden but also aids in reducing the size of 3D printable STL files and the development of extensive IWP structures.

Table 3.3 The calculation of x_i , y_i and z_i . ($C_p=17$ and $l=1$).

x_1, y_1, z_1	x_2, y_2, z_2	..	x_i, y_i, z_i	x_{16}, y_{16}, z_{16}	$x_{C_p}, y_{C_p}, z_{C_p}$
$-0.5l$	$(-0.5 + \frac{2-1}{C_p-1})l$		$(-0.5 + \frac{i-1}{C_p-1})l$		$(-0.5 + \frac{16-1}{C_p-1})l$	$0.5l$

The selection of these finite points is governed by a specific simplification parameter, denoted as C_p . The simplified TPMS is comprised of numerous triangular surfaces, the vertices of which are determined by solving the coordinates through $\Phi(x = x_i, y = y_j)$, $\Phi(y = y_j, z = z_k)$ and

$\Phi(x = x_i, z = z_k)$. This yields multiple sets of coordinate points (x_i, y_j, Z_{ij}) , (X_{ik}, y_j, z_k) and (x_i, Y_{ik}, z_k) . The i, j, k range from 1 to C_p . The values for x_i, y_j , and z_k are specified in Table 3.3, with C_p established at 17. The y_i and z_i have the same value with x_i . It is imperative to underscore that when the simplification parameter, C_p , falls below the threshold of 10, the resultant TPMSs exhibit an excessive coarseness, detracting significantly from their inherent geometric characteristics. Conversely, a C_p exceeding 20 precipitates suboptimal convergence within FEM simulation. Subsequently, the introduction of indeterminate points (x_i, y_j, Z_{ik}) into the TPMSs' equations facilitates the derivation of Z_{ik} , with both i and k range from 1 to 17. It warrants mentioning that Z_{ik} could present multiple results. In a parallel manner, points (X_{ik}, y_j, z_k) and (x_i, Y_{ik}, z_k) can be obtained. This technique enables the assembly of points at uniform intervals on the TPMS, thereby constructing an approximate facade reflective of the quintessential TPMS. The subsequent phase involves the interconnection of the aforementioned points with their immediate neighbours via linear segments. The triangular segments delineated by the convergence of three such lines are designated as the triangular surfaces. An approximate polygonal representation of the TPMS is synthesised through the amalgamation of these triangular facets. The encapsulation of this polygonal TPMS construct into an STL file paves the way for subsequent 3D modelling and simulation endeavours. Figure 3.3 illustrates the simplification process of the smooth IWP surface, showcasing the segmentation into polygonal facets inclusive of the calculated points and their interconnected lines, which demarcate the edges of the polygonal facet elements. This methodical approach markedly facilitates the generation of TPMSs for diverse applications, including 3D printing and the construction of complex, large-scale structures.

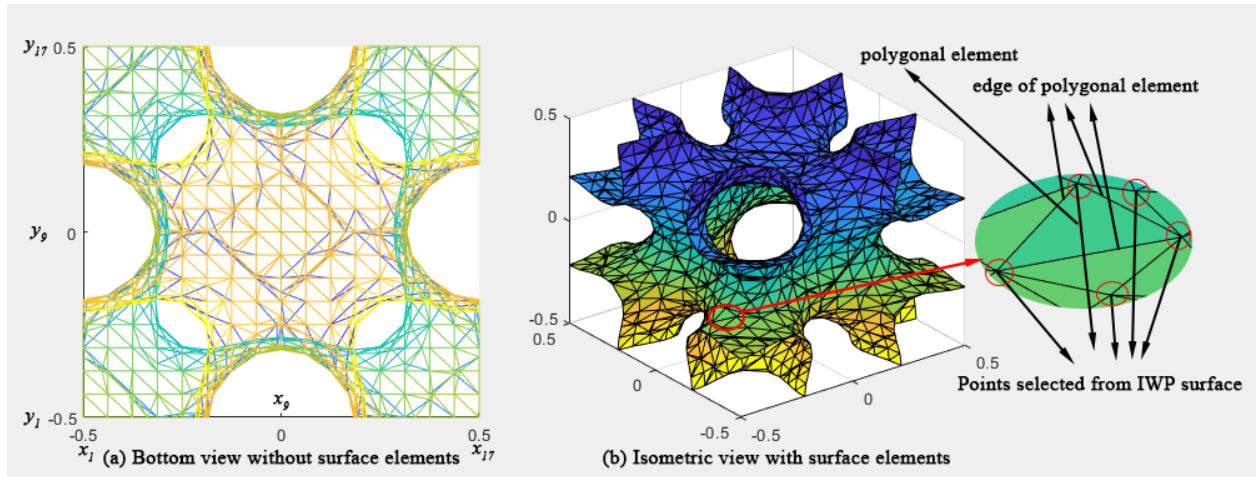


Figure 3.3 Simplified polygonal IWP surface. The facets and points are plotted with different colours according to value of Z-coordinates. (a) beneath view with lines only, (b) perspective view with lines and triangular meshes.

The concrete execution of this process entails the deployment of Matlab's 'isosurface' function [129, 130], which is predicated on the equation characterising the nodal approximation of TPMS surfaces. This function facilitates the generation of a three-dimensional surface by specifying a zero offset value, ensuring the surface precisely mirrors the theoretical model. The domain over which the surface is defined spans the length of a single unit cell along the xyz axes, encapsulating the full extent of the minimal surface within a periodic framework. To discretise this continuous surface into a finite set of points, the 'linspace' function is employed, enabling an even distribution of points along each axis [131]. This methodical approach ensures a comprehensive coverage of the surface area, allowing for an accurate approximation of the TPMS's intricate geometry. Subsequent to the approximation and simplification of the TPMS surface, the 'stlwrite' function is utilised to facilitate the exportation of the model into an '.stl' (Stereolithography) file [132, 133]. This file format is instrumental in the realm of 3D printing and numerical simulations, as it supports the representation of the surface geometry in a format that is both compatible with a multitude of software applications and conducive to the efficient fabrication of complex structures. Through this meticulous process,

the mathematical abstraction of TPMSs is translated into a tangible model, bridging the gap between theoretical constructs and their practical application in engineering and design.

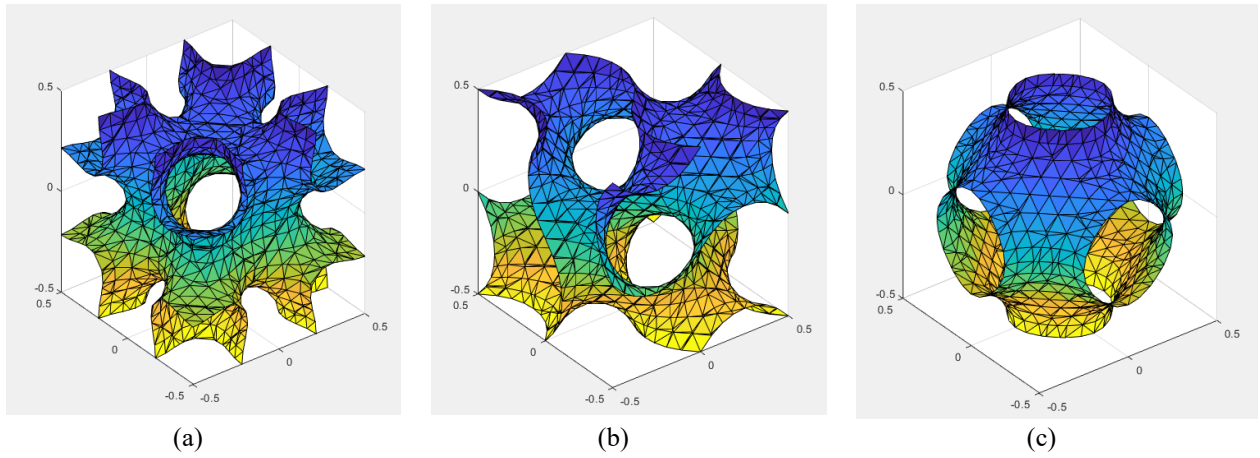


Figure 3.4 Several simplified TPMSs with their facets and points are plotted using different colours according to value of Z-coordinates. (a) IWP, (b) Gyroid and (c) Primitive.

This section is centrally concerned with the examination of IWP, Schwarz Primitive (SP), and Gyroid surfaces, with a particular emphasis on their simplification into polygonal representations. The essence of this research lies in the transformation of these complex TPMSs into simplified models that retain the fundamental geometric characteristics of the original surfaces while facilitating a range of practical applications, including 3D printing and numerical simulation. The simplification process involves the conversion of the smooth, continuous surfaces of the IWP, SP, and Gyroid into polygonal surfaces. These polygonal approximations are achieved through a strategic reduction in the number of points defining the surfaces, thus rendering them more manageable for computational processes. The resultant polygonal surfaces are illustrated in the figures provided within this document, offering a visual representation of the outcomes of this simplification process. Each polygonal surface is constructed to approximate the intricate geometries of the original TPMSs, maintaining a balance between fidelity to the original structures and the practicalities of digital representation and fabrication, as shown in Figure 3.4.

3.5 SOLID TPMS STRUCTURES

Commonly encountered TPMSs structures can be classified into two principal types [79, 134, 135]: solid (skeletal) and sheetal as shown in Figure 3.5. The foundational principles governing TPMSs, as detailed in Section 3.2, reveal that their approximated surfaces are solutions to the equation $\Phi(r) = 0$. This equation delineates a spatial division, segmenting space into two distinct solid entities based on the conditions $\Phi(r) \geq 0$ and $\Phi(r) \leq 0$. Notably, these entities possess equal volumes, with each occupying half of the spatial domain, a feature that underscores the inherent symmetry and balance within TPMSs.

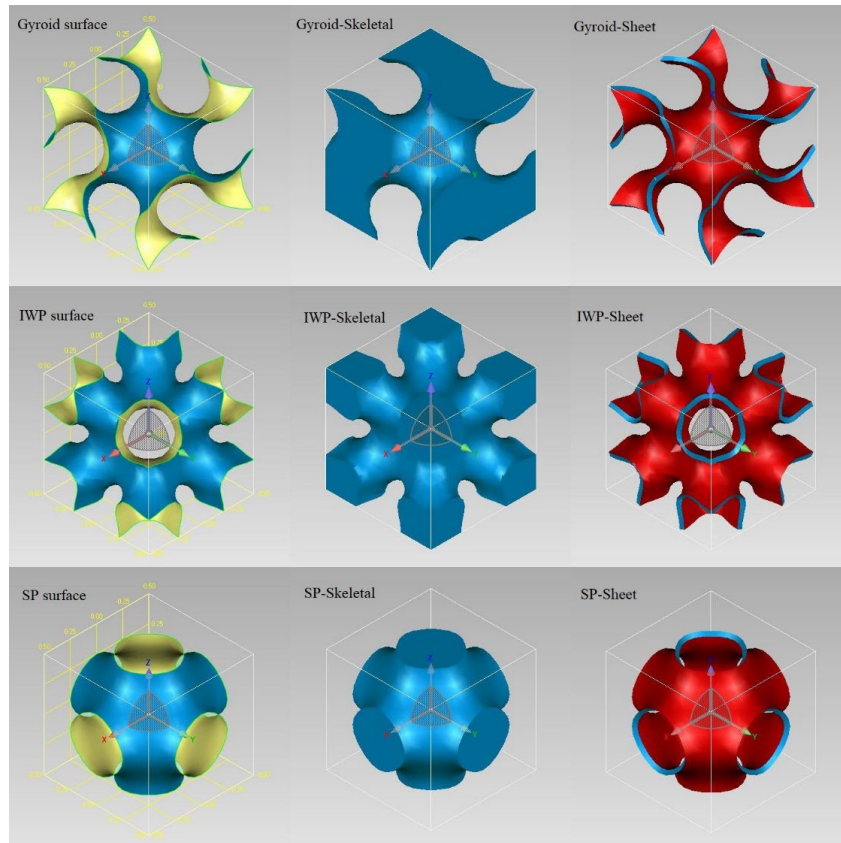


Figure 3.5 Three typical TPMSs and their Main Solid (Skeletal) and Sheetal unit cells.

In the framework of our study, the solid entity characterized by $\Phi(r) \geq 0$ is referred to as the main or primary solid (skeletal) type, while the entity where $\Phi(r) \leq 0$ is termed the secondary or

complementary solid (skeletal) type. This nomenclature facilitates a clear differentiation between the two types of structures that emerge from the partitioning process. By leveraging the geometric properties of TPMSs to divide a cubic block, whose dimensions are determined by the cell size, into two complementary solid parts, one can effectively generate two varieties of skeletal-TPMS entities. This approach underscores the versatility and adaptability of TPMSs in creating structures that are not only geometrically intricate but also capable of fulfilling diverse functional requirements. Furthermore, the transformation of TPMS surfaces into thicker configurations leads to the formation of sheetal-TPMS structures. This process involves augmenting the minimal surface to create a more substantial, sheet-like form, which offers enhanced structural integrity and potentially broader application possibilities, ranging from architectural design to biomimetic materials. Illustrating these concepts with the example of the Schwarz Primitive (Primitive or SP) surface provides a tangible understanding of how TPMSs can be manipulated to yield various structural types, as shown in Figure 3.6. The unit cell representation of the main solid and secondary solid types, alongside the Sheetal type of Primitive structures, visually conveys the practical implications of these theoretical constructs. Such graphical representations are instrumental in bridging the gap between abstract mathematical models and their practical applications, facilitating a deeper comprehension of the intricate relationship between geometry, physics, and engineering. By extending the study to include detailed visual aids, we not only elucidate the theoretical underpinnings of TPMSs but also highlight their practical applications. This comprehensive approach underscores the significance of TPMSs in contemporary scientific and engineering disciplines, showcasing their potential to inspire innovative solutions in a wide array of fields.

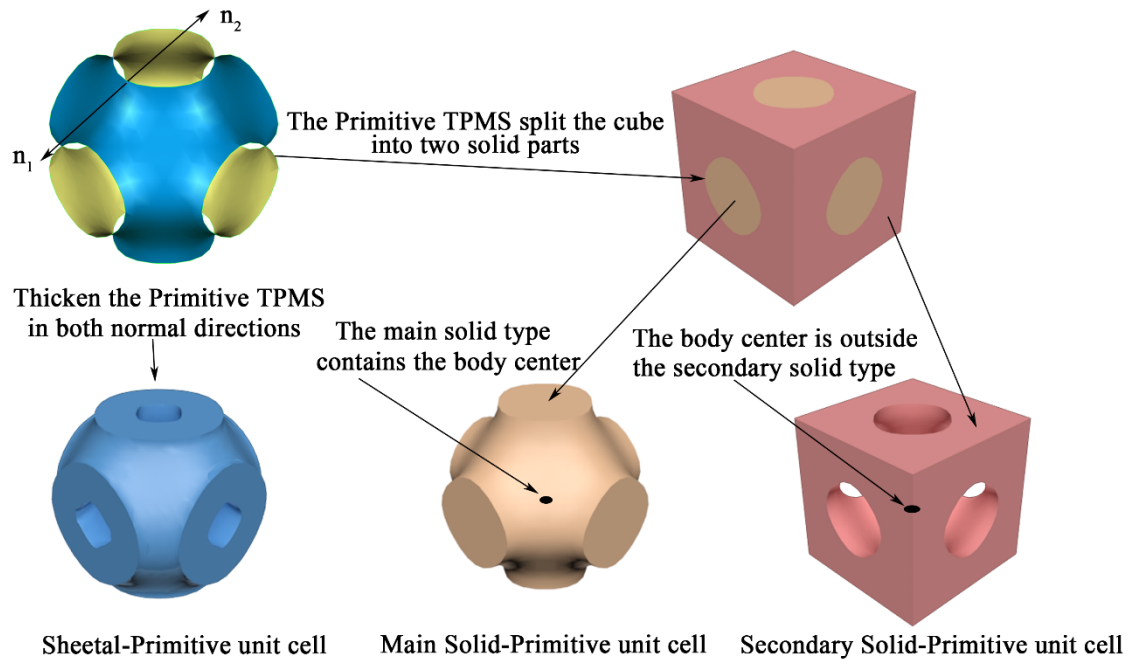


Figure 3.6 Design of the sheetal type and two solid types of Primitive based unit cells.

The geometric characteristics of structures generated by various TPMSs exhibit significant variations. An examination of two skeletal types (solid type) of IWP unit cells, as illustrated in Figure 3.7, reveals notable distinctions in their topological attributes. The analysis of these illustrations elucidates that the primary and secondary Skeletal-IWP units possess distinctly different topological properties. In the primary Skeletal-IWP unit, the structural elements, or 'bones', intersect at the unit cell's geometric centre. Conversely, in the secondary structure, these elements are aligned along the symmetry axes of the six faces of the unit cell cube, suggesting a divergent spatial organization. This variance in topological properties between the two skeletal-IWP units implies that they will exhibit disparate behaviour responses when subjected to force excitation. Understanding the nuanced differences between these skeletal configurations is paramount, as it bears directly on their mechanical performance, particularly in terms of resistance to external stresses and susceptibility to cracking. Investigating the cracking behaviours of IWP structures with varying unit cell arrangements becomes essential for advancing the application of these materials

in practical engineering solutions. Moreover, the structural composition of IWP differs markedly from that of the Schwarz Primitive (SP) structures. This contrast underscores the diversity within TPMSs and highlights the importance of a thorough characterisation of their geometric and topological nuances. Such an understanding is crucial for the development of materials and structures optimized for specific functional requirements, ranging from mechanical strength and durability to innovative applications in design and architecture.

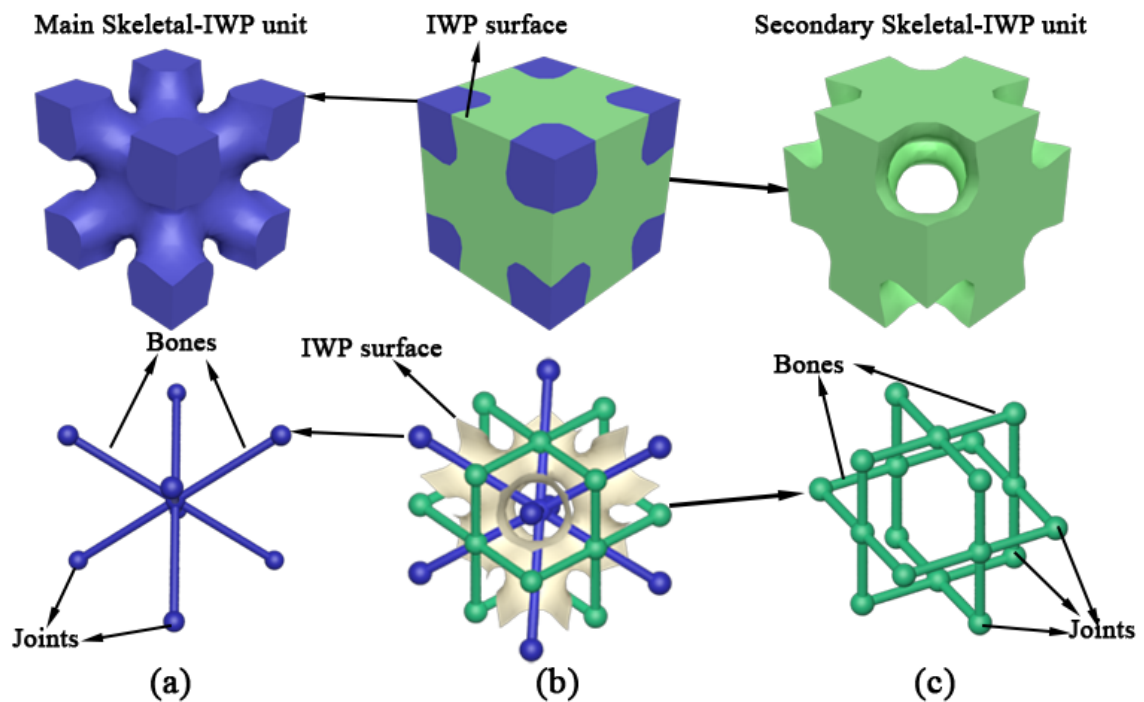


Figure 3.7 The two types of Skeletal-IWP units and their main frames.

The process of transforming TPMS surfaces into corresponding TPMS structural entities predominantly involves the following steps, meticulously carried out using advanced software tools. Initially, the simplified TPMS surfaces, exported from Matlab, are imported into the Geomagic Studio graphics processing software. For the creation of sheetal-type TPMS structures, the 'thicken' function is employed to augment the thickness of the surfaces. It is imperative to note that while the 'shell' function can also transform TPMS surfaces into lamellar structures, it only thickens in a

singular direction. Conversely, the 'thicken' command enables the simultaneous thickening of TPMS surfaces in both directions along the polygonal surfaces. An illustrative example employing the SP surface demonstrates the thickening of TPMS by 0.05 of a unit cell size, as showcased in Figure 3.8. Surfaces thickened using the 'thicken' command exhibit a more uniform spatial distribution, a methodology that has been consistently applied in generating sheetal-type TPMS structures within this research.

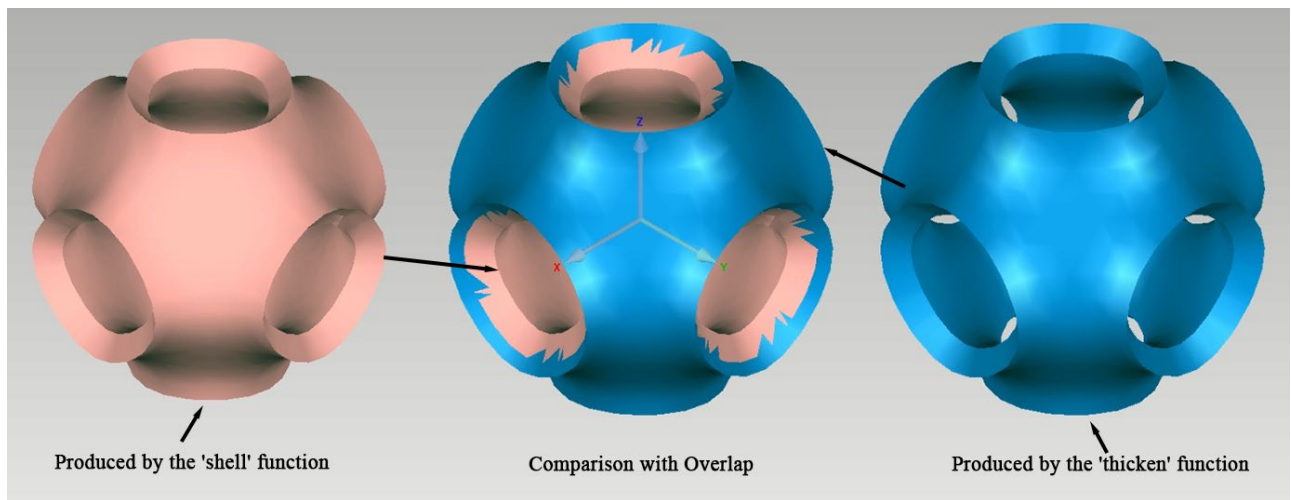


Figure 3.8 A Comparison of Sheetal SP Structures: the left image illustrates the structure produced by the 'shell' function, highlighting its unidirectional thickening, whereas the right image showcases the structure formed through the 'thicken' function, demonstrating uniform thickening in two directions.

Geometric studio facilitates the export of enclosed models as .STL files, compatible with 3D printing. However, these exported files are not directly transferrable to finite element models and require conversion into AutoCAD DXF files, subsequently transformed into the .sat file format commonly used in numerical simulations. To generate Main and Secondary Solid (Skeletal) types of TPMS unit cells, the boundary box of the unit cell is employed to enclose the TPMS surface, thereby achieving the Main Solid type. In Geomagic software, the 'Fill' command, set to the 'Flat' closure type, is utilized to seal the TPMS surface, as illustrated in Figure 3.9a.

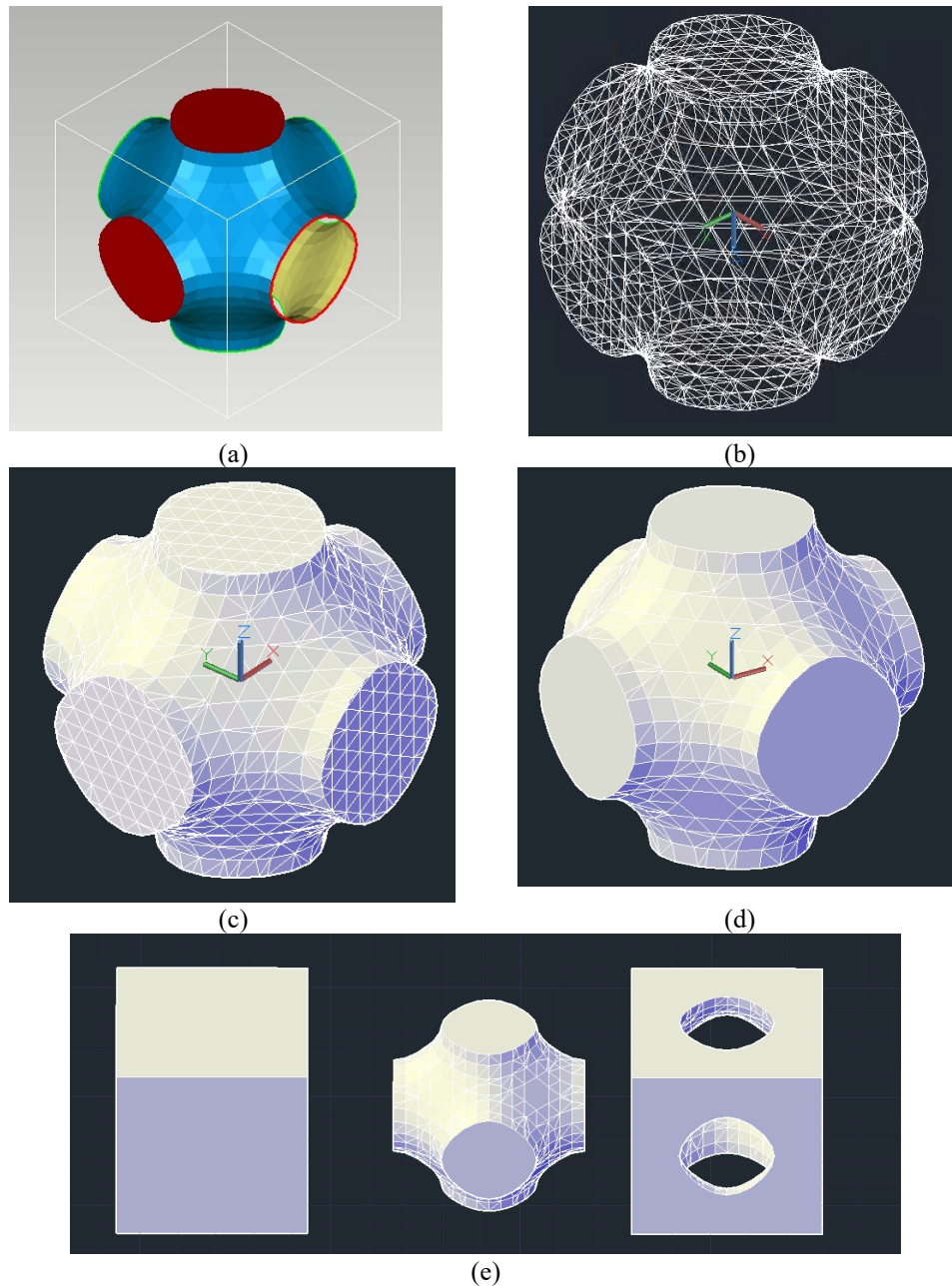


Figure 3.9 Fabrication Process of Solid Types (Skeletal Types) SP Structures. This sequence illustrates the transformation from surface to solid SP structures: (a) demonstrates sealing the SP surface using the 'Fill' command in Geomagic software; (b) presents the DXF file of the SP surface in AutoCAD; (c) depicts the conversion to a planar domain within AutoCAD; (d) shows the creation of the solid model for the Main Solid SP unit cell in AutoCAD; and (e) the generation of the Secondary Solid SP unit cell.

The file is then exported as a DXF and imported into AutoCAD for model conversion. It is crucial to acknowledge that the exported DXF file does not represent a solid model but contains multiple triangular facets, as illustrated in Figure 3.9b. The 'region' command is first used to convert these

triangular facets into a planar domain (Figure 3.9c), followed by the application of the 'SURFSCULPT' command to transform the aggregated planar domains into a solid model (Figure 3.9d) [136], thus yielding the Main Solid (Skeletal) type TPMS unit cell. The Secondary Solid (Skeletal) unit cell is then created by subtracting the Main Solid from a cube of identical dimensions to the unit cell (Figure 3.9e).

3.6 FABRICATION OF TPMS STRUCTURES

To research the performance of TPMS units and to corroborate the numerical models of TPMS structures delineated in subsequent chapters, a series of experiments involving the fabrication of five distinct types of specimens via 3D printing are undertaken. These specimens encompass a cube block reference (hereinafter designated as CB-R), Main Solid-IWP (henceforth termed IWP-1), Secondary Solid-IWP (subsequently referred to as IWP-2), Main Solid-SP (now called SP-1), and Secondary Solid-SP (hereafter known as SP-2). For each variant of the TPMS units, three replicas have been produced, culminating in a total of fifteen specimens fabricated by the 3D printing firm WeNext, located in China. The method of Stereolithography (SLA) is utilised for the creation of all specimens, employing composite photosensitive resin as the primary material [137].

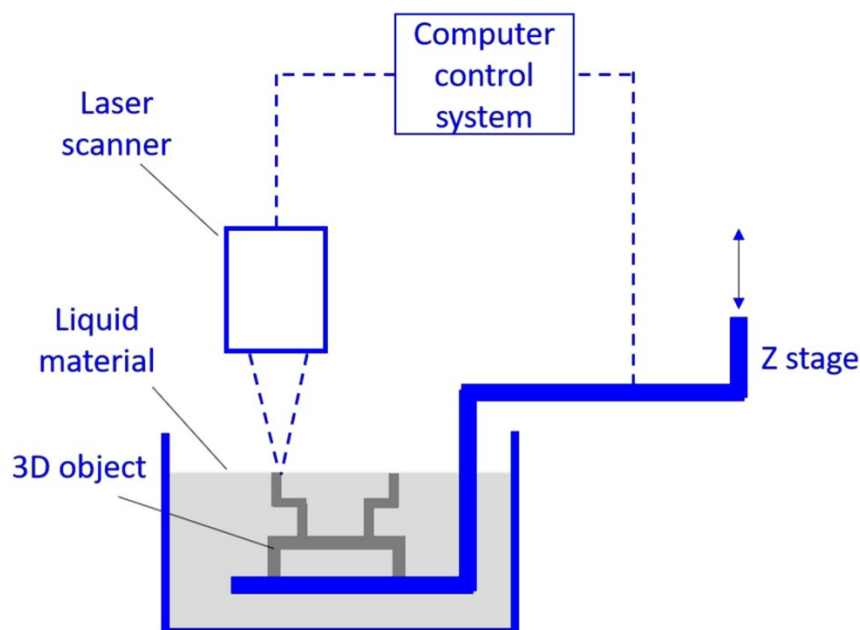


Figure 3.10 Schematic Diagram of SLA 3D printing process.

Stereolithography (SLA) technology is a pioneering form of 3D printing or additive manufacturing technology that enables to produce precise and intricate 3D objects [138, 139]. Developed in the 1980s, SLA works by focusing an ultraviolet (UV) laser on the photopolymer photosensitive resin which can harden upon exposure to UV light. Through this process, the laser traces a pre-programmed design onto the surface of the liquid resin, solidifying the material layer by layer to form a solid 3D object. An example of typical SLA system is illustrated in Figure 3.10. The procedure begins with the generation of a three-dimensional model. This model is then converted into a series of thin, horizontal cross-sections—effectively a set of instructions for the SLA machine on where to "draw" with the laser. As each layer is completed, the build platform descends incrementally, exposing a fresh layer of resin to the laser beam. This sequence is perpetuated, layer by layer, until the entire object is fabricated. After printing, the object is usually rinsed with a solvent and then placed in a UV oven for final curing, ensuring the strength and stability of the material.

The methodology of stereolithography depicted in Figure 3.11a commences with an STL file, currently the ubiquitous standard for additive manufacturing processes as referenced in literature. This file undergoes a transformation process where the three-dimensional CAD model is segmented into bi-dimensional sections, providing detailed cross-sectional information. These sections facilitate the sequential construction of the physical model on a layer-by-layer basis. Expounded in Figure 3.11b, the STL file's format is structured by an assemblage of minute triangular facets. Each facet's geometry is defined by the coordinates of its vertices and a unidirectional normal vector that projects outward, signifying the facet's orientation.

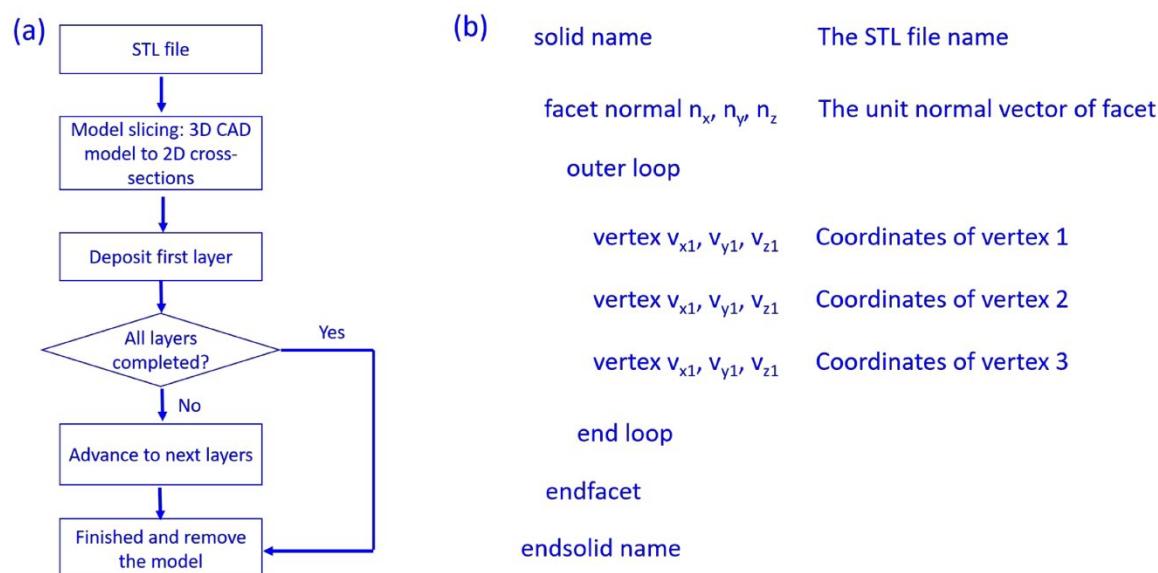


Figure 3.11 (a) Process flow diagram of stereolithography beginning with an STL file and concluding with model completion; (b) Detailed breakdown of the STL file structure showing the format of triangular facets with their vertices and normal vectors.

In a departure from earlier investigations primarily focused on bioengineering applications, this thesis aims to explore the potential of TPMS structures within the realm of civil engineering, necessitating a substantial increase in the size of the units. The dimensions of the boundary box for all units are set at 5cm×5cm×5cm. This dimensioning strategy is adopted to mitigate the risk of pore

obstruction by debris and to enhance drainage capabilities, whilst also ensuring uniform load distribution across the units. The exactitude of the Stereolithography (SLA) printing technique is recorded at a 0.1mm precision, with instances of the fabricated specimens illustrated in Figure 3.12.

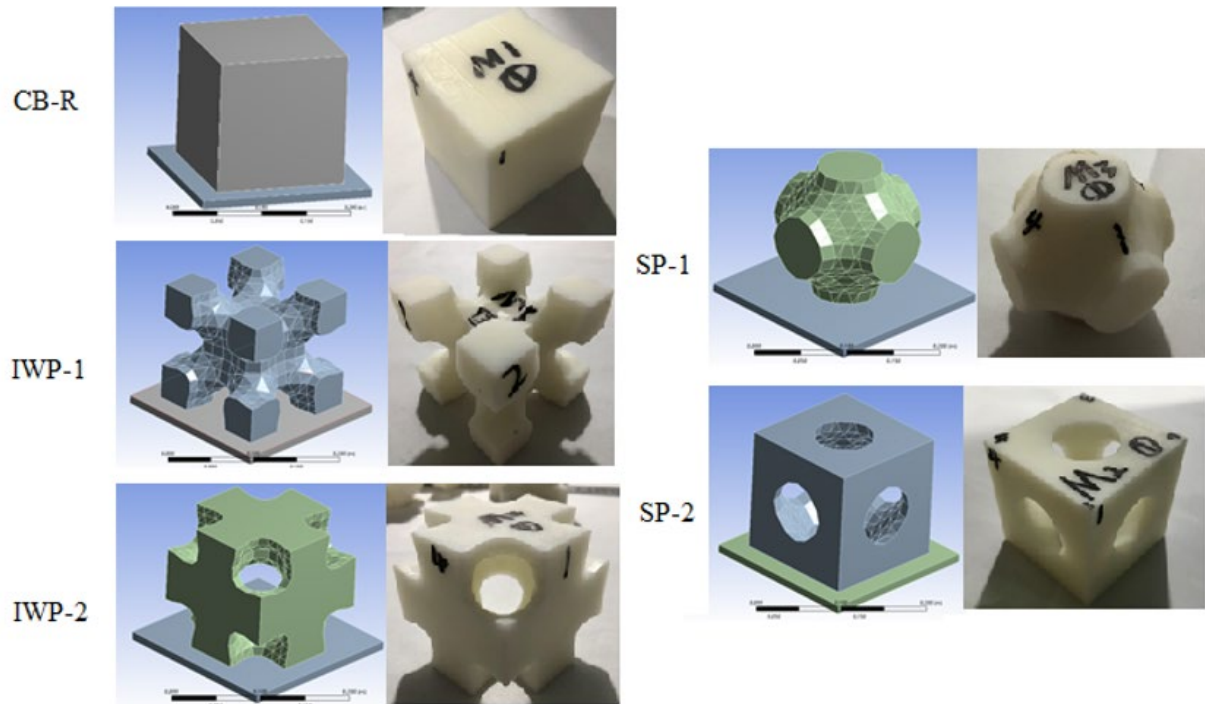


Figure 3.12 Schematic diagrams and examples of printed units.

Utilising stereolithography (SLA) technology, the 3D printing operations are executed by WENEXT Ltd, employing a commercial-grade material known as “photosensitive 8200.” The density printing apparatus, RSPRO600, has been calibrated to a layer height of 0.05 mm and a laser moving velocity of 6 m/s. The utilised laser, a solid-state, frequency-tripled Nd: YVO₄, features a beam radius of 0.06 mm and operates at a wavelength of 355 nm. The UnionTech™ RSCON software governed the printing process, with the operational environment maintained at a temperature between 23 – 25°C and a relative humidity inside the printing apparatus not exceeding 40%. Default settings, as controlled by the machine's system, have been applied across all printing tasks. Prior research, as documented in references[140, 141], highlights the significant impact of

3D printing settings on the mechanical properties and behaviours of the 3D printed specimens. Consequently, printing settings are standardised across all specimens to minimise variance attributable to the printing process. The specimens are crafted from composite resin, called “photosensitive resin 8200”. Its mass per unit volume is 1160kg/m^3 . The material is provided and mechanical properties have been tested by Royal DSM Inc in alignment with American society for testing and materials standards. For ensuing finite element simulations, material parameters are adopted as the median of the specified range, as detailed in Table 3.4, to facilitate a standardised basis for comparison.

Table 3.4 Mechanical properties of 3D printed “photosensitive resin 8200”.

Properties, unite	Test method	Value
Hardness, Shore D	ASTM D 2240	76~88
Flexural modulus, Mpa	ASTM D 790	2692~2775
Flexural strength, Mpa	ASTM D 790	69~74
Tensile modulus, Mpa	ASTM D 638	2589~2695
Tensile strength, Mpa	ASTM D 638	38~56
Elongation at break	ASTM D 638	12~20%
Poisson's ratio	ASTM D 638	0.4~0.44

3.7 CONCLUSION

This chapter establishes a solid foundation for the numerical modelling and experimental validation of TPMS structures through DEM and FEM presented in subsequent chapters. It comprehensively covers the theoretical underpinnings, mathematical formulations, and practical methodologies necessary for generating these structures. Furthermore, the chapter outlines the design and fabrication of solid TPMS prototypes using Stereolithography (SLA) techniques for 3D printing. These prototypes are essential for the experimental validation of the numerical models in later chapters. Additionally, the simplified models discussed serve as the basis for DEM and FEM simulations, significantly easing the computational demands of these simulations.

CHAPTER 4

MECHANICAL BEHAVIOURS

OF TPMS CELLULAR UNITS

UNDER VARIOUS LOADS

4.1 INTRODUCTION

Previous researches have indicated that both Skeletal-TPMS structures and sheet-TPMS structures have better energy absorption performance than honeycomb structures, lattice, and aluminum. However, there has been little agreement on the selection of Skeletal-TPMS or sheet-TPMS as the most high-performance structure. The researchers mostly considered the Sheet-TPMS structures with various TPMSs in recent years, and the investigation on the mechanical properties of Skeletal-TPMS structures is relatively scarce. Moreover, the sizes of TPMS structures' units were designed from 0.1 millimeters to 4 millimeters to utilize the TPMS structures in artificial bones. Such unit sizes lead to the difficulty of the utilisation of the space inside the TPMS structures for cable installation or drainage; thus, construction of the micro-TPMS structures is not well applicable to civil engineering fields. The Sheet-TPMS structures split the space into two parts, the interior and exterior regions of the TPMS surface, while skeletal-TPMS structures concentrate the space on one side of the TPMS. The space of the Skeletal-TPMS structure is more concentrated and easier to be utilized than the Sheet-TPMS structure with the same relative quality.

Importantly, while TPMS have been extensively studied in various scientific fields, their application in civil engineering remains largely unexplored. This oversight highlights a significant opportunity to harness the unique geometrical and structural properties of TPMS for civil engineering, where complex challenges such as bearing capacity and load distribution are paramount. Along with the additive manufacturing technology development, the smart TPMS structures may be applied in civil engineering for their excellent energy-absorbing capacity. However, the mechanical properties of the units of the TPMS structures are unclear yet. Hence, this evidence highlights the importance of

evaluating the TPMS units with large sizes. In this section, two TPMSs (Schwartz-P and IWP) are selected for designing the units. Several Skeletal-TPMS units are designed based on the two TPMSs and then manufactured with SLA. The compressive behaviour of the various single Skeletal-TPMS units is studied based on tests and numerical simulations. The compressive experiments are carried out for the cube blocks and four types of TPMS units with the same bounding box. Furthermore, the numerical calculation of compressive tests is achieved using the FEM using Ansys software. A growing body of literature has looked into the modelling of the Sheet-TPMS structures under axial loads. Nevertheless, none numerical assessment of the compressive behaviour of the single Skeletal-TPMS units has been examined. In this regard, after the validation of FEM modelling via compressive test results, the numerical analysis of other types of the skeletal-TPMS units is carried out. The significance of researching TPMS cellular units cannot be understated, particularly given their periodic nature. Understanding the mechanical responses of TPMS cellular units under different loading conditions is instrumental in predicting the overall performance of TPMS structures. By systematically studying these units, researchers can gain insights into the deformation mechanisms, stress distribution, and failure modes inherent to TPMS designs. Such knowledge is crucial not only for validating theoretical models and simulations but also for advancing practical applications in fields requiring precision in stress management and material resilience, such as civil engineering. This exploration can also foster the development of new TPMS configurations tailored to specific engineering requirements, thereby enhancing their utility in construction and other critical applications. This chapter is mainly based on Paper 2 and uses some parameters from Paper 10 listed in list of publication.

4.2 DETAILS FOR COMPRESSIVE TESTS

The compression assessments are conducted using an electro-hydraulic servo-controlled universal testing apparatus as shown in Figure 4.1. The instrument has been calibrated before the test. For these assessments, the specimens are placed at the centre of the support plate to guarantee that the samples are evenly loaded. The subsurface of each test specimen, in contact with the loading plate, is aligned as it is during the 3D printing phase, to avoid the orientation of the printed sample from affecting the compressive tests. Because the mechanical behaviour of the composite resin specimens is influenced by the loading rate, the testing apparatus' loading plate is set with a constant vertical speed for all tests. The displacement and loading force are automatically recorded by the machine's data acquisition system throughout the. The accuracy of displacement is 0.01mm and the accuracy of force is 0.01kN. The strain rate is controlled at 0.001 per second, and the loading plate's speed is 0.05 mm per second adhering to [142]. The specimens are subjected to load before their failure. The five types of 3D printed specimens tested are the cube block (CB-R), IWP-1, IWP-2, SP-1 and SP-2. Each of the five types of samples has been subjected to three individual assessments. The conditions of the five types of specimens during, preceding, and following the compressive assessments are exhibited in Figure 4.2.

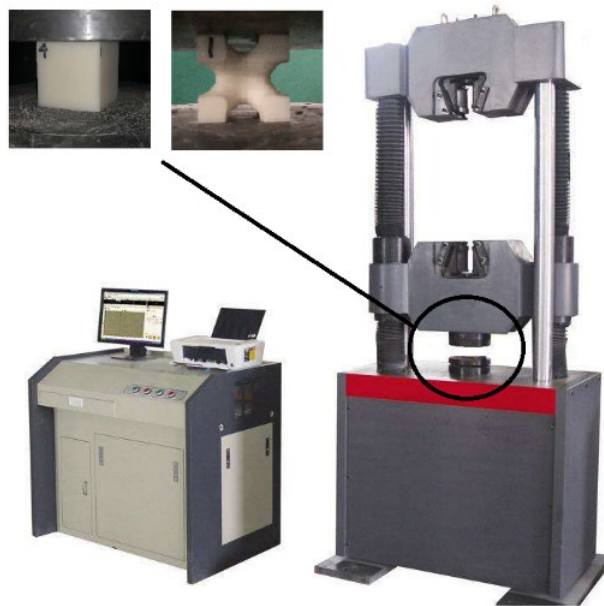


Figure 4.1 Schematic of compressive tests.

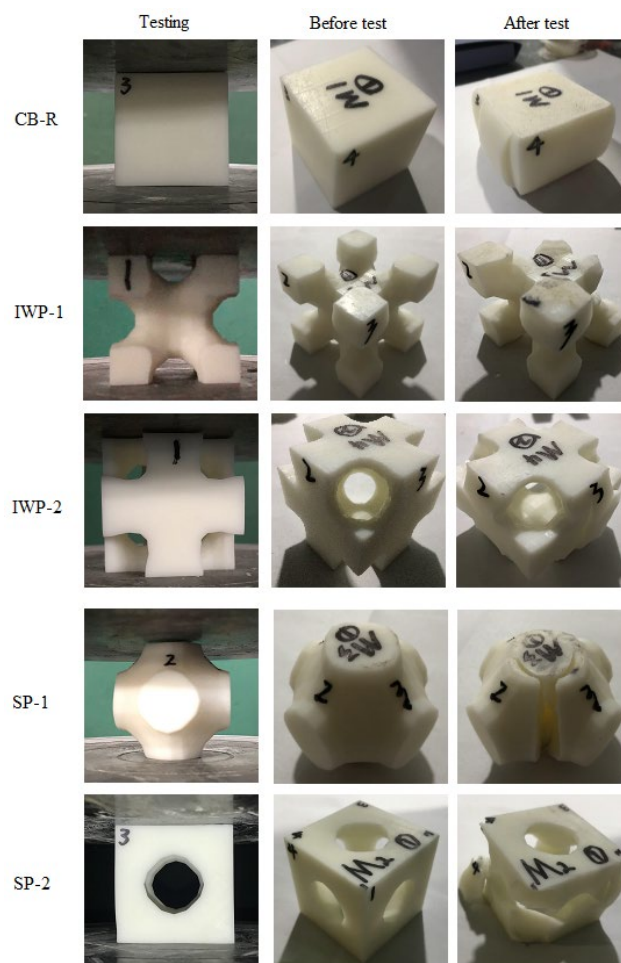


Figure 4.2 Five tested samples before and after the test.

4.3 TEST RESULTS FOR COMPRESSION

4.3.1 Load-displacement curve

Each category of unit underwent a triplet of evaluations, from which a mean value is then deduced. The load-displacement curves of CB-R, IWP-1, IWP-2, SP-1 and SP-2 are displayed in Figure 4.3 (a), while Figure 4.3 (b) elucidates the TPMS unit trends in a proper view without showing the case of 'CB-R'. As exemplified by the CB-R-TA in the key, CB-R represents the type of the test specimen, and 'TA' means the averaged test outcome. Legends bearing resemblance to CB-R-TA adhere to this denotation. The gradient of the lines represents the unit's axial stiffness.

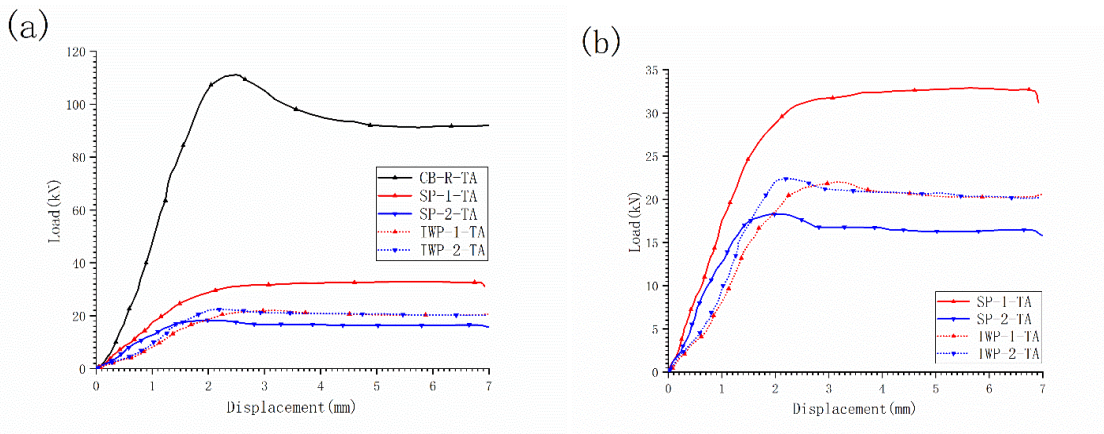


Figure 4.3 Load-displacement curves of experimental compression assessments.

The force-displacement response for most unit types, barring SP-1, presents three distinct phases. Initially, there is an almost linear escalation of force with displacement, plateauing at a threshold or displacement margin ranging from 1.5 to 2.5 mm. Subsequently, the structures commence elastic-plastic transition, with rigidity decreasing from positive towards a neutral point. Upon further displacement, force ascends to a maximal point before it recedes. The

tertiary phase is characterised by a marginal force decline, thereafter the curve stabilises and the rigidity of the construction asymptotically diminishes to nullity. This behaviour parallels observations made of UV resin in cuboidal form as documented by Zhengning Li [143]. Regarding the SP-1 case, the initial and terminal stages of the load-displacement curve resemble other unit types, but there is no negative phase during the second stage in the load-displacement curve of SP-1 type. Here, the gradient of force-displacement tapers to nought progressively. The divergence between SP-1 and alternative units is owing to their distinct geometrical shapes.

4.3.2 Compressive strength and stiffness

The calculation of compressive strength of the units can be conducted by dividing the peak load by the cross-sectional dimensions (50mm by 50mm) of their encasement. Depicted in Figure 4.4, the CB-R specimen exhibits a compressive strength superior to that of the remaining TPMS-based models. Compared with CBR, the compressive capacities of IWP-1, IWP-2, SP-1, and SP-2 show a decrement of 80.19%, 79.92%, 72.18%, and 83.55% correspondingly. As mentioned in the table 1 and table 2, the relative density of IWP-1, IWP-2, SP-1 and SP-2 compared to CBR are 0.53, 0.47, 0.5 and 0.5, respectively. The reduction in compressive strength of these TPMS constructs is more pronounced than the decrease in their relative densities. This phenomenon arises from the shorter path of stress propagation in the cubic sample as opposed to that within TPMS constructs, where numerous internal elements may not fully contribute to the overall compressive efficacy akin to the cubical model. This can also elucidate why the SP-1 sample's compressive strength surpasses that of the SP-2 sample and the IWP-1 and IWP-2 samples, which possess comparable relative densities, by 40.47%,

38.58%, and 69.08% respectively. In addition, the stiffness of the TPMS specimens has been found to be less than half that of the cubical sample. as illustrated in Figure 4.5. Of the four Skeletal-TPMS types assessed, the SP-1 unit demonstrates the pinnacle of rigidity and compressive fortitude. From the standpoint of compressive aptitude, SP1 unit surpass other TPMS specimens tested.

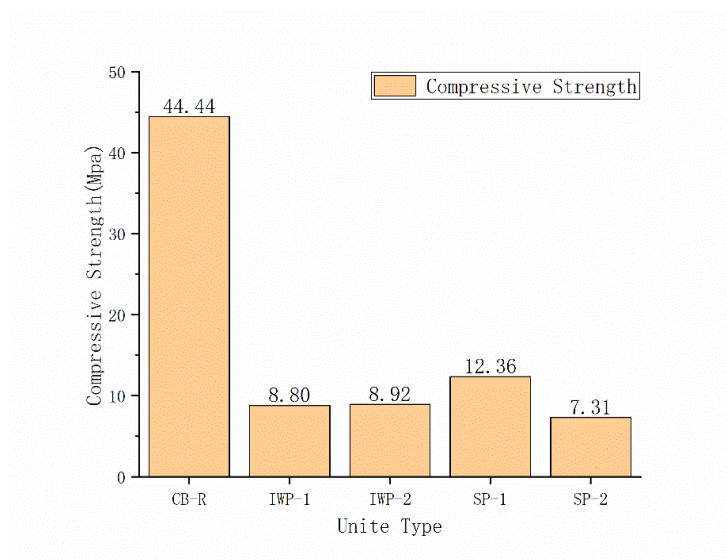


Figure 4.4 Compressive strength of CB-R, IWP-1, IWP-2, SP-1 and SP-2 units from tests.

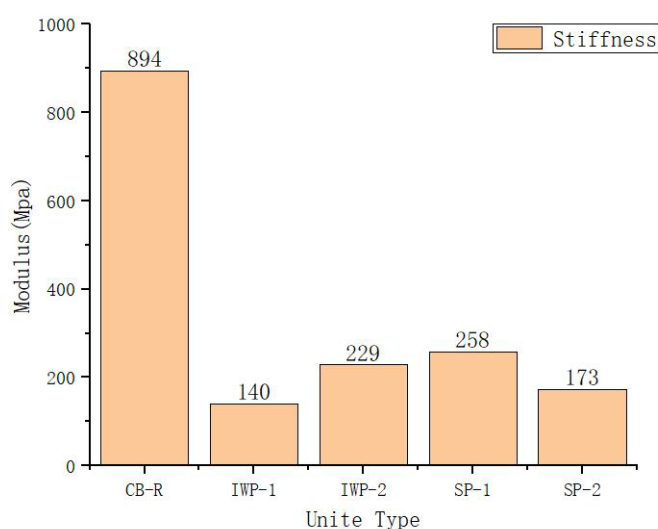


Figure 4.5 Stiffness of CB-R, IWP-1, IWP-2, SP-1 and SP-2 units from tests.

4.4 FEM SIMULATIONS FOR COMPRESSION

In this part, the numerical calculation FEM platform, Ansys, is adopted for simulating the axial load tests for comparison with the corresponding experiments. Subsequent to the corroboration of the FEM parameters and models through compression tests, a broader spectrum of TPMS-derived unit cells, including IWP-3, IWP-4, SP-3, SP-4 and SP-5 unit cells are built and researched using Ansys.

4.4.1 SP and IWP based unit cells

Five types of unit cells of SP-based structures are created on the basis of Primitive surfaces as displayed in Figure 4.6. The opening holes of the SP surface are closed with six planes to obtain the SP-1 unit. The derivation of the SP-2 cell involves the removal of an SP-1 cell from a homogeneously dimensioned solid cube. Arrange SP-1 units in an array of $2 \times 2 \times 2$ to get a structure, which is then scaled down to 50% of its initial volume, yielding the SP-3 cell. The geometry of the smallest periodic unit of SP-3 is the same as it of SP-1. Meanwhile, SP-4 results from an amalgamation of SP-1 and SP-3 cells, and SP-5 is generated through the amalgamation of SP-2 and SP-3 cells. The geometry properties of the five types of SP units, relative to a solid cubic block, are illustrated in Table 4.1.

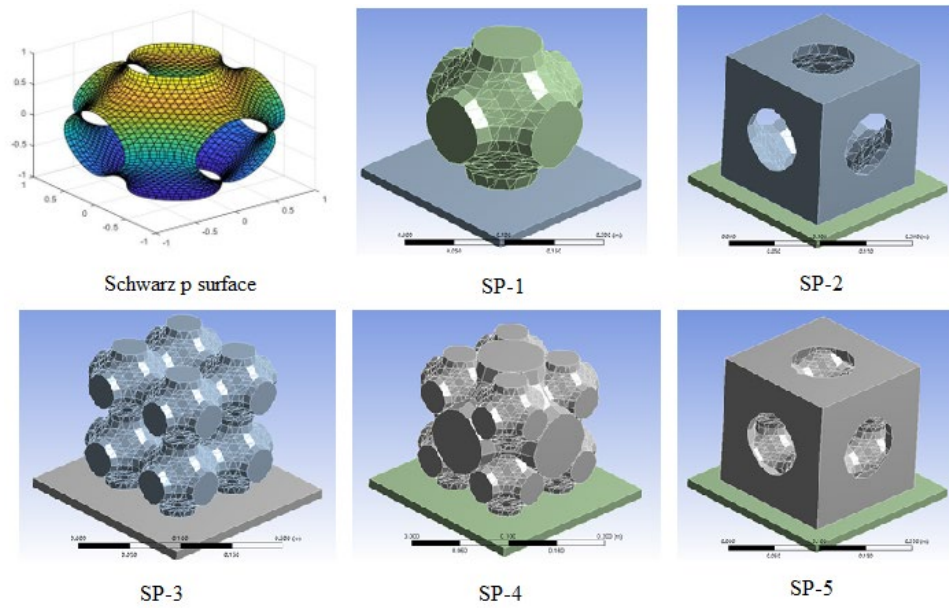


Figure 4.6 Various types of units based on SP surface.

Table 4.1 Comparison of geometric properties and relative density of SP unit cells to the cube block.

Unit type	Relative density (relative to CB-R)	Surface area ratio (relative to CB-R)
CB-R	1.00	1.00
SP-1	0.50	0.57
SP-2	0.50	1.22
SP-3	0.50	0.97
SP-4	0.75	0.88
SP-5	0.75	1.35

Four types of units of IWP-based structures are fabricated based on IWP surfaces as illustrated in Figure 4.7. The open holes of the IWP surface on the boundary are closed by six planes of $X = \pm 1, Y = \pm 1$, and $Z = \pm 1$ to create the IWP-1 unit. The IWP-2 unit is obtained by subtracting the IWP-1 unit from an identically sized solid cube. Arrange IWP-1 units in an array of $2 \times 2 \times 2$. Then the structure is scaled to half of the original size to get the IWP-4 unit. The smallest periodic unit of IWP-3 has the same geometrical shape as SP-1 has. IWP-4 emerges from the integration of IWP-1 and IWP-3 structures. The geometry properties of the four types of IWP units compared with the cube are illustrated in Table 4.2.

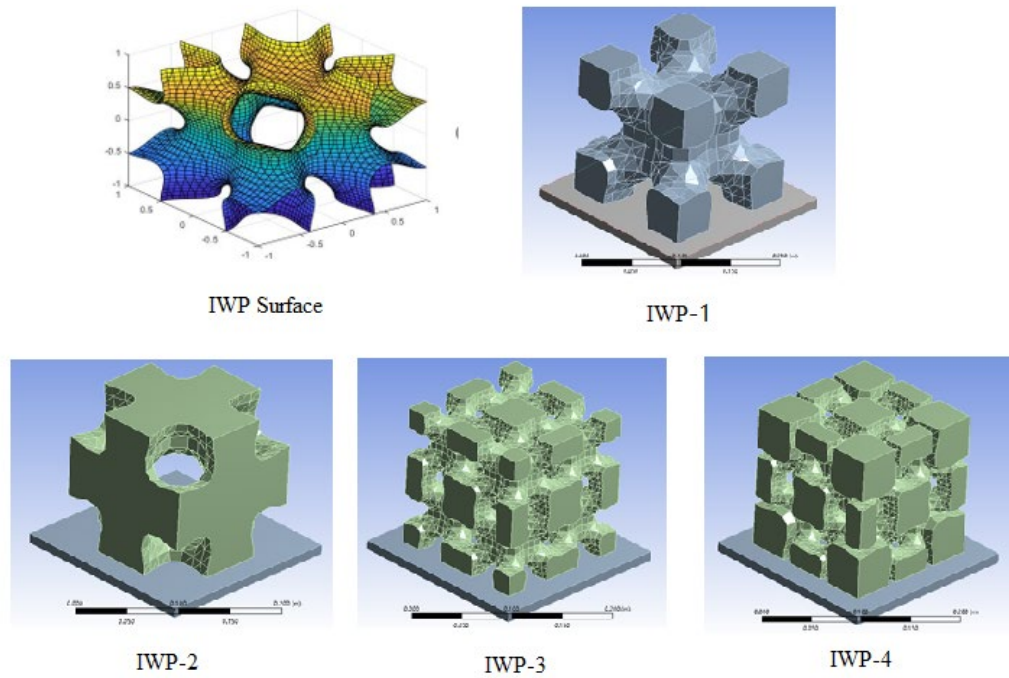


Figure 4.7 Various IWP unit cells and IWP surface.

Table 4.2 Comparison of geometric properties and relative density of IWP unit cells to the cube block.

Unite type	Volume ratio (compared to CBR)	Surface area ratio (compared to CBR)
CB-R	1.00	1.00
IWP-1	0.53	0.97
IWP-2	0.47	1.24
IWP-3	0.53	1.58
IWP-4	0.77	1.64

4.4.2 FEM Model settings

As illustrated in Figure 4.8, each FEM model comprises three integral components: a) the loading plate, b) the test sample and c) the bearing plate, to be consistent with the compression tests. As suggested by [144, 145], it is possible to streamline the models with negligible impact on accuracy, courtesy of the TPMS units' symmetry, applied loads, and boundary conditions. Thus, all the FEM models have been reduced to a quarter scale of their original dimensions to curtail simulation duration. Symmetry constraints are imposed along the plane of symmetry

within the model. Comparative simulations ascertain that the discrepancy between the results of the quarter-scale models and their full-sized predecessors is marginal, less than 0.1%. The dimensions of both the loading and support plates in the quarter-scale models stand at $35\text{mm} \times 35\text{mm} \times 35\text{mm}$.

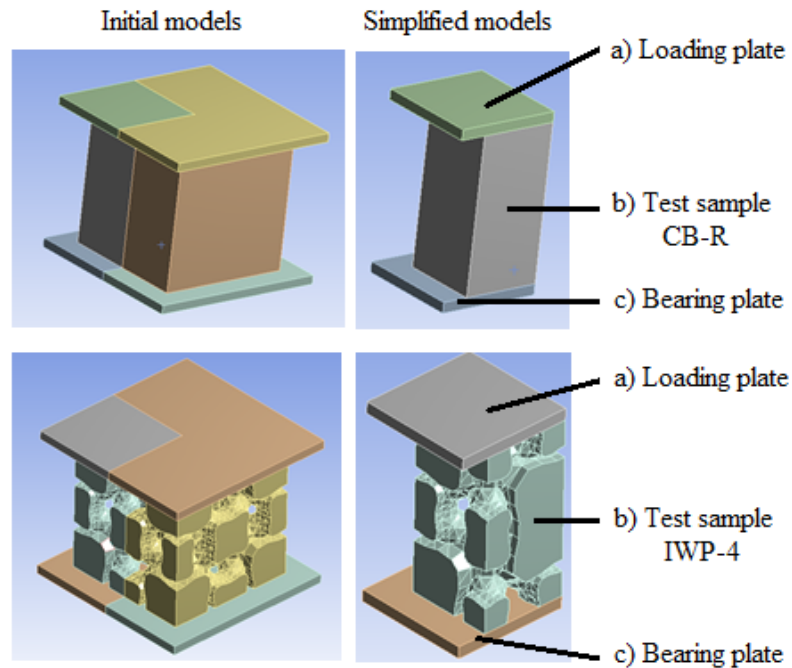


Figure 4.8 Full-sized and quarter-scaled FEM models for CB-R and IWP-4 units.

Fabricated from steel, both the loading and support plates adopt the structural steel material parameters from the ANSYS material library for simulation, as listed in Table 4.3. The failure and yield of steel structures are not considered in this simulation. The solid186 elements defined by 20 nodes are used to in the two steel plates and the elastic constructive behaviour is chosen. The mesh size of the steel plates is uniformly established at 3.5mm.

Table 4.3 Material properties of the two steel plates in FEM simulation.

Properties	Value
Density	7.85g/cm ³
Young's modulus	200Gpa
Poisson's ratio	0.3

The base material (photosensitive resin) of the 3D printed samples exhibits elastoplastic characteristics inherent to polymeric substances. The Drucker-Prager plasticity constructive behaviour is employed to account for the nonlinear material responses as indicated in [146]. This model, complemented by an appropriate yield condition, is capable of simulating material failure scenarios. Both Dean and Wright[147] and Wenzhi Wang[148] adopted the Drucker-Prager constitutive model for rendering the 3D printed photosensitive resin. Both of their FEM outcomes from both sources corroborated well with experimental data, showing the applicability of Drucker-Prager in this chapter. The Drucker-Prager constitutive model is an extension of the von Mises yield criterion and is often utilised in the analysis of materials that exhibit pressure-dependent yielding. This model is particularly suited to materials that do not possess a constant yield stress, such as soils, rocks, and certain classes of concrete and metallic powders. The Drucker-Prager model is isotropic and assumes that yield occurs when a stress state reaches a certain condition described by a yield function. The advantages of the Drucker-Prager model include its relative simplicity and adaptability to a range of materials exhibiting pressure-sensitive yielding. It allows for the analysis of complex loadings with a reasonably accurate approximation of yield behaviour. When applied to resin materials, the Drucker-Prager model may be advantageous in simulating the non-linear, pressure-dependent behaviour of such polymers, which can be particularly relevant for resins used in structural applications or those subjected to complex loadings. The ability to incorporate material-specific parameters like cohesion and internal friction makes it a versatile tool for predicting the onset of yield in these materials. Consequently, every TPMS model and the CB-R model are characterised within the FEM simulations as homogenised elastoplastic entities, guided by a linear Drucker-

Prager material definition. In this constitutive model, a suite of variables is requisite as shown in Figure 4.9 and Table 4.4. Ductile fracturing alongside the progression of material damage is utilised as the benchmark for failure. The parameters listed in Table 4.4 reflecting the material parameters offered by WeNext Ltd and the experimental results, are selected for the FEM simulations. The solid-187 element type, featuring 10 nodes and a 2mm mesh resolution, is employed across all Skeletal-TPMS units.

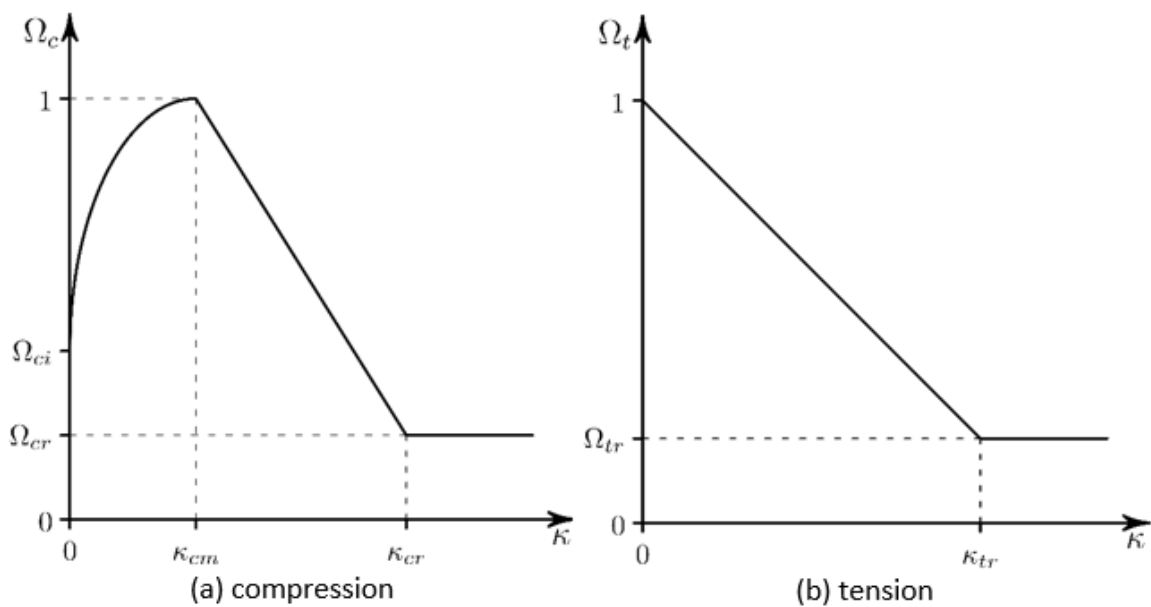


Figure 4.9 Stress path of Linear Drucker-Prager Model in both compression and tension.

Table 4.4 Parameters of the 3D printed samples in FEM simulations using Ansys.

General parameters	
Density	1.16g/cm ³
Young's modulus	2.6Gpa
Poisson's ratio	0.42
Parameters of linear Drucker-Prager material model	
Plastic strain at uniaxial compressive strength / κ_{cm}	0.04
Ultimate effective plastic strain in compression / κ_{cr}	0.13
Relative stress at onset of nonlinear harding / Ω_{ci}	0.1
Residual compressive relative stress / Ω_{cr}	0.67
Plastic strain limit in tension / κ_{tr}	0.15
Residual tensile relative stress / Ω_{tr}	0.4

As illustrated in the schematic representation provided in Figure 4.10, the FEM models incorporate

standard terrestrial gravity across all modelled elements. This approach is designed to closely simulate the environmental conditions typically encountered during compression testing. The velocity of the nodes on the base surface of the bearing plate are fixed to zero during the simulation for replicating the constraints present in an actual test setup, thereby ensuring the fidelity of the simulation to real-world scenarios.

In accordance with established experimental protocols, a precise vertical displacement is administered to the loading plate, set at 5 mm for a computed timeframe of 100 seconds. This specific adjustment is meticulously chosen to mirror the conditions prevalent in analogous compressive testing methodologies. The resultant effect is a calculated vertical velocity of 0.05 mm per second, which corresponds to a strain rate of 0.001 per second. This rate is deliberately matched to those obtained in similar experimental studies, thereby validating the consistency and relevance of the simulation parameters.

To accurately model the dynamic interactions and load distribution among the various components within the FEM, a general frictional contact mechanism is employed. This specification is critical for simulating the complex interplay between differing materials and surfaces under load. The selection of a friction coefficient of 0.2 for the contact surfaces of the test specimens and the steel plates is based on empirical data and is intended to closely approximate the physical properties of the materials involved. This level of detail in the simulation parameters is essential for achieving a realistic representation of the mechanical behaviour observed during physical testing, thereby enhancing the predictive power and utility of the FEM analysis.

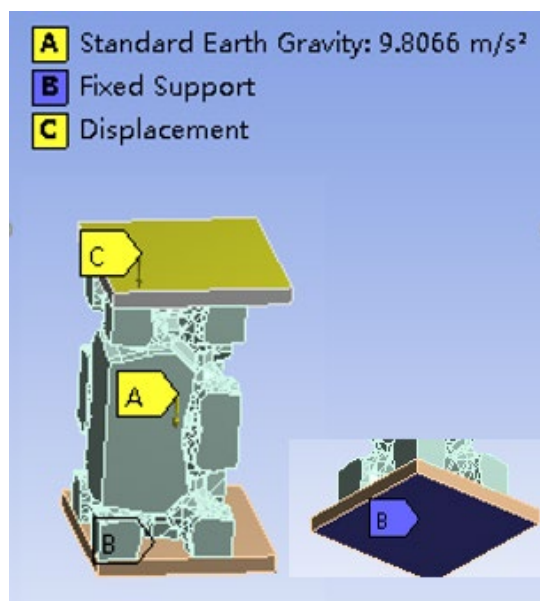


Figure 4.10 Boundary and loading conditions of FEM models.

4.4.3 Validation of FEM models

To corroborate the accuracy and reliability of the FEM models, compression experiments are carried out on five distinct samples as displayed in Figure 4.11. Utilising Ansys for the simulation, the load-displacement responses of CB-R, SP-1, SP-2, IWP-1, and IWP-2 units under axial displacement of the loading plate is meticulously recorded and found to be in remarkable congruence with the outcomes of the corresponding physical compression tests. This assessment is strategically designed to establish a benchmark for the validation of subsequent compressive modelling efforts targeting SP-3, SP-4, SP-5, IWP-3, and IWP-4 TPMS units. As elucidated in Figure 4.12, panels (a), (b), and (c) present a comparative analysis between the numerically derived and experimentally obtained load-displacement curves for each TPMS unit type, including the CB-R unit, when subjected to vertical loads. Notably, the trend of displacement across the entire range exhibited a consistent pattern, underscoring the fidelity of the simulation process.

A detailed examination reveals acceptable discrepancies in the peak between the simulation

outcomes and the experimental averages for the CB-R, IWP-1, IWP-2, SP-1, and SP-2 units, with deviations pegged at approximately 0.9%, 7.8%, 6.1%, 3.1%, and 5.9%, respectively. Such variances can largely be attributed to the idealised symmetry inherent in the FEM models, contrasted against the slightly asymmetrical realities observed in the actual compressive tests, especially concerning the contact areas and the printed specimens.

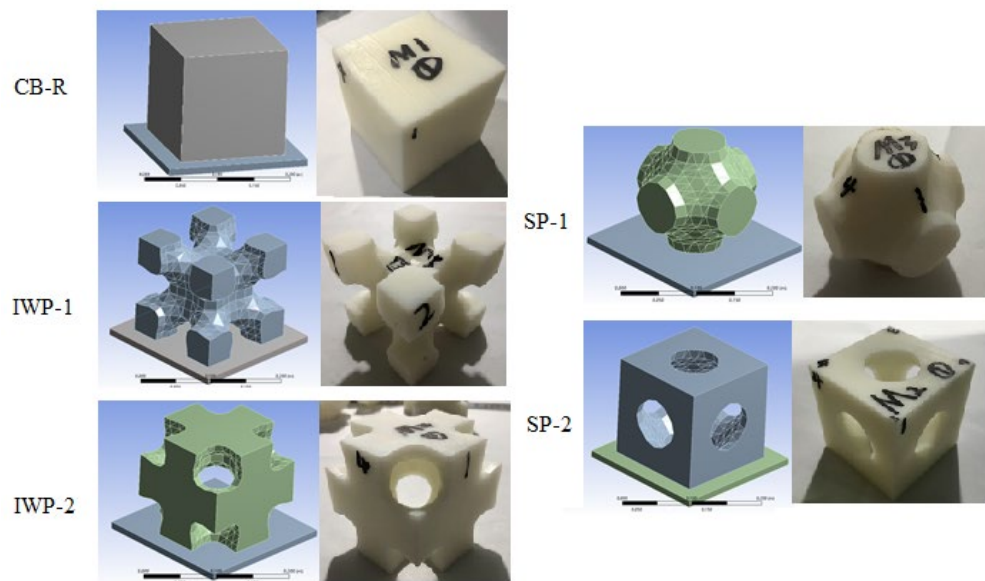
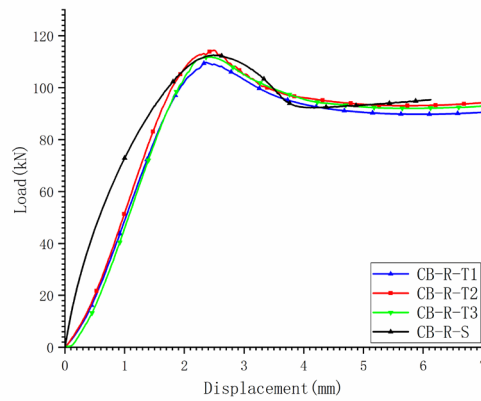


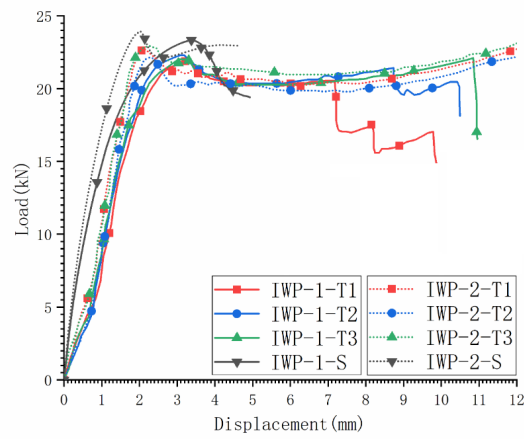
Figure 4.11 Schematic diagrams and examples of printed units.

The observed discrepancies between the FEM simulations and the physical compression tests are deemed acceptable, given that the outcomes of compression tests conducted on identically classified units also exhibited variations within the range of 5% to 10%. Consequently, the material properties selected for the components in FEM models have been validated through this comparative analysis. These parameters have been uniformly applied across all numerical calculations involving the TPMS unit cells, ensuring consistent and reliable simulations for further investigative modelling within the study. This methodological rigour enhances the robustness of the FEM as a predictive tool for assessing the mechanical properties and behaviours of TPMS unit cells subject to

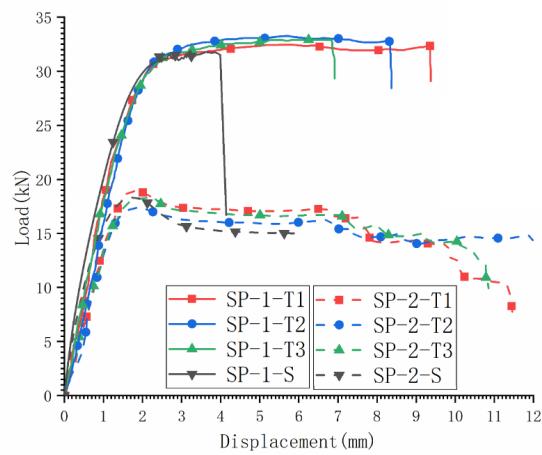
compression forces.



(a)



(b)



(c)

Figure 4.12 Comparison of load-displacement curves between FEM simulation and experiments for (a) CB-R unit, (b) IWP unit cells and (c) SP unit cells.

4.5 FEM RESULTS FOR COMPRESSION

4.5.1 Load-displacement curve

After the FEM simulations are verified, the numerical simulations of IWP-3, IWP-4, SP-3, SP-4, SP-5 type units subject to compression are conducted. The load-displacement curves of each variety of units are listed in Figure 4.13(a) and (b). It can be seen that there are three stages of load-displacement for all types of units. Initially, there is a near-linear escalation of force with increasing displacement. Subsequently, this rate of force augmentation moderates and may even exhibit a reduction. In the final stage, the structural stiffness of the TPMS units converges towards zero. All TPMS unit variants, with the exception of SP-1 and SP-4, manifest a regressive segment during the second phase. It can be roughly inferred that the change of the element types does not affect the overall load-displacement response relationship, but only affects the stiffness and the strength of the unit. The diagrams further reveal that the plastic yielding phase predominantly spans between 1.5-3mm of displacement for all units. In general, the specific design of the unit structure impacts the displacement value at the onset of the second phase, with higher values correlating to increased peak loads sustained by the structure.

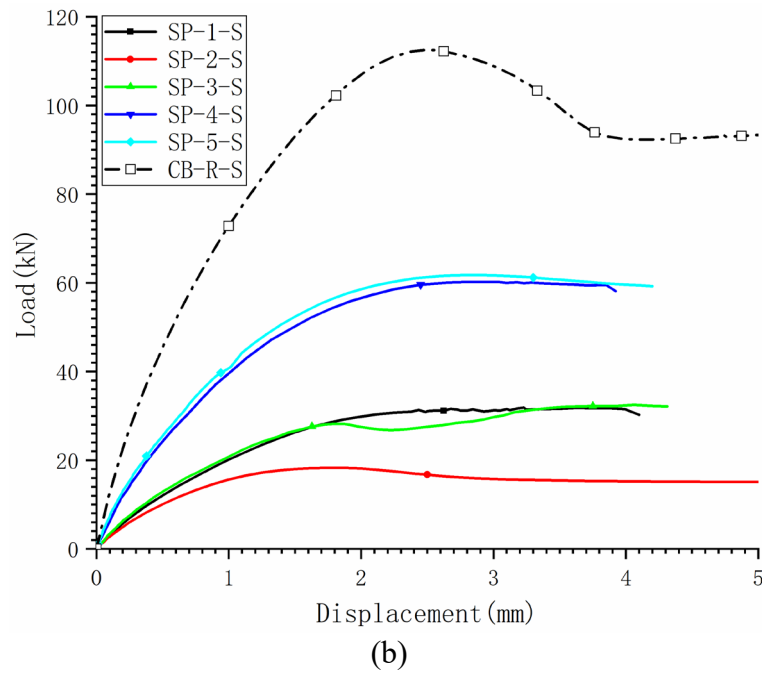
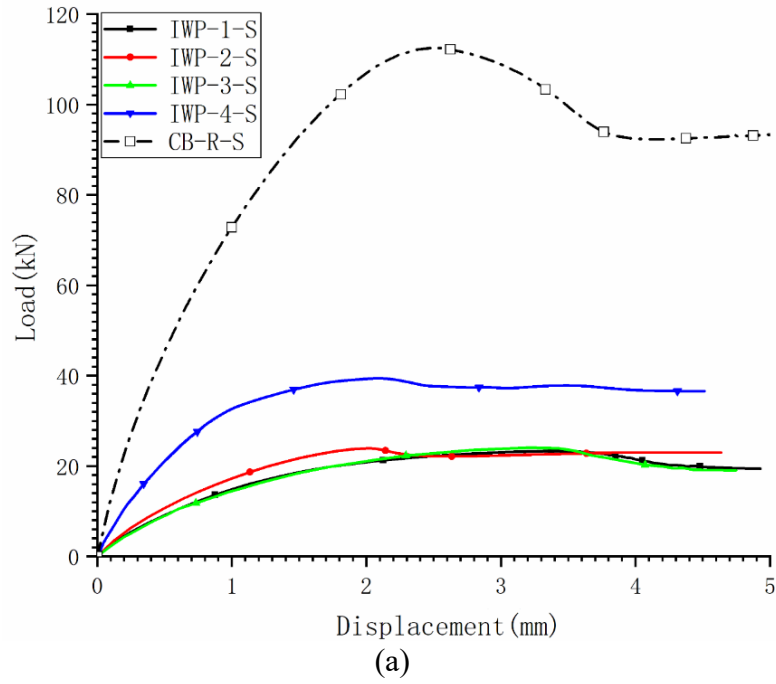


Figure 4.13 Load-displacement curves of all TPMS unit cells from FEM. (a) SP unit cells compared with CB-R unit and (b) IWP unit cells compared with CB-R unit.

4.5.2 Compressive strength and stiffness

Compressive strength and stiffness are critical properties in the field of civil engineering, particularly relevant to the design and evaluation of structures that must withstand loads without

undergoing excessive deformation or failure. Take the peak of the second phase in the load-displacement curve of the FEM modelling as the ultimate load. The compressive strength of the structure is determined by dividing the ultimate load by the cross-sectional area, which measures 50mm by 50mm. One may estimate the units' stiffness by calculating the quotient of compressive strength and the nominal strain corresponding to the displacement. As shown in Figure 4.14, the compressive strength of all the TPMS units, neither IWP or SP based units, does not meet that of the CB-R sample. When benchmarked against the cubic test block, the strength of SP-series units declines by 58.9% to 83.7%, while IWP-series units exhibit a decrease in compressive strength ranging from 64.9% to 79.3%. SP-3's compressive strength marginally trails behind that of SP-1, and a negligible variance is observed in the compressive strengths between IWP-1 and IWP-3 units. It can be inferred that as long as the geometry shape of the smallest unit is identical, the overall compressive behaviour of the whole structures with the same size is not much different. In comparison, SP-series units demonstrate a more pronounced resistance to compression than those within the IWP series.

Table 4.5 FEM modelling results of all TPMS unit cells compared to CB-R.

Unit type	Compressive strength	Stiffness	Relative density (compared to CBR)	Compressive strength/RD	Stiffness/RD
CB-R	45.03	902	1	45.03	902
IWP-1	9.33	138	0.53	17.61	261
IWP-2	9.58	237	0.47	20.38	505
IWP-3	9.63	150	0.53	18.17	283
IWP-4	15.81	372	0.77	20.54	483
SP-1	12.75	197	0.5	25.50	395
SP-2	7.32	209	0.5	14.65	419
SP-3	11.27	213	0.5	22.55	426
SP-4	24.07	431	0.75	32.10	575
SP-5	24.40	476	0.75	24.40	635

The stiffness measurements for various TPMS units derived from FEM modellings are illustrated in Figure 4.15. In general, TPMS units boasting superior compressive strength exhibit increased

stiffness. Taking the relative density of the TPMS units into consideration, both the compressive strength and stiffness are normalised by the unit's relative density compared to that of a cubic block. This process is undertaken to ascertain the comparative compressive strength and stiffness, which are detailed in Table 4.5. Findings reveal that the units from the SP series outperform those from the IWP series in terms of their compressive behaviour. In civil engineering, compressive resistance is an important indicator, thus the application of SP series units in civil engineering has better application prospects.

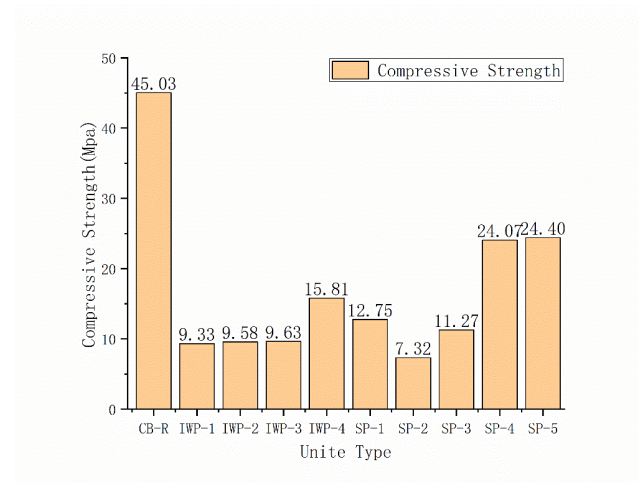


Figure 4.14 Compressive strength of all types of units from FEM.

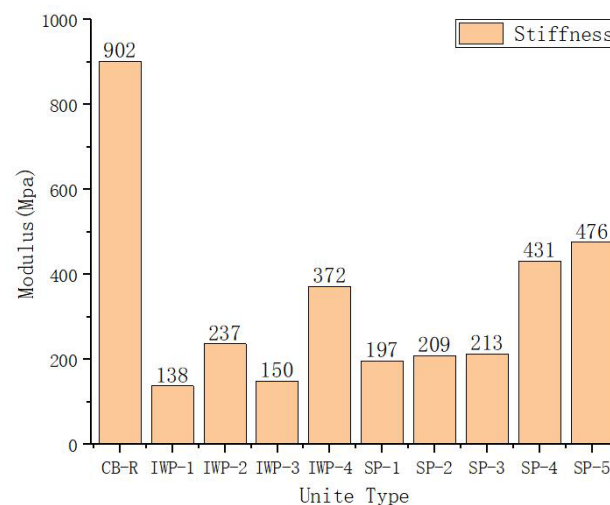


Figure 4.15 Stiffness assessed from FEM simulations for all TPMS units and CB-R.

4.5.3 Equivalent stress

The stress distribution inside all the TPMS units of quarter-scale models at their maximum load is illustrated in Figure 4.16. Upon comparison, the IWP-2, SP-1, and SP-4 models exhibit a broader distribution of zones where the equivalent stress is near its maximum value. This suggests a more uniform dissemination of axial forces applied by the top plate throughout the unit, potentially accounting for the enhanced compressive strength observed in these three models relative to other TPMS-based structures. As shown in Figure 4.17. It can be found that the area where the test specimen is damaged is the area of heightened stress concentration identified in the finite element analysis, thereby reaffirming the fidelity of the FEM approach.

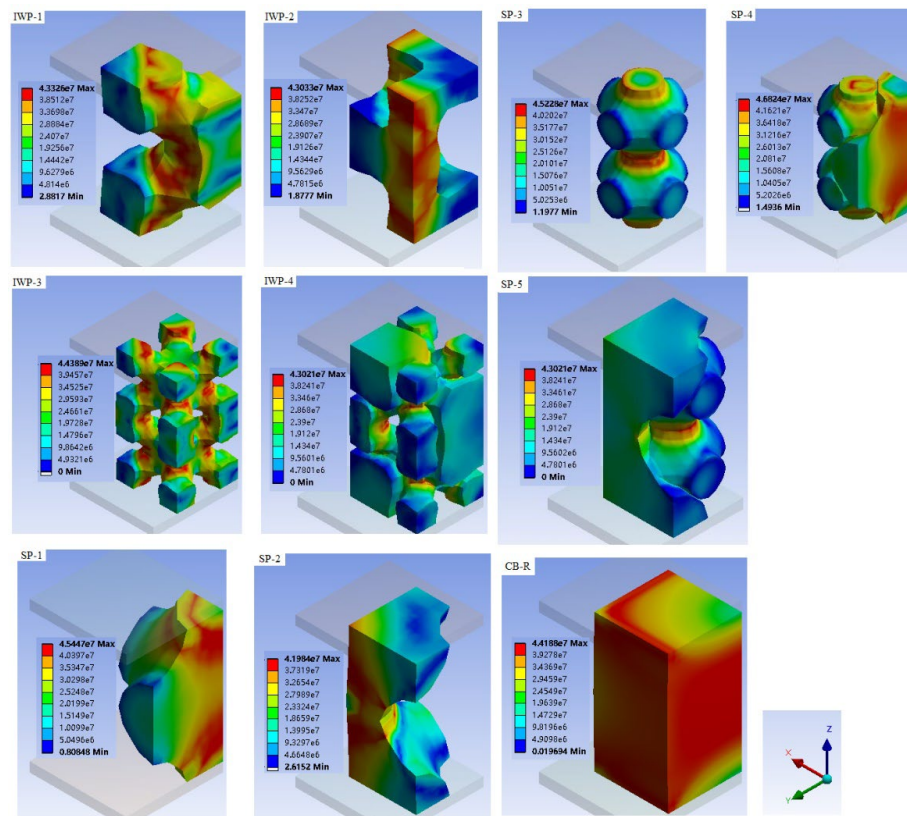


Figure 4.16 Stress at the maximum load in quarter-scale TPMS units in Ansys.

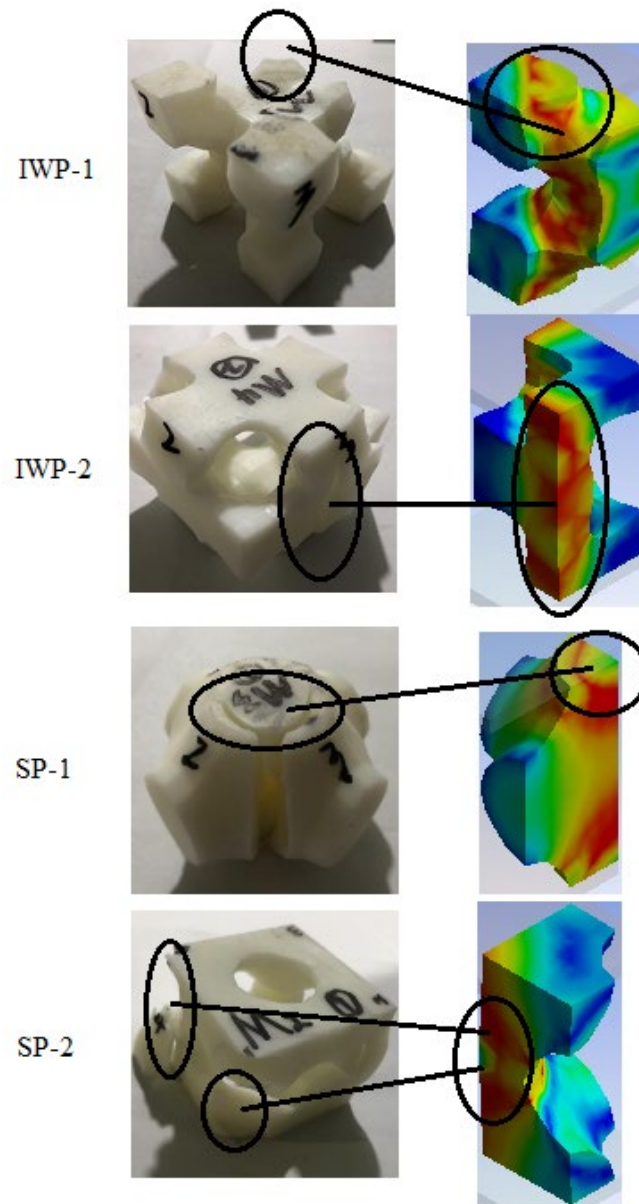


Figure 4.17 Comparison between the cracking area in experiments and stress concentration area in quarter-scale TPMS units in Ansys.

4.6 CONCLUSION OF COMPRESSIVE BEHAVIOURS

Although the TPMS structures are characterised with their superior vibration damping characteristics and energy absorption potential. Nevertheless, crucial to verify that these intelligent porous TPMS designs possess adequate compressive strength to withstand loads in the domain of

civil engineering. In this section 4.2 to 4.5, a series of compressive experiments and FEM numerical calculations are conducted to investigate the compressive behaviour of SP based units (five types) and IWP based units (four types). In the experiments, the cube block as a reference and four TPMS based units with a size of $5\text{cm} \times 5\text{cm} \times 5\text{cm}$ are tested. The FEM simulation is used to further analyse additional TPMS variants and the internal force dispersal within the porous units, revealing the difference of the strength and stiffness of the TPMS based structures. Based on the results and discussion, the following conclusions are given.

The load-bearing capacity of units derived from SP and IWP materials manifests a pronounced reduction when benchmarked against a cubic block specimen of the same scale. Within the scope of civil engineering applications, it becomes imperative to holistically assess a TPMS structure's efficacy in energy absorption as well as its mechanical robustness and resilience. FEM simulations, coupled with experimental outcomes, serve to delineate the compressive response characteristics of TPMS unit cells and to pinpoint the zones of critical stress within such a complex structure.

Those unit cells based on SP surface exhibit enhanced resistance to compression, incorporating superior rigidity and compressive strength in contrast to IWP designs. Consequently, the SP based unit cells are deemed more suitable for sustaining greater loads, thereby offering a more expansive range of applicability in load-bearing contexts as compared to the IWP counterparts.

4.7 FEM SIMULATION FOR TORSION AND SHEAR

In this part, the commercial FEM software, Ansys, is utilised for numerically analysing the mechanical performance of the designed Skeletal-TPMS units under compressive, shear and torsional loads. Notably, the unit cells' size is 50mm, which is considered a proper block size in

civil engineering. The FEM models are calibrated and validated using compressive test data of several Skeletal-TPMS units. After the model material properties are validated, the brand new hybrid Skeletal-TPMS units are investigated in their mechanical behaviours when supporting compressive and shear force and torsional moment.

4.7.1 Skeletal-TPMS unit model

The nodal approximation of a TPMS is a combination of sine and cosine functions. It also means brand new TPMSs can be obtained by combining two or more discovered TPMSs. For example, the IWP TPMS surface is a combination of the W surface and P surface. The mathematic formula of the W surface is expressed using Equation 4.1. The hybridisation of W and P TPMSs, H-WP TPMSs, can be obtained by adding the W-related character with a P-related surface as listed in Equation 4.2 [7, 44]. The constant C equals zero. The visual H-WP related TPMSs with λ_1 and λ_2 from -2 to 2 are shown in Figure 4.18. It is evident that the H-WP surfaces have both the features of W surfaces and P surfaces, while the weights of the features changes according to the evolution of the parameter λ_1 and λ_2 . The IWP TPMS is a particular case of H-WP surfaces when λ_1 equals to 2 and λ_2 equals to -1, as shown in Equation 4.3. Even though the range of λ_1 and λ_2 in Figure 4.18. is from 2 to -2, there is no limitation for λ_1 and λ_2 in Equation 4.2. Not all of the λ_1 and λ_2 can make the nodal approximation represent a valid TPMS. If the absolute values of the ratio of λ_1 and λ_2 are the same, the curved surfaces indicated by the formulas are the same TPMS. Besides, if the wavelength, l , in ϕ_w does not equal to half of it in ϕ_p , the formula will stand for another series of hybrid W and P TPMSs.

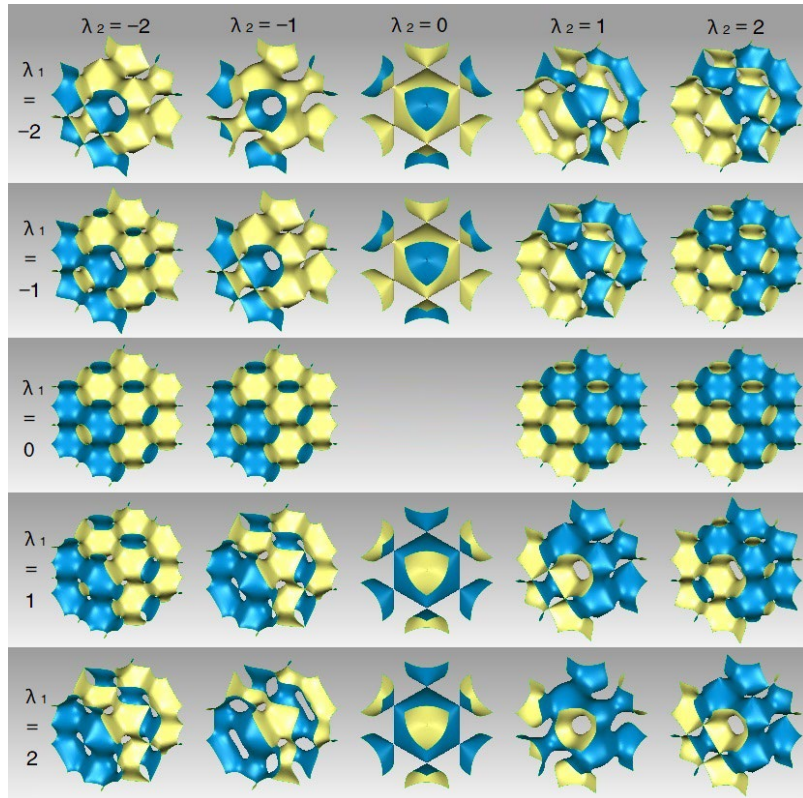


Figure 4.18 Hybrid surfaces of W and P TPMSs (H-WP surfaces) with various λ_1 and λ_2 .

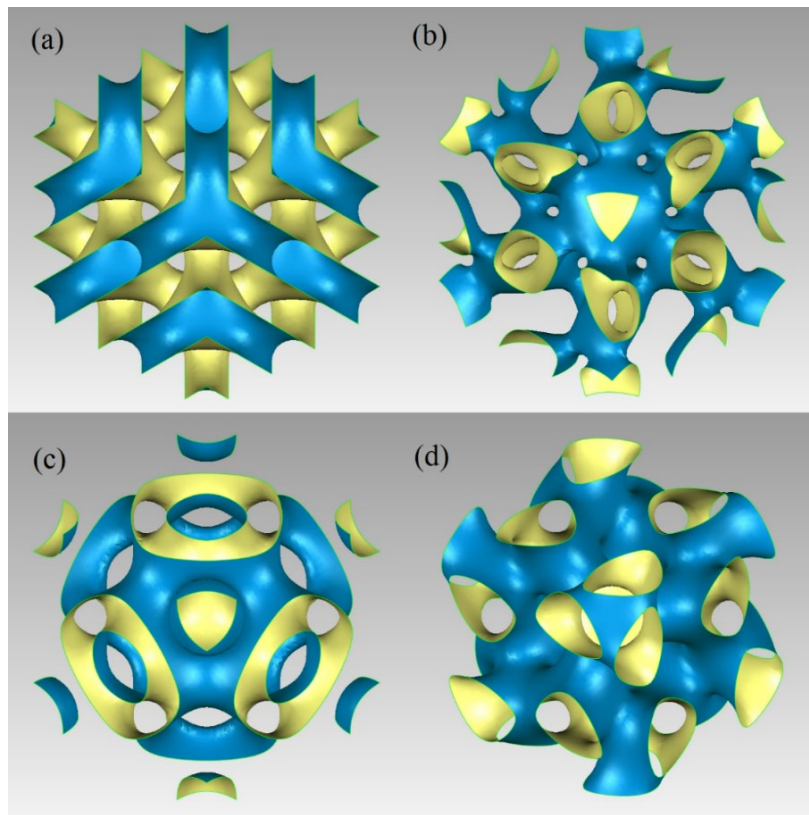


Figure 4.19 The visual surfaces of new types TPMSs (a) H-DX, (b) H-DW, (c) H-XX and (d) H-RWP.

Many other new types of TPMSs are able to be determined by fusing the mathematic formulas of the known TPMSs of certain weights and wavelengths. The visual surfaces of the newly designed TPMSs by mixing several TPMSs are shown in Figure 4.19. The nodal approximations of the TPMSs are as follows: Equation 4.4 hybridisation of several X-TPMSs (H-XX), Equation 4.5 hybridisation of D and X TPMSs (H-DX), Equation 4.6 hybridisation of D and W TPMSs (H-DW), Equation 4.7 hybridisation of R, W and P TPMSs (H-RWP).

$$\phi_W = \cos\left(\frac{2\pi x}{l}\right)\cos\left(\frac{2\pi y}{l}\right) + \cos\left(\frac{2\pi y}{l}\right)\cos\left(\frac{2\pi z}{l}\right) + \cos\left(\frac{2\pi z}{l}\right)\cos\left(\frac{2\pi x}{l}\right) = C \quad 4.1$$

$$\phi_{H-W_{\lambda_1}P_{\lambda_2}} = \lambda_1 \cdot \phi_W(l=n) + \lambda_2 \cdot \phi_P(l=\frac{n}{2}) = C \quad 4.2$$

$$\phi_{IWP} = 2 \cdot \phi_W(l=n) + (-1) \cdot \phi_P(l=\frac{n}{2}) = C \quad 4.3$$

$$\begin{aligned} \phi_{H-X} = & \cos\left(\frac{2 \cdot 2\pi x}{l}\right)\cos\left(\frac{2\pi y}{l}\right)\cos\left(\frac{2\pi z}{l}\right) \\ & + \cos\left(\frac{2\pi x}{l}\right)\cos\left(\frac{2 \cdot 2\pi y}{l}\right)\cos\left(\frac{2\pi z}{l}\right) \\ & + \cos\left(\frac{2\pi x}{l}\right)\cos\left(\frac{2\pi y}{l}\right)\cos\left(\frac{2 \cdot 2\pi z}{l}\right) = 0.4 \end{aligned} \quad 4.4$$

$$\begin{aligned} \phi_{H-DX} = & \sin\left(\frac{2\pi x}{l}\right)\sin\left(\frac{2\pi y}{l}\right) + \sin\left(\frac{2\pi y}{l}\right)\sin\left(\frac{2\pi z}{l}\right) + \sin\left(\frac{2\pi z}{l}\right)\sin\left(\frac{2\pi x}{l}\right) \\ & + \cos\left(\frac{2\pi x}{l}\right)\cos\left(\frac{2\pi y}{l}\right)\cos\left(\frac{2\pi z}{l}\right) = 0 \end{aligned} \quad 4.5$$

$$\begin{aligned} \phi_{H-DW} = & (\sin\left(\frac{2 \cdot 2\pi x}{l}\right)\sin\left(\frac{2\pi y}{l}\right)\cos\left(\frac{2\pi z}{l}\right) + \sin\left(\frac{2\pi x}{l}\right)\sin\left(\frac{2 \cdot 2\pi y}{l}\right)\cos\left(\frac{2\pi z}{l}\right) + \sin\left(\frac{2\pi x}{l}\right)\sin\left(\frac{2\pi y}{l}\right)\cos\left(\frac{2 \cdot 2\pi z}{l}\right)) \\ & - (\cos\left(\frac{2 \cdot 2\pi x}{l}\right)\cos\left(\frac{2 \cdot 2\pi y}{l}\right) + \cos\left(\frac{2 \cdot 2\pi y}{l}\right)\cos\left(\frac{2 \cdot 2\pi z}{l}\right) + \cos\left(\frac{2 \cdot 2\pi z}{l}\right)\cos\left(\frac{2 \cdot 2\pi x}{l}\right)) = -0.3 \end{aligned} \quad 4.6$$

$$\begin{aligned} \phi_{H-RWP} = & 1.1(\sin\left(\frac{2 \cdot 2\pi x}{l}\right)\cos\left(\frac{2\pi y}{l}\right)\sin\left(\frac{2\pi z}{l}\right) + \sin\left(\frac{2 \cdot 2\pi z}{l}\right)\cos\left(\frac{2\pi x}{l}\right)\sin\left(\frac{2\pi y}{l}\right) + \sin\left(\frac{2 \cdot 2\pi y}{l}\right)\cos\left(\frac{2\pi z}{l}\right)\sin\left(\frac{2\pi x}{l}\right)) \\ & - 0.2(\cos\left(\frac{2 \cdot 2\pi x}{l}\right)\cos\left(\frac{2 \cdot 2\pi y}{l}\right) + \cos\left(\frac{2 \cdot 2\pi y}{l}\right)\cos\left(\frac{2 \cdot 2\pi z}{l}\right) + \cos\left(\frac{2 \cdot 2\pi z}{l}\right)\cos\left(\frac{2 \cdot 2\pi x}{l}\right)) \\ & - 0.4(\cos\left(\frac{2 \cdot 2\pi x}{l}\right) + \cos\left(\frac{2 \cdot 2\pi y}{l}\right) + \cos\left(\frac{2 \cdot 2\pi z}{l}\right)) = 0 \end{aligned} \quad 4.7$$

TPMSs partition the spatial volume into dual segments, thereby facilitating the synthesis of two distinct Skeletal-TPMS configurations when the sextet of faces constituting the boundary cube is

sealed. These dual configurations of Skeletal-TPMS exhibit mutual complementarity within their enclosure. The variant with the lesser enclosed volume is termed the primary type or main type, whereas its counterpart is known as the complementary type or the secondary type. The constructed variants are designated as Skeletal-TPMS-P for the primary type or main type and Skeletal-TPMS-C for the complementary type or the secondary type. These variants are illustrated in Figure 4.20 (a) to (d). The synergistic correspondence between the pair of Skeletal-TPMS types within an identical TPMS culminates in a cubic amalgamation, depicted in Figure 4.20e. In Figure 4.20f, the genesis of the Skeletal-H-DW-P configuration is expounded; the method involves sealing the apertures in the H-DW TPMS, resulting in extraneous elements which are then excised to form an integrated lattice. A parallel process is employed in fabricating the Skeletal-H-XX variants, where select elements are likewise excised. Quantitative details regarding the volume and density of the Skeletal-TPMS constructs relative to the cubic block are catalogued in Table 4.6.

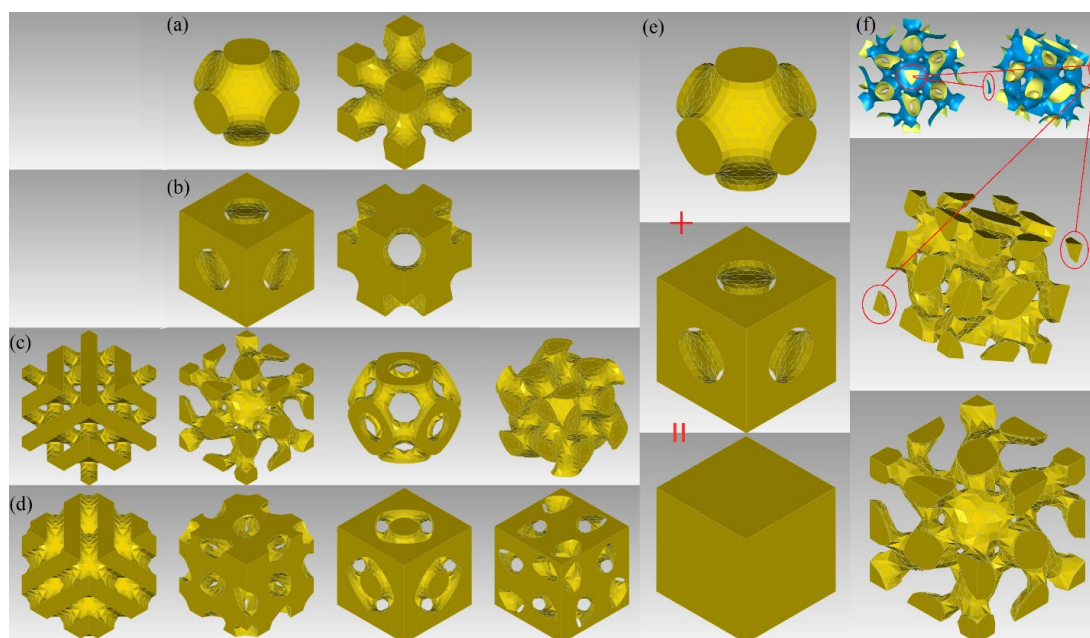


Figure 4.20 Skeletal-TPMS unit cells. (a) and (b) are the primary and complementary type of Primitive (SP) and IWP units, (c) and (d) are the primary and complementary type of H-DX, H-DW, H-XX and H-RWP units, (e) cubic amalgamation of Primitive (SP) unit; (f) excise dispersed element to form H-XX-P units.

Table 4.6 The specific density of the TPMS units compared to cube block.

TPMS	Type	Volume/mm ³	specific density
Cube block	-	125000.00	1.00
H-DX	primary	125000.00	0.40
	complementary	50253.22	0.60
H-DW	primary	74746.78	0.39
	complementary	48947.98	0.61
H-XX	primary	76052.02	0.21
	complementary	25699.14	0.79
H-RWP	primary	99300.86	0.49
	complementary	61255.19	0.51

4.7.2 FEM model settings

The geometric shapes are exported into Sat file to be imported into the Ansys. The SP and IWP skeletal units are used to validate the FEM models, while the other eight types of Skeletal-TPMS units based on hybrid TPMSs are used for research. All the Skeletal-TPMS units are of a complex shape and simulated by an individual solid with solid-187 element type. The solid-187 element is a ten-node brick element with a diamond geometry and is well suited to modelling the complex meshes of a Skeletal-TPMS unit [149]. Their element sizes are 2 mm. The element type and size are determined to curtail the duration of simulations for mechanical analysis while preserving the fidelity and precision of the outcomes. It is important to note that the element meshing size influences the precision of results. The meshing size are determined as the simulation results start to converge to a consistent value. 3D printed samples are thought to have some internal defects compared with the designed model because of the roughness of the printing process. Additionally, the mechanical properties of 3D printed materials are also a bit different from the casted materials. Thus, hypotheses are made in the FEM simulation to simplify the material model. Firstly, the 3D printed sample is considered to be a perfect solid without voids. Secondly, the printed material is assumed to be homogeneous and isotropic, and has the same material properties obtained from standard tests carried out by Royal DSM Inc according to ASTM standards. These two hypotheses

are reasonable for qualitatively analysing the mechanical behaviours of TPMS structures. An elastic-plastic constitutive model has been adopted [150]. The material properties set in the FEM simulation are based on a composite photosensitive resin same in Table 3.4, which has been used to fabricate Skeletal-TPMS units to validate the FEM simulation.

The loading conditions are set according to the type of load types. In compressive research, a constraint of the translation freedom along the vertical direction is applied on all the bottom surface of all the Skeletal-TPMS units, while a fixed constraint is applied to the same areas in shear and torsional research. The boundary conditions are explained using the Skeletal-IWP unit as an instance. The bottom supporting regions are shown in Figure 4.21 (a). A velocity of 0.05 mm/s, which can apply a strain rate of 0.001/s to the TPMS units, along vertical direction is set to the upper surfaces of the TPMS units for compressive study, as shown in Figure 4.21 (b). A corresponding velocity is applied laterally along the X-axis for shear investigations, as detailed in Figure 4.21 (c). A torque in increments of 10N·m/s is applied to the top surface for the torsional analysis, as shown in Figure 4.21 (d). The reaction force and moment are recorded over time during the simulation until the applied load or moment reaches the maximum value and stabilises.

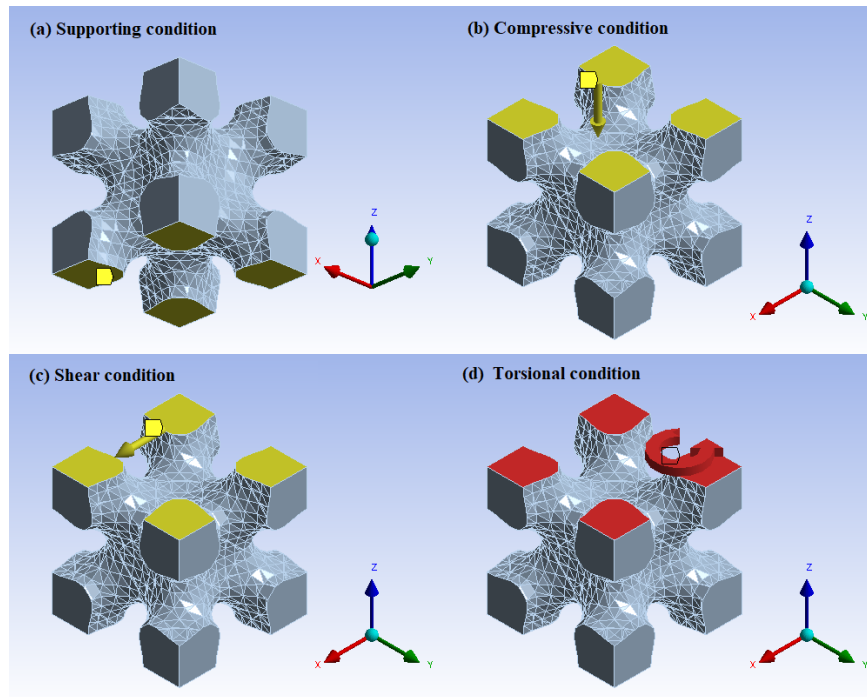


Figure 4.21 The boundary conditions: (a) Supporting condition , (b) Loading condition for compressive research, (c) Loading condition for shear research, (d) Loading condition for torsional research.

4.7.3 Validation of FEM models

The cubic block (CB) as well as primary and complementary variants of skeletal IWP and SP units, constructed from a composite photosensitive polymer, are realised through Stereolithography (SLA) additive manufacturing. These specimens are then subjected to a succession of compression assays. Triads of samples for each configuration have been produced, with an equivalent number of compression evaluations executed. The mean outcome of these assays is employed for validation against FEM data. The numerical and experimental compressive results are compared for verifying the reliability of the material properties under compression. A tensile simulation of a standard sample is carried out to validate the reliability of the material properties under tension. The printed samples and the FEM tensile models are displayed in Figure 4.22.

The simulation and test results under compression are compared in Figure 4.23. The compressive

test results of CB have been adopted to input the stress-strain curves for the 3D printed TPMS units in FEM simulations. As illustrated in Figure 4.23, there exists a substantial congruence between the results from compressive tests and those from the FEM simulations. Up to a displacement threshold of 1.5 mm, the discrepancies in compressive load are marginal. At the displacement of 2mm, the differences are 1.8% (Skeletal-SP-P), 9.8% (Skeletal-SP-S), 3.9% (Skeletal-IWP-P) and 8.8% (Skeletal-IWP-S), respectively. The correlation coefficients between the results of experimental tests and FEM simulation are 0.997 (Skeletal-SP-P), 0.953 (Skeletal-SP-S), 0.995 (Skeletal-IWP-P) and 0.992 (Skeletal-IWP-S), respectively. These discrepancies are deemed acceptable and may be attributed to the development of initial defects inside 3D printed samples. After the displacement of 2mm, the differences start to increase because the initial defects inside printed samples start to develop into cracks in experimental tests and decrease the bearing capacity of the samples. On the other hand, FEM models are assumed to be a perfectly continuous solid structure with no defect. The tensile strength obtained from the FEM modelling is about 40.7 MPa, which is also within the range in Table 2. The simulation of tension and compression is proper and reliable. The material properties used in the FEM modelling of the 3D print composite material can be corroborated through this comparative assessment. These material properties have been used in the numerical calculations for hybrid TPMS unit cells.

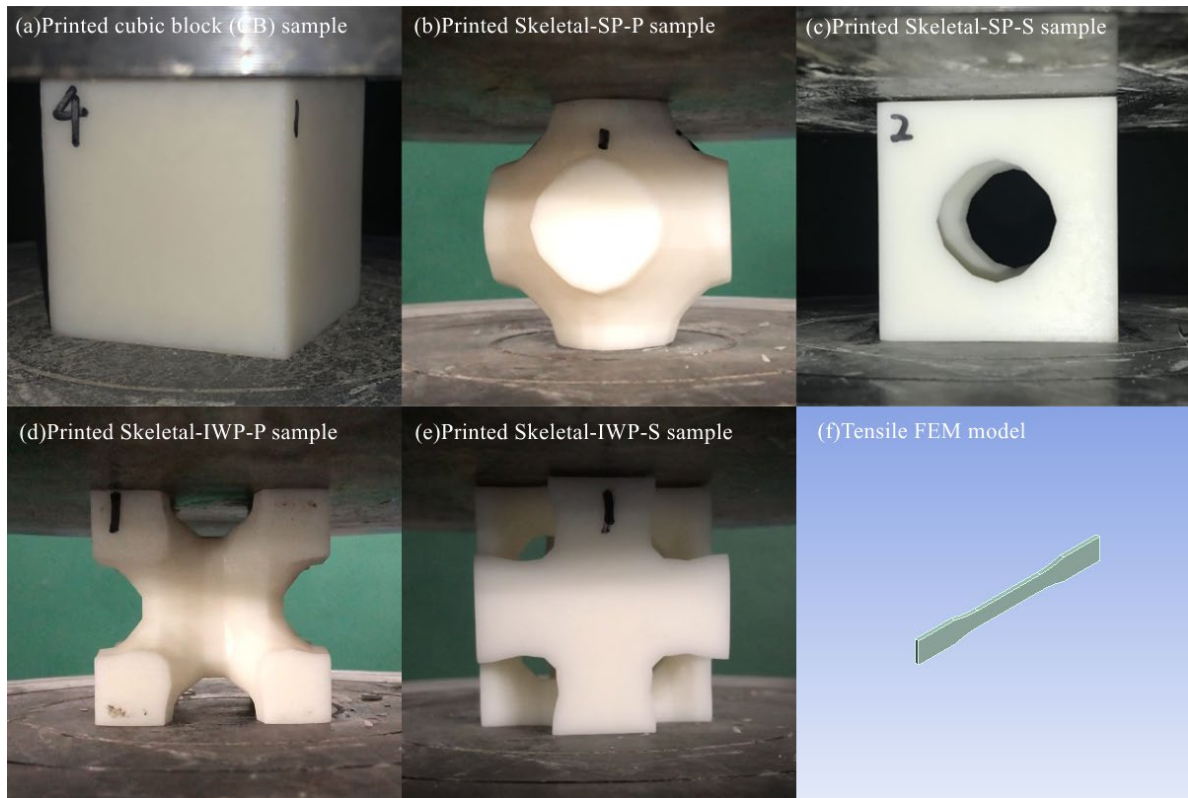


Figure 4.22 (a) to (e) The 3D printed samples;(f) Tensile FEM model.

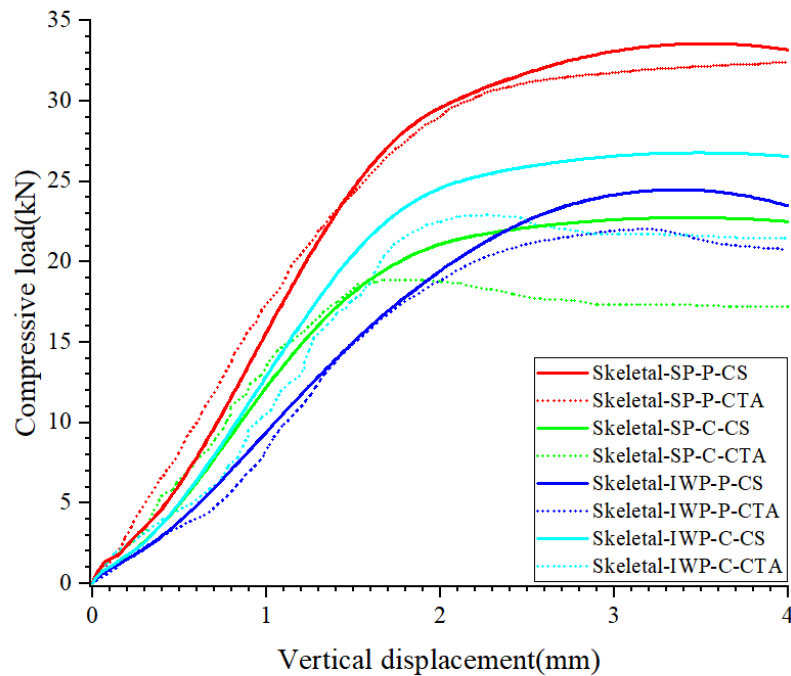


Figure 4.23 Load-displacement curves of skeletal SP and IWP unit cells from compressive tests and FEM simulation.

4.8 FEM RESULTS FOR TORSION AND SHEAR

4.8.1 Compressive behaviour

Figure 4.24 delineates the specific load-displacement curves of skeletal hybrid TPMS unit cells from FEM simulations. The specific loads are obtained by dividing absolute loads by the relative density of unit cells. By comparing the eight curves, we can find that TPMS typologies markedly influence their skeletal units compressive resistance. In addition, the complementary Skeletal-TPMS units outperform their primary types in compressive resistance. All the complementary Skeletal-TPMS units have similar compressive behaviour. Their specific compressive bearing capacity is from 60 kN to 80 kN. The specific compressive bearing capacity of the complementary types of Skeletal-TPMS units are much lower, within 20kN, except for the complementary Skeletal-H-RWP unit, about 36 kN.

Elucidated in Table 4.7 are the absolute and relative compressive loads for the Skeletal-TPMS frameworks alongside their corresponding stress dispersal image at a standardised displacement of 2.5 mm. The data implies that a high absolute compressive strength in Skeletal-TPMS units typically correlates with augmented specific compressive strength. The complementary Skeletal-HXX unit stands out, offering the most robust performance under compressive stress. All complementary Skeletal-TPMS units are of both higher absolute and specific compressive resistance. They are more proper for bearing a heavy load in civil engineering than the primary Skeletal-TPMS units. The compressive resistance of all the primary Skeletal-TPMS units except for the primary skeletal-H-RWP unit is too low. However, they still have the potential to be used as soft supports because of their porous properties that are good for drainage. The critical area of the Skeletal-TPMS units under

compressive load can also be observed in Table 4.7, which is helpful to predict the weak areas inside the units.

Table 4.7 Compressive load and stress distribution of the hybrid TPMS structures at a displacement of 2.5 mm.

TPMS	Type	Absolute compressive load/kN	Stress distribution	
		Specific compressive load/kN	Primary type	Complementary type
H-DX	primary	4.09		
		10.17		
	complementary	36.28		
		60.67		
H-DW	primary	5.24		
		13.38		
	complementary	37.72		
		62.00		
H-XX	primary	2.31		
		11.24		
	complementary	53.58		
		67.45		
H-RWP	primary	18.65		
		38.06		
	complementary	30.46		
		59.73		

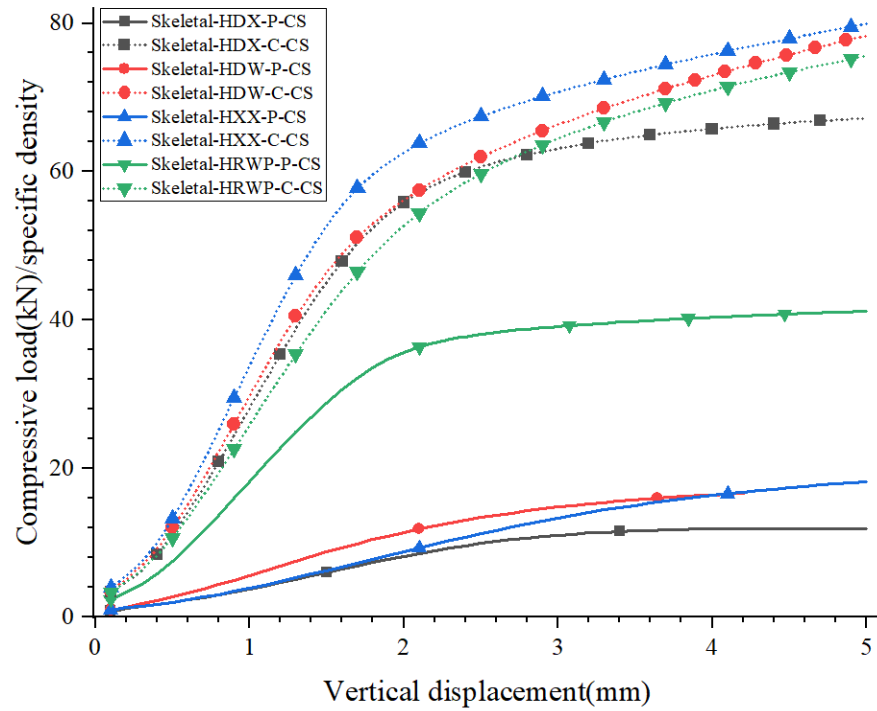


Figure 4.24 Specific Load-displacement curves of skeletal hybrid TPMS structures from compressive FEM simulation.

4.8.2 Shear behaviour

Figure 4.25 displays the shear load-displacement response curves for diverse skeletal hybrid TPMS specimens derived from FEM simulations. It is evident that the group of complementary Skeletal-TPMS units has better specific shearing resistance than the group of primary Skeletal-TPMS units. The complementary Skeletal-HXX unit performs the best. The complementary skeletal H-DX, H-DW, and H-RWP units have a similar specific shearing resistance with less than 10% difference. The specific shearing resistance of the primary skeletal H-XX and H-DX units is worst and almost the same. The curves of primary types of Skeletal-TPMS units are nearly linear, indicating that these units are still in the elastic stage under a lateral displacement of less than 5mm of their top surfaces. Besides, the complementary types show an elastic-plastic behaviour.

Table 4.8 provides a detailed comparison of the absolute and specific shear forces at a standard lateral

deformation of 2.5 mm across all porous skeletal hybrid TPMS units. It is discerned that the Skeletal-TPMS structures with elevated absolute shear loads correlate to heightened specific shear resistance. Nevertheless, there is no simple linear relationship between specific and absolute shearing resistance. The complementary Skeletal-HXX unit has both the best specific and absolute shearing resistance, but its primary unit performs the worst. The group of complementary Skeletal-TPMS units performs much better than the group of primary Skeletal-TPMS units in supporting a shear load. The H-RWP's primary and complementary skeletal units differ the least in shear resistance compared with other hybrid TPMSs. The critical area of the Skeletal-TPMS units under shear load can also be observed in Table 4.8, which is helpful to predict the weak areas inside the units.

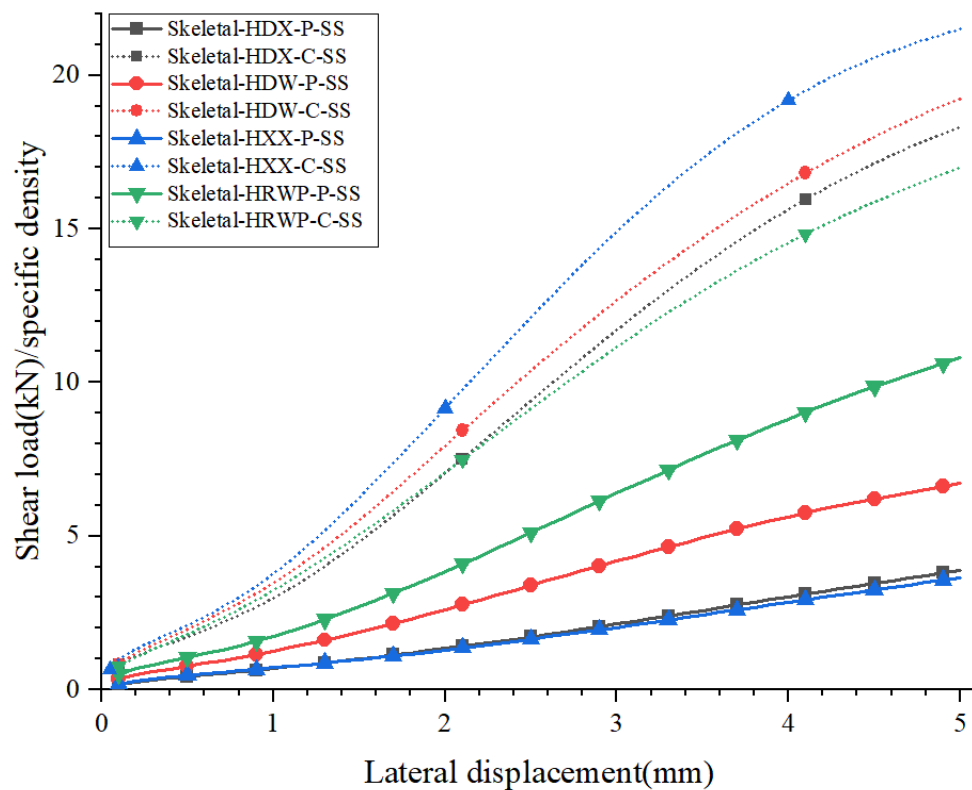
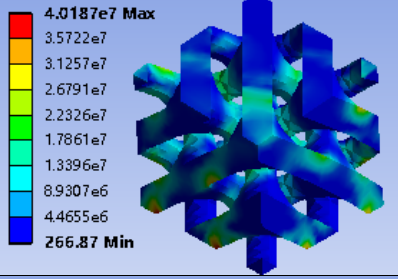
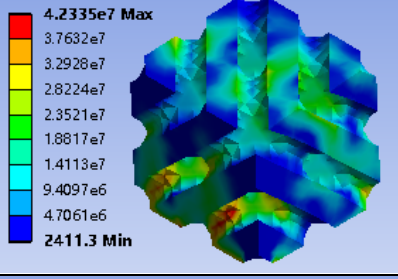
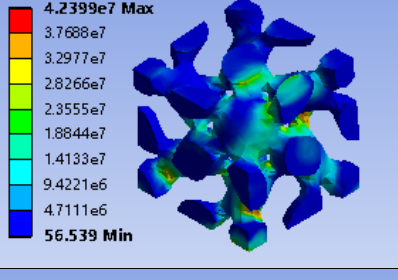
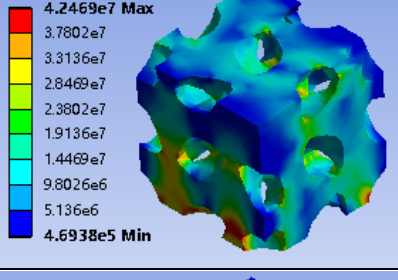
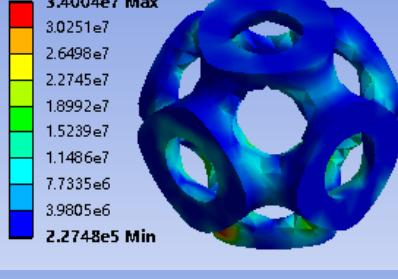
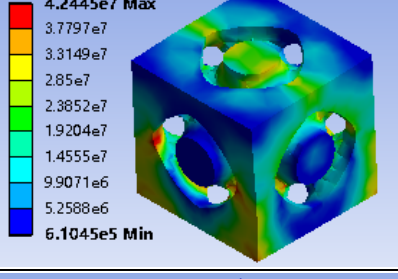
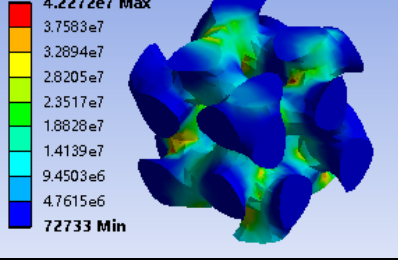
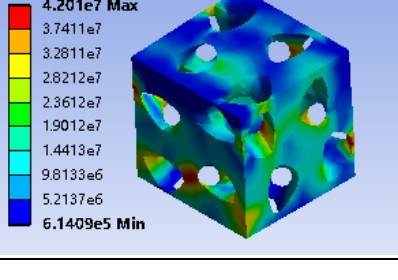


Figure 4.25 Specific Load-displacement curves of skeletal hybrid TPMS structures from shear FEM simulation.

Table 4.8 Shear load and stress distribution of the hybrid TPMS structures at a displacement of 2.5 mm.

TPMS	Type	Absolute shear load/kN	Stress distribution	
		Specific shear load/kN	Primary type	Complementary type
H-DX	primary	0.69		
		1.71		
	complementary	5.62		
		9.41		
H-DW	primary	1.33		
		3.39		
	complementary	6.32		
		10.39		
H-XX	primary	0.34		
		1.64		
	complementary	9.63		
		12.13		
H-RWP	primary	18.65		
		38.06		
	complementary	2.50		
		9.15		

4.8.3 Torsional behaviour

Figure 4.26 displays the FEM outcomes of the specific torque versus rotation angle of the upper surface relations in the hybrid skeletal TPMS models. The complementary Skeletal-HDW unit outperforms other types of TPMS units in specific torsional resistance. It also shows an elastic-plastic behaviour under the torsional load when the average rotation angle of its top surfaces exceeds

10°. The complementary Skeletal-TPMS units have better torsion resistance than the primary Skeletal-TPMS units. The complementary skeletal H-DX and H-XX units perform the second-best in resisting torque. Besides, the primary skeletal H-DW and H-RWP units have a similar specific torsional curve.

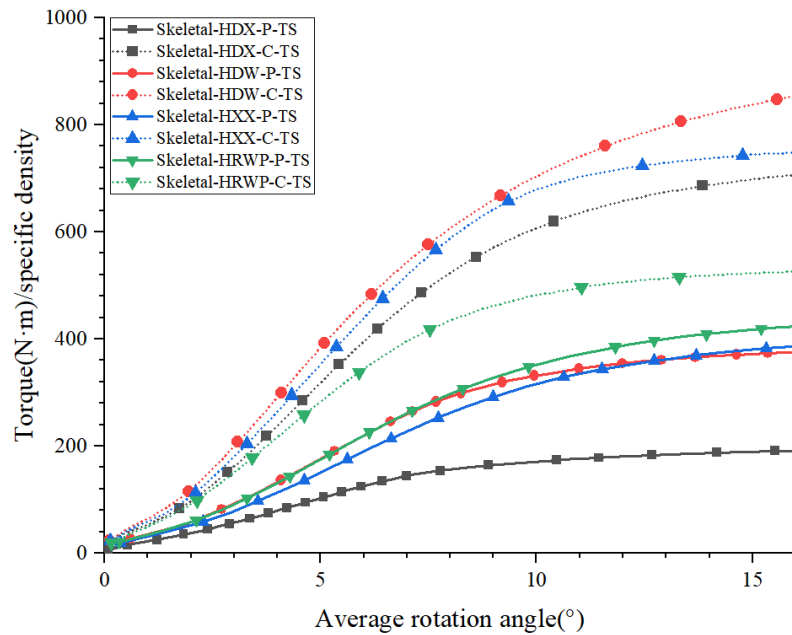
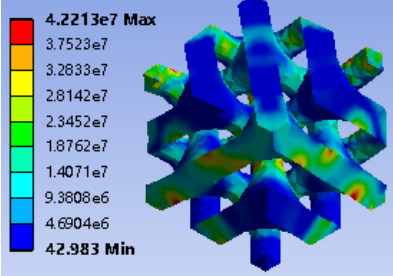
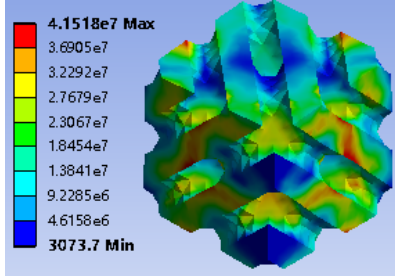
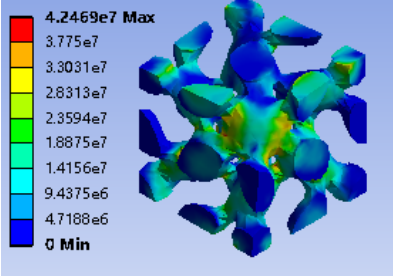
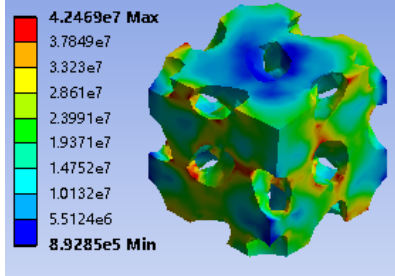
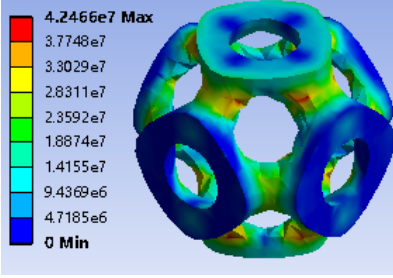
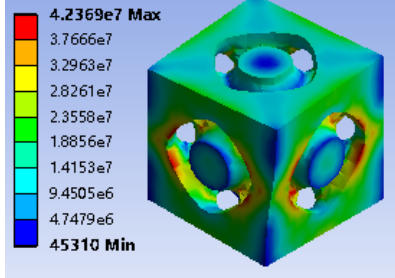
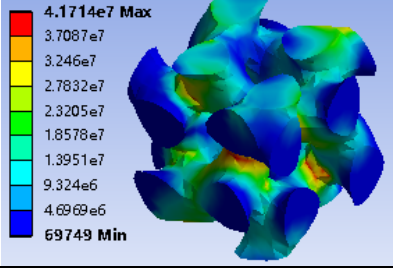
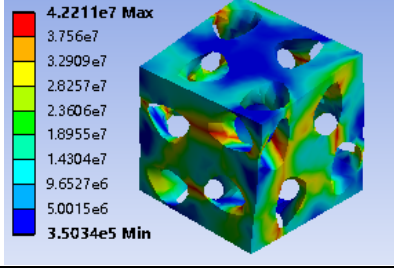


Figure 4.26 Specific torque-rotation angle curves of skeletal hybrid TPMS structures from torsion FEM simulation.

Table 4.9 delineates the absolute and specific torque measurements for the Skeletal hybrid TPMS units at a mean rotational angle of 5° from the numerical models. The data indicates that the complementary Skeletal-HDW unit model exhibits the secondly best torque bearing capacity and the optimal relative torque value, about 238.23 N·m and 391.56 N·m, respectively. On the other hand, the complementary Skeletal-HXX unit has the best absolute torque and the second specific torque, about 277.99 N·m and 349.93 N·m. In general, the torsion resistance of these two types of complementary Skeletal-TPMS units is similar. On the whole, the Skeletal-TPMS units with a higher absolute torque usually have a higher specific torque. The primary skeletal H-DX unit has

the worst torsional resistance. The critical area of the Skeletal-TPMS units under torsional load can also be observed in Table 6, which is helpful to predict the weak areas inside the units.

Table 4.9 Torque and stress distribution of the hybrid TPMS structures at average rotation angle of 5°.

TPMS	Type	Absolute torque/ N·m	Stress distribution	
		Specific torque/ N·m	Primary type	Complementary type
H-DX	primary	42.00		
		104.46		
	complementary	190.69		
		318.89		
H-DW	primary	70.69		
		180.52		
	complementary	238.23		
		391.56		
H-XX	primary	32.00		
		155.64		
	complementary	277.99		
		349.93		
H-RWP	primary	85.43		
		174.32		
	complementary	143.80		
		281.98		

4.9 CONCLUSION OF TORSION AND SHEAR BEHAVIOURS

Section 4.7 to section 4.8 aim to design brand new types of TPMS structures and explore the potential of applying TPMS structures to civil engineering. In this regards, four types of brand new hybrid TPMSs has been designed. A method of generating an approximate polygonal surface for a TPMS has been put forward. A primary Skeletal-TPMS unit and a complementary Skeletal-TPMS unit have been build based on every type of the new TPMSs. Eight types of new hybrid TPMS solid structures have been established. Their mechanical behaviours, encompassing compression, shear, and torsion, analysed and juxtaposed through Finite Element Modelling (FEM), subsequent to empirical validation against extant tests. The following salient conclusions are drawn from the study.

An inexhaustible diversity of TPMS designs can be originated by hybridising nodal approximations of extant TPMS configurations. A hybrid TPMS retains the morphological characteristics of its progenitor structures, with the feature ratios modulating as per the respective weights assigned during the hybridisation phase.

Typically, a complementary skeletal-TPMS unit demonstrates enhanced performance in bearing compressive, shear, and torsional forces compared to a corresponding primary skeletal-TPMS unit derived from the same TPMS.

There is a discernible association between the definitive and proportional resistances to compression, shear, and torsion for a Skeletal-TPMS unit. Commonly, a Skeletal-TPMS unit exhibiting notable definitive resistance also possesses a commensurately high specific resistance.

The complementary Skeletal-HXX construct exhibits supreme definitive and proportional

resistances to compression and shear, as well as exceptional definitive torsional resistance and considerable specific torsional resistance. These attributes underscore the auxiliary Skeletal-HXX framework as possessing optimal viability for civil engineering applications.

CHAPTER 5

MECHANICAL PERFORMANCE

AND CRACKING PATTERNS OF

SP AND IWP STRUCTURES

5.1 INTRODUCTION

The investigation into the mechanical properties of engineered structures under compression is critical for assessing their performance and reliability in practical applications. From the last chapter we can find that IWP and Schwarz Primitive (SP) structures are the two basic TPMSs for many hybrid TPMSs and owns good mechanical properties under various loads. This chapter delves into the compressive tests of structures based on two distinct design: IWP and SP structures. These tests are crucial for understanding the mechanical behaviours, including strength, deformation, and failure patterns, of these advanced architectural designs under compressive loads.

Given the complexity and variety of these structures, Discrete Element Method (DEM) modelling presents a sophisticated approach to simulating their mechanical responses. This chapter outlines the comprehensive methodology employed in the compressive testing and DEM modelling of IWP and SP based structures. It covers the preparation, execution, and analysis of compressive tests, the detailed process of DEM modelling including unit cell modelling, contact models, and simulation settings, and finally, model validation against laboratory test data. Further, it explores the results of these investigations, focusing on compressive strength, force distribution, cracking patterns, and the load-displacement curve alongside energy absorption characteristics of both IWP and SP structures. Each of these aspects provides insights into the material behaviour under load, contributing to a deeper understanding of the structural integrity and resilience of IWP and SP designs. The goal of this chapter is to offer a thorough examination of the compressive properties of IWP and SP structures, aiding in the enhancement of design strategies for improved performance in real-world applications. This chapter is mainly based on Paper 1 and Paper 6 as mentioned in list of publication.

5.2 COMPRESSIVE TESTS

5.2.1 IWP based structures

Three specimens are fabricated and subjected to assessment for both main (primary) and secondary (secondary) variants. Monotonic compression trials are executed utilising the apparatus, as previously delineated in in Figure 4.1. The specimens are incrementally loaded in a vertical manner until failure ensued. Concurrent measurements of reactive force and displacement are meticulously recorded. It is acknowledged that polymer behaviour varies with alterations in load velocity, material classification, and thermal conditions; however, these variables are standardised to ambient temperature for all experiments.

As demonstrated in Figure 5.1, the force versus displacement characteristics of two categories of Skeletal-IWP units have been examined. A triplet of trials for each category is performed. Within the illustration, 'S' denotes the secondary (secondary) variants, and 'M' represents the main (primary) variants. In the figure, “S” and “M” indicated the secondary type and main type, respectively; “T1”, “T2”, “T3”, and “TA” represent the three tests and their average. 'T1', 'T2', 'T3', and 'TA' symbolise the individual experiments and their mean result, respectively. Observations indicate that the Skeletal-IWP unit's design has a significant impact on its compression response. Notably, the secondary IWP design exhibits an enhanced capacity for withstanding compressive forces when compared to the main IWP design. Moreover, the displacement at the maximum force observed for the secondary type is lower relative to the corresponding main design. This discrepancy is likely ascribable to the distinct geometric configurations inherent to the different skeletal IWP designs.

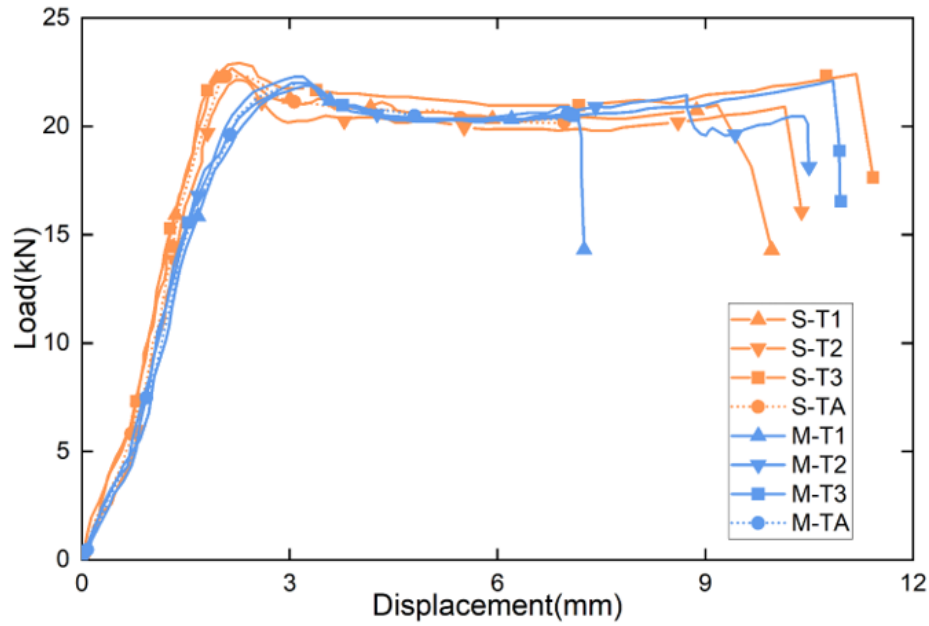


Figure 5.1 Experimental load-displacement curves of the two IWP based designs.

The quantification of energy absorption potential is achieved by integrating the load versus displacement graph. The main and secondary skeletal IWP exhibit energy absorption at 80.6 Joules and 84.1 Joules for a 5mm deformation, respectively. At their respective peak loads, the main type registers a deformation of 3.1mm with an energy uptake of 41.7 Joules, whereas the secondary IWP unit reaches a 22.4 Joule absorption at 2.1 mm deformation. Notably, at 3.1mm deformation, the secondary IWP unit is capable of absorbing 44.3 Joules. It is noteworthy that both the two IWP designs demonstrate akin levels of total energy absorption. However, the main design displays a predilection for higher energy absorption in the elastic region, whilst the secondary IWP variant evidences greater energy absorption during the plastic deformation phase.

Subsequent to the compression examinations, the specimens fractured into multiple segments. Illustrated in Figure 5.2, fracture zones on the 3D-printed specimens are demarcated with crimson ellipses. The schematics, annotated with crimson lines, identify the fracture-susceptible regions of the main and secondary IWP designs. The main IWP units predominantly failed at the junctures,

whereas the secondary IWP units exhibited fractures predominantly in the longitudinal axis.

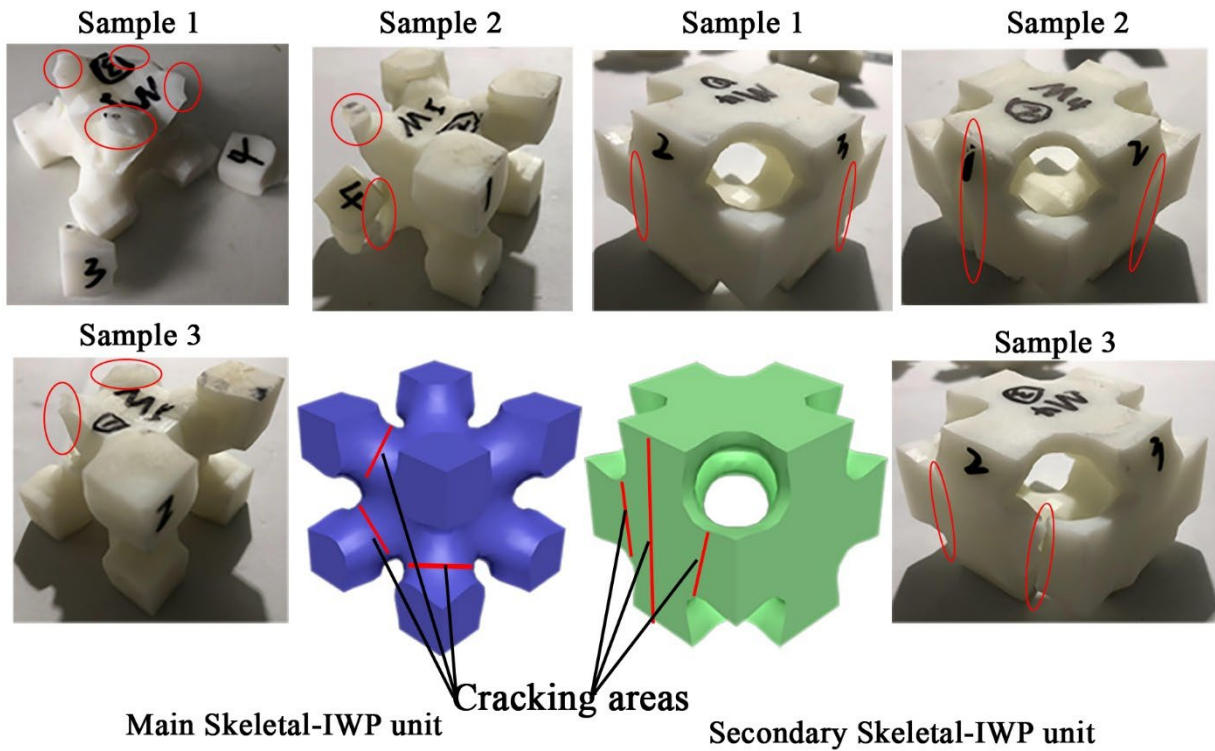


Figure 5.2 Fractured IWP specimens, annotated with crimson lines, identify the crack-susceptible regions from tests.

5.2.2 SP based structures

Figure 5.3 delineates the load-displacement curves for three axially loaded tests conducted on both main and secondary SP designs. As indicated by the legends, 'M' and 'S' designate main (primary) and secondary (complementary) types, respectively, while 'T1, T2, T3, TA' signify the curves of individual tests and their mean values. It can be observed that the main type unit cell manifests a significantly higher axial load-bearing capacity, approximately 30.5 kN, which is roughly 1.7 times greater than the 18.1 kN demonstrated by the Secondary type. Focusing on the curves prior to reaching the peak load-bearing capacity, one notices that during the initial displacement phase of 0-0.5 mm, the stiffness exhibited by Main and Secondary types is relatively indistinguishable. However, in the 1-2 mm displacement range, the Main type maintains higher stiffness levels, whilst

the stiffness of the Secondary type exhibits a minor decrement. This discrepancy is attributable to divergent stress transmission pathways in individual unit cells: stress is disseminated vertically through the centre of the main type, whereas it diffuses diagonally in the Secondary type. Despite for ϕ_{SP} indicating that in infinite space, $\phi_{SP}(x, y, z) \geq 0$ is equal to $\phi_{SP}(x + \pi, y + \pi, z + \pi) \leq 0$, and that the 1/8 sub-elements of both main and secondary SP designs are identical, the mechanical performance of the two structures differs significantly when the cell count is low. This variation necessitates studying the mechanical responses of both SP structural types under varying lattice quantities. In engineering applications, particularly in large-scale civil engineering structures, SP unit cells are often large, and the arrangement along specific axes may be limited in number, resulting in large discrepancy in inner load transferring path and boundary stress state. Thus, the impact of phase differences should not be overlooked.

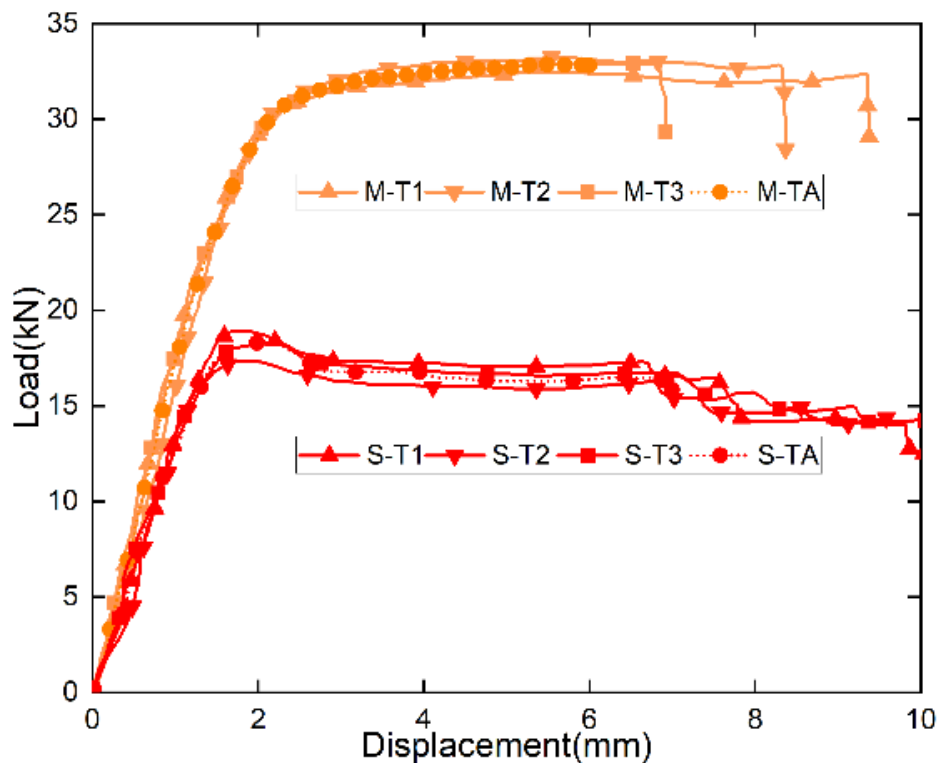


Figure 5.3 Experimental load-displacement curves of the two SP based designs.

The energy absorption characteristics for both main and secondary SP variants are computed by

integrating their respective average load-displacement curves, thus yielding the energy absorption profile for the conducted experiments. At the onset of large deformation for the main SP unit cell—located at its peak load-bearing capacity—the displacement measures 2.26 mm with an energy absorption of 40.2 J. In contrast, at the same displacement, the secondary SP unit cell registers an energy absorption of 27.9 J. At the maximum load-bearing point for the secondary SP, characterised by a displacement of 1.96 mm, an energy absorption of 22.5 J is observed, whereas, at this specific displacement, the main SP unit cell demonstrates an energy absorption of 31.3 J. At a displacement of 0.5 mm, the energy absorbed by the main SP and secondary SP unit cells is 2.1 J and 1.8 J, respectively. It is thus evident that across the entire range of displacements, the main type unit cell manifests superior energy absorption capabilities compared to its secondary counterpart.

As illustrated in Figure 5.4, following axial compression, both main SP and secondary SP exhibit pronounced cracking. The failure in the SP predominantly extends downward from the elliptical area on the top surface, with the four protruding sections on the horizontal plane being extruded and subsequently splitting vertically. In contrast, the failure of the secondary SP manifests as the outward extrusion and rupture of the four pillars of the unit cell; the cracking pattern radiates outward from the centre of the sample. The compression testing resulted in the specimens fragmenting into multiple segments.

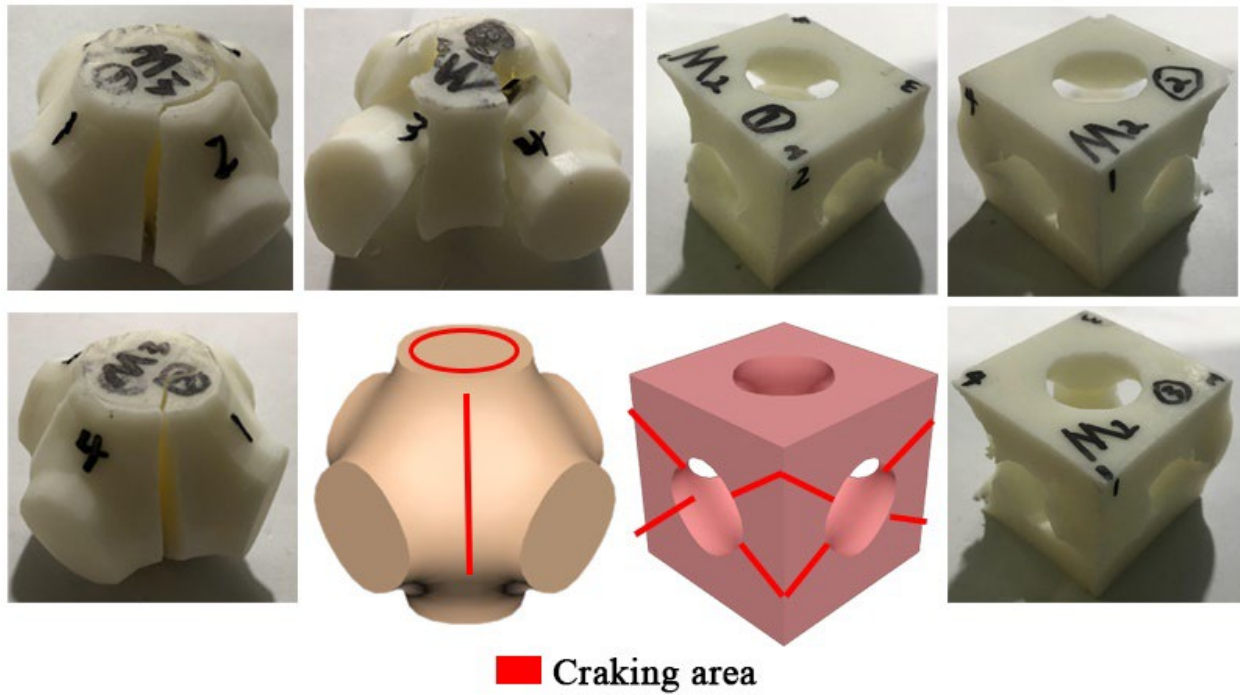


Figure 5.4. Post-compressive test fractured specimens, with Main SP depicted on the left and Secondary SP on the right. Red demarcation lines at the lower section of the image indicate the zones of failure.

5.3 DEM MODELLING OF IWP AND SP BASED STRUCTURES

This section elaborates on the DEM numerical calculations conducted for the IWP and SP models of various cell arrangement. DEM models can reflect the inner contact forces of TPMS structures and show the crack patterns of models after failure. For the representation of the TPMS structures, a constructible assemblage of Ball elements has been utilised. The contact interactions within the elements are characterised using a Linear Contact Model (LCM) in conjunction with a Parallel Bond Model (PBM). To emulate the effect of axial loading, a pair of unyielding Wall elements, advancing at a predetermined velocity, are employed.

5.3.1 Modelling of IWP and SP unit cells

The initial phase involves crafting the cellular contour of the units. Both main and secondary skeletal

IWP variant delineated utilising AutoCAD software. Subsequent to these outlines, Wall elements have been designated to demarcate the periphery of each Skeletal-IWP configuration, resulting in a 3D construct composed of numerous triangular facets, as depicted in Figure 5.5(a).

Progressing to the subsequent phase, the interior of the simulated IWP cell models is populated with intersecting spherical elements, varying in diameter from 2 to 3 mm. Adhering to the granular material modelling methodology detailed in [67, 151], the spherical and wall elements are ascribed appropriate attributes and iteratively adjusted until a balanced force ratio amongst all spherical elements approaches 0.0001. This ensures a homogenous distribution of Spherical elements, thereby accurately representing the contoured surfaces of the Skeletal-IWP cells, illustrated in Figure 5.5(b). For the modelling process, 723 spherical elements are employed for the main cell model, whilst the secondary cell utilised 617 elements.

It is recognised that both Clump and Cluster modelling techniques can be utilised to employed to emulate structures with intricate and non-uniform geometries. The Clump or Cluster approach can share an identical contour, which means that the geometric shape of Clump or Cluster of a model can be totally same. The Clump constitutes a non-deformable model with internal contacts exempt from computational analysis, ensuring spherical elements within maintain a constant spatial relationship. Conversely, the assembly Cluster is capable of fragmentation as the spherical elements are interconnected through adhesive contacts, as per references [152-154]. The Clumps preferred when internal failure mechanisms are not the focus, thus expediting simulation processes. In our investigation, the Cluster approach has been selected to examine fracture patterns within IWP and SP based structures.

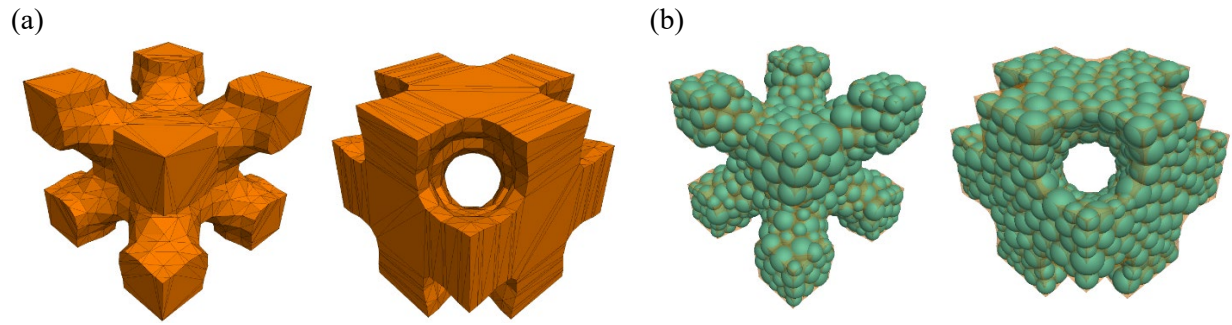


Figure 5.5 Modelling of the two IWP designs in DEM (a) Wall elements for cellular contour (b) breakable Clusters models.

The simplified SP surface segregates the spatial region into two volumetrically equivalent and mutually complementary solid domains as illustrated in Figure 5.6. The domain with $\phi_{SP} \geq 0$ is denominated as the "Main SP," whereas the one with $\phi_{SP} \leq 0$ is labelled as the "Secondary SP." . The process of generating these solid models involves the use of Geomagic Studio and AutoCAD software packages.

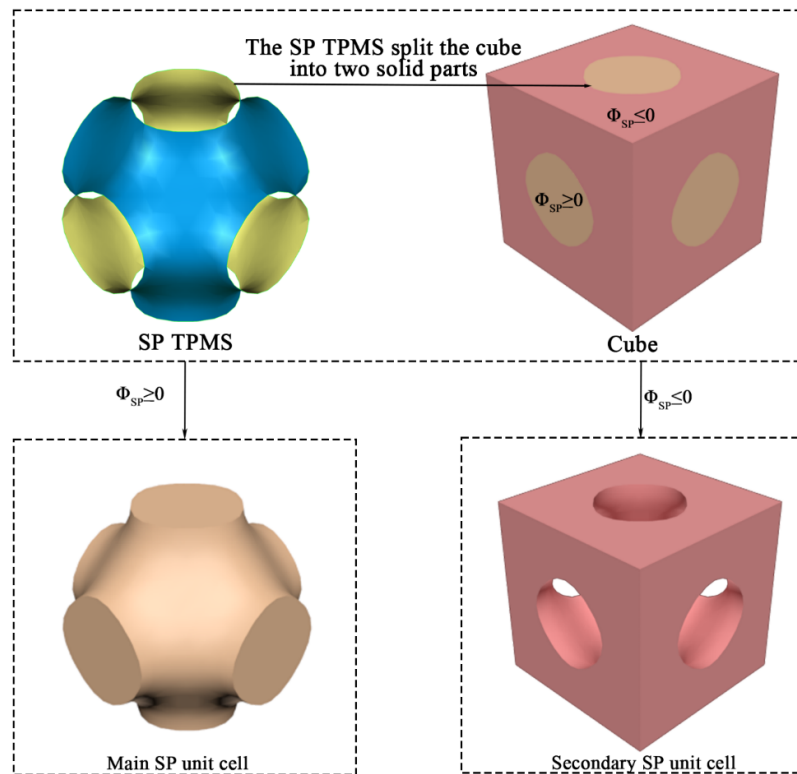


Figure 5.6 The Volumetric Domains of the main and secondary SP unit cells.

Similar as the approach to creating IWP based models, the Main and Secondary SP unit cells depicted in Figure 5.6 are exported as .STL files using the AutoCAD software. Following this, the Wall import command has been employed to introduce the unit cell's STL file into the PFC software, crafting a hollow outline that replicates the SP entity's external silhouette using Wall elements. This external outline consists of a single Wall component with multiple facets elements, as demonstrated in the figure. Subsequently, the Ball distribute command is utilised to populate the Wall component with Ball elements, at which point overlaps between Ball elements existed. Suitable parameters are then designated for both Ball and Wall, alongside the adoption of the linear contact model (LCM). The timestep is maximised to expedite the computational speed, proceeding to solve and allowing for a uniform dispersion of ball elements within the unit cell's outline. The simulation is halted when the ratio-average (average unbalanced force ratio of all Ball elements) reached 0.0001, and the timestep has been set to auto. The radii of the ball elements ranged from 1.5 mm to 3 mm, adhering to a Gaussian distribution. By eliminating the external Wall component, the Ball aggregates embodying the shapes of Main and Secondary SP are obtained, as shown in Figure 5.7. The Main and Secondary SP unit cells comprised 1536 and 1521 Ball elements respectively. Interactions between Ball elements have been bound using the Bonded contact, and with appropriate contact parameters, bond breakage could be achieved. This simulation approach is also referred to as 'Cluster'. Each unit cell is constituted of breakable internal Ball elements, as opposed to the unbreakable internal Clump model. Although Clump shares the same geometric shape and fundamental ball element count as Cluster and can speed up the simulation process, it overlooks the intrinsic damage within the unit cell [152, 153].

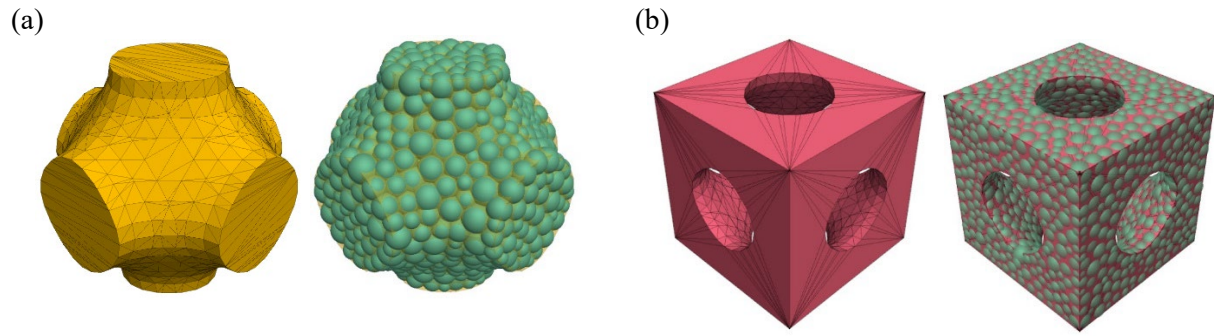


Figure 5.7 DEM representations of (a) Main SP unit cell and (b) Secondary SP unit cell. To the left, the Wall component comprising numerous facets elements; to the right, the cluster embodying the SP unit cell configuration.

5.3.2 Contact models

In computational endeavours via discrete element software, forces and torques (moments) are principally transmitted through contacts. Each contact is characterised by a contact model, which prescribes a particle-interaction law, dictating the manner in which internal forces and moments are updated [155]. Every contact has both a specified activity distance and a particular activity state. An active contact necessitates the execution of the particle-interaction law at that specific cycle point. If inactive, both the internal force and moment default to nil, bypassing the computations associated with the particle-interaction law.

In the sophisticated landscape of Discrete Element Method simulations, various contact models are tailored to depict the intricate interactions between particles with remarkable precision. The Null Model, serving as a rudimentary placeholder, lacks the capacity to simulate physical interactions, highlighting its utility in purely theoretical or preliminary analyses. The Linear Model stands as the cornerstone for simulating basic elastic interactions, prized for its simplicity but limited by its inability to capture complex material behaviours. Advancing in complexity, the Linear Contact Bond Model introduces an element of cohesion, allowing for the simulation of adhesive forces

between particles, yet it may oversimplify the nuanced nature of material bonding. The Linear Parallel Bond Model expands upon this by simulating bonds over a finite contact area, offering a more nuanced representation of particle adhesion and fracture, though at the expense of increased computational demand. The Soft-Bond Model caters to materials exhibiting softer bonding characteristics, providing a balance between realism and computational efficiency, yet it may struggle with highly rigid materials. The Rolling Resistance Linear Model introduces resistance to particle rotation, enhancing the realism of simulations involving granular materials, though it complicates the model with additional parameters. The Adhesive Rolling Resistance Linear Model further complicates this by incorporating adhesion in rolling resistance, offering detailed insights at the cost of increased model complexity. The Flat-Joint Model excels in simulating materials with distinct joint planes, offering precision in scenarios where traditional models falter, albeit with a focus that may not generalize well to materials lacking flat joints. The Smooth-Joint Model is adept at simulating smooth interfaces within particulate assemblies, bridging the gap between idealized and realistic contact behaviours, though it may not fully capture the complexity of rougher interfaces. The Hertz Model, rooted in classical contact mechanics, excels in simulating elastic contacts with a high degree of accuracy, yet its application is constrained by the assumptions of elastic behaviour. Lastly, the Hysteretic Model, with its capacity to simulate energy dissipation through hysteresis during unloading cycles, provides a sophisticated tool for capturing non-linear material responses, though at the cost of increased mathematical and computational complexity. Each model, with its distinct advantages and limitations, plays a pivotal role in the nuanced simulation of particulate matter, guiding researchers towards insights that bridge theoretical models with practical applications in engineering and science.

In the context of an innovative study on the structural behaviour of 3D-printed resin materials, the Linear Parallel Bond Model is judiciously selected to simulate the intricate adhesive interactions within the resin structure. This choice is particularly advantageous for its ability to accurately replicate the complex bonding phenomena inherent to the 3D printing process, thereby offering a realistic representation of the material's mechanical integrity and failure mechanisms. The model's proficiency in simulating both the normal and shear forces across the bonds provides a comprehensive understanding of the material's response under various loading conditions, an essential aspect for predicting the performance of 3D-printed structures. Concurrently, the Linear Model has been employed to simulate the contact between the compression and support plates with the specimen during compressive strength tests. This model is aptly chosen for its simplicity and efficiency, effectively capturing the essential aspects of the contact interaction without overcomplicating the simulation. The Linear Model's straightforward approach to modelling elastic contacts is particularly beneficial in this scenario, as it offers sufficient accuracy for understanding the distribution of stress at the contact interfaces, which is crucial for interpreting the specimen's behaviour under compression. The synergy between these models encapsulates the multifaceted nature of material behaviour, from the microscale interactions within the material to the macroscale responses observed in experimental testing, thus providing a robust framework for advancing the field of material science and engineering. The contact mechanisms of linear contact model and linear parallel bond model are illustrated in Figure 5.8 and Figure 5.9.

Dashpot force (\mathbf{F}^d), viscous.

Linear force (\mathbf{F}^l), linear elastic
(no tension) and frictional.

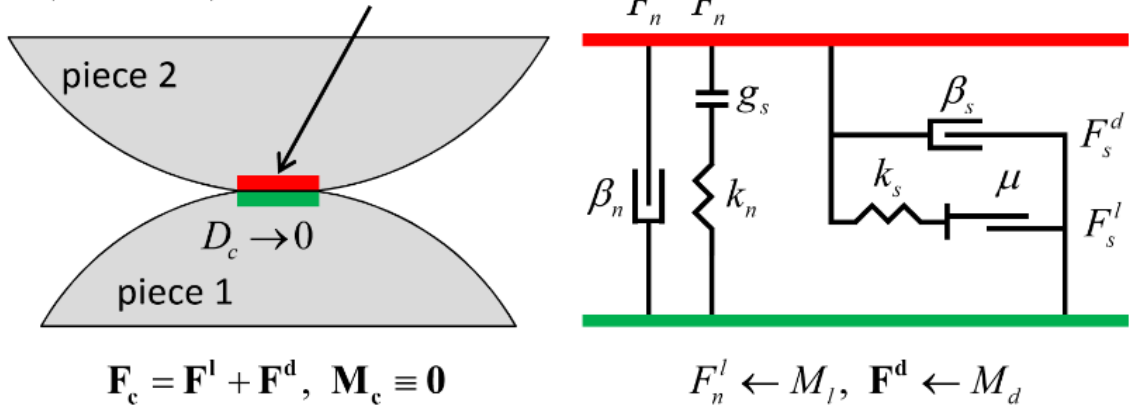


Figure 5.8 Illustration of contact mechanisms Linear contact model for Wall-Ball contacts.

Dashpot force (\mathbf{F}^d), not shown.

Linear force (\mathbf{F}^l), linear elastic
(no tension) and frictional.

Bond load ($\bar{\mathbf{F}}$ and $\bar{\mathbf{M}}$),
linear elastic & bonded.

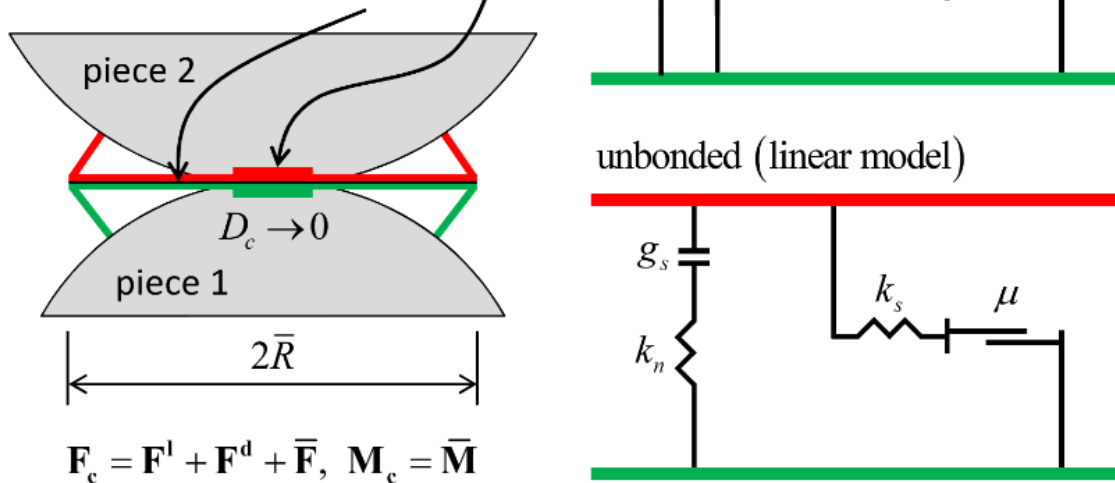


Figure 5.9 Illustration of contact mechanisms Linear parallel model for Ball-Ball contacts.

In the framework of Particle Flow Code (PFC) documentation, the Linear Model is elaborated as facilitating the simulation of an infinitesimally thin interface, which inherently lacks the capacity to counteract relative rotational movements, thereby rendering the contact moment null ($\mathbf{M}_c \equiv \mathbf{0}$). This model intricately decomposes the contact force into its constituent linear and dashpot elements ($\mathbf{F}_c = \mathbf{F}^l + \mathbf{F}^d$), as indicated from Equation 5.1 to Equation 5.6, with the linear segment ensuring a linearly elastic (exhibiting no tension) and frictional comportment, whilst the dashpot segment introduces viscous characteristics. The generation of the linear force is attributed to linear springs, characterized by constant normal and shear stiffnesses, denoted as k_n and k_s respectively. Conversely, the dashpot force emanates from dashpots, whose viscosity is quantified by the normal and shear critical-damping ratios, β_n and β_s , operating in tandem with the linear springs.

A critical aspect of this model is the definition of a surface gap, g_s , established as the disparity between the contact gap g_c and the reference gap g_r , which facilitates the alignment of the notional and piece surfaces when the reference gap attains a zero value, as shown in Figure 5.10. Activation of the contact is contingent upon the surface gap not exceeding zero, with the force-displacement relationship being bypassed for contacts deemed inactive. Notably, the linear springs are designed to preclude tension, with slip accommodation being achieved through the application of a Coulomb limit to the shear force, governed by the friction coefficient, μ . The model delineates the normal and shear components of the linear force as F_n^l and \mathbf{F}_s^l , with F_n^l being updated based on either the absolute surface gap or its incremental variations, influenced by the chosen normal-force update mode, M_l . Conversely, \mathbf{F}_s^l undergoes incremental updates predicated on relative shear-displacement variations. The $m_{(a)}$ is the mass of contacted Ball element (a).

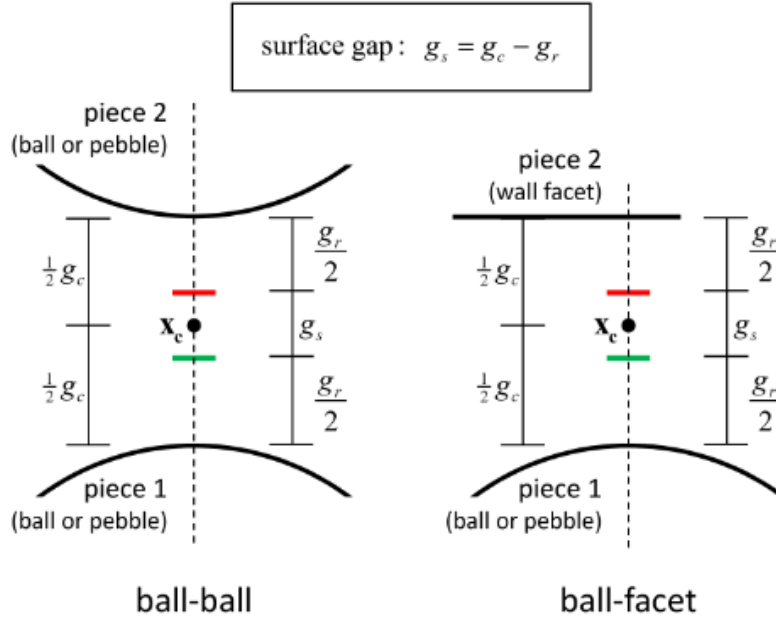


Figure 5.10 Illustration of surface gaps for the linear-based models in PFC 6.0.

$$F_n^l = k_n \delta_n \quad 5.1$$

$$F_{s*}^l = (F_s^l)_0 - k_s \Delta \delta_s \quad 5.2$$

$$F_s^l = \begin{cases} F_{s*}^l, & \text{if } F_{s*}^l \leq \mu F_n^l \\ \mu F_n^l, & \text{if } F_{s*}^l > \mu F_n^l \end{cases} \quad 5.3$$

$$F_s^d = (2\beta_s \sqrt{m_c k_s}) \dot{\delta}_s \quad 5.4$$

$$F_n^d = (2\beta_n \sqrt{m_c k_n}) \dot{\delta}_n \quad 5.5$$

$$m_c = \begin{cases} \frac{m_1 m_2}{m_1 + m_2} & (\text{ball} - \text{ball}) \\ m_1 & (\text{ball} - \text{facet}) \end{cases} \quad 5.6$$

The Linear Parallel Bond Model encapsulates the mechanics of a cement-like material interposed between two contacting entities. This model is akin to the process whereby epoxy cements glass beads, facilitating an elastic linkage that operates concurrently with the linear interaction component. The unique structure of the parallel bond, capable of transmitting both forces and moments between the contact points, is conceptualised as an array of elastic springs. These springs, possessing constant normal and shear stiffness, are evenly distributed across a geometrically pertinent cross-section—rectangular for two-dimensional scenarios and circular in three-dimensional contexts—

centred upon the point of contact. Upon the establishment of a parallel bond, any subsequent relative movement at the contact point engenders forces and moments within the bond material, exerting influence upon the contacting pieces. These forces and moments correlate with the maximal normal and shear stresses at the bond's periphery. Should these stresses surpass the bond strength, the parallel bond fractures, leading to the elimination of the bond material from the model, alongside its associated force, moment, and stiffness properties.

In essence, the linear parallel bond model delineates two distinct interfaces. The first interface mirrors the Linear Model, characterised by a linear elastic (exhibiting no tension) and frictional behaviour, solely conveying force and accommodating slip through a Coulombic shear force limitation. Conversely, the second interface, or parallel bond, when bonded, resists relative rotation and adheres to a linear elastic demeanour until such a point where the strength threshold is breached, resulting in bond failure. This bond's presence introduces a dimension of load-bearing capacity absent in its unbonded state, where it reverts to the characteristics akin to the Linear Model. Such a detailed portrayal of the linear parallel bond model underscores its sophistication in simulating the mechanical interactions within bonded particulate systems, offering invaluable insights into the behaviour of materials under various loading conditions, thereby enhancing the predictive modelling capabilities within the field of material science and engineering.

Upon the disruption and subsequent detachment of the parallel bond interface, it ceases to bear any load, rendering the entire Parallel Bond Model (PBM) functionally analogous to the Linear Contact Model (LCM). The force and moments update follows the Equation 5.7 to Equation 5.10. The force exerted at the Particle Contact Model (PCM) interface is a synthesis of forces from both the linear contact (F^l and F^d) and the parallel bond interfaces (F^d), with the contact moment (M_c) being

equivalent to that generated by the parallel bond (\bar{M}). The update mechanisms for the linear and dashpot forces (F^l and F^d) adhere to the protocols established in the linear model. Conversely, the dynamics of the force and moment within the parallel bond (\bar{F} and \bar{M}) follow the specifications detailed in Equation 5.7 to Equation 5.10. The force associated with the parallel bond (\bar{F}) is composed of the normal (\bar{F}_n) and shear forces (\bar{F}_s), whereas the moment (\bar{M}) encompasses both the twisting (\bar{M}_t) and bending moments (\bar{M}_b). These equations incorporate the increments in relative displacement in both shear ($\Delta\delta_s$) and normal ($\Delta\delta_n$) directions, alongside the increments in relative twist-rotation ($\Delta\theta_t$) and bend-rotation ($\Delta\theta_b$), with the shear (\bar{k}_s) and normal stiffness (\bar{k}_n) of the parallel bond contact, the cross-sectional area of the contact plane (\bar{A}), and the polar moment of inertia of the parallel bond cross-section (\bar{J}) also being integral to the calculations. This detailed framework ensures a comprehensive approach to modelling the interactions within bonded particulate assemblies, offering nuanced insights into their mechanical response under varied conditions, thereby enriching the analytical depth within engineering and material science research.

$$\bar{F}_{s*} = \bar{F}_s - \bar{k}_s \bar{A} \Delta\delta_s \quad 5.7$$

$$\bar{F}_{n*} = \bar{F}_n + \bar{k}_n \bar{A} \Delta\delta_n \quad 5.8$$

$$\bar{M}_{t*} = \bar{M}_t - \bar{k}_s \bar{J} \Delta\theta_t \quad 5.9$$

$$\bar{M}_{b*} = \bar{M}_b - \bar{k}_n \bar{J} \Delta\theta_b \quad 5.10$$

To accurately replicate the behaviour of 3D printed IWP and SP unit cells, the assignment of material parameters is meticulously based on the properties of photosensitive resin provided by WENXT Ltd., as delineated in Table 5.1. The inherent variability in the 3D printing process can introduce undetectable flaws within samples, leading to a non-uniform distribution of strength across different regions of a 3D printed specimen. A distinctive advantage of Discrete Element Method (DEM) simulations over Finite Element Method (FEM) simulations lies in the capability to

individually assign the strength values to each contact element, thereby accommodating the material strength variations naturally occurring in 3D printed objects. To mirror the actual conditions more closely, the tensile strengths for the contacts in the parallel bond model (PBM) are assigned using a Gaussian distribution, characterised by a mean (μ) of 47 MPa and a standard deviation (σ) of 3 MPa.

Table 5.1 Parameters for DEM IWP and IWP unit cell models.

Parameters	Ball elements	Wall elements	LCM	PBM
Density(kg/m ³)	1160	-	Auto-updated	Auto-updated
Friction	0.3	0.3	0.3	0.3
Young's modulus (N/m ²)	2.6e9	1e11	2.6e9	2.6e9
Poisson's ratio	0.42	0.42	0.42	0.42
Reference gap, g_r (m)	0	0	0	0
Tensile strength, (N/m ²)	-	-	-	38~56e6
Shear strength, (N/m ²)	-	-	-	17~23e6
update mode	-	-	absolute	incremental

To facilitate this functionality, a bespoke function has been developed, enabling the iteration over all linear parallel bond (LPB) contact elements within the model for the purpose of strength assignment. This tailored approach permits the application of distinct tensile strength values to each contact element, effectively capturing the heterogeneity inherent in the material properties of 3D printed objects. This approach draws inspiration from established methodologies, utilising the three-sigma (3σ) rule to ascertain the expected value and standard deviation, thereby ensuring a 99.7% likelihood that the tensile strengths of all contact elements fall within the specified range of the material's strength. The stiffness values for the contacts are computed algorithmically, taking into account the material's modulus and Poisson's ratio. The update mechanism for linear contacts is set to an absolute mode, whereas the Parallel Bond Model employs an incremental update strategy. This is designed to alleviate initial stresses within the Ball elements and PBM contacts, thereby enhancing the simulation's fidelity to real-world material behaviour. It should be noted that the

contact models and assumptions do not consider the plastic behaviours of the 3D printed TPMS samples.

5.3.3 Loading procedures for IWP and SP of multi-units

In this segment, the development and analysis of compressive models for IWP and SP based structures, comprising numerous unit cells, are delineated separately. These IWP configurations are constructed utilising Ball elements, which are interconnected through Parallel Bond Model (PBM) contacts. The apparatus for load application and support consists of two rigid walls, representing the loading and supporting plates respectively. The procedural steps for conducting these simulations are outlined herein.

Table 5.2 The introduction of case abbreviation of IWP and SP designs with numerous units.

Case abbreviation	Type	i_x	i_y	i_z	Note: The case is abbreviated by number of units in three directions. The case M553 means the model is the main type and has 5, 5 and 3 units in x,y and z directions.
Mabc	Main type	a	b	c	
Sabc	Secondary type	a	b	c	
XaYbZc	-	a	b	c	
M553	Main type	5	5	3	
S771	Secondary type	7	7	1	
X5Y5Z1	-	5	5	1	

Initially, geometric profiles for the IWP based cells are generated to accommodate the Ball elements, which are created within the specified geometry with diameters ranging from 2 to 3 millimetres. The process of generating Ball elements continues until their cumulative volume reaches 120% of the geometric shape's volume. Due to the random placement of Ball elements, considerable overlap among spheres is observed. To attain a state of equilibrium, the model undergoes stabilisation using elevated damping forces until the average ratio of unbalanced forces amongst the Ball elements descends to 0.0001. Subsequently, the Ball assembly, encapsulated within the geometric confines of the Skeletal-IWP units for a singular unit cell, is exported as Bricks for subsequent replication and analysis of structures comprising multiple unit cells. Visual representations of the Bricks for

both primary and secondary Skeletal-IWP unit cells are provided in Figure 5.5.

Following this, the Brick, a densely compressed and cohesively adhered aggregate of sphere elements, is replicated and strategically arranged in the various axes (x, y, and z axes), based on a predefined number of copies (i_x , i_y and i_z), which denote the replication count along the respective axes. The assembly of these Bricks is interconnected through PBM contacts, culminating in the resolution of the system towards an equilibrium state for the entire multi-cellular structure. A multitude of scenarios involving various configurations of unit cells for both the primary and secondary Skeletal-IWP structures are simulated. For ease of reference and clarity in discussion, abbreviations are employed to denote distinct scenarios, as indicated in Table 5.2.

$$\bar{V}_{ball} = |\mathbf{V}_{wall}| \cdot (L_{ball}^z - L_{midplane}^z) \quad 5.11$$

Conclusively, two rigid Wall elements, serving the roles of a supporting plate at the base and a loading plate at the apex, are established to encompass the IWP structures featuring multiple unit cells. Figure 5.11 illustrate two distinct DEM models for the main and secondary IWP structures with $5 \times 5 \times 5$ unit cell configuration. These Wall elements are assigned velocities of 7.5 mm/min at the top and bottom in mutual direction to impose a deformation on the structures that mimics the strain rate observed in laboratory tests. Additionally, an vertical speed is imparted to each Ball element at the beginning, calculated to prevent abrupt shocks from the first movements of the loading and supporting plates. This calculation, detailed in Equation 5.11, utilises the velocity (V_*) of an element and its z-direction location (L_*^z) to apply a velocity gradient across the Ball elements. Accordingly, Ball elements proximal to loading and supporting plates exhibit velocities similar to the Walls themselves, whereas those positioned centrally within the structure approach a state of rest. Throughout the simulation, both the displacement of the Walls and the reactionary forces they

encounter are meticulously recorded. The displacement loading process persists until the reactionary force exerted by the top Wall diminishes to less than 40% of the observed peak reactionary force, ensuring a controlled and measured application of load to the structure.

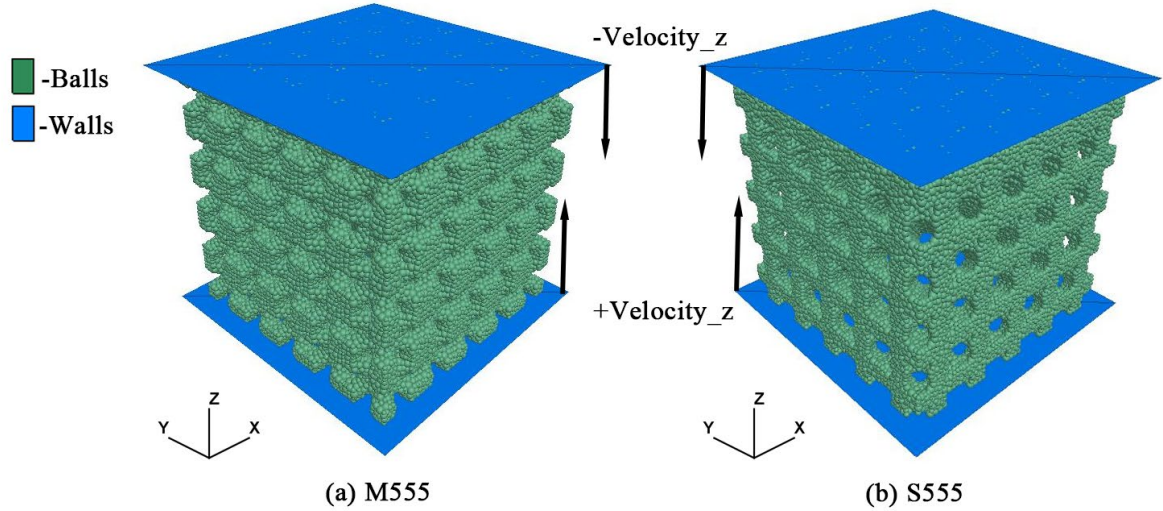


Figure 5.11 DEM analysis of IWP designed structures: (a) main type for case M555 and (b) secondary type for case S555.

The simulation of SP samples with numerous cellular units bears resemblance to the procedure adopted for IWP configurations. In an effort to evaluate the effect of unit cell quantity on the axial load-bearing capabilities of both main and secondary SP structures, it is essential to arrange the main and secondary SP unit cells along the three axes. Within the framework of the DEM software PFC, Wall elements are strategically positioned above and below the SP assembly to apply displacement loading. The configuration of the SP structure's unit cell arrangement is succinctly described using the notation “ABC”, where “ABC” denotes a periodic arrangement of unit cells along the x, y, and z axes, with quantities A, B, and C, respectively. The designation 'MABC' refers to the main SP structure with the “ABC” unit cell configuration, while 'SABC' represents the secondary SP structure with a similar configuration. Each MABC and SABC configuration signifies

a distinct simulation. Due to the axial symmetry of the main and secondary SP variants, configurations “ABC” and “BAC” are considered equivalent, leading to simulations being conducted only for configurations where $A \geq B$.

To execute the DEM simulation for the “ABC” unit cell arrangement, a series of precise steps must be followed. Initially, the cluster models of two types of SP based designs, as illustrated in Figure 5.7, are exported. It is critical to configure the DEM model's domain with periodic conditions, setting all contact models to 'Null'. The 'Brick Export Command' is utilised to export the cluster. A new simulation is then initiated, incorporating the unit cell clusters according to the “ABC” configuration via the 'Brick Import Command'. Interactions among Balls are defined using the LBM contact model, while interactions between the Wall elements, the loading and supporting plates, and Balls are facilitated using the LCM model. The next step involves the application of antiparallel movements at predetermined velocities to the Walls at both ends, with the velocity determined by the 'C' value in “ABC”, set to $3C$ mm/min, resulting in a velocity (Velocity_z) for each wall of 1.5mm/min in opposite directions, aligning with experimental loading rates. Additionally, the SP structure's spherical units are assigned an initial velocity to prevent instability during sudden loading.

Subsequently, model parameters are allocated to all Balls, Walls, and Contact elements, with the time step being automatically adjusted. A custom servo command is designed to apply a force of 0.1kN to the upper Wall, ensuring a secure fit between the loading plate and the SP structure within the DEM model. The simulation is halted upon reaching stability. The simulation proceeds until the force exerted on the uppermost plate decreases to less than 40% of the peak load, with both the contact force and the displacement of the upper plate being comprehensively documented. Figure 5.12 presents the simulations for M557 (Main SP structure with a “557” unit cell arrangement) and

S332 (secondary SP structure with a “332” unit cell arrangement), showcasing the meticulous approach adopted for these simulations.

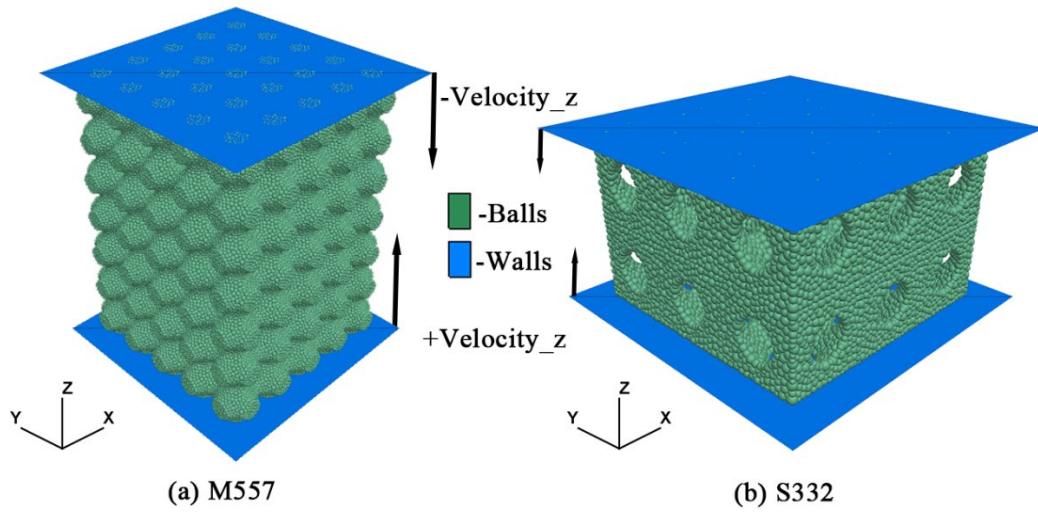


Figure 5.12 DEM analysis of IWP designed structures: (a) Main SP structure adopting a “557” unit cell alignment and (b) Secondary SP structure with a “332” unit cell pattern.

5.3.4 Model validation

The comparison between the outcomes derived from DEM analysis and experimental observations for two IWP designs (cases M111 and S111) subject to a consistent load serves as a basis for calibrating the model parameters. Demonstrated in Figure 5.13, the outcomes of the DEM simulations exhibit commendable concordance with the average experimental results prior to achieving maximum load. The deviations at the critical loading between DEM outcomes and experimental results amount to 1.2%, 2.1%, and 3.1% for the main IPW unit, and 0.4%, 1.4%, and 3.8% for secondary IWP unit, respectively. The correlation coefficients comparing the mean experimental load-deformation responses with its DEM computational counterpart stand at 0.97 for the main IWP unit and 0.98 for the secondary IW Punit, indicating a high degree of similarity when the load remains below peak levels. Nevertheless, post-peak load, the alignment between experimental and numerical results diminishes (with correlation coefficients of -0.15 for the main

IWP unit and 0.74 for the secondary IWP unit), a reflection of the divergent structural properties captured in numerical simulations compared to experimental assays.

The simulation and experimental analyses reveal that the energy absorption capabilities at the peak load for the main skeletal IWP unit at a displacement of 2.7 mm are 32.1 J and 28.3 J, respectively, and for the secondary type at a displacement of 2.4 mm, are 29.2 J and 25.3 J, respectively. It is important to note that DEM simulations presume an isotropic linear elastic behaviour for the contact elements, leading to a brittle failure mode upon the internal stress reaching ultimate strength. Conversely, the Skeletal-IWP specimens, fabricated from photosensitive resin for experimental purposes, exhibit a more plastic failure behaviour. This discrepancy is deemed acceptable, given the focus on assessing the peak load, load-displacement relations, and cracking patterns within the Skeletal-IWP structures. Figure 5.14 delineates the areas of cracking in both Skeletal-IWP units, illustrating that DEM simulations successfully mirror the fractures observed in the experiments, as previously shown in Figure 5.2. This underscores the reliability of numerical simulation in forecasting the damage zones within IWP structures under compressive loading, highlighting its effectiveness in capturing critical structural responses.

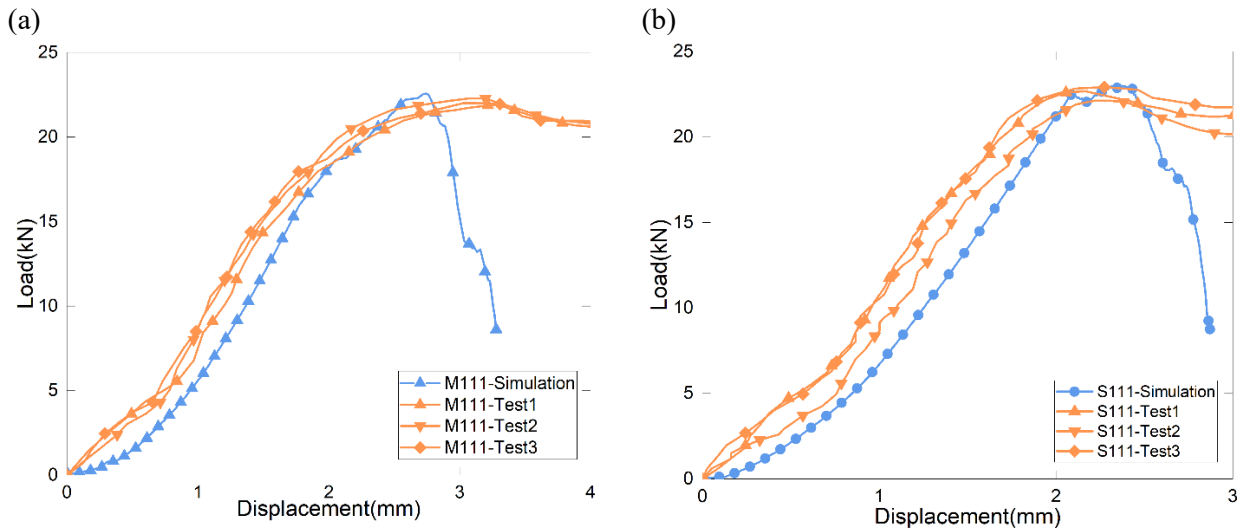


Figure 5.13 Comparison of outcomes from experiments and DEM calculations for IWP designs (a) main type and (b) secondary type.

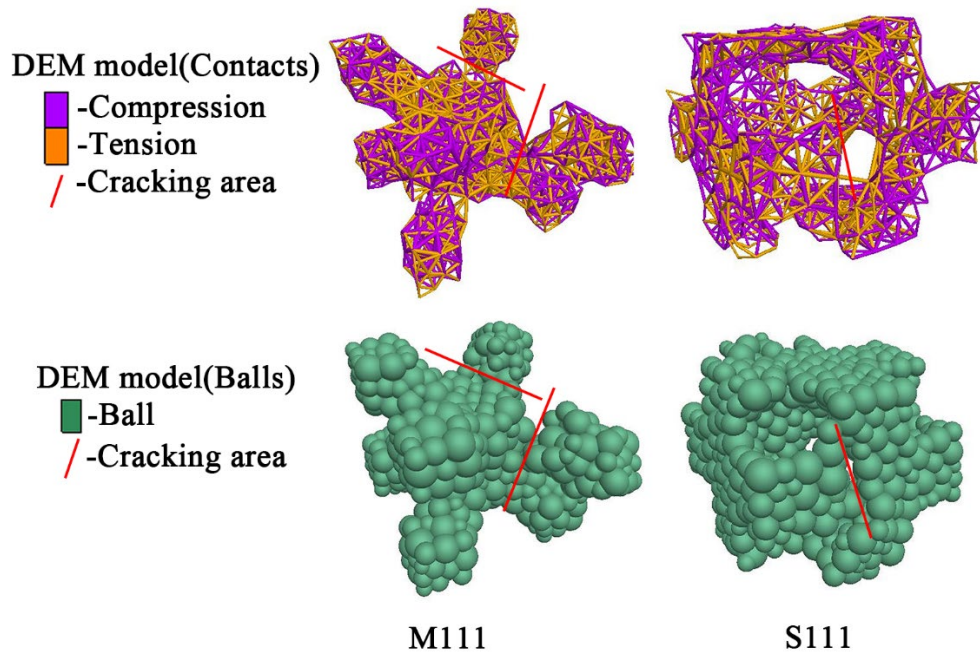


Figure 5.14 Post-compression visualisation of fragmented DEM representations for IWP units.

Figure 5.15 offers a detailed comparison of the load-displacement trajectories obtained from both experimental observations and DEM simulations under axial loading conditions, focusing on the main SP and secondary SP unit cells. The curves from both methodologies reveal parallel trends, with each structure reaching its maximum load-bearing capacity at approximately 2 mm of

displacement. In the DEM simulations, the main SP and secondary SP unit cells demonstrate peak strengths of 33.1kN and 18.9kN, respectively, with the variation from experimental measurements remaining under 5%. This minor deviation underscores the efficacy of the DEM simulation technique in accurately determining the apex axial load-bearing strengths of the SP structures. The simulated main SP and secondary SP unit cells achieve these peak strengths at displacements of 2.45mm and 1.84mm, respectively. Before the attainment of peak load, the correlation coefficients for the mean load-displacement curves from simulations and experiments for the main and secondary SP cellular units are notably high, at 0.97 and 0.98 respectively, highlighting the significant alignment between DEM simulations and experimental results up to the point of maximum load-bearing capacity. At a displacement of 2.45mm, the energy absorption recorded for the main SP unit cell in both experimental and simulated scenarios is 46.2J and 36.53kJ, respectively. Similarly, for the secondary SP unit cell at a displacement of 1.84mm, the energy absorption figures stand at 20.4J for the experiment and 17.3J for the simulation. Figure 5.16, utilising Ball and Contact visualisations, depicts the fracture outcomes post-simulation for both the main SP and secondary unit cells, with the fracture patterns closely mirroring those noted in experimental assessments. This concordance affirms the DEM's formidable capability to predict the compressive functions across various unit cell configurations and to identify the modes of failure accurately.

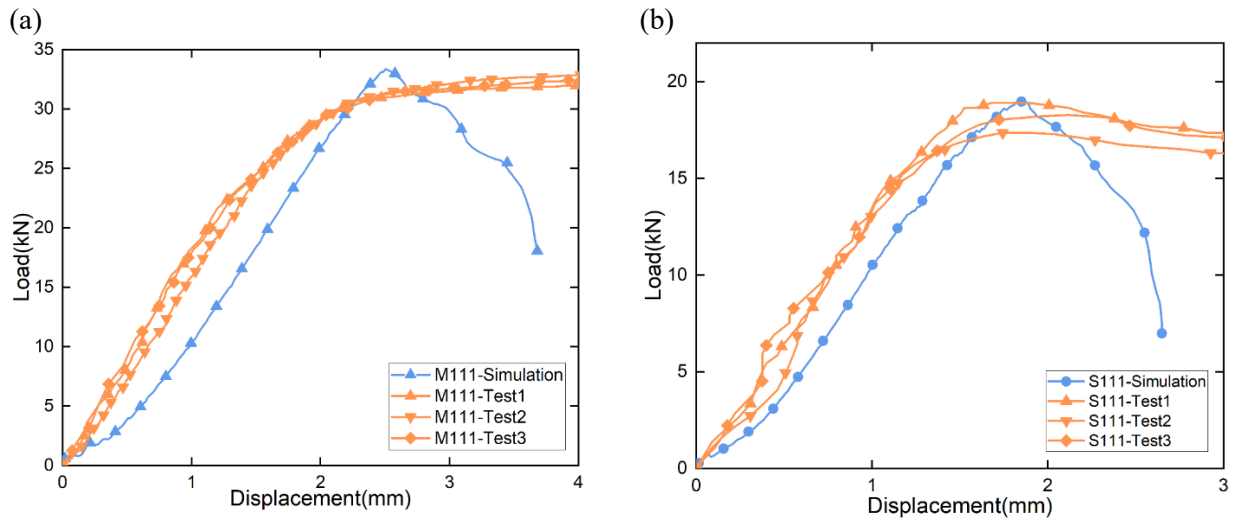


Figure 5.15 Comparison of outcomes from experiments and DEM calculations for SP designs (a) main type and (b) secondary type.

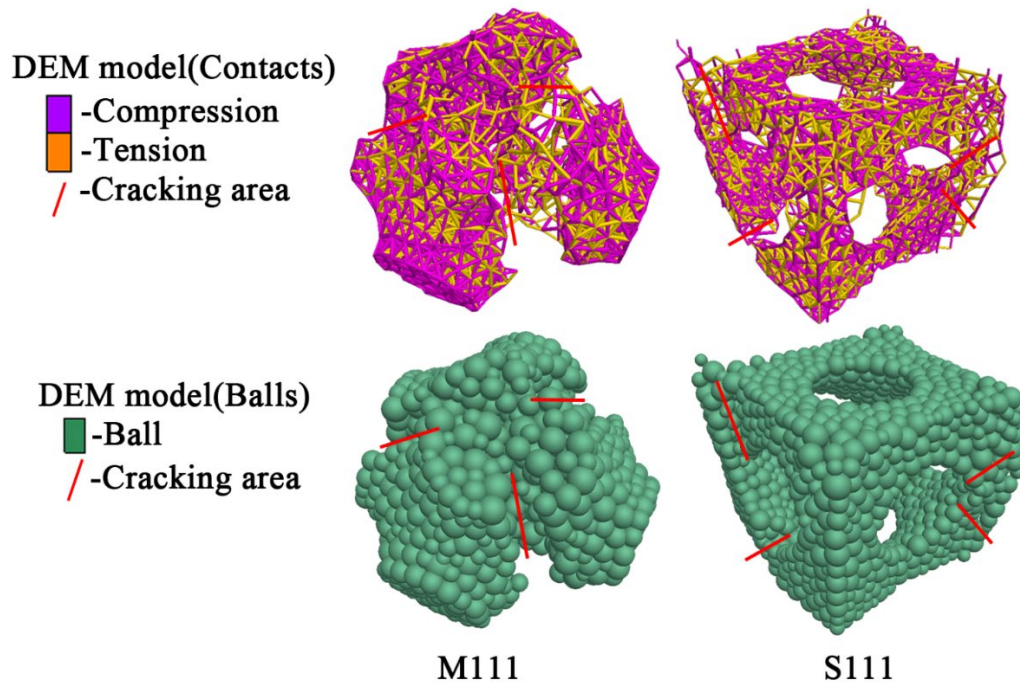


Figure 5.16 Post-compression visualisation of fragmented DEM representations for SP units.

5.4 COMPRESSIVE STRENGTH

5.4.1 IWP structures

To assess the compressive strengths of IWP structures with varied configurations of cells, the engineering strengths have been determined by dividing the maximum reactionary force recorded

from the top wall by the cross-sectional area of the simulated samples. The derived engineering strengths for both IWP configurations, encompassing assembled unit cells in the xy plane and a singular layer along the z-axis as acquired from DEM modelling, are depicted in Figure 5.17 (a) and (b). It is important to highlight that due to the reflectional symmetry of both IWP variant designs across the all the orientations, the configuration $X_aY_bZ_c$ mirrors $X_bY_aZ_c$ for IWP variant designs. The findings indicate an augmentation in the engineering strength for both IWP variant structures with an increase in unit amount along the x and y axes, albeit with a diminishing rate of strength enhancement with additional cells. For instance, an addition of three units along y-axle (from case M311 to M341) results in an increase of 1.7 MPa in the engineering strength for the main IWP structure, with a subsequent lesser increment of 0.7 MPa from case M341 to M371. A similar trend is observed for the secondary Skeletal-IWP structure, with an increase of 1.5 MPa from S311 to S341 and a subsequent smaller increase of 0.8 MPa from S341 to S371. Structures configured in a singular row exhibit lower strengths, with marginal improvements upon expanding the units in xy planes. When arranged in a $X3Y3Z1$ configuration, the compressive strengths of the primary and secondary Skeletal-IWP structures reach 134.4% and 148.8%, respectively, of the strength of a sole unit, approaching 90.3% and 95.1% of the strength in $X7Y7Z1$ model. The variance in compressive strengths for the secondary IWP designs is minimal (0.3kN) with an increase from three to five unit cells in xy plane (from $X3Y3Z1$ to $X5Y5Z1$), whereas the main design shows a difference of 0.8kN.

Figure 5.18 (a) and (b) include the compressive strengths of the two Skeletal-IWP variant models with varying unit counts in xy (unit counts equal in x and y axes) and z direction. An increase in unit cells along the z-axis marginally enhances the compressive bearing capacity of the two IWP variant designs. Nevertheless, this augmentation is less pronounced compared to expanding the

loading area (i.e., the number of unit cells along the x and y axes), signifying that heightening the two IWP variant structures (adding layers in the compressive direction) is less influential on bearing capacity. Beyond a particular value, when the number of z-direction layers surpasses the quantity in the x and y axes, the impact on compressive strength becomes negligible, with z-layer numbers exerting a more pronounced effect on the secondary structures' carrying capacity than on the primary ones.

From the analyses presented in Figure 5.17 and Figure 5.18, it is evident that the secondary IWP variants exhibit marginally superior bearing capacity (ranging from 2.2% to 9.5%) compared to the primary variants with identical unit cell configurations. Elevating the unit amounts to seven across the three Euclidean space orientations enables the IWP specimens to achieve compressive strengths of 180% (primary design) and 195% (secondary design) relative to the sole IWP unit's strength.

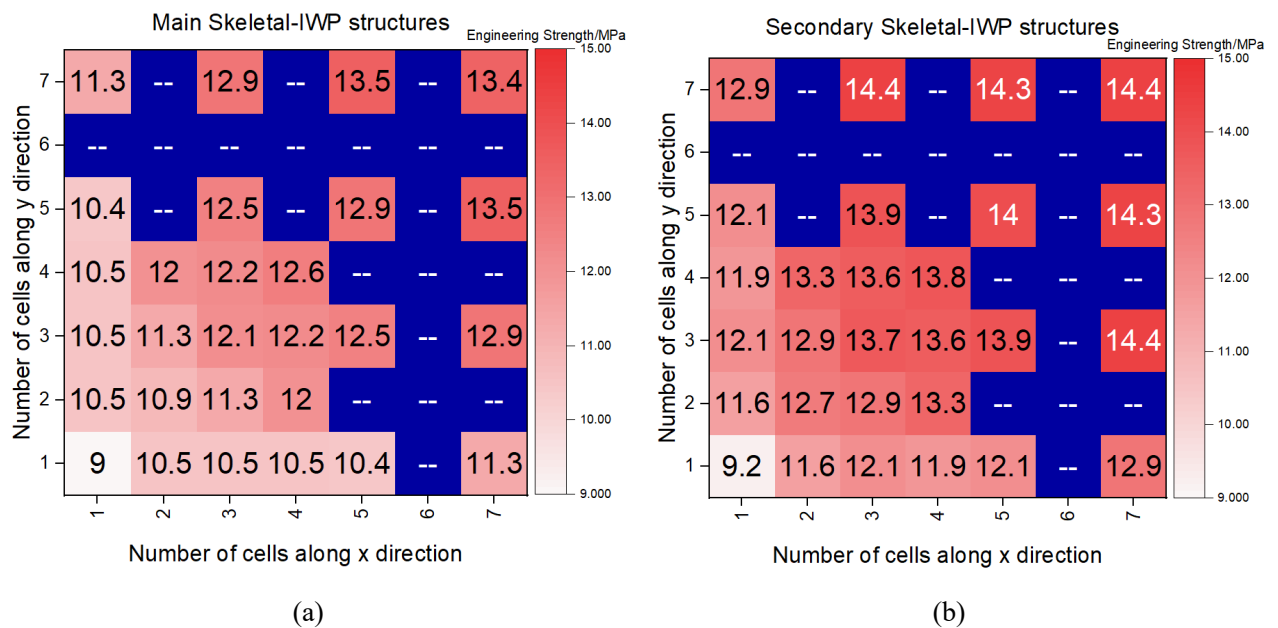


Figure 5.17 Engineering strength outcomes from sole layered DEM models of various unit cell configurations. (a) Main IWP variant designs and (b) Secondary IWP variant designs.

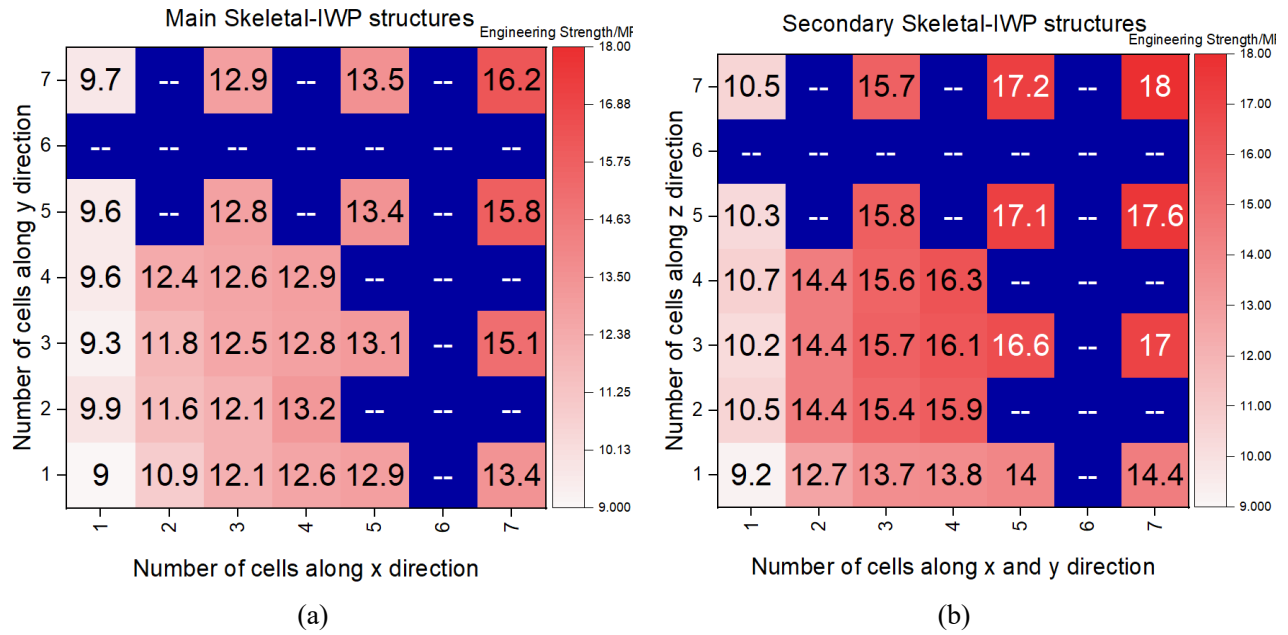


Figure 5.18 Engineering strength outcomes from multi-layered DEM models of various unit cell configurations. (a) Main IWP variant designs and (b) Secondary IWP variant designs.

5.4.2 SP structures

To explore the influence of unit cell arrangement on the axial load-bearing capacity of SP structures, a set of DEM simulations have been undertaken, with engineering compressive strength employed as the criterion for assessment. This strength is determined by dividing the maximum load observed from DEM simulations by the cross-sectional area of the structure's envelope. Figure 5.19(a) depicts the engineering compressive strength of main SP structures, varying the quantity of units along the x and y axes, maintaining a singular unit cell along the z-axis (represented as "MAB1", where A and B indicate different quantities). Meanwhile, Figure 5.19(b) examines the influence of increasing unit cells along the z-axis on the compressive strength of main SP structures, where the x and y axes hold equal and varied numbers of unit cells (denoted as "MABC", with A and B equal and C varying).

For main SP structures, augmenting the amount of units in the x and y directions appears to have a

negligible influence on the compressive capacity, with the strength in 'MAB1' configurations averaging around 13 MPa and displaying minimal variance of up to 0.3 MPa. Intriguingly, the strength of a single unit cell is on par with that of a main SP structure configured as '771'. Apart from singular unit cell scenarios, an upward trend in compressive capacity is observed with an increase in unit cells along the x and y axes. In contrast, as shown in Figure 5.19(b), a marked decline in strength is noted as the number of z-axis unit cells rises to four, five, and six, primarily due to model instability before fracture under loading, as illustrated in Figure 5.20. Excluding these instances, variations in the number of z-axis unit cells exhibit a limited impact on the compressive strength of main SP structures, ranging from 12.8 MPa to 13.27 MPa.

Similarly, Figure 5.21(a) showcases the engineering strengths of secondary SP designs of variations in the unit amounts across the x and y axes within a single-layer setup, under compression. Figure 5.21(b) delves into how z-axis unit cells affect the compressive strength of secondary SP structures amidst varying x and y unit cell counts. The findings suggest an increase in the compressive strength of secondary SP structures with an uptick in unit cells along all three axes, with each axis contributing significantly to the overall strength. Excluding the '11C' scenarios for main SP structures, which displayed stability issues, secondary SP structures exhibit enhanced stability. The 'S777' configuration, for instance, shows a compressive strength of 10.32 MPa, a 36.9% increase (2.78 MPa) from the 'S111' case, which recorded 7.54 MPa. However, as the number of unit cells escalates, a deceleration in strength gain is observed, suggesting a limit to this effect. Despite the more substantial increments in compressive strength witnessed in secondary SP structures due to additional unit cells in the x and y directions, their strength, peaking at 10.32 MPa, still falls short of the main SP structures' average (13 MPa), equating to approximately 79.4% of the main SP's

capacity.

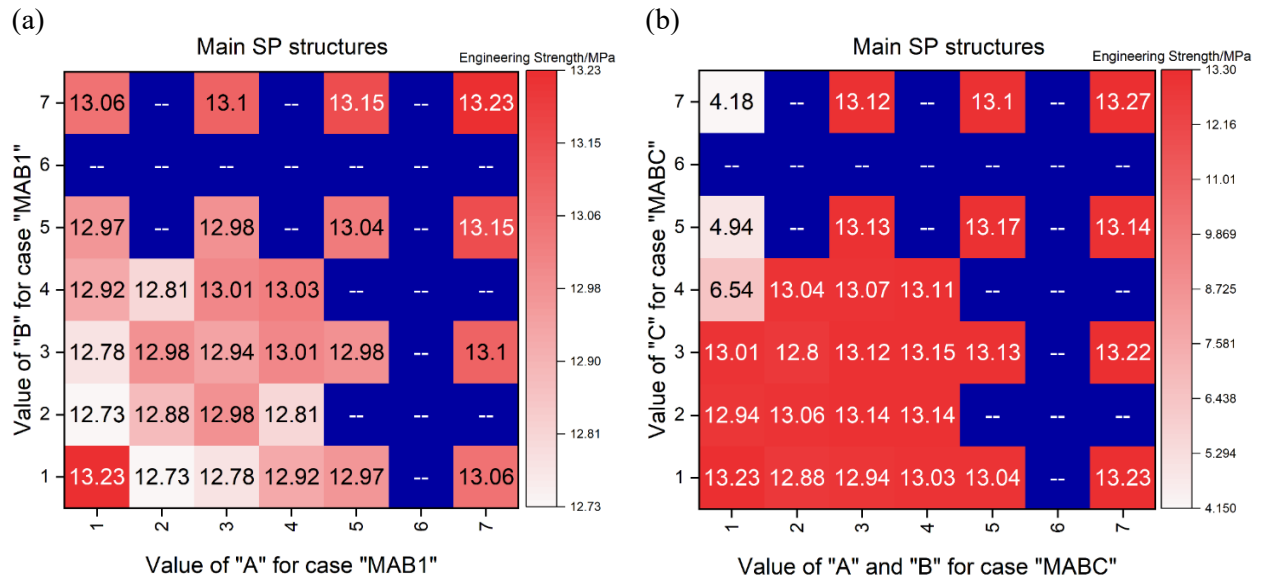


Figure 5.19. Engineering strength outcomes from Main SP DEM models of various unit cell configurations. (a) sole-layer in z direction and (b) multi-layer in z direction.

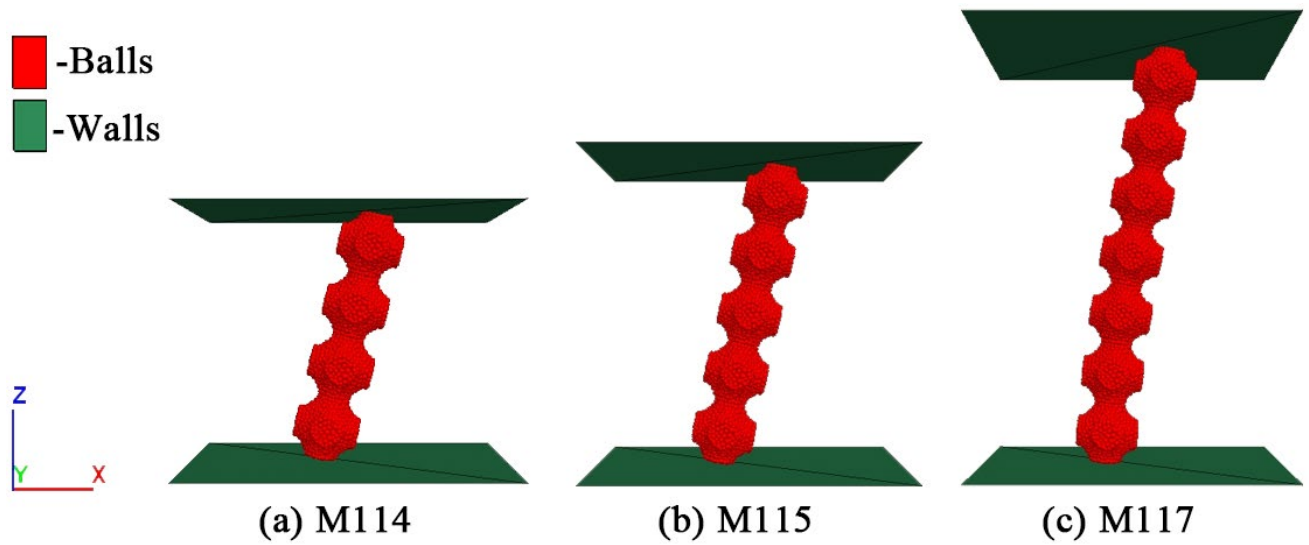


Figure 5.20. Axial load advancement in DEM models M114, M115, and M116, underscoring the instability preceding fracture initiation.

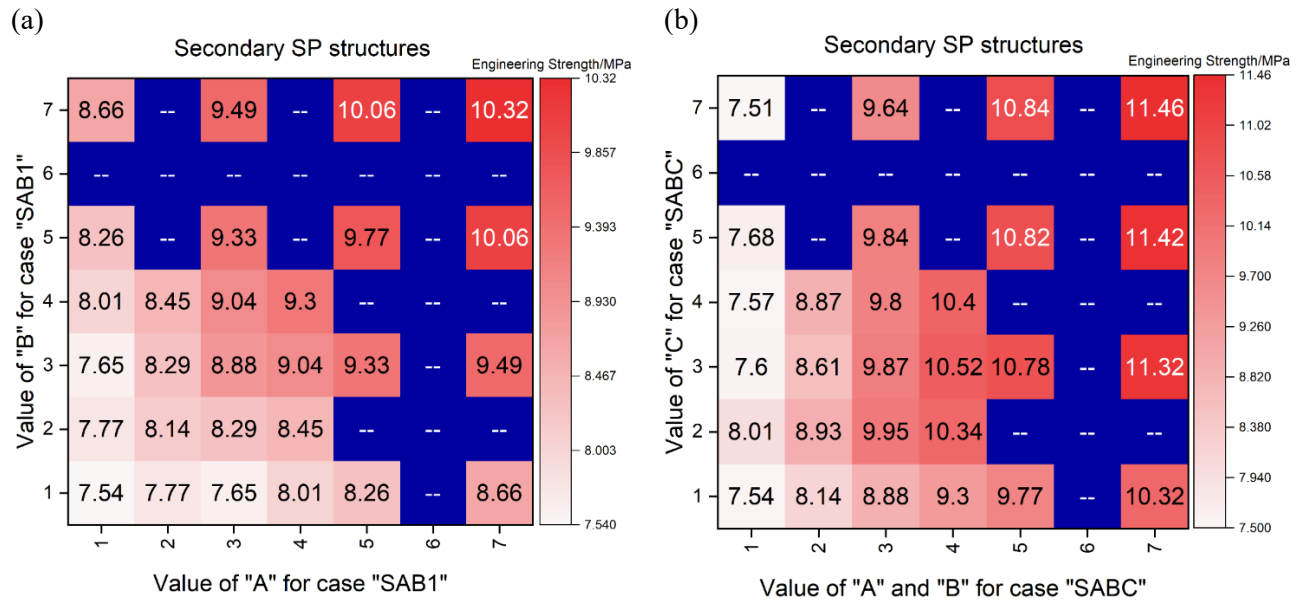


Figure 5.21. Engineering strength outcomes from Secondary SP DEM models of various unit cell configurations. (a) sole-layer in z direction and (b) multi-layer in z direction.

5.5 FORCE DISTRIBUTION

5.5.1 IWP structures

Figure 5.22 delineates the contact force chains within main IWP variants, showcasing variations across distinct cellular configurations at an engineering strain of 3%. These force chains, particularly those at the core of each structure, are magnified and depicted as cylinders to facilitate an in-depth examination of force distribution patterns. While the central illustration maintains a consistent cylinder size for comparative purposes, the force chains depicted on the right are proportionally scaled according to the magnitude of contact forces, offering insights into the density and dimensions of these forces and their distribution within cellular unit. It emerges that main IWP variants, regardless of their unit cell arrangement, exhibit analogous patterns of force distribution, with compressive forces directed along the loading path and tensile forces distributed across planes orthogonal to the compression direction. An analysis of the force chains in cases M111, M151, and M551 reveals that an expansion in unit cells following the x and y directions results in more focused

tension and compression contact forces. Particularly for case M555, the areas of the two force types are most distinctly demarcated, with compression forces predominantly located on the external zone of the eight corner area as well as the internal side of the body centre, whereas tension forces primarily occupy the internal zone of the corner area and the external side of the body centre.

Table 5.3 presents detailed data about contact elements within main IWP designs, indicating a probable increase in compression contacts per unit cell with a rise in unit cell numbers. Conversely, the average count of tension contacts exhibits minimal variation with an increase in unit cells along the x and y axes and is likely to decrease with additional layers along the z-axis. This data elucidates the observed tendency of escalating engineering strengths across main IWP designs with diverse cellular configurations.

Figure 5.23 displays the contact force chains for secondary IWP designs at 3% engineering strain under various scenarios. An analysis of cases S111 versus S115 and S551 versus S555 suggests that the presence of additional z-layers marginally influences the distribution of tension and compression. The contrast in contact forces between cases S111, S551 and cases S115, S555 illustrates that augmenting unit cell counts in the xy axes tends to shift tension zones towards the structure's vertical edges. The scaled force chains for secondary Skeletal-IWP structures reveal predominant force transmission along the structure's vertical axes, with horizontally oriented bones acting as connectors despite bearing lesser force magnitude. Table 5.3 also details the contact characteristics of secondary IWP designs across various configurations, showing that an increase in unit amounts across all three axes boosts the two types of contacts counts on each cellular unit. Furthermore, elevating the unit cell count in three directions enhances the average compression force magnitude. When compared with primary structures under identical scenarios, secondary IWP designs

consistently exhibit higher mean compression forces, elucidating the slightly superior compressive strengths of secondary structures compared to their primary counterparts for equivalent unit cell arrangements.

Table 5.3 Contact characteristics for main and secondary IWP designs for various cases.

Case	Average compressi on force /N	Average tension force /N	Total compression contact amout	Total tension contact amount	Contact amount /each unit cell	Compressive contact amount /each unit cell	Tension contact amount /each unit cell
M111	57	-27	2473	1925	4398	2473	1925
M311	59	-27	7672	5908	4527	2557	1969
M511	59	-26	12862	9900	4552	2572	1980
M131	58	-27	7773	5799	4524	2591	1933
M331	59	-28	24402	17560	4662	2711	1951
M531	60	-28	41025	29327	4690	2735	1955
M151	58	-27	13084	9662	4549	2617	1932
M351	59	-28	41135	29208	4690	2742	1947
M551	60	-28	69208	48734	4718	2768	1949
M115	59	-23	10734	11739	4495	2147	2348
M335	60	-24	132767	85098	4841	2950	1891
M555	60	-26	376401	236256	4901	3011	1890
S111	57	-16	1832	1010	2842	1832	1010
S311	72	-20	5735	3395	3043	1912	1132
S511	72	-20	9679	5736	3083	1936	1147
S131	72	-20	5786	3390	3059	1929	1130
S331	74	-19	17851	11530	3265	1983	1281
S531	74	-18	29942	19643	3306	1996	1310
S151	72	-20	9761	5747	3102	1952	1149
S351	74	-18	29951	19683	3309	1997	1312
S551	74	-18	50297	33456	3350	2012	1338
S115	77	-16	9135	5820	2991	1827	1164
S335	98	-23	99154	56812	3466	2203	1263
S555	99	-22	277577	168001	3565	2221	1344

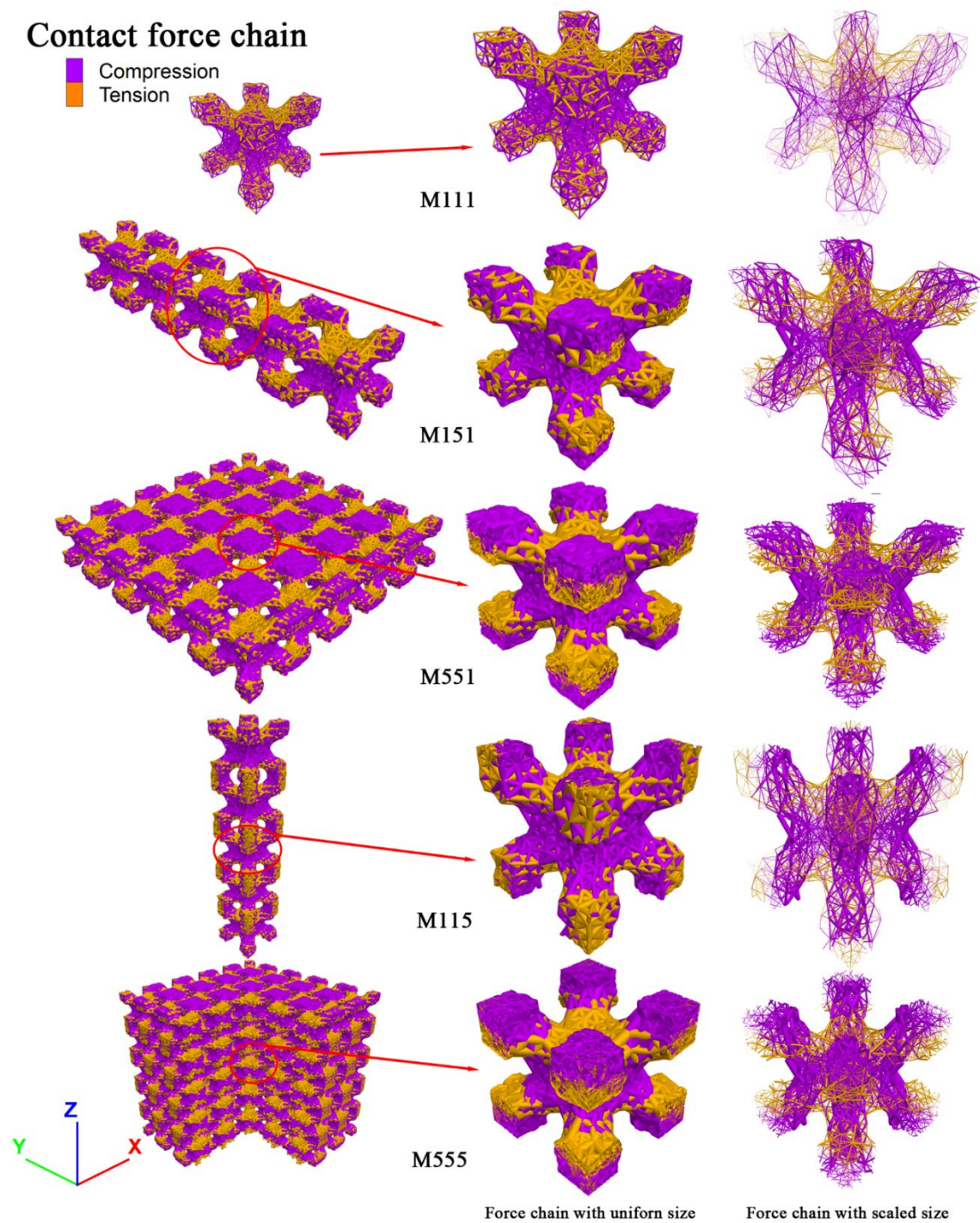


Figure 5.22 Analysis of contact force chains inside main IWP designs for various cases.

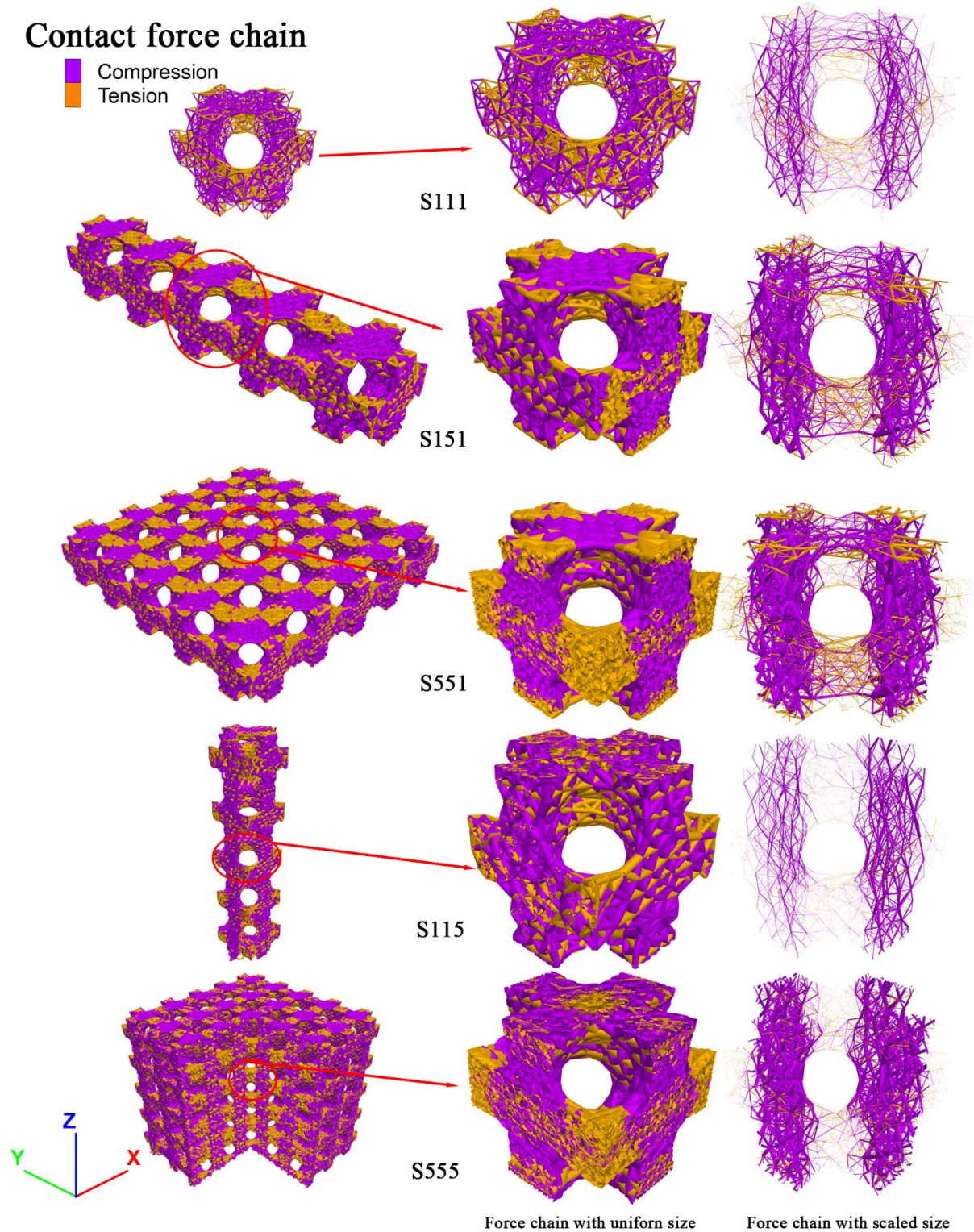


Figure 5.23 Analysis of contact force chains inside secondary IWP designs for various cases.

5.5.2 SP structures

Figure 5.24 and Figure 5.25 provide a detailed visualisation of the contact force chains within the

central unit cells of both main SP and secondary SP structures at a strain rate of 2%, covering four specific unit cell configurations: ‘111’, ‘151’, ‘551’, and ‘555’. To enhance the clarity of the visual representation, four distinct methodologies are applied to depict the force chains. The initial approach employs cylinders of uniform diameter to simultaneously illustrate both compression and tension forces; this is followed by the use of cylinders whose diameters are scaled according to the contact force magnitude. Subsequently, compression and tension contacts are individually highlighted using cylinders of uniform diameter. Table 5.4 furnishes comprehensive details on the contact forces across these configurations for both main and secondary SP structures.

Table 5.4 Specification of contact elements within Main and Secondary SP models for cases ‘111’, ‘151’, ‘551’ and ‘555’.

Case	Average compression force /N	Average tension force /N	Total compression contact amount	Total tension contact amount	Contact amount /each unit cell	Compressive contact amount /each unit cell	Tension contact amount /each unit cell
M111	17.49	-2.83	6711	3816	10527	6711	3816
M151	17.37	-2.84	34202	19190	10678	6840	3838
M551	17.10	-2.81	173614	97149	10829	6944	3885
M555	17.87	-2.98	892432	481842	10993	7139	3854
S111	17.10	-5.40	5488	3115	8603	5488	3115
S151	19.90	-5.82	28941	17296	9247	5788	3459
S551	21.98	-6.50	153020	94289	9891	6120	3771
S555	34.07	-5.86	848996	468550	10539	6791	3748

An analysis of Figure 5.24 reveals a relatively homogeneous distribution of pressure within the main SP unit cells, where larger contact forces are aligned axially, facilitating a continuous compressive pathway. Tensile forces are primarily observed encircling the unit cell's centre, creating a ring-like structure that mitigates lateral expansion under compression and thereby provides structural support. With an increment in the SP cellular unit amount, irrespective of the direction (x, y, or z), the force chain distribution becomes more compact but maintains a consistent pattern. Table 5.4 substantiates this finding, indicating that changes in the quantity of SP cellular units across three axes minimally impact the average contact force. Nevertheless, a marginal increase in the mean count of both

compressive and tensile contacts on each cellular unit is noted as the cell number expands along these axes.

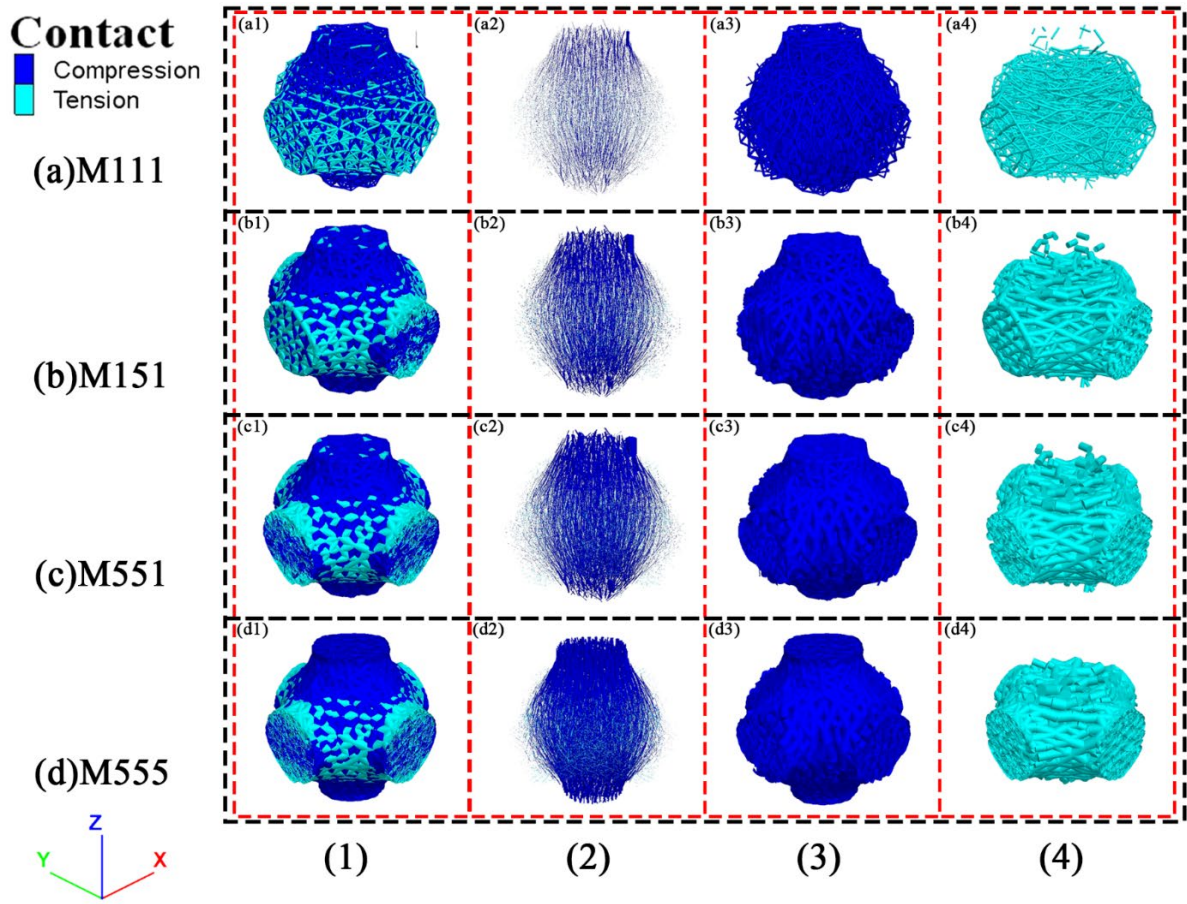


Figure 5.24 Depiction of contact force chains within the core unit cell of Primary SP frameworks across variable unit cell arrangements. Rows (a) to (d) delineate the contact force chains for configurations M111, M151, M551, and M555, correspondingly. Column (1) visualises both compressive and tensile force chains via uniformly sized cylinders; Column (2) displays these chains with cylinders scaled to the force magnitude; Column (3) is dedicated to the compressive force chain with uniform cylinder sizes; and Column (4) focuses on the tensile force chain, similarly utilising cylinders of a consistent diameter.

In Figure 5.25, the force distribution within secondary SP unit cells showcases a uniform compression, with tensile forces predominantly located at the unit cells' top and bottom areas. The second column of this figure elucidates that force transmission within secondary SP unit cells chiefly occurs vertically through the four corner columns, with tensile bonds linking these columns to ensure integrated structural functionality. This mode of force distribution becomes more marked

with an increase in the unit cell count across all directions. As delineated in Table 5.4, augmenting the unit quantity in each axle direction markedly elevates both the average number of compressive and tensile contacts per unit cell and the average contact force. This finding corroborates the finding that the engineering strength of secondary SP structures improves with a higher unit cell count, underscoring the efficacy of the discrete element method in predicting structural performance across varying configurations.

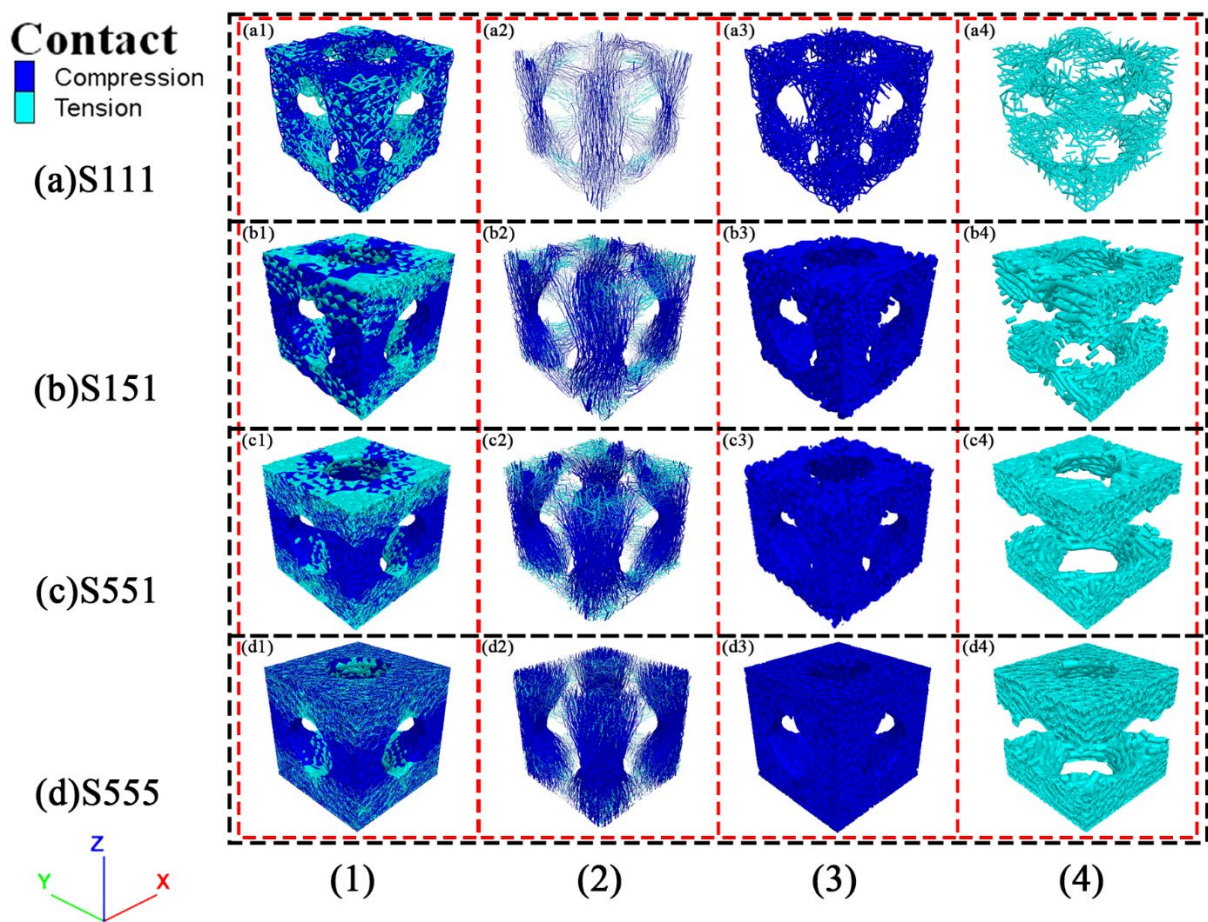


Figure 5.25 Illustration of contact force chains within the central unit cell of Secondary SP structures for varied unit cell configurations. Rows (a) through (d) illustrate the contact force chains for setups S111, S151, S551, and S555, respectively. Column (1) shows both compression and tension force chains represented by uniformly sized cylinders; Column (2) portrays these chains with cylinders sized according to contact force magnitude; Column (3) exclusively features the compression force chain with uniform cylinder diameters; and Column (4) exclusively presents the tension force chain, also with uniform cylinder diameters.

5.6 CRACK PATTERN

5.6.1 IWP structures

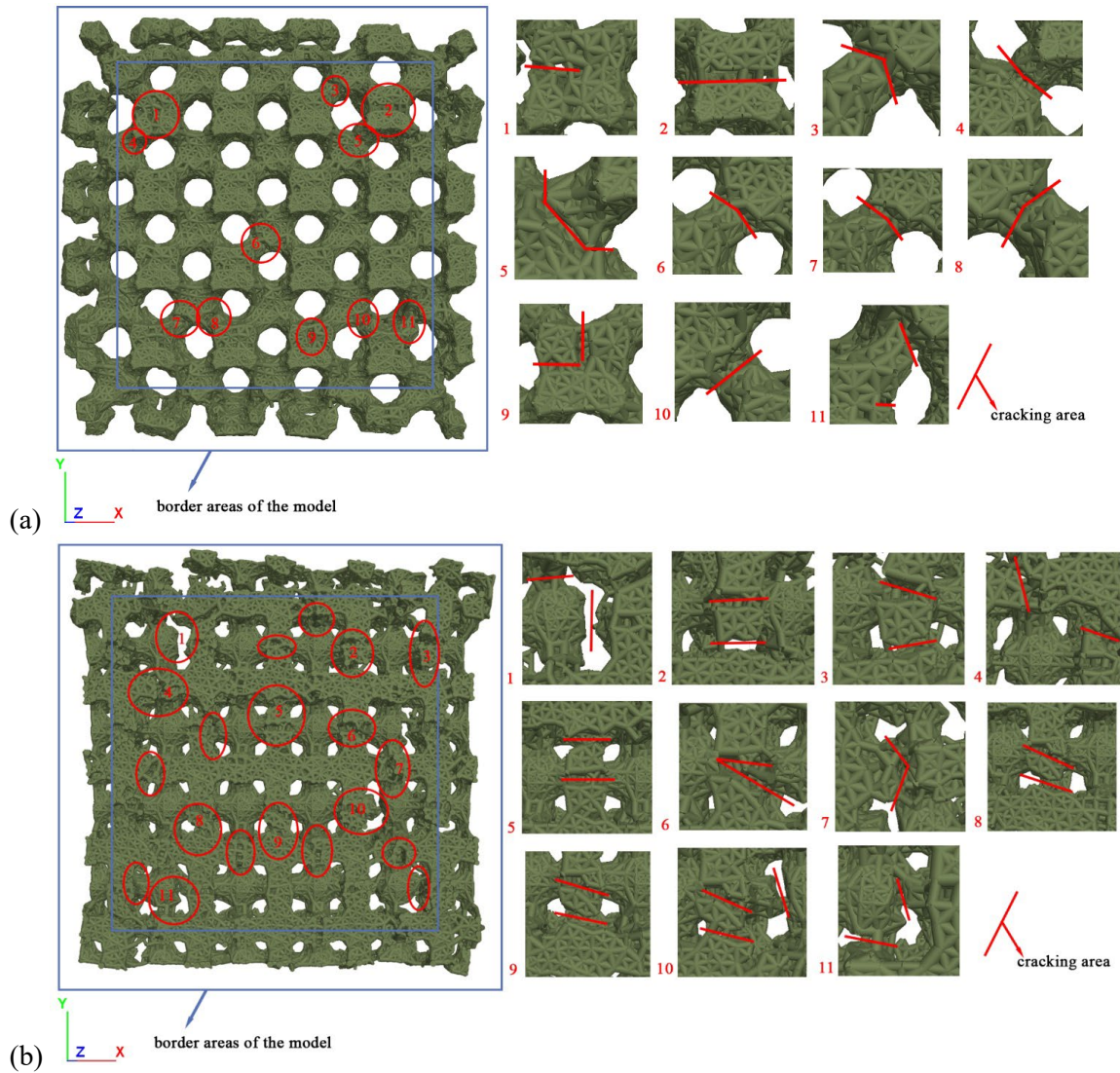


Figure 5.26 Illustration of fracture manifestations identified via contact elements upon model failure with fracture zones for case M551, denoted by red marks. (a) Main IWP design and (b) Secondary IWP design.

Figure 5.26 (a) and (b) display the contact points within both primary and secondary IWP designs, configured of case M551, subsequent to model failure, incorporating data on crack formation. These illustrations highlight that both primary and secondary IWP designs, when comprising numerous cellular units, exhibit a heightened susceptibility to cracking at the periphery, delineated by two blue rectangles. Central crack locations are identified with red circles, underscoring a notable observation:

the secondary IWP designs manifest more cracks, suggesting a more uniform distribution of stress under compressive loading. A closer examination of some cracks, accentuated with red lines, reveals that in the primary structures, fractures typically emerge along the 'bones'—as previously identified in Figure 5.2—and at junctions between unit cells. In contrast, the secondary structures predominantly exhibit crack initiation at the junctures where areas of tension and compression forces intersect, as indicated in the earlier Figure 5.23. This distinction underscores a nuanced difference in the failure mechanisms and stress distribution patterns between the two IWP variant designs under similar loading conditions.

Figure 5.27 (a) to (g) delineate the dynamic movement of sphere elements within a main IWP cellular unit from various perspectives. It becomes evident, particularly from Figure 5.27 (b) to (f), that spheres situated at the peripheral zone exhibit movement and rotation towards the unit cell's body center. In Figure 5.27 (f) to (g), four spinning trends are discernible at the central joint of the unit cell, generated by the motion of balls in the eight peripheral regions at the corners of the unit cell cube.

Conversely, the motion patterns of spheres within a secondary IWP cellular unit, as captured in Figure 5.28 (a) to (g), display a distinct divergence. Here, elements at the upper and lower regions migrate to the central zone in vertical direction, whereas those on the sides appear to bulge outward. This behavioural pattern of the secondary IWP cellular unit mirrors that of a vault, renowned for its compressive load-bearing efficiency. Analyzing the element movements within these units suggests that the secondary IWP design demonstrates characteristics akin to a positive Poisson's ratio, indicative of lateral expansion under axial stress. On the other hand, the primary Skeletal-IWP unit seems to exhibit a negative Poisson's ratio tendency, as the internal spheres of the cellular unit

converge towards its geometric centre upon loading.

The structural failures of the two IWP variant designs, of unit cell configuration X5Y5Z3 and X5Y5Z5, are illustrated in Figure 5.29. The primary design manifest a “\” fracture mode, whereas the secondary design reveal a “X” fracture mode, each indicative of the distinct stress distribution and failure mechanisms inherent to their respective designs.

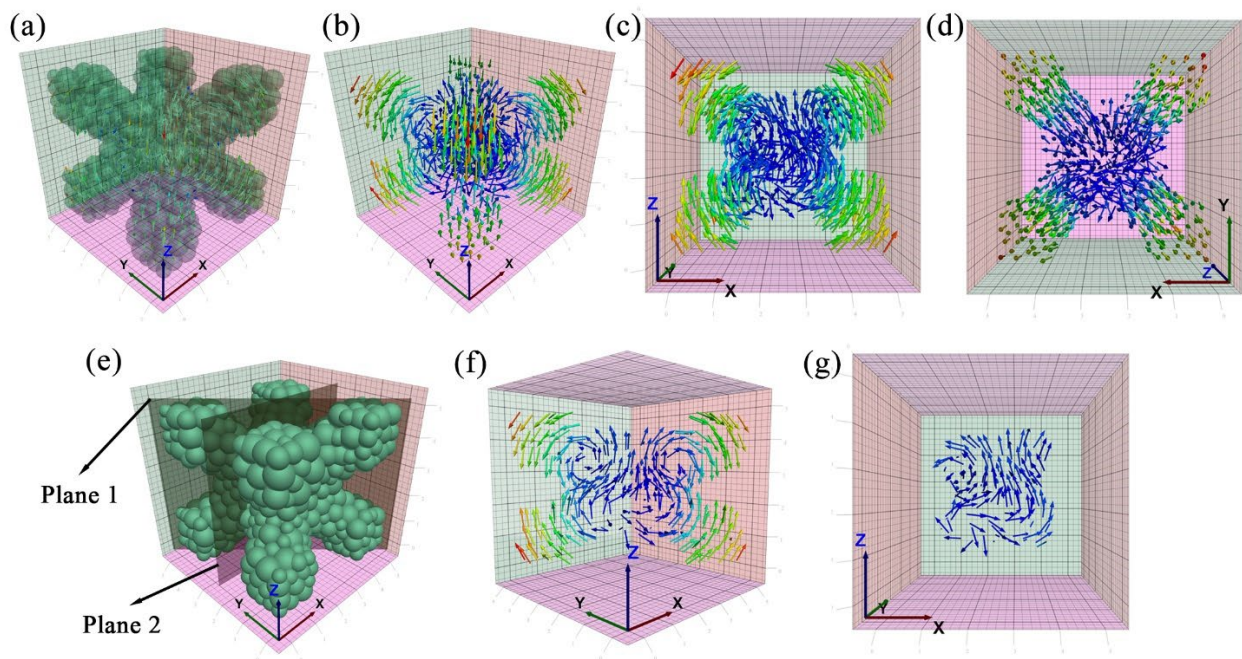


Figure 5.27 Trends of sphere movements inside the main IWP unit. (a) isotropic perspective with spheres and speed vectors, (b) isotropic perspective focusing solely on speed vectors, (c) frontal perspective of speed vectors, (d) overhead perspective of speed vectors, (e) sectional planes, (f) speed vectors in sectional plane 1, and (g) speed vectors in sectional plane 2.

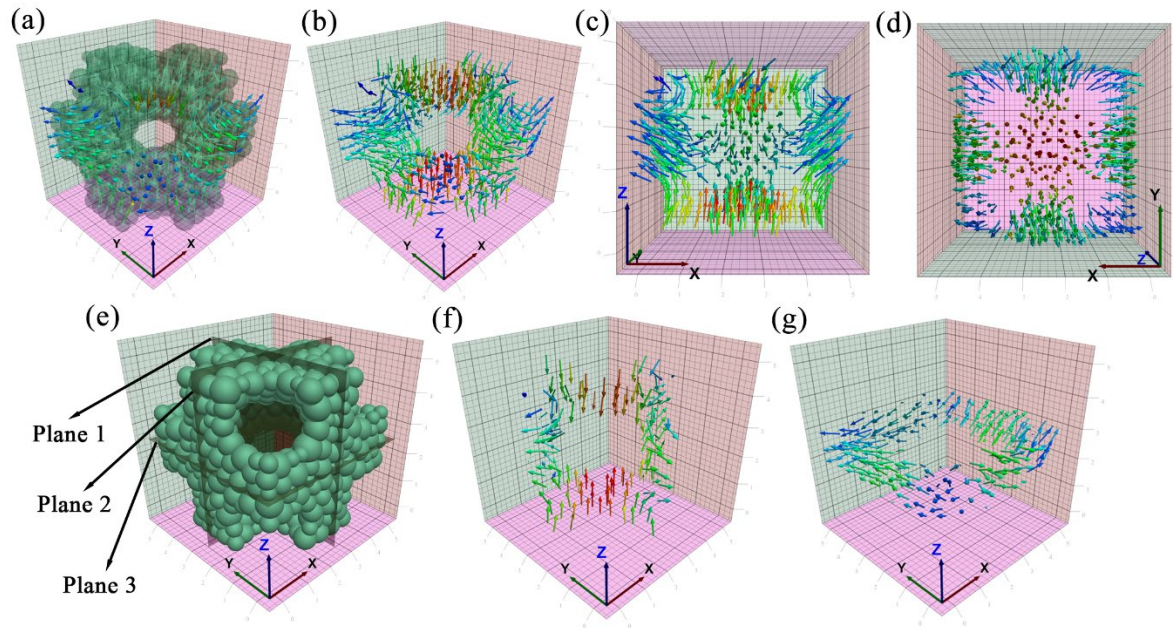


Figure 5.28 Trends of sphere movements inside the secondary IWP unit. (a) isotropic perspective with spheres and speed vectors, (b) isotropic perspective focusing solely on speed vectors, (c) frontal perspective of speed vectors, (d) overhead perspective of speed vectors, (e) sectional planes, (f) speed vectors in sectional plane 1 and 2, and (g) speed vectors in sectional plane 3.

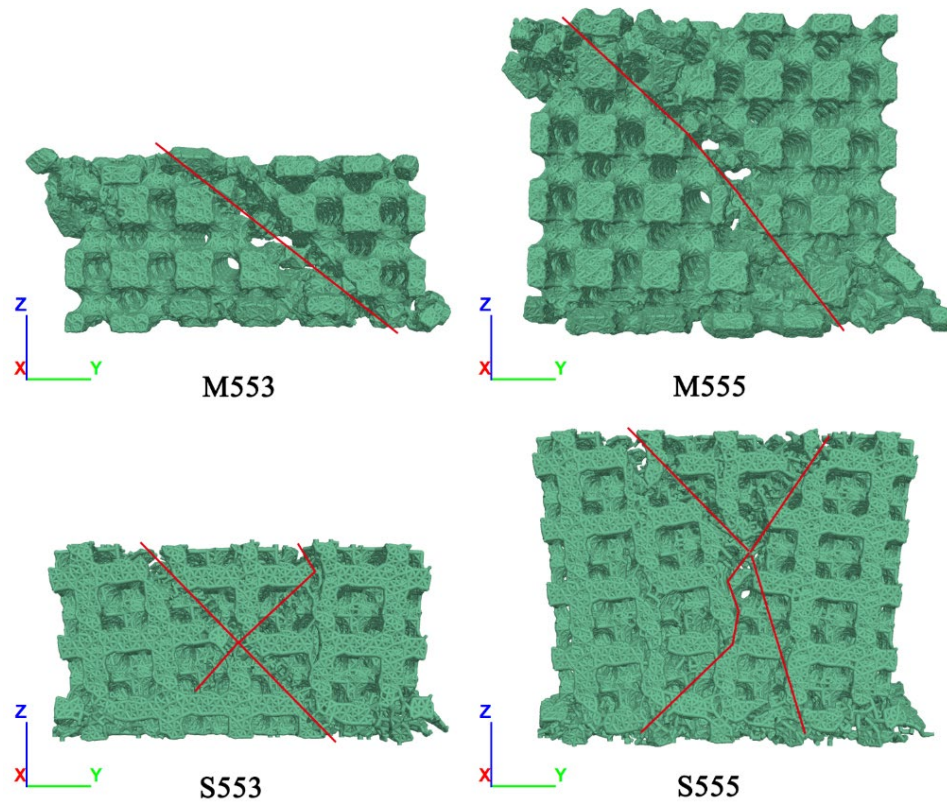


Figure 5.29 Fractures in main and secondary IWP designs.

5.6.2 SP structures

Figure 5.30 showcases the aftermath of axial compression tests alongside DEM simulations for both main SP and secondary SP structures, each configured with a '444' unit cell arrangement, viewed from the front, sides, and rear. Red ellipses are employed to underscore the regions of cracking and failure within both the experimental structures and the DEM models, facilitating a direct comparison. It's pertinent to mention that the unit cell size within the DEM models is set at 5 cm, contrasting with the 2.5 cm unit cell size of the physical structures. Despite the inability to conduct a quantitative analysis of load-bearing capacities due to this dimensional disparity, a notable alignment is observed between the fracture zones identified in the physical tests and those predicted by the DEM models. A closer examination of Figure 5.30 (a) and (b) reveals that main SP structures are prone to spalling at the horizontal extensions under compression, with fractures predominantly aligned along the vertical axis. In Figure 5.30 (c) and (d), secondary SP structures are observed to fracture primarily at the unit cell junctions, with the slimmer central sections protruding and breaking away vertically.

Figure 5.31 illustrates the internal force distribution within '555' unit cell configurations of main SP and secondary SP DEM models at a 2% strain, with contact elements differentiated by the intensity of contact forces. This, combined with the observations from Figure 5.30, indicates that the sites of cracking in SP structures correspond to areas where internal forces are markedly concentrated, leading to material separation around these focal points. Figure 5.32 further displays the contact models following compression tests for cases M551 and S551, with the colouration and dimensions of contact elements reflecting the force magnitude. These depictions suggest that under a single-layer setup, both main SP and secondary SP structures experience transmission and fracturing along

their skeletal framework. The main SP is characterised by a more homogenous force distribution, whereas the secondary SP exhibits reduced load-bearing efficiency at its periphery, placing greater reliance on its central area. Upon examining the central zones, the force chain distribution in both structures shows similarities, yet the fractures in secondary SP structures are more uniform and linear compared to the slightly angled fractures observed in main SP structures under similar conditions. Given the shared 1/8th structural basis of main SP and secondary SP unit cells, it is projected that with an escalation in unit cell numbers across each axis, the force transmission and mechanical performance of both SP structures would converge. Integrating this insight with previous analyses, the main SP structure is posited to demonstrate a more refined configuration for enduring compressive stresses.

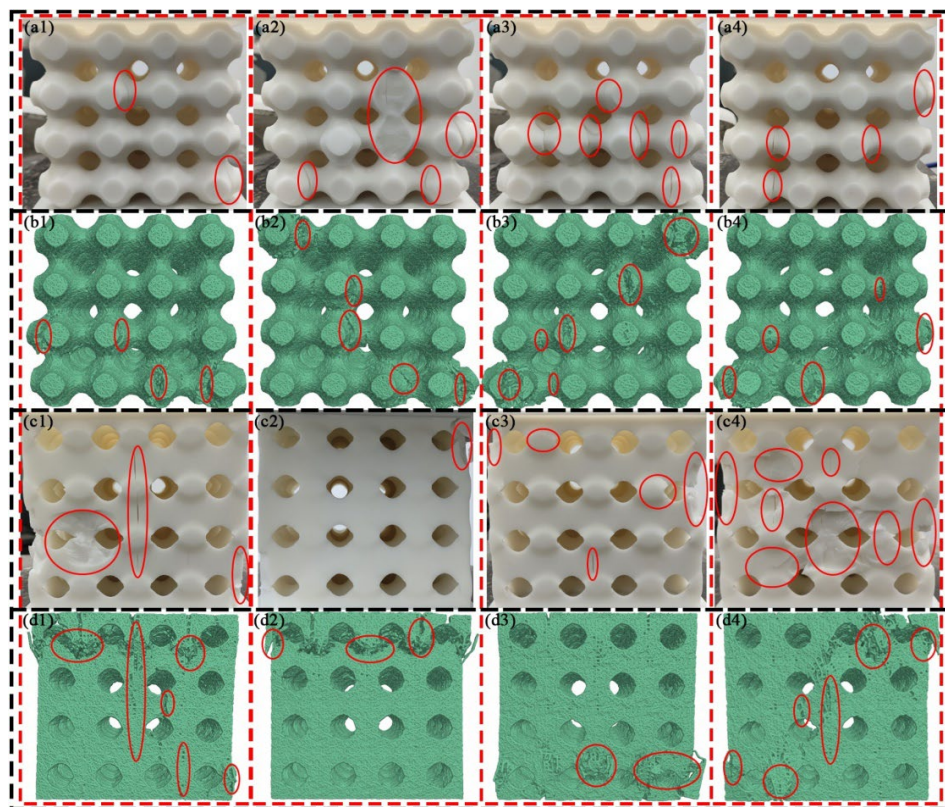


Figure 5.30 Comparison of '444' unit cell configuration SP samples following axial compression tests, presented from the front, both sides, and the rear. (a) the 3D printed Main SP structure; (b) the DEM-simulated Main SP model; (c) the 3D printed Secondary SP structure; and (d) the DEM-simulated Secondary SP model.

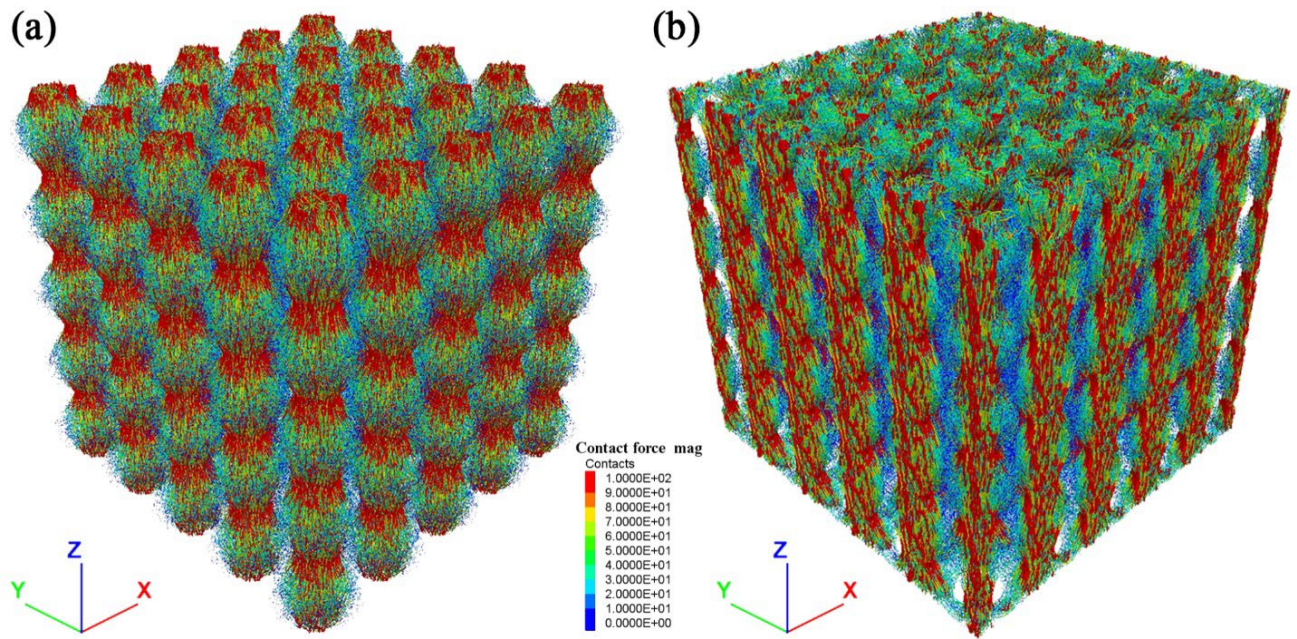


Figure 5.31 Contact force chain coloured by the magnitude of contact forces at a strain of 2%: (a) Main SP structure for the '555' configuration, and (b) Secondary SP structure for the '555' configuration.

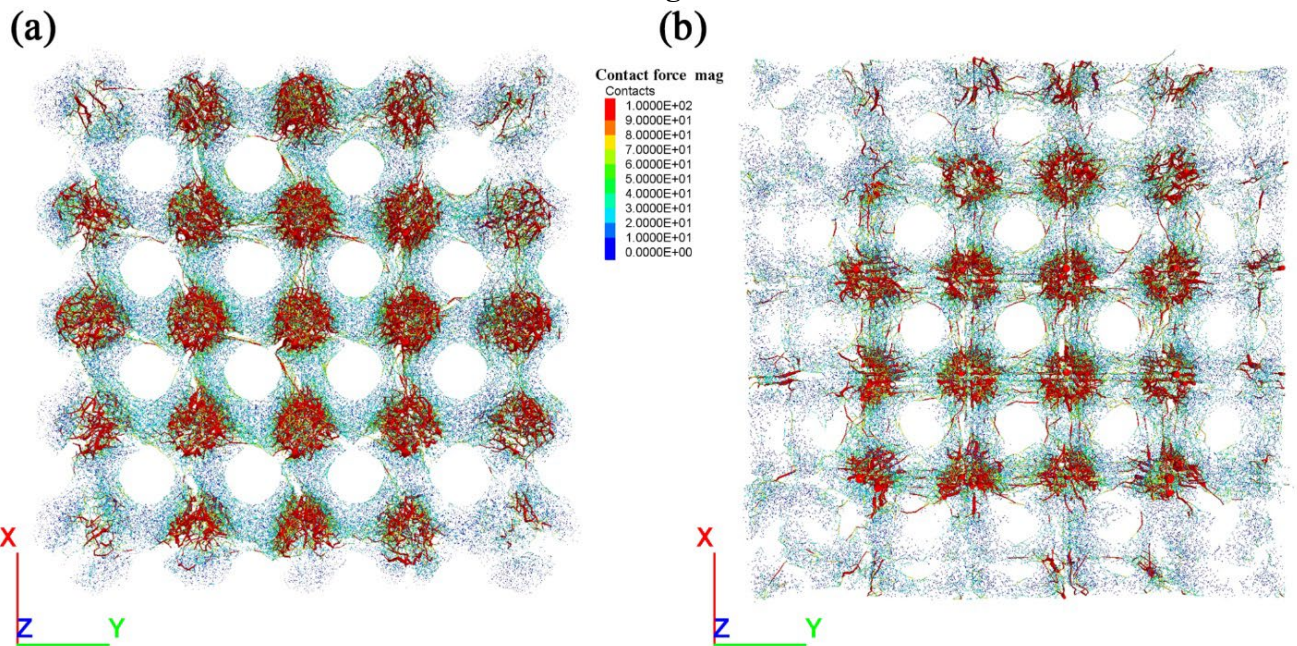


Figure 5.32 Contact force chain coloured and scaled by the magnitude of contact forces at a strain of 2%, within (a) Main SP structure and (b) Secondary SP structure, with '551' unit cell configuration.

5.7 LOAD-DISPLACEMENT CURVE AND ENERGY ABSORPTION

5.7.1 IWP structures

Figure 5.33 (a) and (b) depict the mean load-displacement responses for various configurations of unit cells within both IWP designs, as derived using DEM modelling. These illustrations reveal that an augmentation in the count of cellular units across all axes notably improves the axial load-bearing capabilities of an individual unit for both IWP designs, with regard to peak load capacity, stiffness, and energy absorption capacity. Specifically, an expansion in unit cells universally bolsters the maximum compressive capacity and the deformation at maximum load for both IWP variant designs. Furthermore, it has been discerned that enlarging the unit cell count in the x and y axes predominantly enhances the unit structural stiffness from deformation onset up to the point of peak load. Conversely, an increase in unit cell volume in the z-axis predominantly augments the stiffness of the two IWP designs at the start of deformation, specifically when displacement remains below approximately 1mm.

Through an integration of the load-displacement graphs, the mean energy absorption capacity is ascertainable. Figure 5.34 (a) and (b) showcase the energy absorption graphs for the two IWP variant designs. It emerges that a proliferation of cellular units in the z-axis exerts a more substantial bolstering influence on the mean energy absorption capacity than increases in xy axes for the two IWP variant designs. Moreover, this enhancement in energy absorption capacity is more pronounced at lower displacement levels than at higher displacement magnitudes. Table 5.5 compiles the energy absorption data for the two IWP variant designs across diverse cellular configurations when the axial force is ultimate. An analysis reveals a significant escalation in energy absorption for the two

IWP variant designs as the unit cell count expands from one to five across every orientation. Nevertheless, the rate of increasement in energy absorption begins to decelerate once the unit cell count exceeds five, indicating a diminishing return on energy absorption with further increases in unit cell quantity.

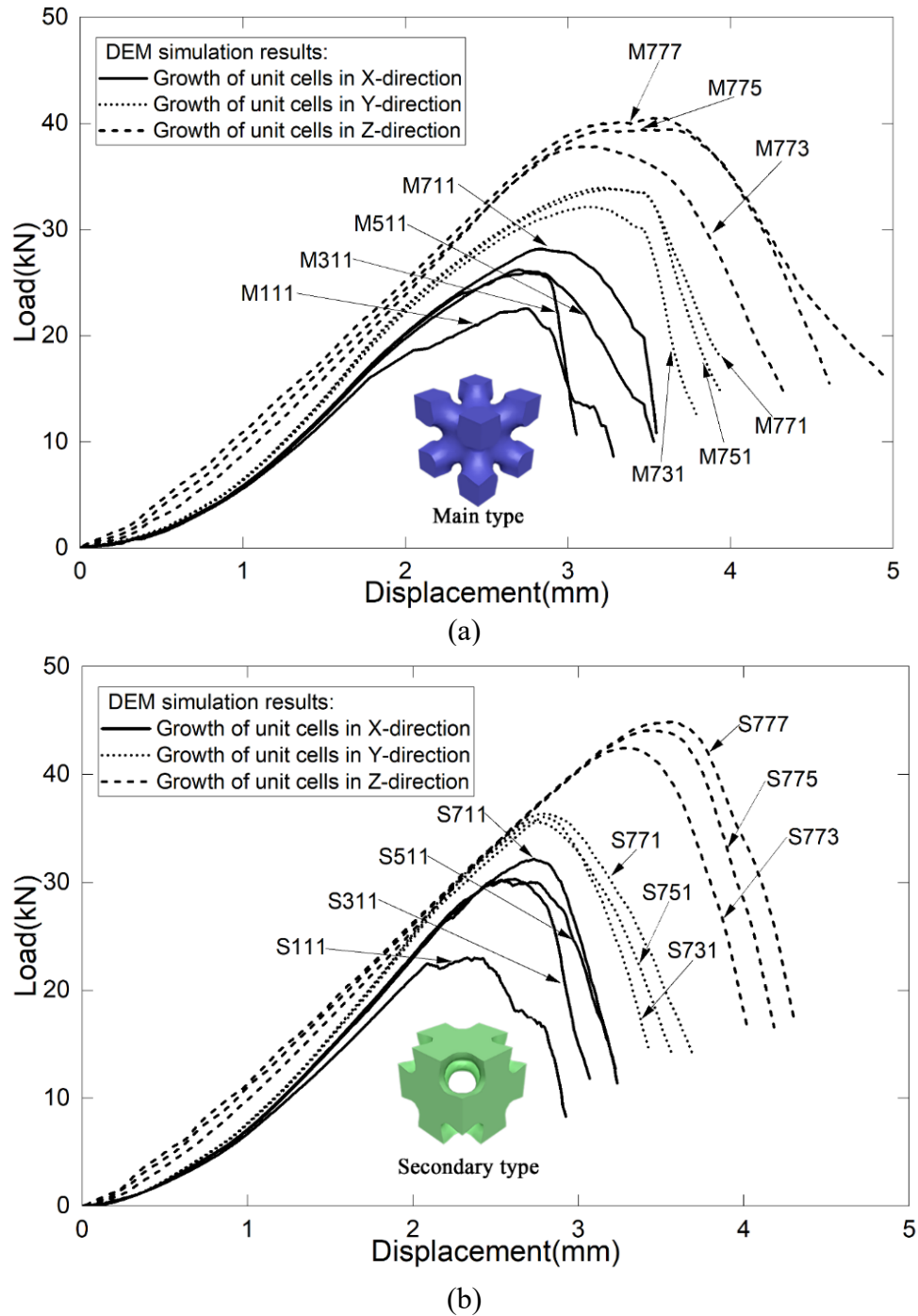


Figure 5.33 The average load versus displacement curves of the two IWP designs of different cases. (a) Main IWP designs and (b) Secondary IWP designs.

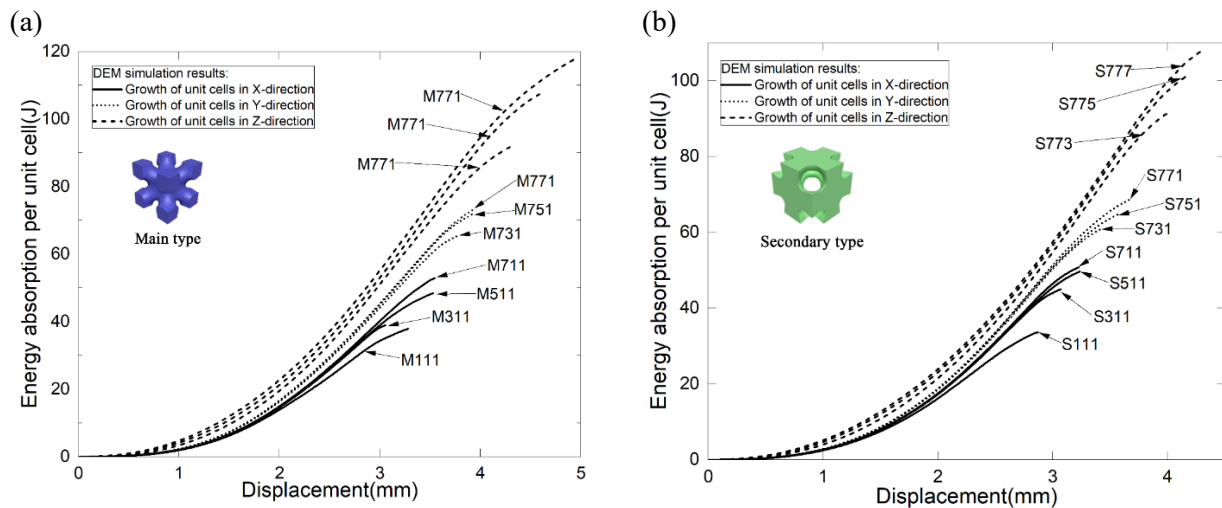


Figure 5.34 The average energy absorption versus displacement curves of the two IWP designs of different cases. (a) Main IWP designs and (b) Secondary IWP designs.

Table 5.5 Energy absorption capacity and displacement at their peak loads for the IWP variant designs

Unit cell arrangements	Main Skeletal-IWP type		Secondary Skeletal-IWP type	
	Displacement (mm)	Energy absorption (J)	Displacement (mm)	Energy absorption (J)
X1Y1Z1 (M111/S111)	2.74	29.1	2.37	24.5
X3Y1Z1 (M311/S311)	2.70	31.0	2.53	31.6
X5Y1Z1 (M511/S511)	2.75	32.7	2.62	34.7
X7Y1Z1 (M711/S711)	2.82	35.3	2.73	38.5
X7Y3Z1 (M731/S731)	3.11	47.7	2.79	43.0
X7Y5Z1 (M751/S751)	3.26	52.6	2.74	41.3
X7Y7Z1 (M771/S771)	3.22	52.7	2.79	43.8
X7Y7Z3 (M773/S773)	3.11	55.5	3.30	67.4
X7Y7Z5 (M775/S775)	3.61	76.9	3.45	75.7
X7Y7Z7 (M777/S777)	3.59	78.6	3.57	82.0

5.7.2 SP structures

Figure 5.35 (a) and (b) showcase the load-displacement responses for Main SP and Secondary SP structures, respectively, calculated on an average per unit cell basis across a variety of unit cell configurations. Analysis of Figure 5.35 (a) reveals that for Main SP structures, expanding the count of cellular units in the xy axes has a minimal effect on the average load-bearing performance, as evidenced by the overlapping curves within the displacement range of 0.0 cm to 2.0 cm for groups 'A11' and '7B1'. The '77C' group, however, illustrates a slight improvement in the initial stiffness of

the Main SP structure upon adding unit cells along the z-axis, though this does not markedly influence the overall bearing capacity. In contrast, Figure 5.35 (b) indicates that for Secondary SP structures, increasing the number of unit cells across all three directions, x, y, and z, contributes positively to both the average load-bearing capacity and structural stiffness. The comparative analysis of the 'S111', 'S711', 'S771', and 'S777' configurations demonstrates that enhancements along the x and y axes are more impactful than those made along the z-axis.

The energy absorption profiles derived from the integrated load-displacement curves of both structures are depicted in Figure 5.36 (a) and (b) for Main SP and Secondary SP structures, respectively. For Main SP structures, the configurations grouped as 'A11' and '7B1' in Figure 5.36 (a) indicate a marginal influence on energy absorption capacity from increasing cellular units in the xy axes. However, the '77C' configuration suggests that a rise in unit cells along the z-axis slightly bolsters the energy absorption capacity at the commencement of loading. Conversely, Figure 5.36 (b) demonstrates that for Secondary SP structures, augmenting unit cells in all directions enhances the average energy absorption capacity, albeit with a decelerating rate of enhancement as the unit cell count ascends, eventually reaching a plateau.

A comparative analysis of the load-displacement and energy absorption profiles for Main SP and Secondary SP structures under identical unit cell configurations highlights distinct disparities in load-bearing capacities, especially in configurations with extensive dimensions and fewer cells. This discrepancy underscores the necessity for customised design solutions tailored to specific application requirements within the realm of civil engineering. Notably, the Main SP structure is characterised by superior axial load-bearing and energy absorption capabilities during the elastic deformation phase compared to the Secondary SP structure, illustrating the critical importance of

selecting the appropriate structure type based on the anticipated engineering demands.

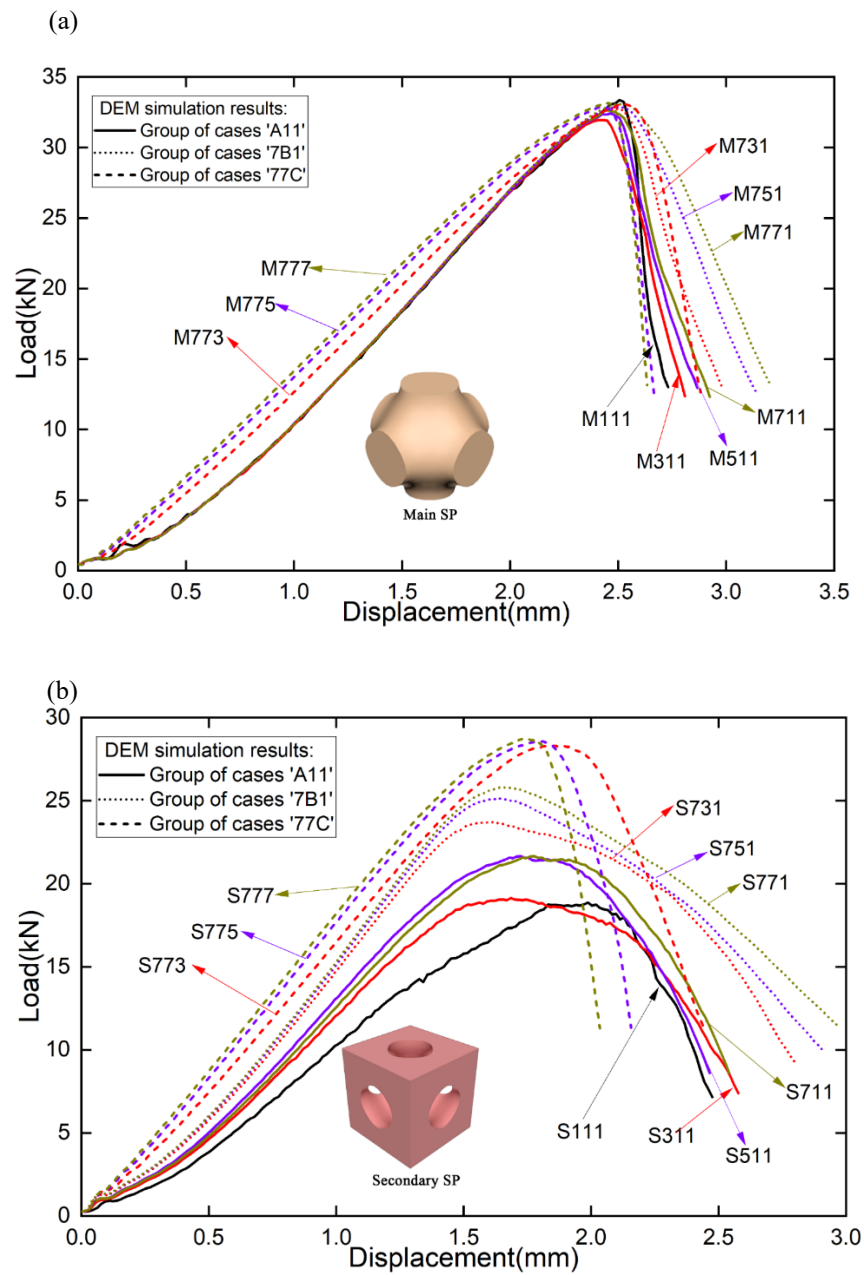


Figure 5.35 The average load versus displacement curves of the two IWP designs of different cases. (a) Main SP designs and (b) Secondary SP designs.

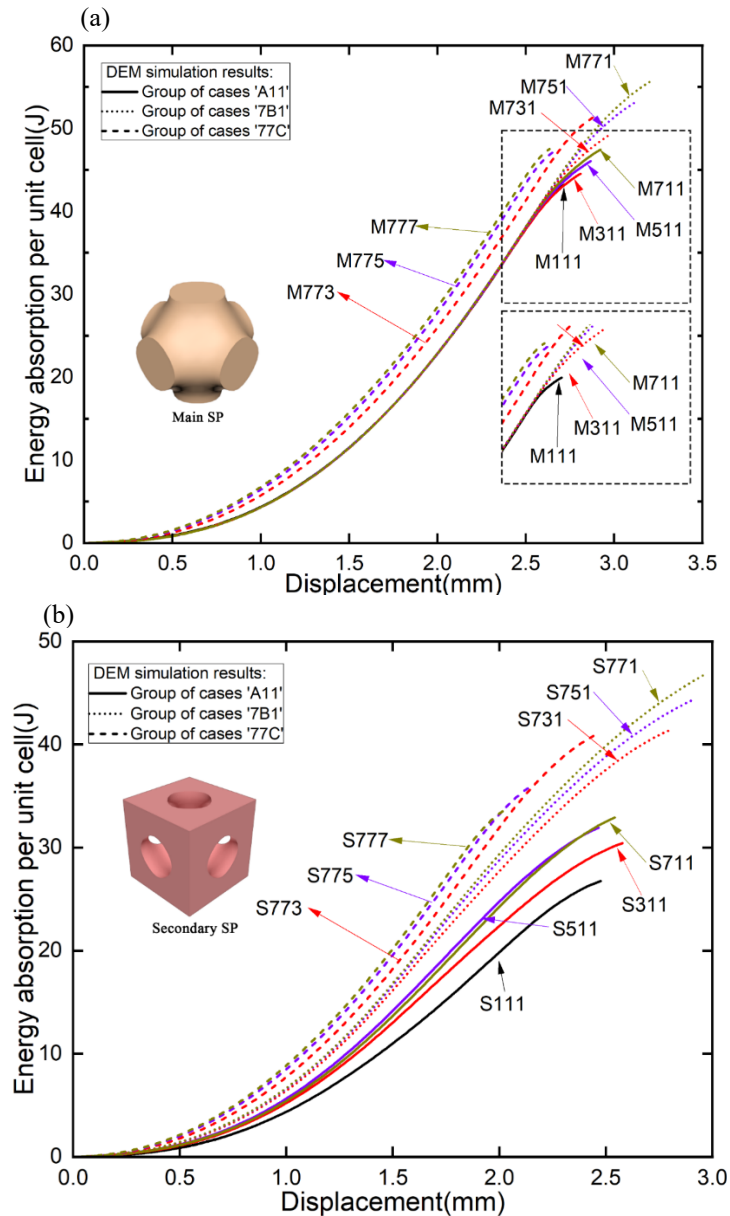


Figure 5.36. The average energy absorption versus displacement curves of the two IWP designs of different cases. (a) Main SP designs and (b) Secondary SP designs.

5.8 CONCLUSION

This chapter investigates the compressive mechanical responses of two basic TPMS structures, IWP and SP, as studied in Chapter 4, under various unit cell quantities. The simplified surface methods for IWP and SP, along with the solid models and 3D printing techniques, originate from the previous Chapter 3. The main conclusions derived are discussed as follows, categorised by structural type.

In the subsequent Chapter 6, the IWP and SP structures are further examined through impact hammer tests, and a comparative analysis of their dynamic properties is conducted against the Gyroid structure.

5.8.1 IWP structures

Through a comprehensive investigation involving compression experiments and DEM calculations, this chapter explores the compressive behaviours of two IWP variant designs, employing a groundbreaking approach to analyse 3D printed TPMS specimens for the first time. A novel simplification technique has been introduced, transforming a smoothy TPMS into a polygonal surface to significantly decrease the amount of data of the 3D printable file size, which facilitates the examination of the fracture areas within the two IWP based variant designs.

The use of DEM modelling has enabled an unprecedented analysis of the compressive engineering strength, cracking patterns, load-displacement characteristics, and energy absorption capacities of these structures, underpinned by experimental validation. Notably, the transition from a singular unit cell to a complex $7 \times 7 \times 7$ configuration markedly enhances the axial loaded engineering strength of the two Skeletal-IWP variant designs from 9 MPa to 13.4 MPa and from 9.2 MPa to 14.4 MPa, respectively. Similarly, this configuration adjustment augments the average energy absorption capacity at their maximum loads from 29.1 J to 78.6 J for main IWP design, and from 24.5 J to 82.0 J for secondary structures. Nonetheless, the mean energy absorption capacity stabilizes beyond a quintuple cell count, highlighting a nuanced understanding of structural performance enhancements.

Further analysis reveals that secondary Skeletal-IWP structures not only exhibit superior

compressive strength compared to their primary counterparts for identical unit cell configurations but also demonstrate more uniform load distribution, akin to that of arch structures. This distinction is mirrored in the observed cracking patterns, with primary structures revealing a "\-shaped pattern, whereas secondary structures display a "×"-shaped pattern, indicative of their differentiated mechanical responses under stress.

The study confirms that increasing the unit cell count across all three axial directions bolsters the compressive strength of both Skeletal-IWP structure types. This enhancement is more pronounced when increasing the loaded area (in the x and y directions) compared to extending the loading path (in the z-direction), with compressive strengths of multi-unit cell configurations reaching up to 180% and 195% for primary and secondary structures, respectively. Moreover, the analysis of cracking patterns reveals that primary structures are prone to cracking at the junctures of connection bones and unit cell junctions, whereas secondary structures are more susceptible at interfaces where tension and compression forces intersect, with an increased likelihood of cracking in multi-unit cell configurations.

This integrative study not only advances the application of DEM simulations in analysing the mechanical behaviours of 3D printed TPMS specimens but also provides critical insights into the micro-mechanisms governing the structural integrity and performance of IWP-based structures. The findings underscore the potential of these structures in engineering applications, offering a foundation for future research aimed at optimizing their design and material composition for enhanced mechanical properties.

5.8.2 SP structures

Discrete Element Method (DEM) simulations have been meticulously conducted to investigate the axial load-bearing behaviour and fracture mechanics of both primary and secondary SP structures across various unit cell arrangements, following validation through experimental procedures. This research meticulously examines the impact of unit cell adjustments across the x, y, and z axes, offering essential insights into the structural integrity and mechanical resilience of SP configurations under axial compression.

The findings indicate that the load-bearing capability of primary SP structures is largely consistent despite variations in the unit cell numbers along the x and y axes, as demonstrated by the parallel load-displacement curves for groups 'A11' and '7B1'. Conversely, an increase in the unit cell count along the z-axis has been observed to bolster the initial stiffness of primary SP structures, albeit without markedly affecting the overall load-bearing capacity. This revelation highlights the anisotropic nature of load distribution within these structures and suggests the possibility of modulating stiffness properties through targeted adjustments in unit cell orientation.

Additionally, analyses of energy absorption reveal that enhancing the unit cell quantity along the z-axis marginally improves the initial energy absorption efficiency of primary SP structures. In the case of secondary SP structures, augmenting unit cells across all three axes not only elevates the load-bearing capacity but also enhances energy absorption efficiency. Nevertheless, this incremental enhancement approaches a threshold, indicating a diminishing return on reinforcement with additional unit cell integration.

A comparative examination of load-displacement and energy absorption behaviours between

primary and secondary SP structures unveils pivotal insights. Despite their similar microstructural features, the two structures exhibit unique mechanical behaviours, especially in configurations with larger dimensions and fewer cell alignments. This distinction is vital for their application in the civil engineering sector, where precise performance under load is critical.

In summary, this chapter enriches our comprehension of SP structures, elucidating the complex interplay between microstructural arrangements and macroscopic mechanical properties. Primary SP structures, in particular, have shown superior axial load-bearing and energy absorption efficiencies, underscoring their potential applicability in scenarios demanding robust structural integrity. These contributions not only furnish valuable insights for the civil engineering field but also pave the way for future investigations into hybrid configurations and optimisation through material diversity. The derived insights lay a foundation for engineers to innovatively employ SP structures in the development of resilient and long-lasting civil infrastructure.

CHAPTER 6

DYNAMIC PROPERTIES OF TPMS BASED STRUCTURES

6.1 INTRODUCTION

Over the past two decades, cellular structures inspired by TPMSs have garnered considerable interest for their geometric similarities with microstructures observed in natural organisms. TPMS structures stand out among porous architectures for their exceptional mechanical properties, including elevated specific strength and capacity for energy absorption. The advent of additive manufacturing has simplified the creation of complex TPMS geometries, leading to their proposed application in various domains such as sound shields, impact resistance designs, and artificial bone substitutes. While the quasi-static attributes like strength, modulus, and energy absorption of TPMS structures have been extensively explored, the examination of their dynamic characteristics remains limited, thereby restricting their broader application in engineering projects.

Among the most studied TPMS geometries are the I-graph-wrapped package surface (IWP), Gyroid surface, and Primitive (Schwarz P) surface. Previous research has predominantly focused on the elastic-plastic compressive behaviour of porous structures based on these TPMS geometries, yet the understanding of their dynamic performance is still evolving. Recent investigations have begun to explore the dynamic and vibration response of TPMS structures, albeit sparingly. For instance, studies have examined the natural frequencies and modal shapes of Sheetal-TPMS structures under varied TPMS designs, highlighting how changes in wall thickness and material influence these dynamic properties. However, comprehensive comparisons of various TPMS designs with an identical porosity have been lacking, as have detailed examinations of their damping properties.

This gap in knowledge is particularly relevant for civil engineering applications, where many components work as bearing structure subject to impact forces from vehicular traffic, potentially

leading to failures and fatigue issues. Understanding dynamic and vibration responses of various TPMS designs, including the damping ratios and performance under actual boundary conditions, is crucial for their effective integration into civil constructions for bearing dynamic forces.

Previous chapters have researched the quasi-static performance of several TPMS structures. This chapter aims to bridge this gap about dynamic performance by conducting impact hammer tests on nine types of porous structures of three TPMS designs featuring IWP, Gyroid, and Primitive topologies, assessing them as single-freedom systems. It marks the first comprehensive comparison of the dynamic performance across different TPMS topologies, including an analysis of their damping ratios. This research lays the groundwork for the deployment of advanced TPMS-based supports in civil engineering, expanding the potential applications of these innovative structures. This chapter is mainly based on Paper 3 as listed in list of publication.

6.2 TPMS STRUCTURES

This chapter conducts a comprehensive examination of both sheetal and solid TPMS structures. A TPMS uniquely segments space into two distinct, non-overlapping regions, facilitating the creation of two varieties of solid TPMS structures. Within this research framework, three specific kinds of TPMS designs, all maintaining uniform size, mass and volume, are scrutinised: the Sheetal TPMS (SH-TPMS) type, the Main Solid TPMS (MS-TPMS) type, and the Secondary Solid TPMS (SS-TPMS) type. For the inaugural exploration of their dynamic characteristics, three TPMS geometries are utilised to fabricate these TPMS structures. This approach allows for an integrated analysis of the structures' dynamic properties, leveraging the distinctiveness of the IWP, Gyroid, and Primitive TPMS, as indicated in Figure 6.1, to enhance our understanding of their potential engineering

applications.

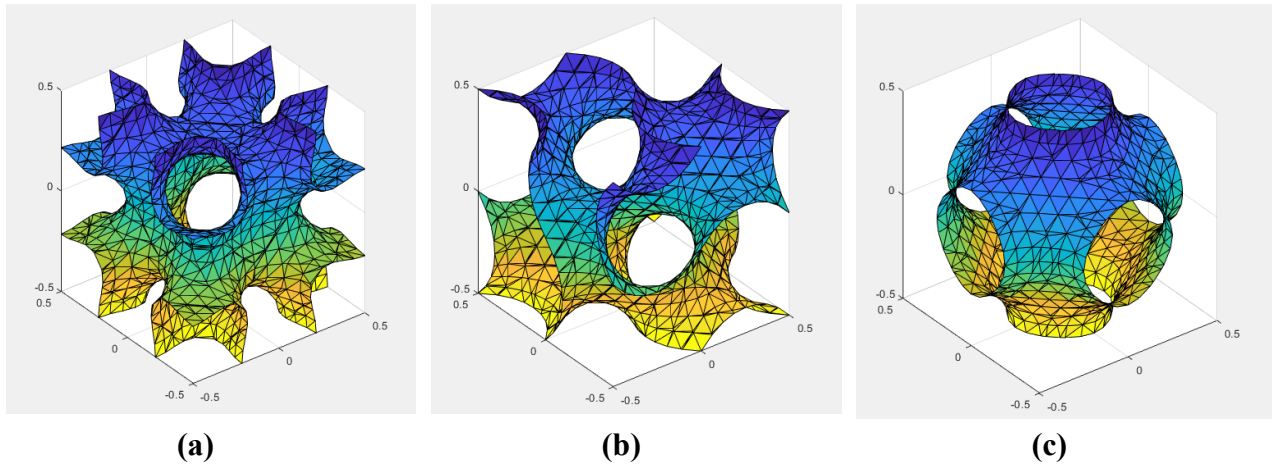


Figure 6.1 Simplified polygonal (a) IWP, (b)Gyroid and (c) Primitive surfaces. The facets and points are plotted with different colours according to value of Z-coordinates.

This chapter delves into the research of both main or primary and secondary or complementary solid TPMS designs, which are conceptualised by the solidifying the regions bisected from the TPMSs defined by the conditions $\Phi_{TPMS} \geq 0$ and $\Phi_{TPMS} \leq 0$, respectively, same as indicated in Figure 3.6. Given the uniform geometric topology of the three TPMS geometries across the three axes and their mirror-image and periodic characteristics in three orientations, the centre of body and centre of mass for these solid TPMS structures resides at the origin point (0,0,0), as the coordinates are indicated in Figure 6.1. The structure encompassing the centroid within its volume and satisfying $\Phi_{TPMS} \geq 0$ is designated as the Main Solid (MS) type, whereas its counterpart, fulfilling $\Phi_{TPMS} \leq 0$, is referred to as the Secondary Solid (SS) type. Notably, for the Gyroid TPMS structures, the centroid lies on the exterior surface of the structure since Φ_{Gyroid} at the origin is zero.

Owing to the TPMS's capability to partition a cubic zone into two disjoint regions volumes of equal size, the relative density of both Solid-TPMS structure types is established at 0.5. Conversely, the SH-TPMS structures are crafted by augmenting the thickness of the TPMS in two opposite normal orientations (\mathbf{n}_1 and \mathbf{n}_2). The generation process for the three Primitive designs of a single cellular

unit is exemplified in previous Figure 3.6. The generation procedures are detailed in previous chapter 3. The thickness of the SH-SP designs is 0.11255 time of cellular unit length, ensuring a uniform relative density of 0.5.

Figure 6.2 showcases the cellular units for the TPMS designs investigated in this chapter. The thicknesses of sheetal TPMS structures are determined to be 0.07704 and 0.0853 times the cellular unit length for IWP and Gyroid designs, respectively, thereby achieving the stipulated relative density. This approach facilitates a comprehensive study of the dynamic properties of these TPMS structures, offering valuable insights into their potential engineering applications.

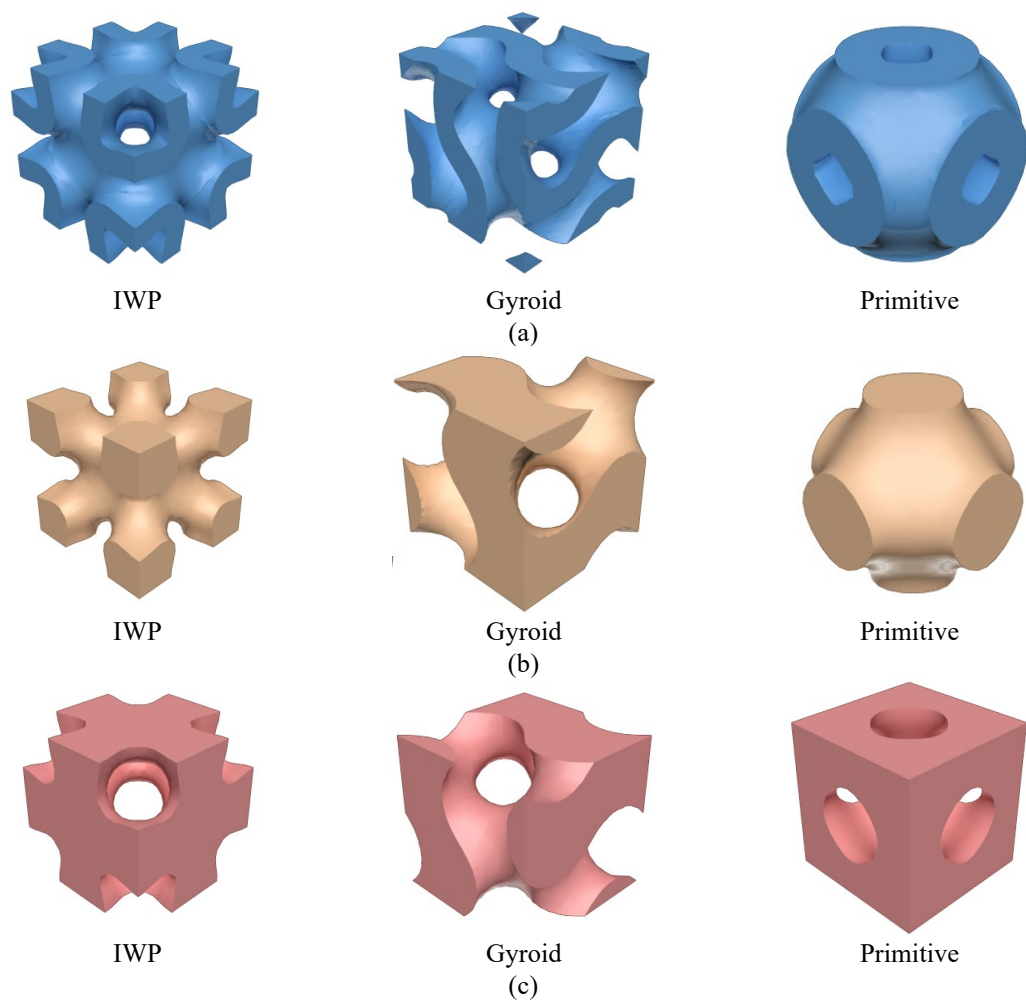


Figure 6.2 Three classes of TPMS based cellular unit of IWP, Gyroid and Primitive designs.

(a) sheetal type, (b) main solid type and (c) secondary solid type.

This chapter is focused on examining the dynamic performance of TPMS structures, for which two plates, each 2.5 mm thick, have been integrated into the upper and lower regions of all nine TPMS structures. The chosen dimension of all nine TPMS cellular units for these experiments are 2.5 cm by 2.5 cm by 2.5 cm, configuring all specimens in a 4×4×4 arrangement, culminating in a total vertical dimension of 10.5 cm including two plates.

Table 6.1 Details of the 3D printing material.

Properties	Value	Test method
Hardness (Shore D)	76~88	ASTM D 2240
Tensile modulus	2589~2775 MPa	ASTM D 638
Tensile strength	38~56 MPa	ASTM D 638
Elongation at break	12~20%	ASTM D 638
Impact strength, Notched Izod	35- 55 J/m	ASTM D 256
Poisson's ratio	0.4~0.44	ASTM D 638

The selected material for manufacturing the TPMS structures is a composite resin, known as “photosensitive 8200”. WENEXT Ltd. conducted comprehensive material property tests on this composite resin, with the values detailed in Table 6.1. This material is distinguished by its alabaster hue and polished exterior, coupled with exceptional robustness, which augments its longevity. These properties render it highly suitable to produce prototypes for product testing and verification. It is noted that models with a wall thickness under 1.5 mm tend to be malleable and prone to deformation, displaying only moderate dimensional accuracy.

The fabrication of the test specimens is achieved through Stereolithography (SLA) 3D printing technology, conducted at ambient room conditions. WENEXT Ltd. is responsible for the 3D printing, utilizing an RSP600 printer with the UnionTech™ RSCON managing the printing operations. The printing environment has been carefully controlled, maintaining temperatures between 23 – 25°C and relative humidity below 40%. The velocity of the laser beam is regulated at

6 m/s. The laser beam diameter is 0.12 mm, and the frequency of the laser is of 8.445×10^{14} Hz. This laser is a solid-state frequency tripled Nd: YVO₄, with printing accuracy of 0.05 mm, while all other printing parameters have been set to default values.

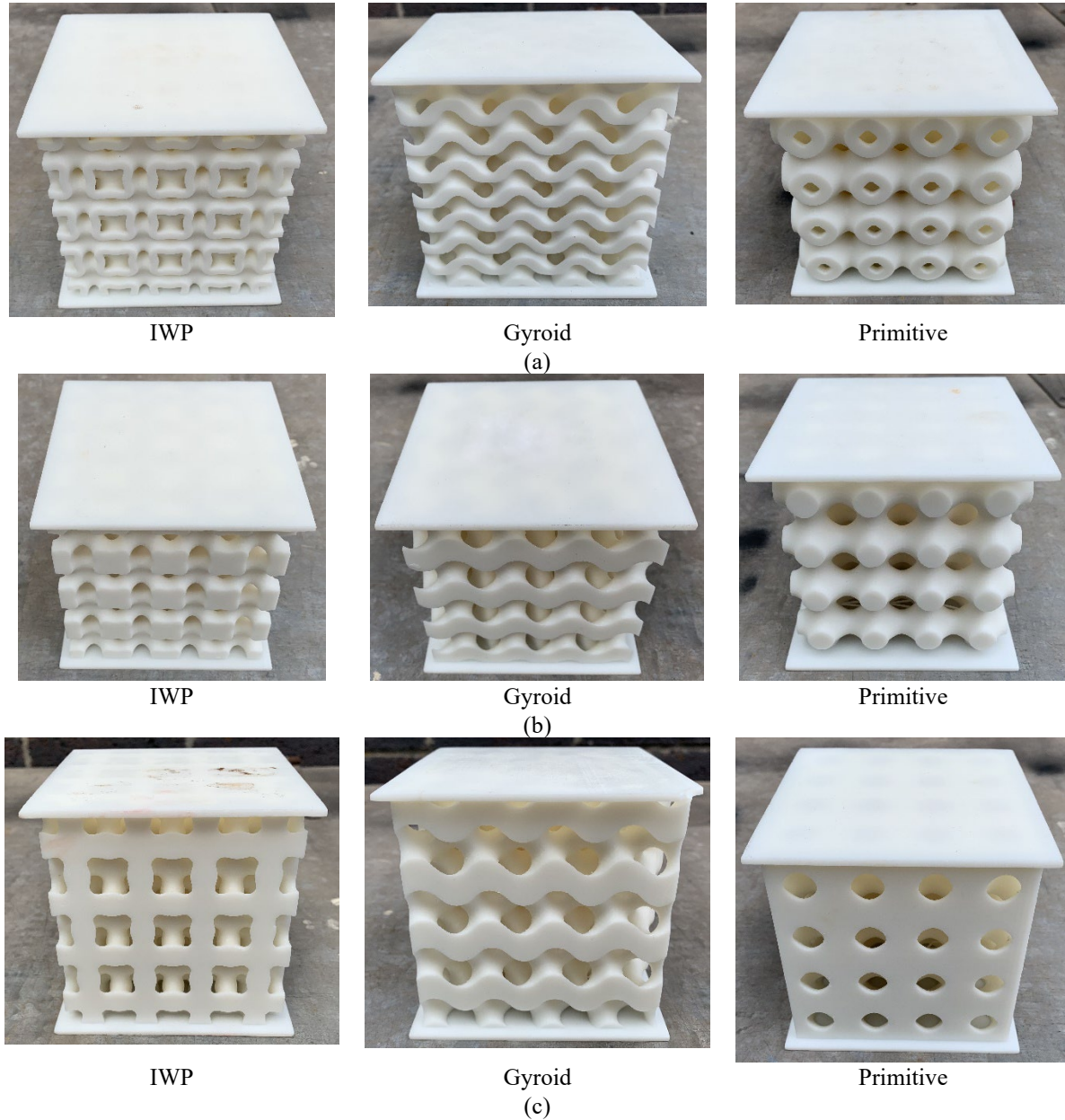


Figure 6.3 3D printed specimens of three classes of TPMS structures in a 4×4×4 arrangement of IWP, Gyroid and Primitive designs. (a) sheetal type, (b) main solid type and (c) secondary solid type.

Given the significant impact of material printing procedures on the structural performance of the fabricated specimens, a uniform printing protocol is adhered to for all TPMS structures to

minimize variability attributed to the printing process. Figure 6.3 displays examples of the printed specimens, showcasing the precision and consistency achieved through this meticulous fabrication approach.

6.3 IMPACT HAMMER TEST

The modal analysis through impact hammer testing is widely utilised for assessing the vibrational characteristics of structural elements, conforming to the ASTM-C215 standards [156-158]. This method is instrumental in identifying the dynamic attributes of specimens under conditions that closely mimic their operational environment. It advocates for the emulation of boundary conditions akin to actual service scenarios, resorting to a free-free condition when replication of real-life conditions is infeasible. Particularly for TPMS structures, which are envisaged as support layers in civil and railway infrastructure, the primary load-bearing mechanism is predominantly vertical. Consequently, the analytical model is simplified as a single degree-of-freedom (SDOF) system in vertical direction to closely simulate real-world dynamics. A notable potential railway TPMS infrastructure, aimed at enhancing the performance under impact loads, is depicted in Figure 6.4 (a). The support layers in such applications are primarily subjected to vertical dynamic loads emanating from the wheel loads [159-162]. The incorporation of a porous TPMS layer serves a dual purpose: mitigating vibrations and absorbing energy, while simultaneously ensuring sufficient vertical support stiffness for the overlaying structures. This approach justifies the adoption of SDOF system to elucidate the dynamic behaviour of TPMS structures, as illustrated in Figure 6.4(b).

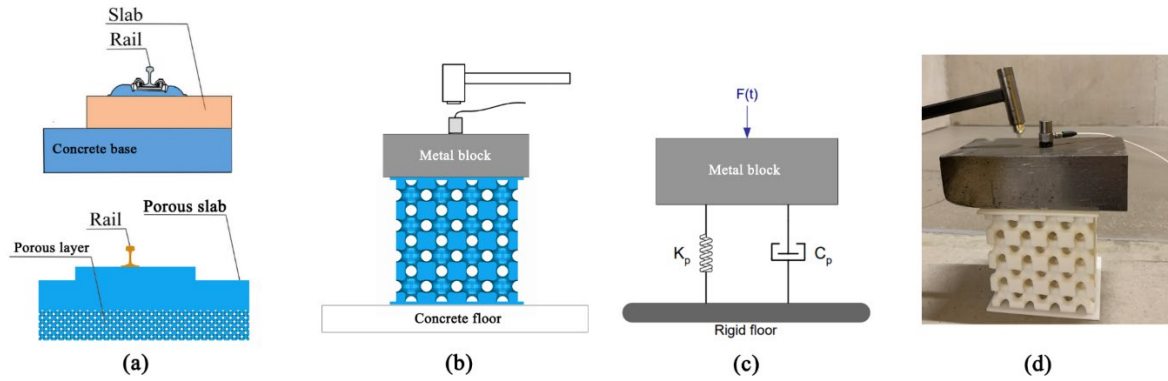


Figure 6.4 Impact hammer tests of TPMS structures. (a) a potential TPMS support in railway tracks; (b) schematic illustration test setup, (c) conceptual illustration of the test setup and (d) an actual test image.

The experimental setup, designed to mirror practical track support conditions and examine the structural response of the TPMS track beds under impulse load, is elucidated in Figure 6.4(c). Following the methodology outlined in [163], specimens are positioned on a concrete base to replicate a stiff platform, topped with a metallic block to which an accelerometer is centrally affixed. The modelling of the test configuration is further detailed in Figure 6.4(d), highlighting the practical assembly of the setup. The accelerometer, characterised by a sensitivity of $1.02 \text{ mV}/(\text{m/s}^2)$, spans a frequency range from 1 to 7000 Hz and can measure accelerations up to $\pm 4905 \text{ m/s}^2$ peak. The vibrational excitation of the specimens is facilitated by a PCB 086D05 hammer, boasting a sensitivity of 2.25 mV/N , measurement range up to 22240 N. The mass of the hammer is 0.32 kg. The sampling rate is 4096 Hz. The execution of dynamic SDOF tests employs the DATS 7.0 software, coupled with a P8004 data acquisition device, from PROSIG Ltd. as demonstrated in Figure 6.5.

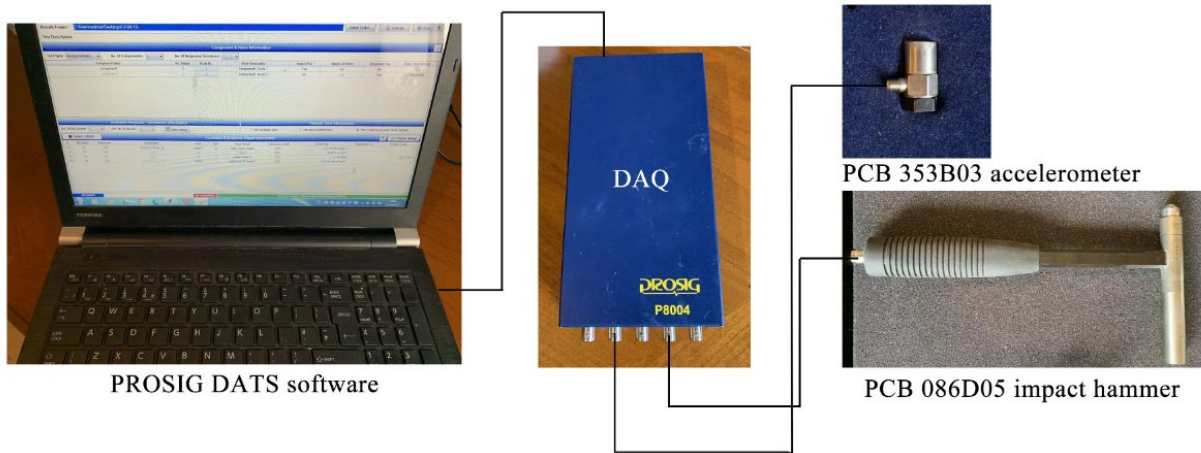


Figure 6.5 Instruments for impact hammer testing from PROSIG Ltd.

The Single-Degree-of-Freedom system is a fundamental concept in dynamics and vibration analysis, representing the simplest form of a mechanical system that can only move in one specific manner or direction [164]. This means it has one natural mode of vibration and requires only one coordinate to describe its motion completely. Examples of a SDOF system includes mass element attached to stiffness element with damping element, where the motion is either translational or rotational about one orientation [165, 166]. The equation of motion for an undamped SDOF system originates from Newton's second law of motion or from energy principles and is given by Equation 6.1. For a damped SDOF system, the equation includes a damping term, and it becomes Equation 6.2. In these two equations, m is the mass, \ddot{x} is the acceleration (the second derivative of displacement x with respect to time t), k is the stiffness of the spring, x is the displacement from the equilibrium position, and $F(t)$ is the external force applied to the system as a function of time.

$$m\ddot{x} + kx = F(t) \quad 6.1$$

$$m\ddot{x} + c\dot{x} + kx = F(t) \quad 6.2$$

For an underdamped SDOF system subjected to a very short duration of input force excitation, the response can be considered as a free vibration after the initial impulse. This is because the external

force $F(t)$ effectively becomes zero after the brief excitation period, leaving the system to vibrate freely under its own inertia and the restoring force of the spring, with the damping force acting to gradually reduce the amplitude of oscillation over time. The equation of motion for such an underdamped free vibration system is derived from the general equation for a damped SDOF system, omitting the external force term as shown in Equation 6.3 to Equation 6.5. This second-order linear differential equation describes the damped oscillation of the system. The term $2\zeta\omega_n$ represents the damping coefficient, and it's related to the rate at which the oscillations decay. The term ω_n^2 means the stiffness of the system, which are related to the speed of oscillation. The solution to this equation will involve exponential decay functions multiplied by sinusoidal functions, reflecting the oscillatory nature of the system with gradually decreasing amplitude. The precise form of the solution would depend on the initial conditions of the system, specifically the displacement $x(0)$ and the velocity $\dot{x}(0)$. The constants in the solution will be determined based on these initial conditions. The ω_n is the natural frequency in radians per second, K_p is the stiffness of the spring (or the proportional constant), and M is the mass of the system. The natural frequency f_n in hertz (Hz) is related to ω_n by the factor 2π since ω_n is the frequency in radians per second and there are 2π radians in one oscillation.

$$m\ddot{x} + c\dot{x} + kx = F(t) \quad 6.3$$

$$\ddot{x} + 2\zeta\omega_n\dot{x} + \omega_n^2x = 0 \quad 6.4$$

$$\omega_n = \sqrt{\frac{K_p}{M}} = 2\pi f_n \quad 6.5$$

An example of the results for MS-IWP structures is listed in Figure 6.6 (a) and (b), showing the impulse load, $F(t)$, and the corresponding acceleration, \ddot{x} . The determination of the natural frequencies within the examined system is achieved by identifying the oscillation frequencies

within the acceleration response. Utilising Fast Fourier Transform (FFT) method facilitates the transposition of the acceleration response into the frequency domain, thereby enabling the identification of the natural frequency from the apex in the FFT graph. Figure 6.7 presents a set of FFT curve examples, obtained from the acceleration records pertinent to the MS-IWP structure. Through scrutiny of the frequency domain's acceleration curve peaks, the inherent resonant frequency for each experiment of the MS-IWP specimens is ascertainable. The recorded resonant frequencies for a set of four evaluations stand at 107 Hz (for the initial two tests), followed by 109 Hz, and culminating at 111 Hz, in sequential order. The peak force excitations corresponding to these frequencies are quantified as 138.1 N, 157.3 N, 110 N, and 66.66 N.

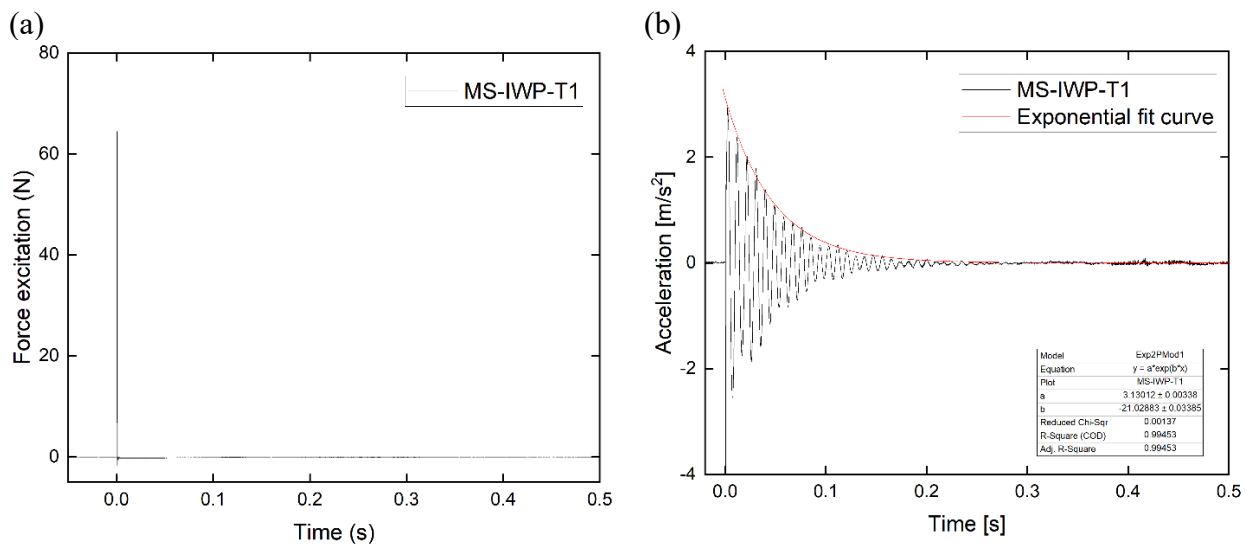


Figure 6.6 Illustration of data from an impact hammer test on the MS-IWP structure (a) impulse load in the time domain and (b) acceleration response in the time domain.

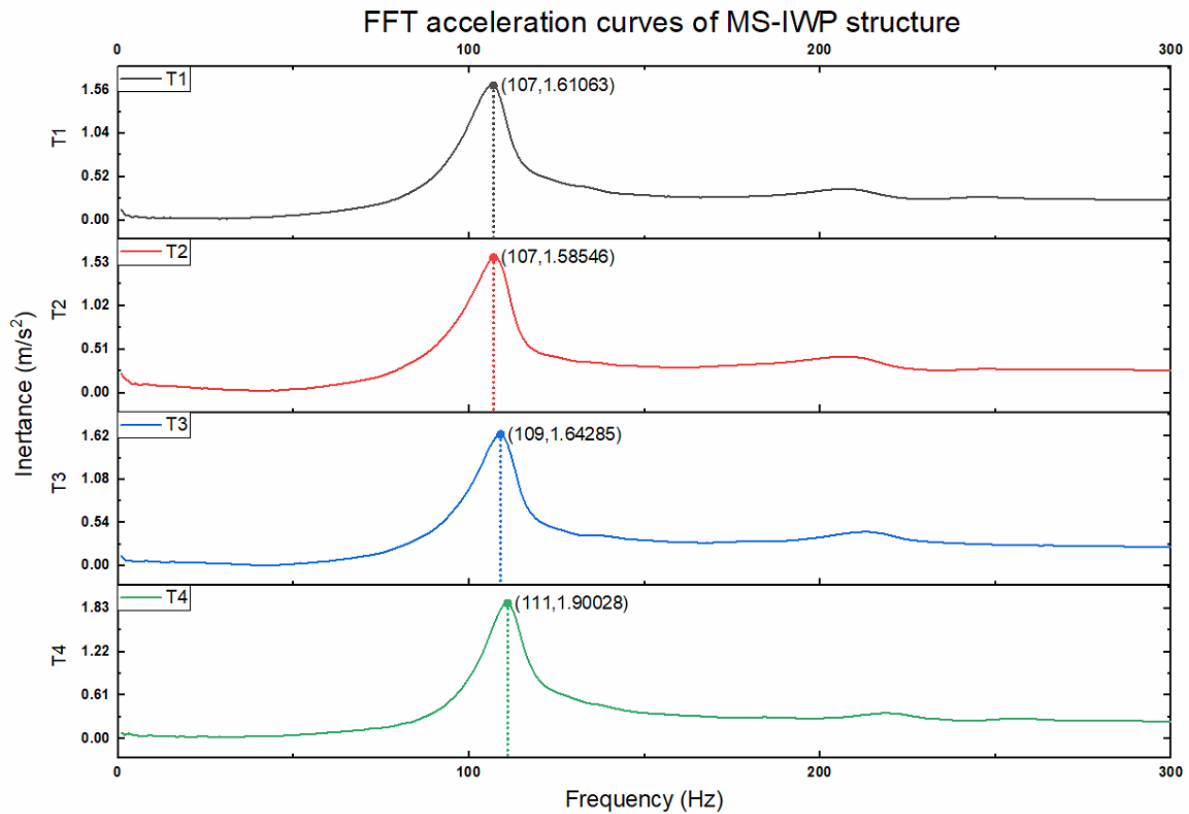


Figure 6.7 Acceleration responses in frequency domain from a set of four evaluations on the MS-IWP structure.

The methodologies of Exponential Curve Fitting (ECFM) [167, 168], Logarithmic Decrement (LDM) [169-172], and Half-Power Bandwidth (HPBM) [173-176] serve the purpose of estimating a system's damping ratio. An analytical comparison is undertaken to scrutinise the outcomes derived from each technique. The ECFM and LDM, in particular, depend upon the acceleration graph in the time domain.

The Exponential Curve Fitting Method (ECFM) for damping ratio estimation is a technique used to analyze the free decay response of a system to fit an exponential decay model to the time-domain data. This method is particularly useful when dealing with systems that exhibit a rapid transient response followed by an exponential decay, such as mechanical systems after being struck or electrical circuits after a surge. The typical model used for curve fitting in ECFM is as Equation

6.6 and Equation 6.7. Here $x(t)$ is the displacement at time t , A is the initial amplitude, ζ is the damping coefficient, ω_n is undamped resonant angular frequency, $\omega_d = \omega_n\sqrt{1 - \zeta^2}$ is the damped natural angular frequency, f_n is the natural frequency, and ϕ is the phase angle. A common approach for curve fitting is to use nonlinear least squares methods, which iteratively adjust the parameters to minimize the error between the model and the data. Figure 6.6(b), an illustration is provided showcasing the acceleration response of the MS-IWP structure, alongside a curve fitted exponentially, expressed mathematically as $y = ae^{bx}$. The calculation of the damping ratio, ζ for this structure is derived from the equation $\zeta = -\frac{b}{2\pi f_n}$, where b represents the coefficient from the exponential fit.

$$x(t) = Ae^{-\zeta\omega_n t} \cos(\omega_d t + \phi) \quad 6.6$$

$$\omega_n = 2\pi f_n \quad 6.7$$

The Logarithmic Decrement Method is a quintessential technique for ascertaining the damping ratio (ζ) of a system exhibiting free vibrational decay. The method entails measuring the diminution in amplitude across successive oscillatory peaks. The logarithmic decrement (δ) is computed thus Equation 6.8. Herein, A_0 denotes the amplitude of the initial peak, A_n represents the magnitude after n full cycles, and n is the number of cycles between A_0 and A_n . Subsequently, the damping ratio (ζ) can be approximated from δ for scenarios where the damping is relatively minor: $\zeta \approx \frac{\delta}{2\pi}$. This simplification holds when the damping ratio is significantly less than unity. For a more precise computation, particularly when the damping ratio is not insubstantial, the complete formula is imperative as Equation 6.10.

$$\delta = \frac{1}{n} \ln \left(\frac{A_0}{A_n} \right) \quad 6.8$$

$$\zeta \approx \frac{\delta}{2\pi} \quad 6.9$$

$$\zeta = \frac{1}{\sqrt{1 + \left(\frac{2\pi}{\delta} \right)^2}} \quad 6.10$$

The HPBM is a frequency domain technique used to estimate the damping ratio. It involves measuring the bandwidth of the system's response at half-power points, which are the frequencies at which the power of the response is half of the peak power. The damping ratio is then estimated based on the relationship between the bandwidth and the damping ratio. This method is particularly useful for systems where the frequency response can be measured accurately. For evaluating the damping ratio using the HPBM, the procedure involves identifying the frequency at which the magnitude of the system's frequency response is at a maximum (resonant frequency) and then finding the frequencies on either side of the resonance peak where the response drops to $1/\sqrt{2}$ (approximately 0.707) of the peak value, as shown in Figure 6.8. The damping ratio (ζ) can then be estimated using the following Equation 6.11. Here: f_1 and f_2 are the frequencies at the half-power points, f_n is the resonant frequency.

$$\zeta = \frac{f_2 - f_1}{2f_n} \quad 6.11$$

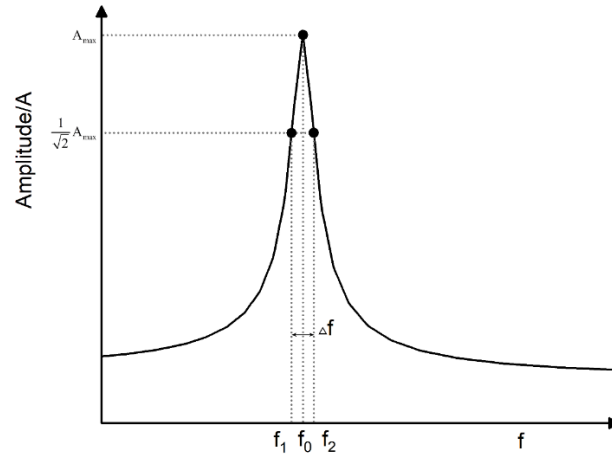


Figure 6.8 Employing the half-power bandwidth technique to deduce damping ratios.

6.4 NATURAL FREQUENCY

Utilising the methodology delineated in Figure 6.7, the determination of the natural frequencies across various TPMS structures has been conducted. The investigation encompasses the frequency analysis of nine porous structures of three TPMS designs under a spectrum of load intensities, with their respective outcomes illustrated in Figure 6.9 (a), (b), and (c). A comparative analysis of the linear relationship between the natural frequencies and the peak force excitations is depicted in Figure 6.9 (d), where the linear fit parameters and their standard errors (SE) are tabulated in Table 6.2. It is observed that TPMS structures exhibit a decrease in stiffness with the escalation of impulse load peak values, as evidenced by the negative slopes (a) across all TPMS configurations. The rate of the decrease in natural frequency varies according to the type of unit cell, indicating that structures with smaller absolute slope values (a) maintain more stable natural frequencies under fluctuating load amplitudes. A strong negative linear correlation between the natural frequency of TPMS structures and the amplitude of force excitation is suggested by Pearson's r , while the residual sum of squares (RSS) signifies the precision of the data points in relation to the linear fit line. Notably, both sheetal IWP and Gyroid structures demonstrate minimal RSS values,

implying a high data concentration around the fit curve and suggesting a robust resistance to positional changes of the load. Furthermore, the main solid IWP and Secondary solid Primitive types exhibit the most negligible slope values (a), indicative of a superior stability in natural frequency against load amplitude variations in contrast with other TPMS designs. In contrast, the main solid Gyroid and IWP type, the sheetal Primitive type and Secondary IWP type show a significantly higher rate of natural frequency decrease, over double that observed in main and secondary Primitive types. The intercept (b) parameter sheds light on the resonant frequency under minimal load conditions.

Table 6.2 Regression analysis specifics for the linear fit of natural frequencies.

TPMS structure		Intercept(b)		Slope(a)		Pearson's r	Residual Sum of Squares	Note
		Value	SE	Value	SE			
MS	IWP	111.98	5.55×10^{-1}	-2.91×10^{-2}	1.28×10^{-3}	-0.97	193.33	The linear fit function is $y = b + ax$
SS		111.25	5.08×10^{-1}	-3.02×10^{-2}	1.14×10^{-3}	-0.97	157.27	
SH		94.82	4.68×10^{-1}	-1.68×10^{-2}	9.25×10^{-4}	-0.95	124.86	
MS	Primitive	93.69	3.08×10^{-1}	-1.33×10^{-2}	6.88×10^{-4}	-0.95	52.08	
SS		92.43	6.45×10^{-1}	-1.29×10^{-2}	1.46×10^{-3}	-0.82	243.44	
SH		113.75	6.05×10^{-1}	-3.10×10^{-2}	1.38×10^{-3}	-0.96	209.96	
MS	Gyroid	103.27	5.11×10^{-1}	-3.18×10^{-2}	9.03×10^{-4}	-0.99	140.35	
SS		118.08	4.66×10^{-1}	-2.58×10^{-2}	9.53×10^{-4}	-0.98	125.54	
SH		99.98	2.48×10^{-1}	-1.65×10^{-2}	5.64×10^{-4}	-0.98	34.81	

Within the load range of zero to 1200 N, the secondary solid Gyroid type stands out with the largest natural frequency, underscoring its stiffness relative to other TPMS frameworks. It is highlighted that TPMS structures with initially larger resonant frequencies at lower load excitations tend to experience a more pronounced reduction in resonant frequency with the escalation of impulse force. This observation finds resonance with Elmadih's research, which noted a lower resonant frequency for the main Gyroid type compared to the sheetal Gyroid type in fully unrestrained conditions [102], and aligns with Simsek's findings that structures with equal relative densities, such as the three sheetal type TPMS structures display comparable first natural frequency ranges [100, 103].

Our study corroborates these insights, identifying similar patterns under loads between 1000 N and 1200 N.

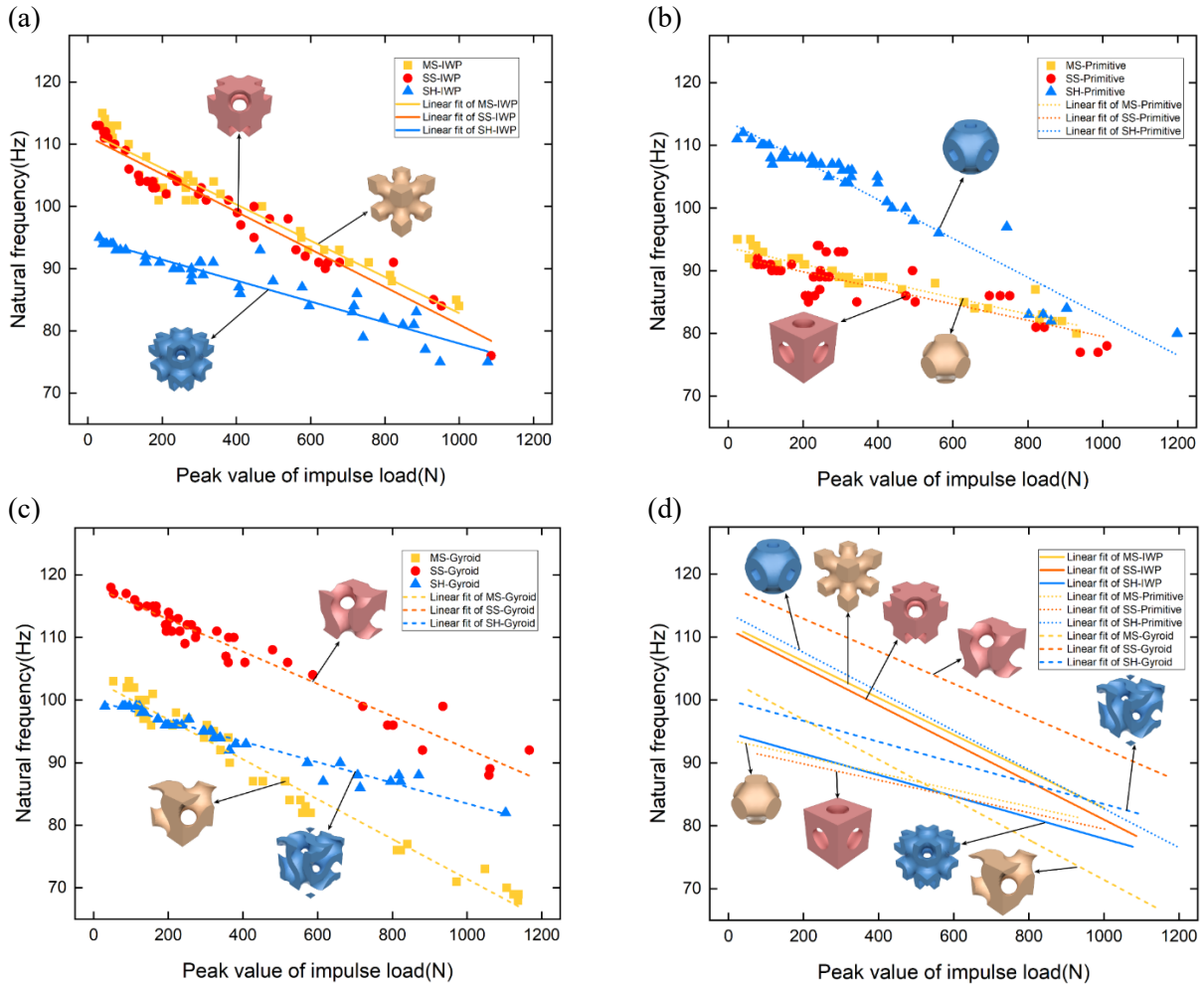


Figure 6.9 Natural frequencies and linear fits all TPMS designs. (a) IWP, (b) Primitive and (c) Gyroid and (d) all TPMS structures.

6.5 DYNAMIC STIFFNESS

Dynamic stiffness, a key parameter in civil engineering [177], is quantified as the quotient of applied load to the resultant displacement at the load-bearing surface, serving as a benchmark for evaluating the dynamic efficacy of structures. In the context of TPMS structures, dynamic stiffness is paramount for addressing dynamic loads in motion. As per the British Standard BS EN 29052-1-1992 [178, 179], the dynamic stiffness (k_p) of various TPMS configurations is computed

through Equation 6.12. Here, k_p denotes dynamic stiffness, f_n symbolises the resonant frequency, and m (5.73 kg) refers to the mass of the metallic cuboid utilised within the impact hammer testing framework.

$$k_p = (2\pi f_n)^2 m \quad 6.12$$

The dynamic stiffness values for nine TPMS structures, evaluated across varying load intensities, are depicted in Figure 6.10 (a), (b), and (c) respectively. Because stiffness exhibits a direct proportional relationship to the frequency squared, a parabolic fitting approach is employed to model the stiffness scatter plots. Comparative analyses of the stiffness against amplitude of the impulse force across all TPMS specimens are illustrated in Figure 6.10 (d), with the parabolic fit curve specifics delineated in Table 6.3. The chi-square reduced value serves to highlight the mean deviation of individual test outcomes from their respective fit curves, revealing a general trend of diminishing stiffness in response to escalating force levels. This pattern of stiffness aligns closely with that observed for natural frequency across the impulse force spectrum (0 N to 1200 N), with the secondary solid Gyroid structure manifesting the maximum stiffness throughout this range. Notably, the parabolic fit curves approach linearity within this load bracket, attributed to the minimal absolute values of the curve fitting parameters (n).

It is also observed that, with the exception of the sheetal IWP and Primitive structures, and the secondary Primitive structure, the stiffness changes of the other TPMS designs exhibit a decelerating rate of decrease. While structures such as the sheetal Gyroid and Primitive, and the two solid Primitive structures demonstrate relatively lower stiffness across the entire impulse force range, their stiffness profiles are notably more consistent with changing load amplitudes. This characteristic suggests a higher suitability of these structures for applications experiencing loads

with fluctuating magnitudes, ensuring a steadier dynamic response.

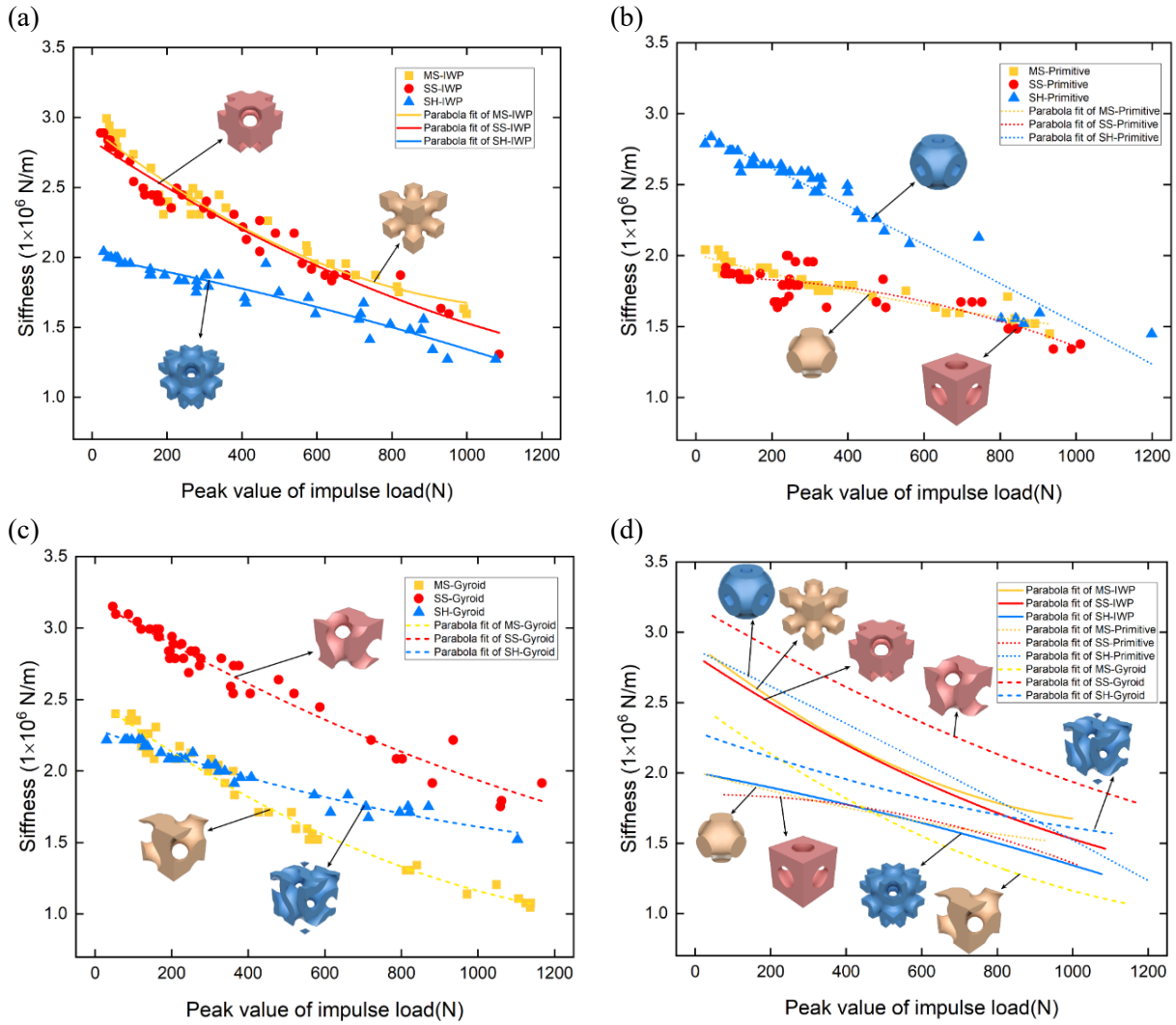


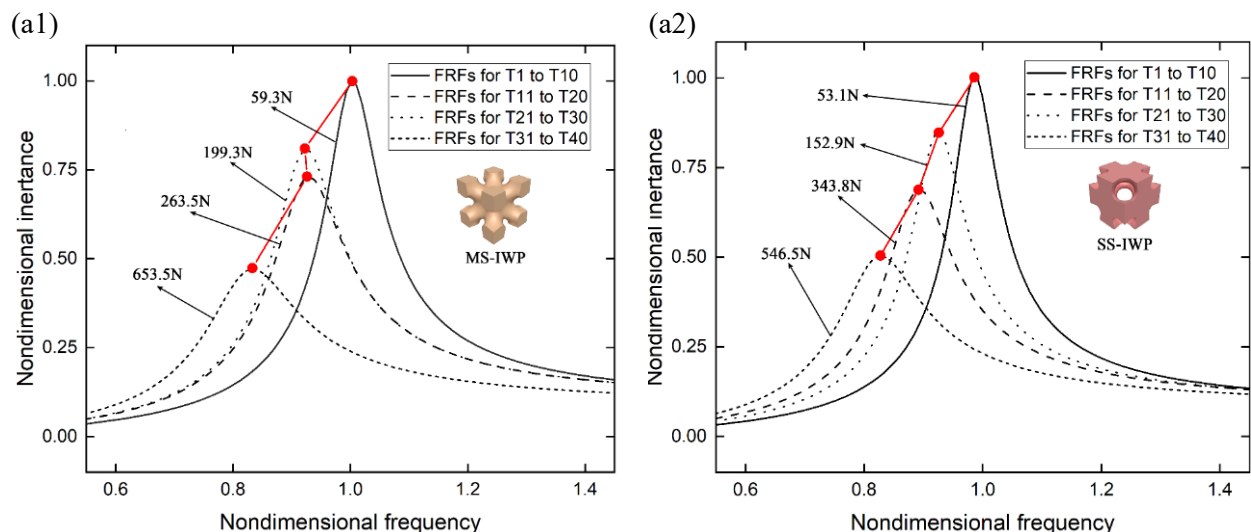
Figure 6.10 Scatter diagram of dynamic stiffness and parabolic fitting three classes of (a) IWP, (b) Primitive, (c) Gyroid and (d) all TPMS structures.

Table 6.3 Regression analysis specifics for Parabola fit of dynamic stiffness.

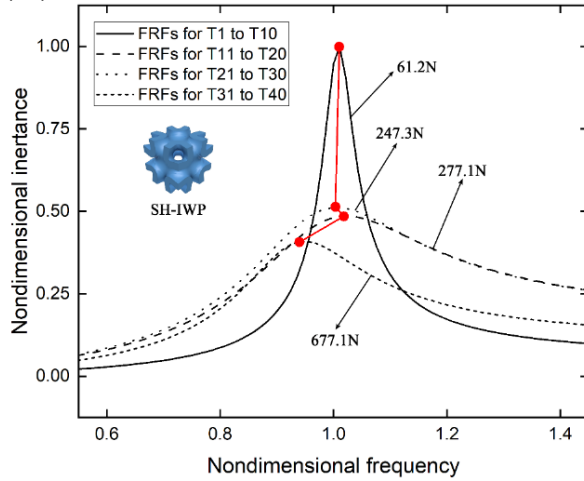
		m		l		n		Reduced Chi-Sqr
TPMS type		Val ue	SE	Value	SE	Value	SE	
MS	IWP	2.92	3.53×10^{-2}	-2.10×10^{-3}	2.09×10^{-4}	8.55×10^{-7}	2.19×10^{-7}	9.60×10^{-3}
SS		2.83	3.06×10^{-2}	-1.77×10^{-3}	1.65×10^{-4}	4.65×10^{-7}	1.68×10^{-7}	8.22×10^{-3}
SH		2.00	2.54×10^{-2}	-5.03×10^{-4}	1.38×10^{-4}	-1.57×10^{-7}	1.37×10^{-7}	4.68×10^{-3}
MS	Primiti ve	2.01	1.92×10^{-2}	-7.15×10^{-4}	1.08×10^{-4}	2.03×10^{-7}	1.13×10^{-7}	2.14×10^{-3}
SS		1.85	4.58×10^{-2}	2.64×10^{-5}	2.55×10^{-4}	-5.12×10^{-7}	2.44×10^{-7}	9.19×10^{-3}
SH		2.88	3.90×10^{-2}	-1.29×10^{-3}	1.93×10^{-4}	-6.80×10^{-8}	1.76×10^{-7}	9.64×10^{-3}
MS	Gyroid	2.50	2.91×10^{-2}	-1.95×10^{-3}	1.30×10^{-4}	6.11×10^{-7}	1.07×10^{-7}	4.55×10^{-3}
SS		3.19	3.80×10^{-2}	-1.58×10^{-3}	1.86×10^{-4}	3.24×10^{-7}	1.60×10^{-7}	6.90×10^{-3}
SH		2.29	1.53×10^{-2}	-9.53×10^{-4}	8.21×10^{-5}	2.71×10^{-7}	8.09×10^{-8}	1.34×10^{-3}
The parabola fit function is $y = m + lx + nx^2$								

The parabola fit function is $y = m + lx + nx^2$

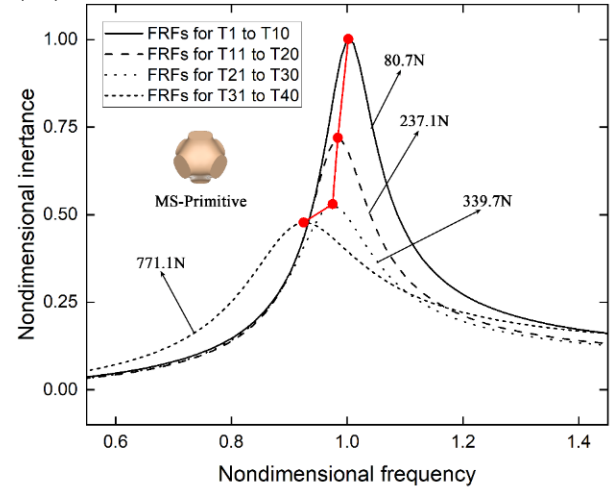
The yielding tendency within TPMS structures is further elucidated through non-dimensional analysis. Figure 6.11 delineates the Frequency Response Functions (FRFs) of these structures across a spectrum of load amplitudes, offering a distinct perspective from time-domain acceleration curves which depict the overall structural response. FRFs uniquely highlight the response of structures to a unit excitation, revealing a trend towards lower resonance frequencies, indicative of softening behaviour, as the excitation force escalates. Notably, structures such as the the three IWP structures and the main solid Primitive structure demonstrate a consistent natural frequency under load excitations not exceeding 200 N. Both the main and secondary IWP structures exhibit heightened sensitivity to variations in force excitation across the entire load range. An intriguing observation is the nondimensional acceleration responses of all nine TPMS structures to unit force excitation reduce with increasing impulse load amplitude. This reduction in dynamic reaction underlines the SDOF system's augmented capacity for energy dissipation, highlighting its potential for applications requiring enhanced energy absorption capabilities.



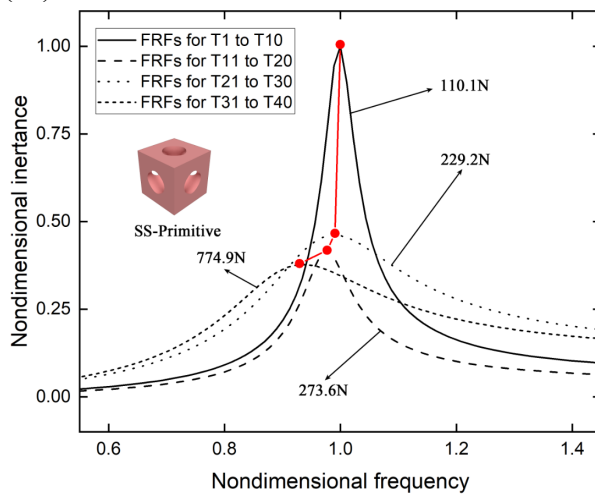
(a3)



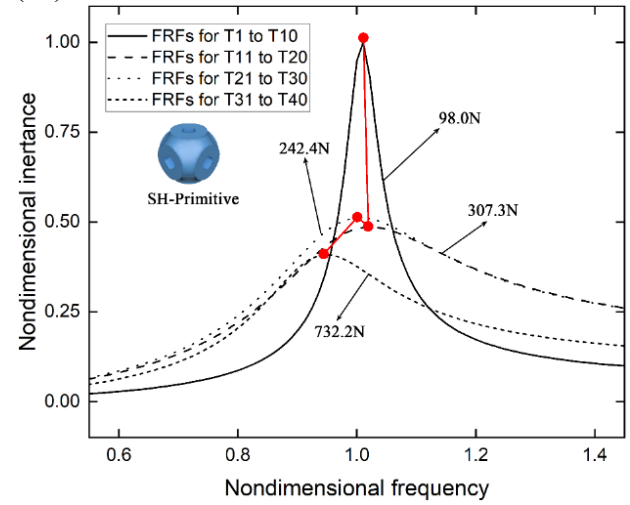
(b1)



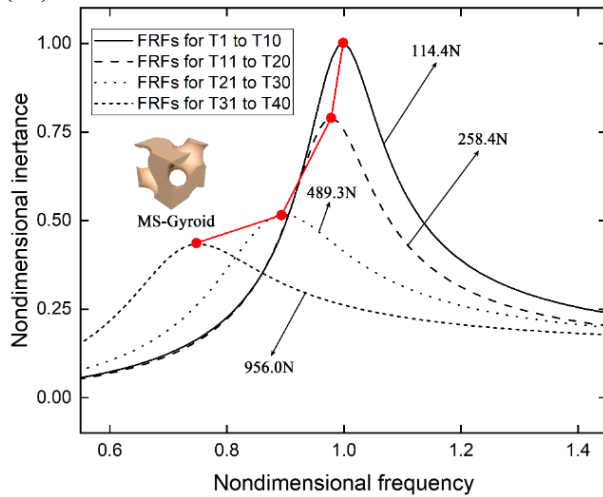
(b2)



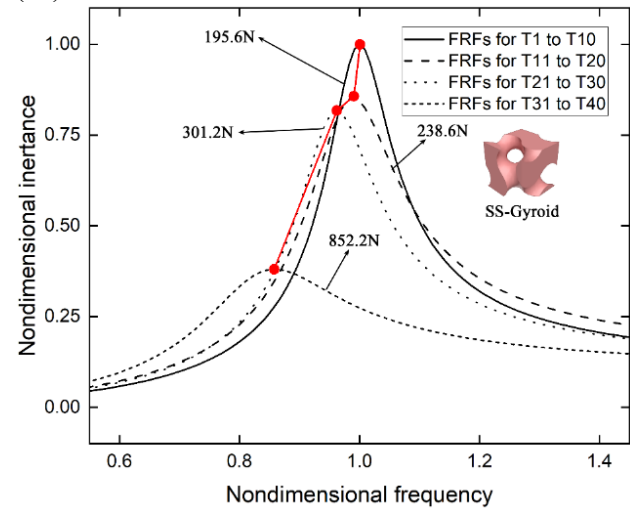
(b3)



(c1)



(c2)



(c3)

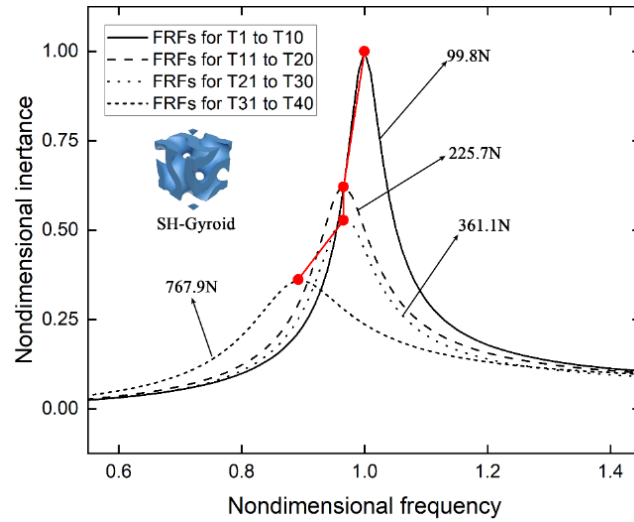


Figure 6.11 Frequency response functions in nondimensional form for the three classes of (a) IWP, (b) Primitive and (c) the Gyroid structures.

6.6 DAMPING RATIOS

To evaluate the damping properties of TPMS structures, various approaches including the ECFM, LDM and HPBM are adopted for the estimation of damping ratios. The comparison of damping ratios derived from these methods for the three classes of IWP structures is visualised in Figure 6.12 (a) to (c), showcasing both data point for individual tests and their regression curves. The efficacy of a structure's energy dissipation capability is directly correlated with its damping ratio, with higher values indicating superior performance. The evaluation reveals that the damping ratios ascertained through these diverse methods exhibit a consistent range and trend across the tested structures. To refine accuracy, mean damping ratios are calculated by averaging the estimates from all three methods, with the results and their corresponding fit curves under varying load excitations presented in Figure 6.13 (a) to (d). Observations indicate that the damping coefficients of numerous TPMS designs range from approximately 1.4% to 10.5%, demonstrating an increase in damping ratio with the escalation of load excitation, which can amplify two to threefold with the impulse force increment from zero to 1000 N.

Given that all the tested specimens are manufactured from the same photosensitive resin via an identical 3D printing process and possess mass and volume, it is inferred that variations in their mechanical properties are attributable to differences in geometric topology. Thus, the geometric configuration of the TPMS unit cells significantly influences both the value and the rate of change of the damping ratio, suggesting that tailored unit cell designs can achieve specific damping properties to meet diverse requirements.

Table 6.4 details the linear analysis regression parameters, with Pearson's coefficient indicating a robust direct linear correlation between the damping coefficient and the magnitudes of impulse loads. The residual sum of squares (RSS) reflects damping coefficient deviations from each test to the linear regression lines, whereas the gradient (a) signifies the rate of increase in damping ratio. Notably, the main solid Gyroid type exhibits the largest increase rate of damping ratio when the loads increase, approximately three times that of the sheetal Gyroid variant, indicating superior linear mechanical response to impulse loads for the sheetal Gyroid type. All the Gyroid variants demonstrates changeable energy dissipation capacity, with sensitivity to force excitation magnitude, while the sheetal Primitive shows the worst energy dissipation capacity at smaller force (below 400 N) and the sheetal Gyroid at larger excitation loads (above 400 N). Structures like the three classes of IWP designs and the main Gyroid design have negligible variance in damping ratios and rates of change across the full impulse load range. Typically, the main and secondary Gyroid variants offer superior damping coefficients in relation to alternative TPMS designs of the same mass and volume.

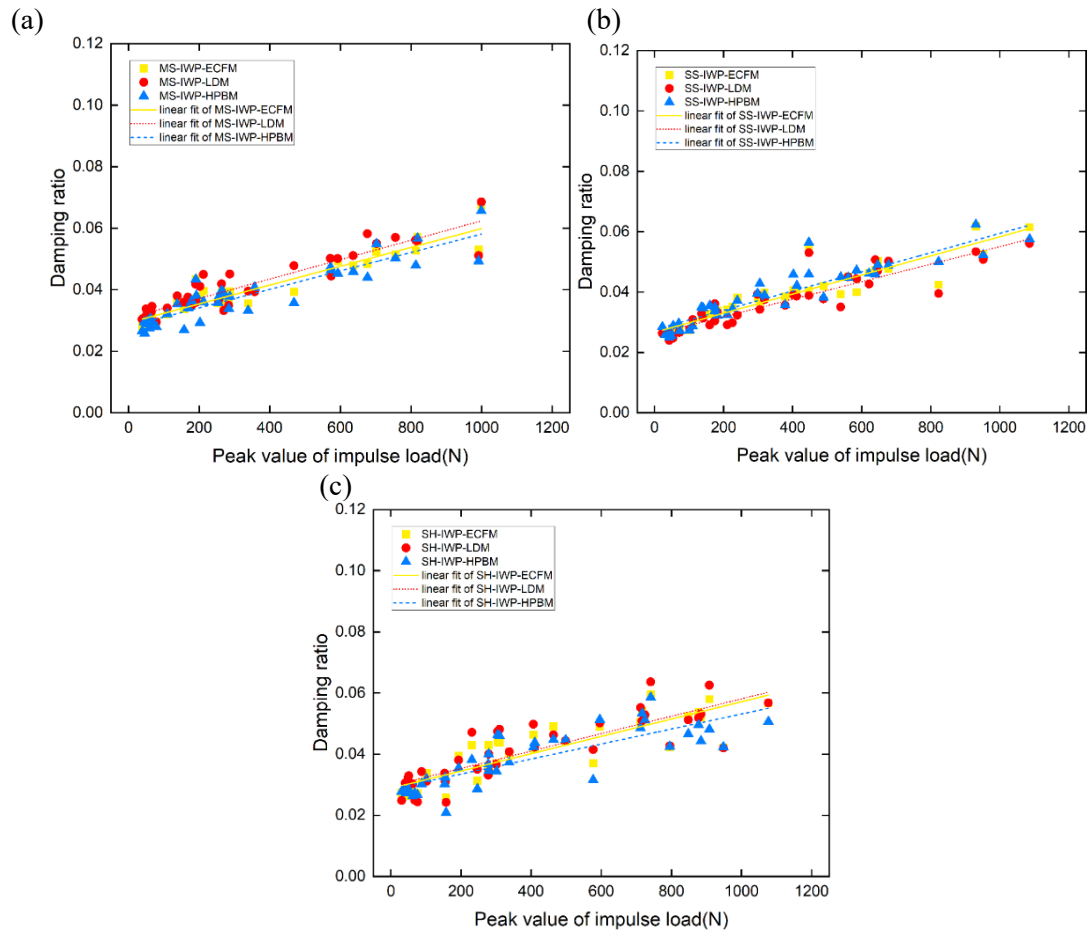


Figure 6.12 Evaluation of damping ratios for IWP designs by different methods for (a) main solid type, (b) secondary solid type and (c) sheetal type

Referencing previous study [180], a damping ratio of 3% is reported to mitigate 20–30% of dynamic responses, with ratios of approximately 4–5% necessary for significant vibration reduction. Consequently, all nine TPMS variants, barring the sheetal Primitive design, are deemed effective in vibration mitigation, with the main and secondary Gyroid types identified as particularly promising. Despite concrete being the predominant material in civil applications for its structural performance and corrosion resistance, its inherent low damping performance is a drawback for vibration reduction. Incorporating rubber into concrete, as suggested by various researchers [181, 182], significantly enhances damping ratios. For instance, the substitution of fine

aggregates with rubber particles resulted in a 156% increase in the damping ratio of concrete specimens [183]. With the advancement of 3D concrete additive manufacturing technologies, the creation of concrete structures featuring complex designs, such as the main and secondary Gyroid variants, offers a novel approach to improving concrete's damping properties.

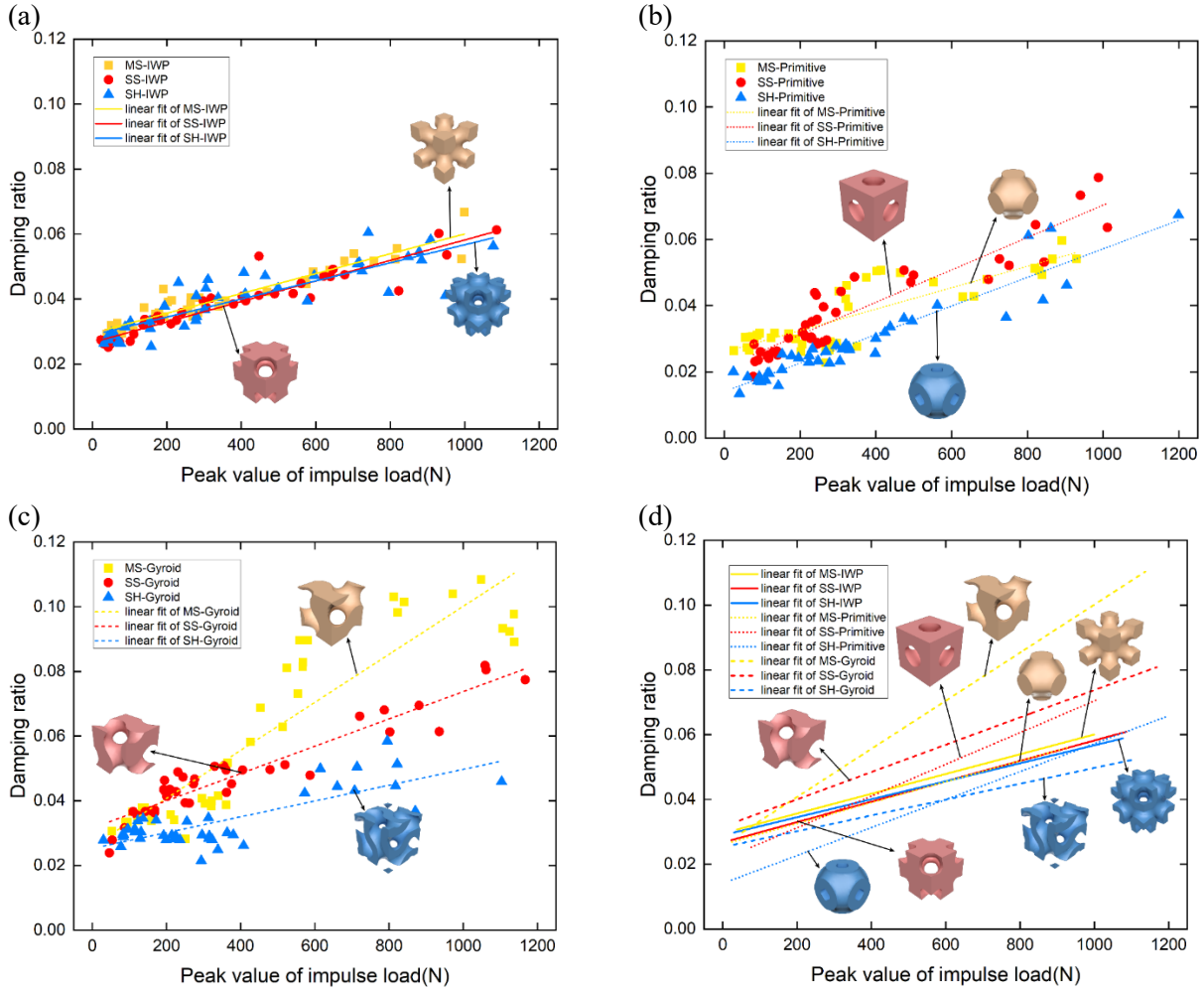


Figure 6.13 Evaluation of damping ratios and linear fit for all three classes of TPMS designs by different methods. (a) IWP, (b) Primitive, (c) Gyroid structures and (d) all nine variants.

Table 6.4 Regression analysis specifics for the linear fit of damping ratios.

TPMS structure		Intercept(<i>b</i>)		Slope(<i>a</i>)		Pearson's <i>r</i>	Residual Sum of Squares	Note
		Value	SE	Value	SE			
MS	IWP	2.95×10^{-2}	6.88×10^{-4}	3.05×10^{-5}	1.59×10^{-6}	0.95	2.97×10^{-4}	The linear fit function is $y = b + ax$
SS		2.67×10^{-2}	8.26×10^{-4}	3.15×10^{-5}	1.85×10^{-6}	0.94	4.16×10^{-4}	
SH		2.89×10^{-2}	1.31×10^{-3}	2.78×10^{-5}	2.58×10^{-6}	0.87	9.72×10^{-4}	
MS	Primitive	2.61×10^{-2}	1.57×10^{-3}	3.23×10^{-5}	3.52×10^{-6}	0.83	1.36×10^{-3}	
SS		2.15×10^{-2}	1.35×10^{-3}	4.89×10^{-5}	3.05×10^{-6}	0.93	1.07×10^{-3}	
SH		1.41×10^{-2}	1.10×10^{-3}	4.32×10^{-5}	2.51×10^{-6}	0.94	6.95×10^{-4}	
MS	Gyroid	2.59×10^{-2}	2.89×10^{-3}	7.42×10^{-5}	5.11×10^{-6}	0.92	4.50×10^{-3}	
SS		3.16×10^{-2}	1.12×10^{-3}	4.22×10^{-5}	2.28×10^{-6}	0.95	7.20×10^{-4}	
SH		2.53×10^{-2}	1.39×10^{-3}	2.45×10^{-5}	3.16×10^{-6}	0.78	1.10×10^{-3}	

6.7 CONCLUSION

TPMS based structures have emerged as encouraging unit cell designs across various domains, garnering significant interest for their mechanical attributes, particularly with the advent of additive manufacturing technologies. In the realm of civil engineering, the damping characteristics of structural components are vital for mitigating vibrations. Structures with inadequate damping ratios may exhibit exaggerated dynamic responses, potentially compromising safety. Despite extensive research into the structural response of TPMS structures to static and quasi-static loads, investigations into their dynamic performances have been relatively scarce, with their damping ratios, until now, remaining unexplored. The research gap has impeded the application of TPMS designs in civil constructions for vibration reduction purposes.

This pioneering study marks the initial foray into understanding the impact performances of various TPMS variants to the impulse force within a SDOF system, facilitated through dynamic response testing. The analysis encompasses the resonant frequency, damping coefficient, and dynamic stiffness of nine TPMS specimens with IWP, Gyroid and Primitive surface properties. A notable discovery is the effect of the geometric shape on the damping properties of the nine TPMS structures, offering new insights into their dynamic characteristics and assisting designer in

develop TPMS structures for impact load resistance. The findings yield several key insights.

The investigation reveals that TPMS specimens, manufactured using composite photosensitive resin, showing nonlinear structural stiffness and damping coefficients. A significant observation is the variation in natural frequency and damping ratio with excitation amplitude, where TPMS structures demonstrate increased softness and vibration-damping capability as excitation amplitude escalates.

The design of TPMS cellular units markedly influences how the natural frequency and damping ratios vary with the magnitude of the applied load. Constructs with elevated initial natural frequencies at minimal excitation forces are inclined to undergo more pronounced reductions in natural frequency with increased excitation magnitudes.

A parallel decrease in stiffness and natural frequency with increasing load amplitude is observed. In the nine TPMS variants, the secondary solid Gyroid design offers the greatest stiffness for the whole excitation amplitudes (zero to 1200 N). Nevertheless, the dynamic stiffness will diminish by 33% with the impulse force increasing from 100 N to 1000 N, with the main Gyroid variant experiencing a reduction exceeding 50%. Despite lower stiffness levels, the sheetal Gyroid and IWP, and the three Primitive variants maintain more stable rigidity levels when subjected to changing excitation amplitudes.

Regarding damping factors, most specimens, with the exception of the sheetal Primitive structure, having a damping coefficient exceeding 0.03 under force magnitudes greater than 400 N. The sheetal Gyroid design, in particular, showcases the largest damping coefficient within the 500 N to 1000 N load amplitude range, making it a preferable choice for achieving enhanced vibration

damping in practical applications. The sensitivity of damping ratios to excitation amplitude is pronounced, with ratios at higher load amplitudes being at least twice those at lower amplitudes.

Understanding how damping ratios and stiffness change with load allows engineers to design structures that are more resilient to dynamic stresses such as vibrations, shocks, and impacts. For instance, in earthquake-prone areas, buildings with higher damping ratios can dissipate more energy from seismic activities, reducing the likelihood of structural failure. The next chapter is going to further study the feasibility of TPMS structures into railway infrastructures.

CHAPTER 7

FEASIBILITY OF TPMS

STRUCTURES AS RAILWAY

SUPPORT LAYERS

7.1 INTRODUCTION

This chapter has embarked on an in-depth exploration of the TPMS structures' potential as supporting layers within railway systems, employing a synergistic methodology that intertwines the Discrete Element Method (DEM) and the Finite Element Method (FEM). The model crafted for this purpose delineates three key components: the subgrade layer, the support layer, and the sleepers, thereby providing a comprehensive representation of a railway track's structure.

Delving into the realm of TPMS support layers, the study introduces six variants based on the IWP, Primitive, and Gyroid surfaces, each engineered with a keen eye on both main skeletal and secondary skeletal configurations. This selection reflects a strategic choice aimed at examining a spectrum of structural behaviours under load. A pivotal aspect of this investigation is the model's concentration on a singular sleeper range, a decision driven by the computational demands of accurately simulating the complex TPMS structures. This approach not only optimises computational resources but also, crucially, maintains the model's focus on the periodic nature of railway systems, thereby enhancing the analysis's relevance to practical applications.

Within the simulations, the coupling between the granular units and finite elements is facilitated through a Wall-Zone Coupling Scheme, a sophisticated technique that ensures the seamless transmission of forces and torques across the model's discrete and continuous domains. This integration is pivotal for capturing the nuanced interactions at play within the track's structure, particularly under the conditions of large strain scenarios which the simulations are specifically configured to accommodate. Initial loading experiments, simulating the downward motion of

sleepers, lay the groundwork for a series of analyses aimed at elucidating the TPMS structures' load-bearing and energy absorption capacities. Notably, the study reveals that TPMS layers based on the Primitive configuration exhibit the most robust support, both in terms of stiffness and energy absorption, a finding that underscores the critical role of material distribution and structural design in determining a support layer's efficacy. The examination of internal stress distribution within the subgrade further reinforces the Primitive structure's superior performance, with a stress distribution analysis indicating a consistent symmetry reflective of the railway system's inherent design characteristics. Moreover, the detailed assessment of contact forces within the TPMS layers provides valuable insights into the forces' transmission mechanisms, highlighting the differences in force distribution patterns among the various TPMS configurations and their implications for the support layer's load-bearing capabilities. This chapter uses some parameter from Paper 5, 7 and 9 as mentioned in the list of publication.

7.2 COUPLED DEM AND FEM MODELS

7.2.1 Model description

To explore the efficacy of TPMS structures as support layers in railway applications, this chapter employs an integrated approach using both the Discrete Element Method (DEM) and the Finite Element Method (FEM). The constructed model comprises three principal components: the subgrade layer, the support layer, and the sleepers, as illustrated in Figure 7.1. The dimensions of the subgrade are specified as 11.6 m in width and 8m in height. The sleepers are modelled as rectangular prisms, with dimensions of 0.185 m in height, 0.28 m in width, and 2.6 m in length.

For the purposes of numerical simulation, six varieties of TPMS support layers are designed,

drawing upon the IWP, Primitive, and Gyroid surfaces and incorporating both main skeletal and secondary skeletal configurations. The TPMS support layers are characterised by a thickness of 0.2 m and a width of 3 m. In contrast to existing studies that construct extensive track models for simulation purposes, the complex nature of TPMS structures necessitates a focus on a single sleeper range to manage the computational intensity attributed to the structural complexity. Railway systems are inherently periodic, with the arrangement of multiple sleepers and tracks exhibiting a repetitive pattern. Consequently, a single sleeper and its immediate surroundings can often serve as a representative unit of the entire system, enabling the extrapolation of the system's overall performance from the behaviour of this unit. By constraining the scope of the model, computational resources can be utilised more efficiently, facilitating rapid iteration and analysis. This is particularly critical for providing decision support within the engineering design and optimisation processes.

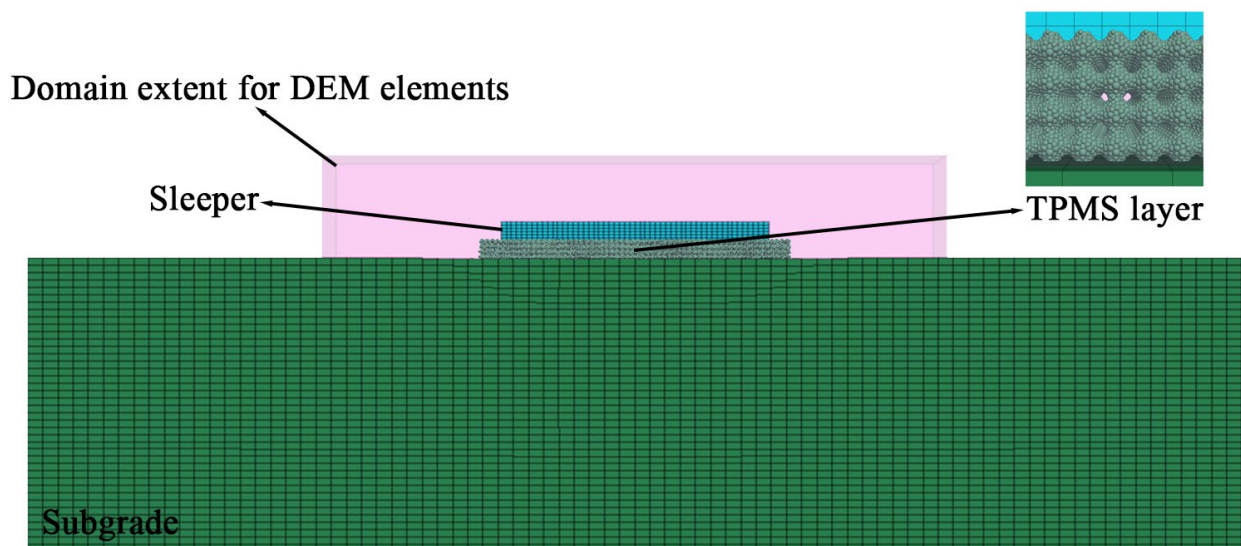


Figure 7.1 An example of track model with TPMS supporting layer.

7.2.2 Model properties

In the construction of the railway track model, the sleepers and the subgrade are simulated using the Finite Element Method (FEM) with zone elements, which are interconnected by grid points. The modelling of the sleepers employs an isotropic elastic constitutive model [184, 185], whilst the subgrade is represented using the Mohr-Coulomb constitutive model [186-188]. The subgrade is discretised into elements along its width, height, and longitudinal direction, numbering 85, 40, and 45, respectively. Conversely, the sleepers are comprised of 52, 6, and 5 elements along the same respective axes. The model parameters for both the sleepers and the subgrade are detailed in Table 7.1, with reference to [189] for the underlying data.

Table 7.1 Parameters for sleeper and subgrade.

Parameters	Sleeper	Subgrade
Density (kg/m ³)	2700	1800
Elasticity modulus (N/m ²)	25×10^9	45×10^6
Friction angel	-	30
Poisson's ratio	0.3	0.33
Cohesion strength (N/m ²)	-	5000
Dilation angel	-	10

The simulation approach for the TPMS layer in this chapter is analogous to the methodology delineated in Chapter 5, utilising breakable clusters for representation. However, a distinctive aspect for the TPMS structure's simulation is the reduction in the quantity of ball elements within the unit cell, tailored to accommodate the complexity of the support layer. The TPMS layer's simulation draws upon the IWP, Primitive, and Gyroid surfaces, incorporating both main skeletal and secondary configurations. The simplified TPMS units are depicted as Figure 7.2. The IWP, Primitive, and Gyroid unit cells in both main and secondary forms are constituted by 190, 158, 171, 167, 170, and 167 ball elements respectively. The rationale behind this simplification is to expedite the simulation process. On the subgrade, the unit cells are arranged according to the

dimensions of the support layer and are interconnected using parallel bonds, with the parameters for the Parallel Bond Model (PBM) presented in Table 7.2.

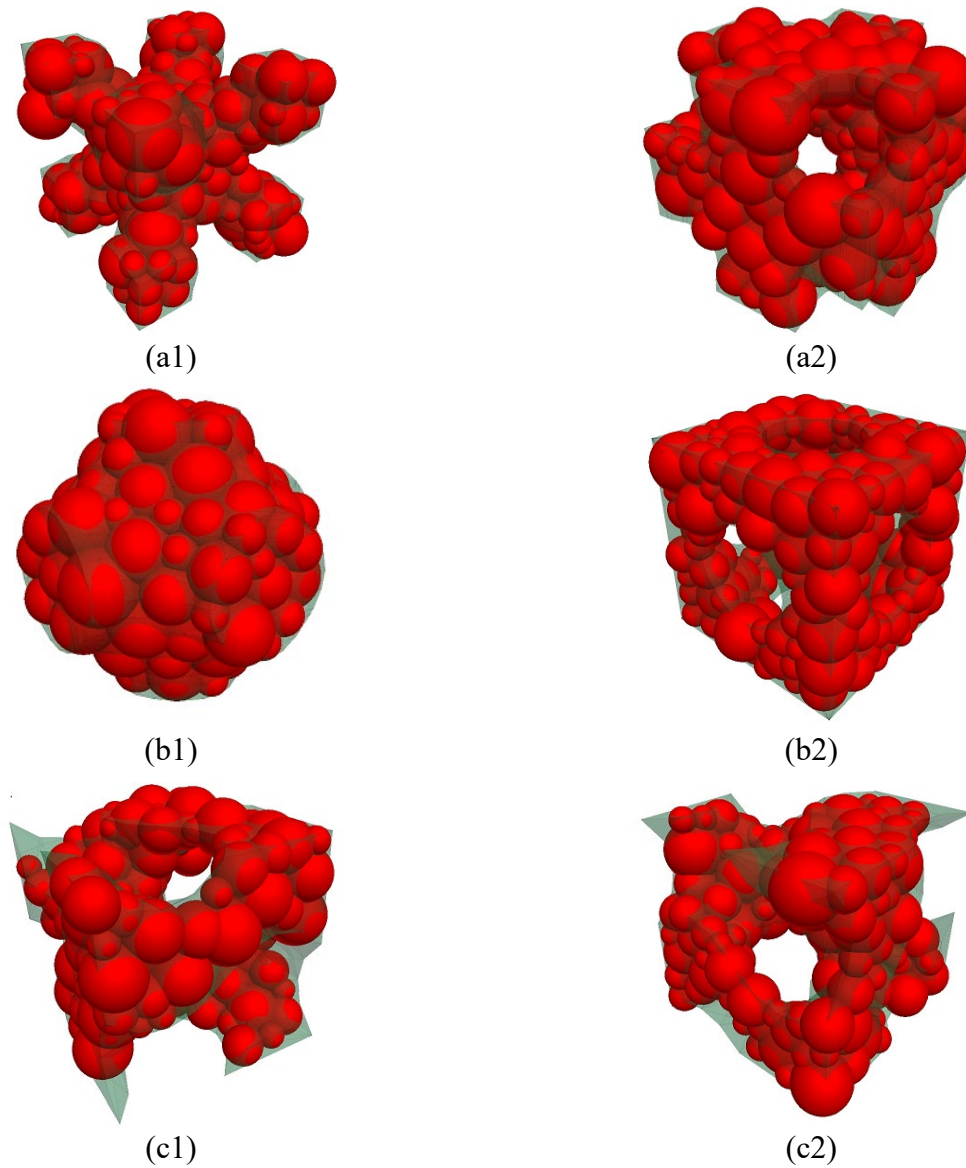


Figure 7.2 DEM modelling of TPMS unit cells used for main (1) and secondary (2) TPMS track supporting layers. (a) IWP (b) Primitive and (c) Gyroid.

Table 7.2 Parameters for DEM TPMS supporting layers.

Parameters	Ball elements	LCM	PBM
Density(kg/m ³)	1160	Auto-updated	Auto-updated
Friction	0.3	0.3	0.3
Young's modulus (N/m ²)	2.6e9	2.6e9	2.6e9
Poisson's ratio	0.42	0.42	0.42
Reference gap, g_r (m)	0	0	0
Tensile strength, (N/m ²)	-	-	38~56e6
Shear strength, (N/m ²)	-	-	17~23e6
update mode	-	absolute	incremental

In the interface between the granular units and the finite elements within the railway track modelling, a Wall-Zone Coupling Scheme is employed to bridge the distinct elements. This methodology involves the utilisation of wall-zone commands to construct wall elements that encapsulate both the sleeper surfaces and the subgrade surfaces [190-192]. These encompassing walls are composed of numerous triangular surface facets, facilitating contact between the discrete element method (DEM) ball units and the finite element method (FEM) zone surface's triangular facets [193]. The mechanism of force and torque transmission is achieved through these triangular facets, which effectively relay these mechanical stresses to the grid points of the Zone elements, as illustrated in Figure 7.3. To ensure the dynamic engagement of the coupling throughout the simulation cycles, it is imperative to configure the mechanical calculations to accommodate large strain scenarios [194]. This is accomplished through the activation of the model's large strain mode via the "model large strain" command [195].

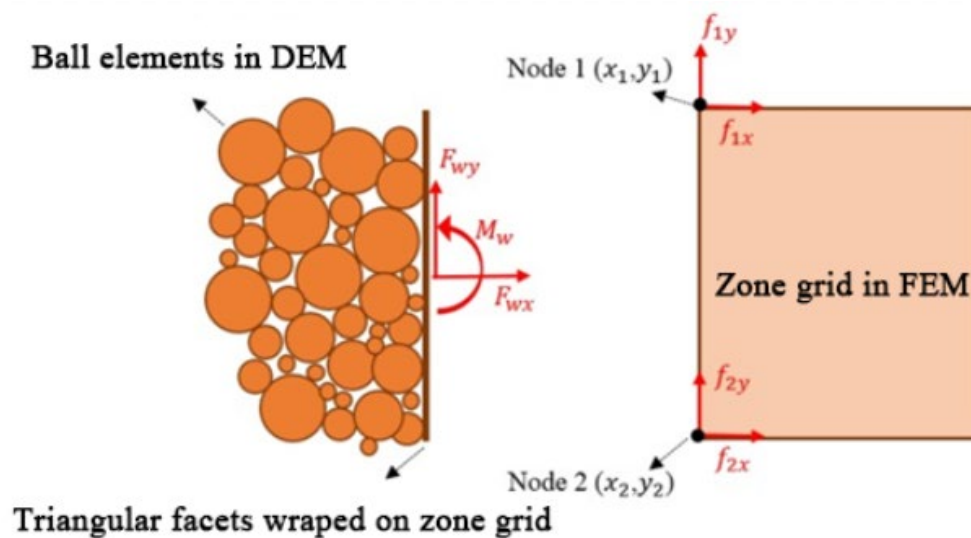


Figure 7.3 Force transfer from DEM elements to FEM elements.

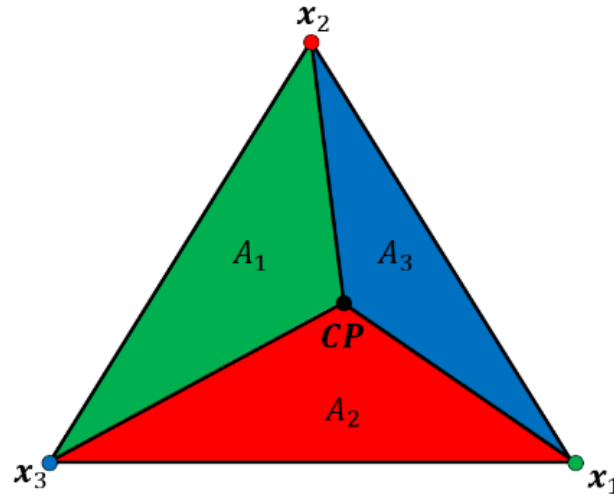


Figure 7.4 Introduction of the DEM and FEM coupling in a contact between a discrete element and triangle vertices.

In the discretised element method (DEM) interfaced with finite element method (FEM) elements, precise computation and application of forces between particulate matter and structural elements are paramount. The engagement points between a particle, such as a spherical entity and a triangular facet is characterised by determining the contact position (C) and the closest point on the facet (CP), as per the logic delineated in the PFC manual. Utilising barycentric interpolation/extrapolation, values from the point of contact CP are extrapolated to the vertices of the triangle, which coincide with the grid points or nodal points of structural elements, as shown in Figure 7.4, where the vertex positions are denoted as $x_i, i = 1 \dots 3$. The areas of the three sub-triangles formed by CP and the triangle's vertices are denoted as $A_i, i = 1 \dots 3$, with the total area of the triangle being $A = \sum_{i=1}^3 A_i$.

The weighting factor for each vertex is determined by the ratio of the corresponding sub-triangle's area to the total area, i.e. $w_i = \frac{A_i}{A}$, ensuring the sum of extrapolated values to vertices equals the value at CP. In the coupling of structural elements, contact forces and rotational stiffness are

extrapolated to nodes using this formula. However, it's pertinent to note that this method of extrapolation does not inherently guarantee physical congruence of the resultant forces and moments with the original contact forces/moments, as the total moment generated by the forces at the vertices may not balance the moment exerted at the contact point C. To address this, a comprehensive method for calculating an equivalent force system is introduced, ensuring the Equation 7.1 and Equation 7.2.

$$\sum F_i = F \quad 7.1$$

$$\sum r_i \times F_i = M \quad 7.2$$

Here F_i represents the forces at each grid point or node, F the contact force at point C, M the moment of the contact force, and r_i the vector from CP to the respective triangle vertex. This approach ensures that the distribution of forces and moments in the coupling of DEM and FEM not only adheres to physical principles but also aligns with the requirements of structural analysis.

7.2.3 Modelling procedures

To undertake a preliminary investigation into the performance of various TPMS structures as support layers within railway track systems, an initial model loading procedure is conducted. The loading methodology involved applying displacement loads to the sleepers. Specifically, a downward velocity of 1 m/s is imposed on 1560 finite elements' gridpoints constituting the sleepers. For the subgrade, the lowest layer of elements has been set to have a vertical velocity of zero as a boundary condition, effectively serving as a constraint. Additionally, periodic constraints are applied to the sides of both the subgrade and TPMS structures, facilitating the re-entry of particles or elements from one side of the domain to the opposite side. This technique is instrumental in

simulating systems that are infinite or exhibit repetitive patterns, thereby ensuring the continuity of motion throughout the model.

The forces and torques exerted on the surfaces of the sleepers and the subgrade are transmitted via wall elements created through the wall-zone command. This setup enabled the forces acting on the wall elements to be logged through custom commands. The displacement of the sleepers during loading could be monitored by tracking the movement of gridpoints on the sleepers. To maintain the fidelity of the simulation, the timestep is set to automatic, ensuring the precision of the computational analysis. Namura investigated the displacement of sleepers with different sizes and the results showed that the vertical settlements of the sleeper were less than 1cm when the load cycled 10000 times [196]. To evaluate the TPMS structures' performance, the loading process is terminated once the displacement of the sleepers reached 2 cm, which is doubled than Namura's research. Since the material properties of FEM components are from validated researches [184-188] and the DEM element parameters has been validated from previous chapter 5, this coupled DEM and FEM models can be used to qualitatively compare and analyze the performance of different TPMS structures as railway support layers.

This approach to modelling and analysis underscores the complexity involved in accurately simulating the dynamic interactions between the railway sleepers, TPMS support layers, and the subgrade, offering valuable insights into the potential of TPMS structures in enhancing the performance of railway track systems. Such an examination not only aids in understanding the mechanical behaviours of these innovative support structures under load but also contributes to the broader discourse on engineering design and optimization for railway infrastructure.

7.3 RESULT AND DISCUSSION

7.3.1 Load-Displacement curves

Figure 7.5 elucidates a comparison of the reaction force and longitudinal displacement curves for sleepers supported by different types of TPMS layers. A steeper curve gradient signifies greater longitudinal rigidity of the railway, indicating that a higher load corresponds to better support at the same displacement level. It is observed that the Primitive structure-based support offers the most effective reinforcement, followed by the IWP-based structure, with the Gyroid-based structure providing the least support. Specifically, the MS-Primitive configuration delivers the highest track stiffness, while the MS-Gyroid affords the lowest. The load-displacement curves for the SS-IWP, SS-Primitive, and SS-Gyroid under a displacement range of 0 cm to 2 cm show minimal variation, suggesting that these three structures offer comparable support as a track bed layer.

At a displacement of 0.5cm, the reaction forces for sleepers with MS-IWP, SS-IWP, MS-Primitive, SS-Primitive, MS-Gyroid, and SS-Gyroid support layers are respectively 1209 kN, 1367 kN, 1556 kN, 1455 kN, 1146 kN, and 1106 kN. At 1.0cm displacement, the forces are 2376 kN, 2020 kN, 2549 kN, 2411 kN, 1497 kN, and 1944 kN respectively. For a 2 cm displacement, the values are 4330 kN, 3446 kN, 4592 kN, 3572 kN, 3058 kN, and 3920 kN. These figures substantiate the discussion outlined above. From Figure 7.6, it is evident that the relationship between load and displacement is approximately linear, permitting the application of a linear fit method for curve fitting, with the parameters presented in Table 7.3. The slope, b , more directly indicates the track stiffness offered by different TPMS structures as support layers. It is noteworthy that, despite the

SS-Primitive structure's fitted slope b being smaller, its actual support stiffness should be calculated at a displacement of 2.0 cm. The fitting error results from higher load values in the smaller displacement range of 0 cm to 0.5cm, which lowers the slope of the fitted curve across the entire range.

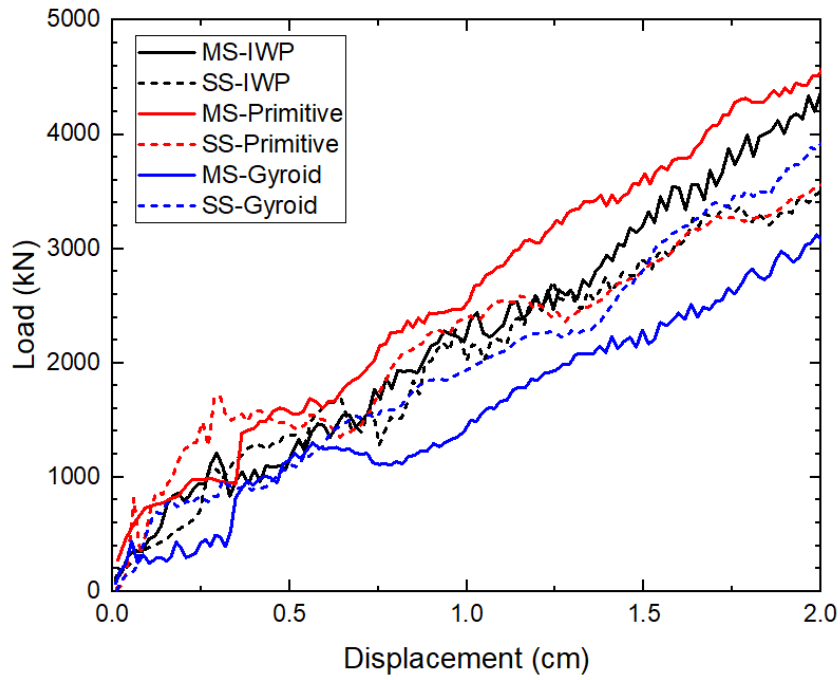


Figure 7.5 Load-Displacement curves of sleeper in the DEM simulation of TPMS tracks.

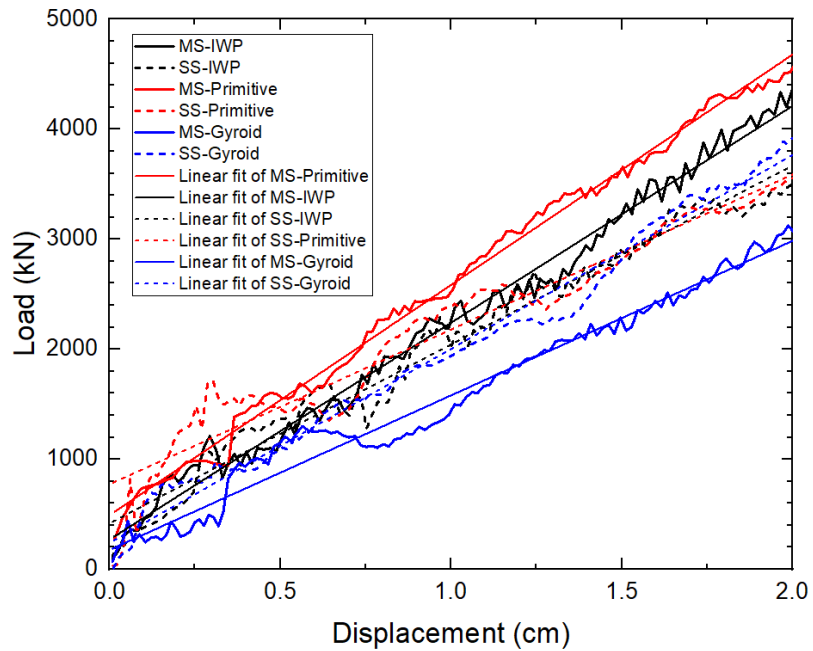


Figure 7.6 Linear fit of Load-Displacement curves for the DEM simulations of TPMS tracks.

By integrating the load-displacement curves, the energy absorption profiles for various TPMS support layers are elucidated, as demonstrated in Figure 7.7. It becomes apparent that TPMS structures offering superior support conditions generally exhibit enhanced energy absorption capabilities at equivalent sleeper displacements when serving as a sub-ballast layer. Specifically, support layers based on the Primitive configuration display the most pronounced vertical energy absorption capacity, followed by the IWP structure, with the Gyroid configuration being the least effective. Despite these six types of support layers possessing identical volume (relative density), discernible differences in their mechanical properties are observed.

Table 7.3 Linear fit details of Load-Displacement curves for the DEM simulations of TPMS tracks.

Equation		$y = a + bx$				
TPMS Type	MS-Primitive	MS-IWP	SS-IWP	SS-Primitive	MS-Gyroid	SS-Gyroid
Weight						
No Weighting						
Intercept a	490.68221 ±	270.38049 ±	417.41626 ±	771.76687 ±	175.02785 ±	240.60996 ±
	17.75159	23.32694	26.65183	35.07096	23.69408	20.64321
Slope b	2093.76076 ±	1970.11078 ±	1625.893 ±	1407.81396 ±	1405.08239 ±	1762.0004 ±
	14.83019	19.90776	23.41627	29.40787	20.63365	17.3444
Residual Sum of Squares	999542.47325	1809341.98535	3221888.63241	5693635.68254	2131874.19639	2408241.9885
Pearson's r	0.99703	0.99423	0.98688	0.97079	0.98741	0.99286
R-Square (COD)	0.99407	0.98849	0.97394	0.94243	0.97498	0.98577
Adj. R-Square	0.99402	0.98839	0.97374	0.94202	0.97477	0.98567

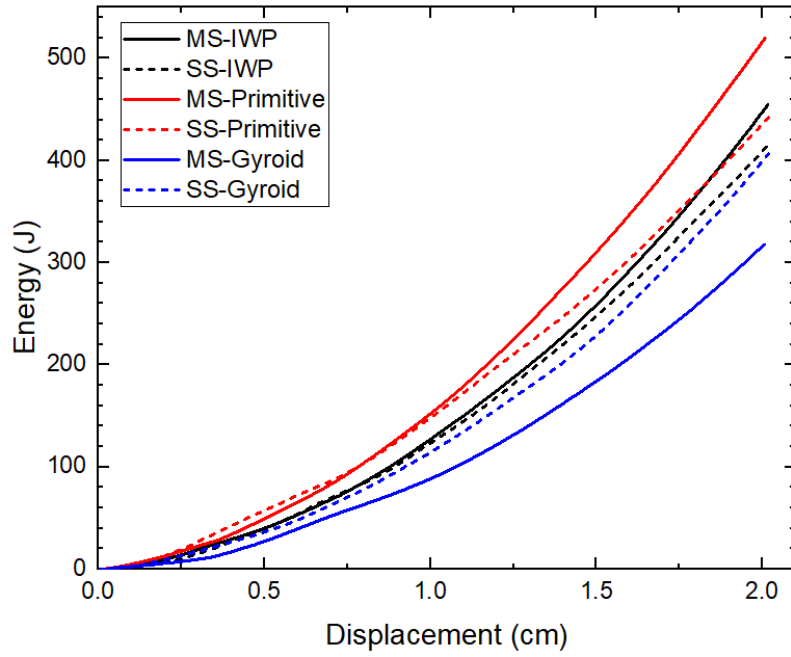


Figure 7.7 Energy absorption-displacement curves for the DEM simulations of TPMS tracks.

7.3.2 Stress distribution

Figure 7.8 contrasts the internal stress distribution within the subgrade at a vertical displacement of 2cm for sleepers, focusing on a cross-section through the centre of the sleepers for both Main and Secondary types of IWP, Primitive, and Gyroid railway tracks. It is observed that the stress distribution within the subgrade is largely uniform across the different types of TPMS support layers. Given the symmetric nature of the railway structure, the distribution of stress within the subgrade also exhibits symmetry, with the maximum stress occurring at the bottom near both ends of the sleepers and gradually diminishing along the depth. The maximum internal stresses recorded for the MS-IWP, SS-IWP, MS-Primitive, SS-Primitive, MS-Gyroid, and SS-Gyroid configurations are 2.74MPa, 2.40MPa, 2.97MPa, 2.44MPa, 2.17MPa, and 2.32MPa, respectively. A direct correlation is discernible between the maximum stress within the subgrade and the supportive force provided by the different TPMS layers, as discussed in the previous section.

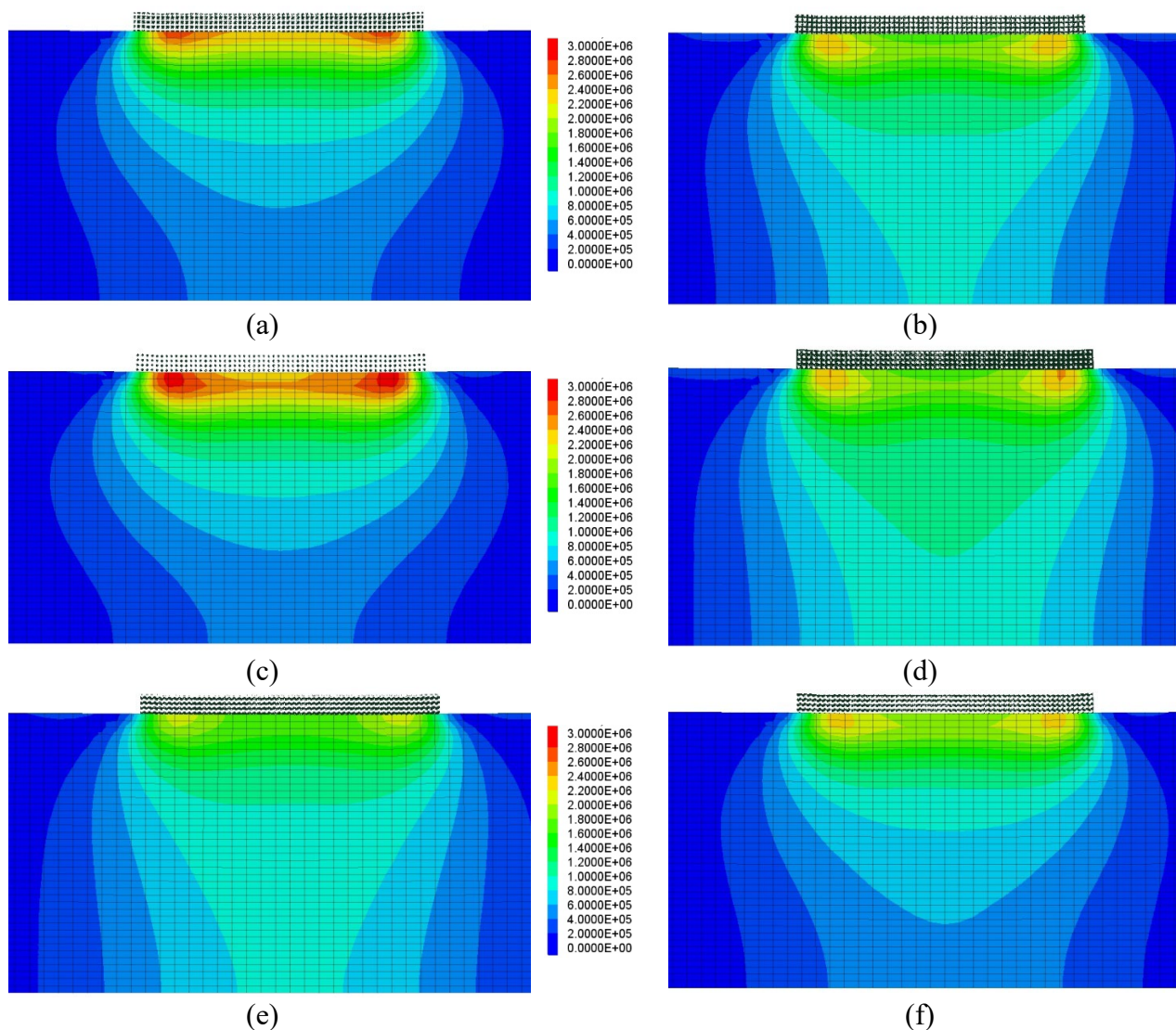


Figure 7.8 The Von Mises Equivalent stress distribution inside the subgrade in DEM modelling of TPMS tracks. (a) Main skeletal IWP type, (b) Secondary skeletal IWP type, (c) Main skeletal Primitive type, (d) Secondary skeletal Primitive type, (e) Main skeletal Gyroid type and (f) Secondary skeletal Gyroid type.

Table 7.4 presents a comprehensive breakdown of the contact details observed in DEM simulations of various TPMS support layers, correlating directly with the load-displacement characteristics illustrated in Figure 7.5. It is noted that TPMS layers with superior support capabilities also manifest higher average pressures at points of contact. Conversely, tension forces do not display a clear correlation with the load-bearing capacity. As the sleepers move downwards, the force exerted on the support layer is primarily transmitted through the internal pressure within the TPMS

structure. Taking MS-IWP as an example, with a sleeper displacement of 2 cm, the contact force beneath a central area of 20 cm \times 20 cm of the sleeper is depicted in Figure 7.9, where contact forces are represented by cylinders whose diameter is proportional to the magnitude of the contact force. This visual representation reveals that pressures are predominantly transmitted vertically, while tensile forces are disseminated laterally. This phenomenon occurs as the sleeper presses downwards, causing the sub-layer to spread outward on both sides, thus exhibiting characteristics of a positive Poisson's ratio.

Table 7.4 Specification of contact elements within coupled DEM and FEM TPMS track models at the sleeper displacement of 2 cm.

TPMS Type	Average compression force /N	Average tension force /N	Total compression contact amount	Total tension contact amount	Contact amount /each unit cell	Compressive contact amount /each unit cell	Tension contact amount /each unit cell
MS-IWP	43.08	-13.82	2120813	911923	317	736	317
SS-IWP	41.81	-17.28	1771445	709532	246	615	246
MS-Primitive	47.94	-17.96	2224711	857194	298	772	298
SS-Primitive	34.85	-16.45	2271562	885684	308	789	308
MS-Gyroid	38.03	-14.63	2133594	888483	309	741	309
SS-Gyroid	52.15	-19.42	1865052	809620	281	648	281

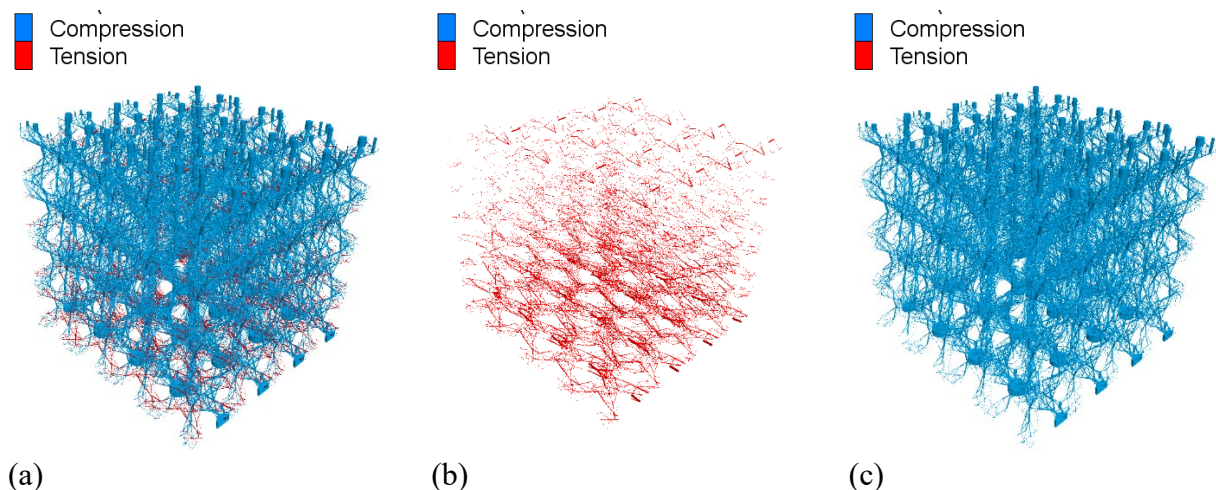


Figure 7.9 The contact force distribution inside the MS-IWP support layer beneath the center of the sleeper. (a) both the compression and tension force are plotted, (b) only the compression contacts are plotted and (c) on the tension contacts are plotted. All the contacted are scaled according to the force.

7.3.3 Force chain inside TPMS layer

Figure 7.10 illustrates the distribution of force chains within the TPMS support layer located beneath the central area of the sleeper, measuring 20cm by 20cm. It becomes evident that the transfer of contact forces within the Gyroid structure predominantly occurs along oblique paths, with only a minor portion transmitted vertically. This characteristic partially accounts for the Gyroid's relatively lower load-bearing capabilities as a railway track support layer. The density of the force chain distribution, particularly in the vertical direction, is most pronounced within the MS-Primitive structure. This feature underlines the superior performance of the MS-Primitive configuration across all six structures evaluated, in terms of both support stiffness and energy absorption capabilities. A closer examination of the microstructural level reveals distinct variations in the internal force distribution among the different types of TPMS support layers, highlighting the unique mechanical properties that each structure brings to the support of railway tracks. This nuanced understanding of force transmission within TPMS layers is crucial for optimising the design and implementation of these structures in railway infrastructure, ensuring that the selection of TPMS configurations is informed by their mechanical behaviours and load-bearing efficacies.

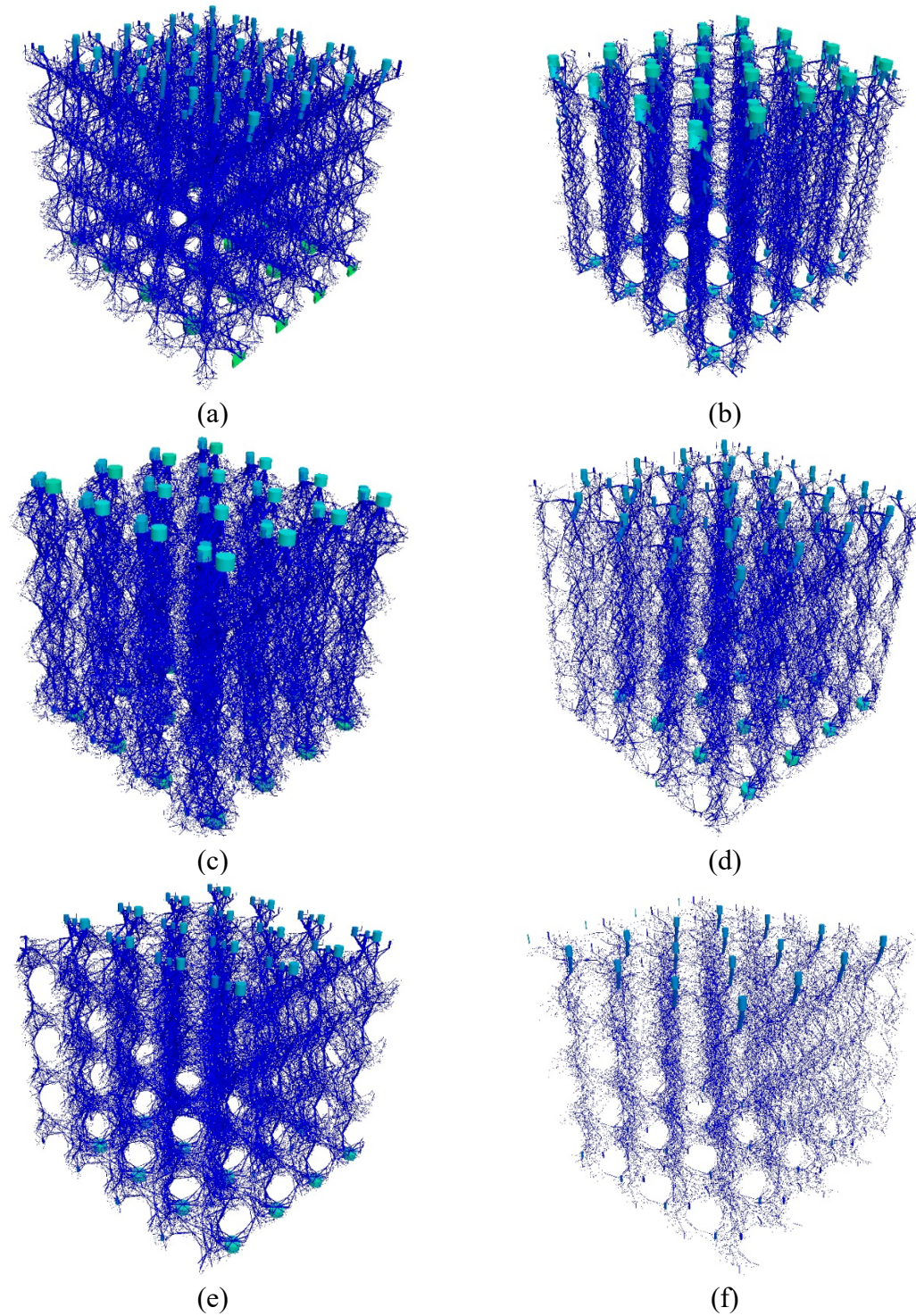


Figure 7.10 The contact force chain of the area beneath the center of the sleeper. (a) Main skeletal IWP type, (b) Secondary skeletal IWP type, (c) Main skeletal Primitive type, (d) Secondary skeletal Primitive type, (e) Main skeletal Gyroid type and (f) Secondary skeletal Gyroid type.

In further discussion, Figure 7.11 illustrates the transmission of force chains within different TPMS layers, with an emphasis on plotting only those contact forces exceeding the median value of

contact force magnitudes. This approach reveals that support is principally provided by the base of the sleeper as it moves downwards. The distribution density of forces in the central part of the TPMS support layer is less than that on either side. Despite minor differences in contact force distribution among various TPMS structures, the propagation of forces across all TPMS configurations exhibits a symmetric trapezoidal distribution in three-dimensional space. Compared to the IWP and Primitive structures, the internal force distribution within both variants of the Gyroid support layers is more uniform.

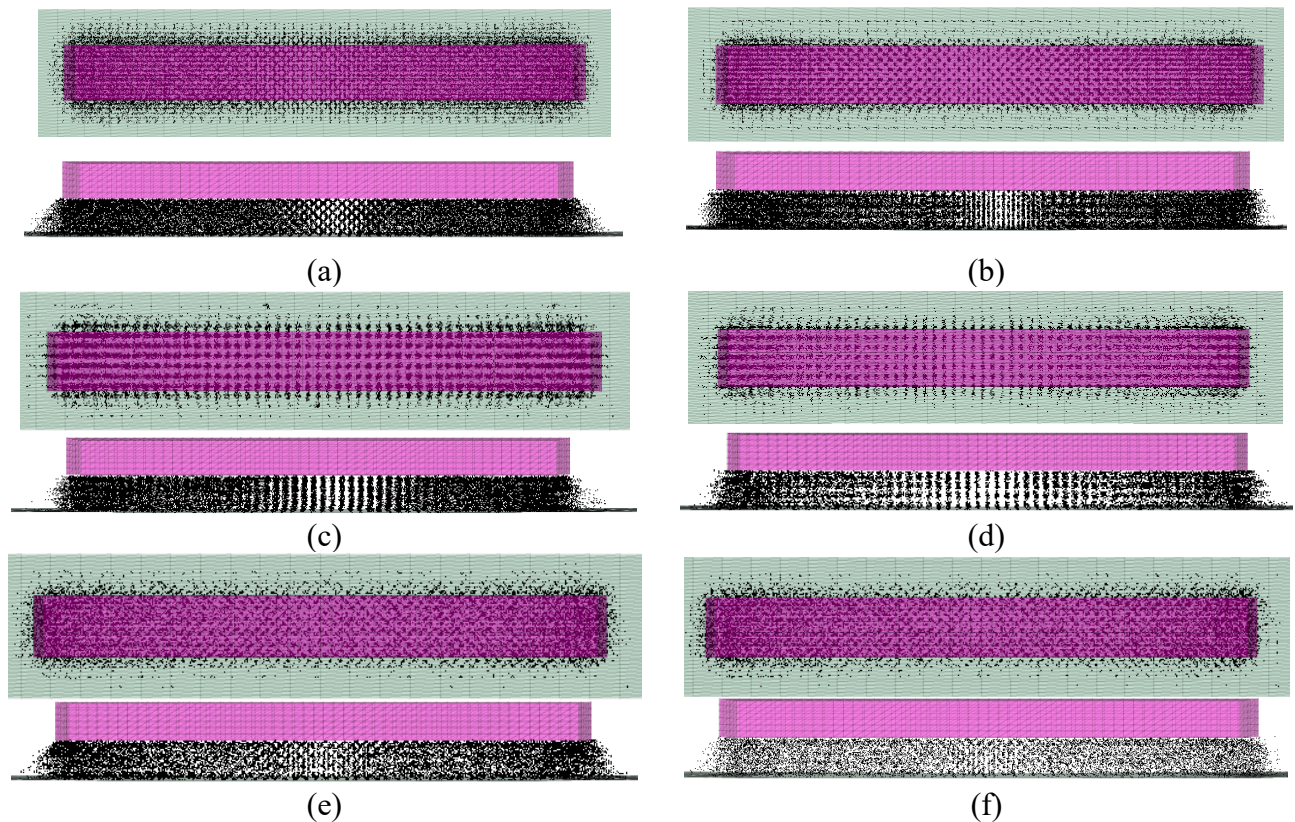


Figure 7.11 The contact force chain inside the TPMS layer from the top view and the front view. (a) Main skeletal IWP type, (b) Secondary skeletal IWP type, (c) Main skeletal Primitive type, (d) Secondary skeletal Primitive type, (e) Main skeletal Gyroid type and (f) Secondary skeletal Gyroid type.

7.4 CONCLUSION

This investigation delves into the application of TPMS structures as support layers in railway systems, integrating the Discrete Element Method (DEM) and Finite Element Method (FEM) to simulate the mechanical behaviour of various TPMS configurations under loads. Focusing on a select range of TPMS structures, including the IWP, Primitive, and Gyroid surfaces, the study examines their load-bearing capacity and energy absorption properties through meticulous modelling and simulation. The main findings are as below.

TPMS support layers based on the Primitive configuration offer the most effective reinforcement against vertical loads, outperforming the IWP and Gyroid structures. The MS-Primitive in particular provides the highest track stiffness, indicating that the structural design of TPMS layers plays a critical role in enhancing the mechanical resilience and performance of railway tracks. Across different types of TPMS support layers, the stress distribution within the subgrade remains largely uniform, showing symmetry that corresponds with the symmetric nature of the railway structure itself. This uniformity in stress distribution, with the maximum stress occurring at the bottom near both ends of the sleepers and gradually diminishing along the depth, underscores the effectiveness of TPMS structures in distributing loads within the subgrade, thereby potentially extending the lifespan of railway infrastructure. Microstructural analysis reveals distinct variations in the internal force distribution among the different types of TPMS support layers. Notably, the force transmission within the Gyroid structure predominantly occurs along oblique paths, contrasting with the more uniform and vertical transmission observed in the MS-Primitive structure. These differences in force transmission and distribution highlight the nuanced

mechanical behaviours of TPMS layers and underscore the importance of selecting the appropriate TPMS configuration for specific load-bearing and energy dissipation requirements within railway track systems.

This chapter and the previous chapters have studied the feasibility of TPMS structures with polymer properties as railway supports. The next chapter is going to study the performance of concrete TPMS structures under combined loads, since concrete-based materials are the most widely used construction materials.

CHAPTER 8

STRUCTURAL PERFORMANCE

OF CONCRETE TPMS

STRUCTURES UNDER

VARIOUS LOADS

8.1 INTRODUCTION

In the past few decades, the realm of layered fabrication, commonly referred to as three-dimensional fabrication, alongside its associated material science, has witnessed significant advancements, marking a departure from traditional manufacturing methods. These advancements have facilitated the creation of structures with complex geometries and enhanced material efficiency, propelling research into intricate macro-porous and micro-porous materials. Cellular structures, in particular, have garnered attention for their periodic architectural forms and advantageous mechanical properties, finding application across diverse fields such as biological engineering, aerospace, and robotics. These applications are primarily attributed to their notable structural strength, rigidity, and energy dissipation potentials, underscoring the promise these TPMS designs hold in the fields of civil engineering and design. The development and investigation of TPMS structures have further enriched this field, offering designs that mimic natural forms with three-dimensional interconnected pores, exhibiting superior mechanical properties over traditional lattice designs, including advanced static mechanical attributes when compared to newer lattice models.

In the context of civil engineering, the need for materials that are both cost-effective and exhibit superior mechanical and chemical properties is paramount. Building on the insights from previous chapters that explored 3D printed resin TPMS structures and concrete's established efficacy in widespread applications due to its excellent compressive strength, this chapter delves deeper into the integration of TPMS designs within concrete properties. The advent of three-dimensional concrete layering techniques has catalysed a transformative shift in construction methodologies, facilitating the creation of intricate porous designs and the incorporation of TPMS structures into

civil engineering applications.

This chapter focuses on the mechanical properties of concrete TPMS structures, which have garnered recognition as viable alternatives for load-bearing and energy-absorbing applications. These structures are celebrated not only for their mechanical robustness but also for their decorative capabilities, enhancing acoustic properties, aesthetic value, and structural lightness. However, despite the advantageous features of TPMS variants, their performance under the simultaneous application of compressive and torsional stresses remains insufficiently explored, highlighting a significant knowledge gap within the field. Accordingly, this chapter seeks to bridge this gap by scrutinising the structural integrity of cement-based TPMS structures when subjected to various magnitudes of combined stresses. This analysis is crucial for assessing their viability as structural components in scenarios typified by complex force interactions. This chapter is mainly based on Paper 4 as mentioned in the list of publication.

8.2 CONCRETE DEM TPMS MODELS

In this investigation, the DEM modelling is utilized for researching the structural responses of cement TPMS models, fabricated from fragile cementitious composite, when subjected to concurrent compressive and torsional stresses, such as the track components in curved lines. This chapter introduces an innovative DEM-based simulation technique for modelling concrete structures with intricate geometries. Through the application of two DEM built-in contact constitutive models, our approach facilitates the transmission of contact forces and moments, thereby enabling the simulation of fracture advancement in various TPMS constructs. To ensure the accuracy of the DEM simulation, the DEM models of the same Gyroid and Primitive designs are

developed from previous research [197], drawing upon their experimental outcomes. Subsequently, both DEM primary and secondary skeletal designs of the two TPMSs are constructed by these confirmed variables, and their mechanical performance is assessed when subjected to a spectrum of compression and torsion forces. This research marks the inaugural contrastive evaluation of the load-supporting potentials of concrete Primitive and Gyroid specimens under varied loading conditions. Furthermore, the effects of torsional stress on the axial load-supporting ability, alongside the influence of compressive stress on the torsional load-supporting capacity of these structures, are meticulously examined. The investigation concludes with an analysis of the fracture extensions observed in the four cementitious Primitive and Gyroid models, offering novel insights into their mechanical behaviour under dual-loading scenarios.

8.2.1 Geometry shape

Reference [197] produced the concrete blocks based on Gyroid and Primitive surfaces and then carried out compression tests as depicted in Figure 8.1. Accordingly, this paper constructs two analogous structures to validate the discrete element model, employing a methodology as previously outlined in Figure 3.6. Initially, MATLAB software is utilised for generating the stereolithography format documents corresponding to the two TPMSs. Figure 8.2 displays solid cellular unit of the main and secondary Gyroid and Primitive variants.



Figure 8.1 Concrete Primitive and Gyroid TPMS structures from [197].

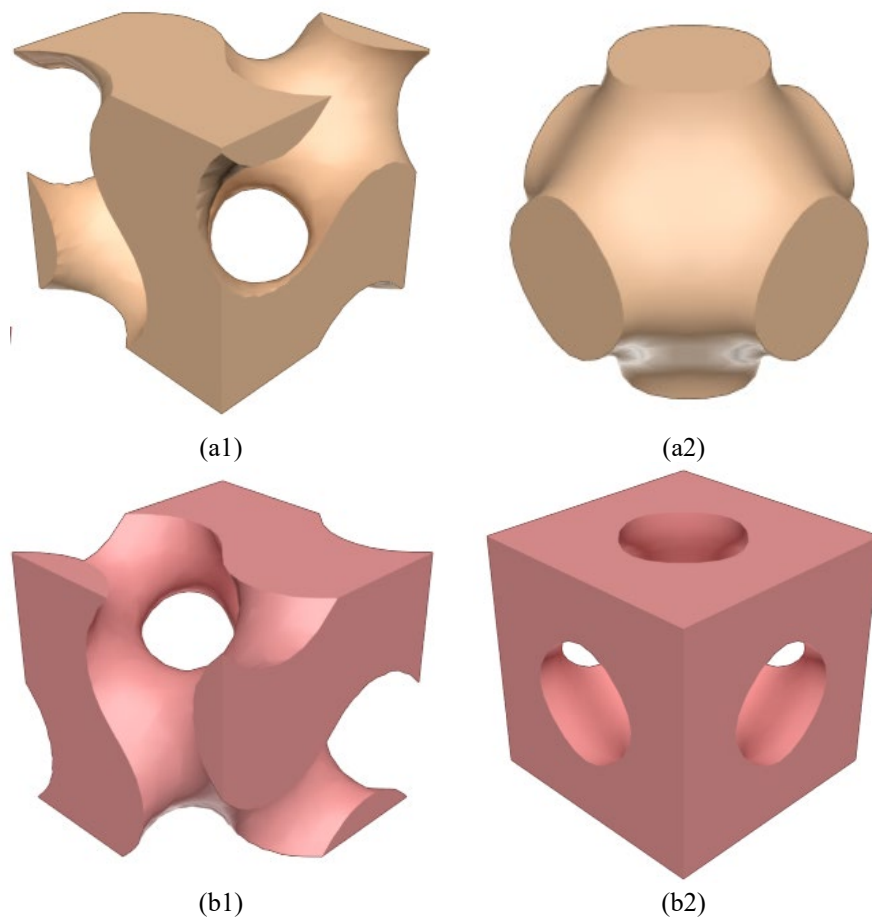


Figure 8.2 Cellular units for the Gyroid (1) and Primitive (2) TPMS. (a) the main skeletal design and (b) the secondary skeletal design.

8.2.2 DEM models

This segment elucidates the methodology employed in modelling TPMS cellular units using the DEM suite, PFC 3D. Initially, stereolithography files of the four solid TPMS variants are extended to an identical dimension ($5\text{ cm} \times 5\text{ cm} \times 5\text{ cm}$) and loaded into DEM software to delineate the geometry of the porous cellular units. The assembly of the cellular units is encased using Wall elements, which consist of multiple triangular facets as illustrated in Figure 8.3. Following this, Ball elements with radii varying between 2 mm and 3 mm are dispersed within the specified confines, permitting intersections. The facets of the walls are turned on to enclose the space, and the spherical balls of the TPMS models are endowed with the characteristics of cementitious substance. These balls undergo application of linear constitutive behaviours, with the simulation proceeding up to the moment when the mean unbalanced force factor across the whole TPMS model attains a value of 1×10^{-4} , confirming a balanced inner force distribution. The cellular units for the main and secondary Gyroid structures are constituted of 1874, 1987 spheres, while the main and secondary Primitive designs have 2035, and 2135 spheres. To integrate the cellular units into a deformable and destructible aggregate of spheres, the build-in soft-bond constitutive behaviours has been employed, facilitating the creation of fracturable contacts between the overlapping spheres. The resultant destructible clusters of TPMS units are thereafter saved as Bricks (the periodic condition) for further modelling TPMS designs of numerous cellular units.

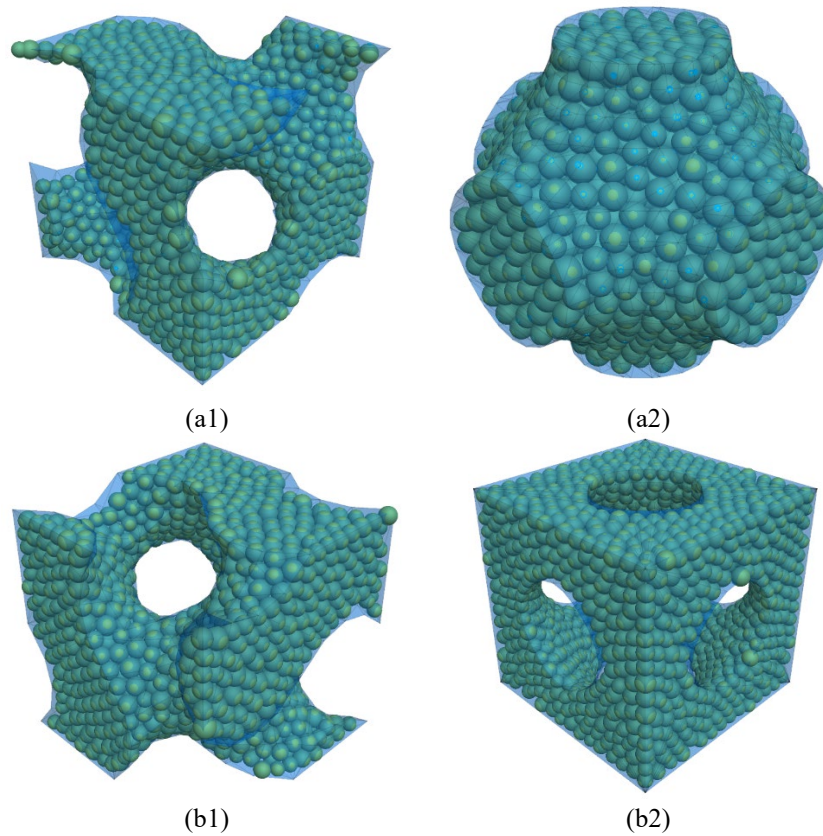


Figure 8.3 DEM cellular units by sphere elements (Balls) for the Gyroid (1) and Primitive (2) TPMS. (a) the main skeletal design and (b) the secondary skeletal design.

8.2.3 Contact models

In DEM simulations, the engaged contacts define the connection between the overarching internal forces and the movement relative to the points of contact according to the force-displacement principle. This interconnection results in the exertion of forces and moments (F and M) on two bodies, producing reactions that are equal in magnitude but opposite in direction, as illustrated in Figure 8.4. Similar to the DEM model studied in chapter five, the Linear Contact Model (LCM) is employed for simulating wall-ball interactions, with compression and torsion forces applied through via the movement and rotation of the facts on the top of the TPMS models. The linear contact is active when the distance between the spherical element and the fact in wall is zero or negative. In the LCM, a combination of a linear spring, to mimic linear elastic (compression-only) responses,

and a dashpot, to model viscous effects, is implemented. These components operate over a small region, facilitating the transmission of force but not moment. Contrary to the Linear Parallel Bond model (LPB) used for numerical simulations in Chapter Five, this chapter adopts the soft-bond method (SBM), as shown in Figure 8.5. The soft bond contact model distinguishes itself by its capacity to emulate the interactions within particle assemblies in both unbonded and bonded states. In its unbonded configuration, the model mirrors the contact mechanics proposed by [198], enabling the conveyance of forces and torques at the point of contact. It incorporates parameters related to frictional resistance to limit tangential force, flexural torque, and rotational torque, thus ensuring realistic simulation of particle interactions without chemical or physical bonds. Transitioning to the bonded state, the model's behaviour aligns with that of a linear parallel bond model, characterised by a frictional strength parameter that limits shear force. Unique to this model is the handling of bond failure; rather than eliminating the bond upon exceeding its strength in shear or tension, the model allows for a softening regime. This regime persists until the stress of a bonded contact diminishes to a predefined limitation, at which point the contact is deemed fractured. The model's capacity to specify the gradient and tensile fracture strength during the softening phase through user-defined factors (softening factor and softening tensile strength factor) marks a significant divergence from traditional linear parallel bond models. This model allows for a realistic representation of cracking and fragmentation in concrete without the need for assumptions typical in continuum-based methods, effectively capturing the detailed mechanical behavior and stress responses under varying conditions.

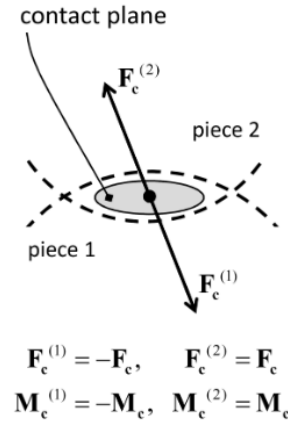


Figure 8.4 A depiction of an active contact mechanism among two spherical bodies.

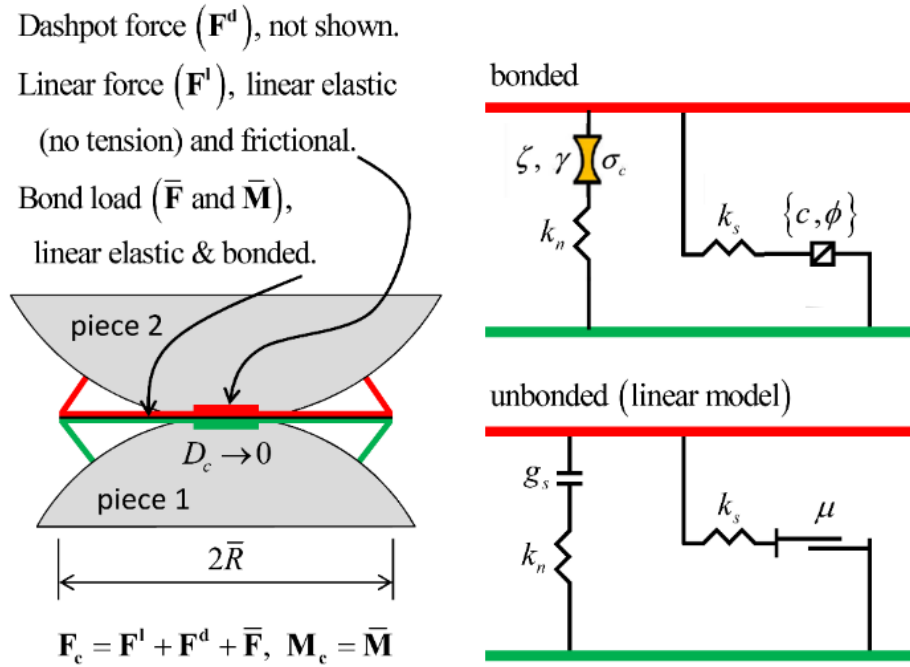


Figure 8.5 The viscoelastic elements of the Soft-bond constitutive model.

The Equation 8.1 to Equation 8.7 reflect the force-displacement relationships that govern the active soft-bonded contacts. Equation 8.1 describes the update rule for the normal contact force (F_n), which is the greater of the initial normal force plus the product of the normal stiffness (k_n), the contact area (A), and the normal displacement increment ($\Delta\delta_n$), or zero. Equation 8.2 updates the shear force (F_s) by subtracting the product of the shear stiffness (k_s), the contact area, and the shear

displacement increment from the initial shear force. Equation 8.3 and Equation 8.4 define the updating of the twisting and bending moments respectively, incorporating the relevant stiffnesses, geometric properties, and angular displacements. Equation 8.5 to Equation 8.7 specify the geometrical properties of the contact area: the area (A), the moment of inertia (I), and the polar moment of inertia (J), all defined in terms of the radius (R) of the contact area.

$$F_n = \max(F_n + k_n A \Delta \delta_n, 0) \quad 8.1$$

$$F_s = F_s - k_s A \Delta \delta_s \quad 8.2$$

$$M_t = M_t - k_s J \Delta \theta_t \quad 8.3$$

$$M_b = M_b - k_n I \Delta \theta_b \quad 8.4$$

$$A = \pi R^2 \quad 8.5$$

$$I = \frac{1}{4} \pi R^4 \quad 8.6$$

$$J = \frac{1}{2} \pi R^4 \quad 8.7$$

8.2.4 Model parameter and validation

To validate the DEM simulations, the development of two distinct models is undertaken: one emulating a secondary Primitive variant, and the other, a primary Gyroid variant. Both models are configured with a X2Y2Z2 layout, aligning with the parameters set for compressive examinations as documented in reference [197]. The dimensions of these TPMS structures are the same as a cubic area with length of 10 cm. The construction elements of both TPMS frameworks are meticulously replicated in a three-dimensional space and interconnected using the soft bond model (SBM) technique. Following their assembly, the DEM models underwent a process of equilibration to mitigate any internal strains, employing an absolute mode for linear contact updates alongside incremental updates for the soft-bond constitutive behaviours. The devised DEM specimens, aimed at model validation and calibration of the parameters, alongside the concrete samples examined as

per the descriptions in [197], are depicted in Figure 8.6.

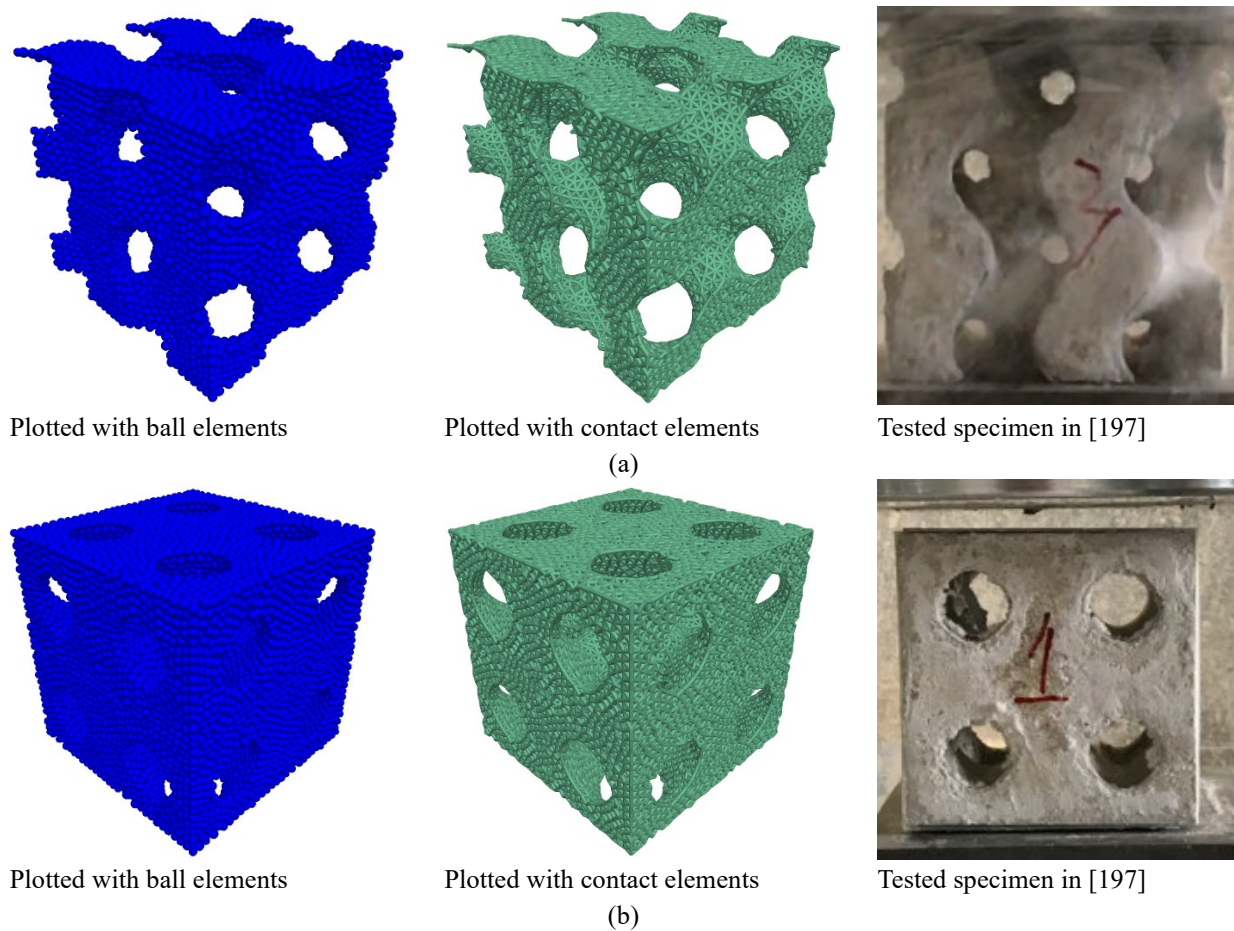


Figure 8.6 The DEM models, and the tested specimens from [197] for validation purpose. (a) main Gyroid design and (b) secondary Primitive design.

Table 8.1 DEM parameters for Balls and Walls.

DEM settings	Sphere Balls	Facets in Walls
Density (kg/m^3)	2100	-
Effective modulus (N/m^2)	$1\text{e}10$	$2\text{e}10$
Friction coefficient	0.6	0.6
Normal to shear stiffness, k_n/k_s	2.4	2.4

Adhering to the concrete characteristics specified in [197] and the parameters for DEM modelling cementitious TPMS specimens as delineated in [199, 200], the material properties for the spherical and activated contacts, including the linear contacts and soft-boned contacts, within the DEM simulations are established, as illustrated in Table 8.1. Concurrently,

Table 8.2 DEM parameters for linear and soft-bond constitutive behaviours.

DEM settings	Linear constitutive behaviour	Soft-bond constitutive behaviour
Effective modulus (N/m ²)	4e9	2e9
Friction coefficient	0.6	0.6
Normal to shear stiffness, k_n/k_s	2.4	2.4
Friction coefficient	0.6	0.6
Damping ratio	0.5	0.5
Poisson's ratio	0.2	0.2
Reference gap, gr (m)	0	0
Tensile strength, (N/m ²)	-	$2.63 \pm 3 \times 0.37$
Shear strength, (N/m ²)	-	auto updated
Update mode	absolute	increment
Softening factor, ξ	-	2.5
Softening tensile strength factor, γ	-	0.7
Friction angle, degrees	-	35

Table 8.2 details the parameters for various contact models utilised within these simulations.

Because that concrete's tensile strength is about 10% of its compressive strength, the ultimate tensile strength of the contacts is determined as one tenth of the concrete compressive strength, identified as 26.3 MPa in [197]. The tensile stress limitations for soft-bonded contacts are set by a self-defined FISH function using a Gaussian distribution, with an average strength of 2.63 MPa and a variability represented by a standard deviation of 0.37 MPa. The selection of local and global damping factors are in line with existing literature [201]. The normal-to-shear stiffness coefficient is derived from concrete Poisson's ratio, employing the methodology described in [202]. Additional properties, including the friction multipliers for bending and twisting and dashpot mode, are maintained at their default settings. The experimental setup for the DEM simulations involves applying the speed of 2 mm/min to the top and bottom facets moving in a opposite direction, respectively, mirroring the displacement load akin to stress rates noted in physical experiments. The vertical displacement of the modelled TPMS structures is quantified through the measurement of the distance between the top and bottom plates moving toward each other. The compressive force is subsequently computed by summing the contact forces along vertical orientation from the contacts of the upper plate and the concrete TPMS model.

The comparative analysis of load-displacement curves for the concrete main Gyroid and secondary Primitive structures, as obtained through numerical simulations and experimental observations under the same strain rate, is depicted in Figure 8.7 (denoted by black lines for experimental data and red lines for DEM outcomes). The experimental forces and displacements, counted from stress-strain relations from [197] and determined by the structural cross-sectional area and specimen height (10 cm). The effective cross-sectional area (50 cm^2) for the concrete main Gyroid and secondary Primitive structures is determined to be half that of their boundary cubic box (100 cm^2), reflecting the 0.5 porosity of the two concrete cellular structures. Notably, the load-displacement curves derived from DEM simulations of these cellular structures showcase behaviour that closely aligns with that observed in experimental findings. Both methodologies reveal that peak load values are attained within a deformation range of 1.0 to 2.0 mm. The discrepancy in peak force between test findings and numerical simulations stands at 1.26% for the main Gyroid variant and 3.02% for the secondary Primitive variant.

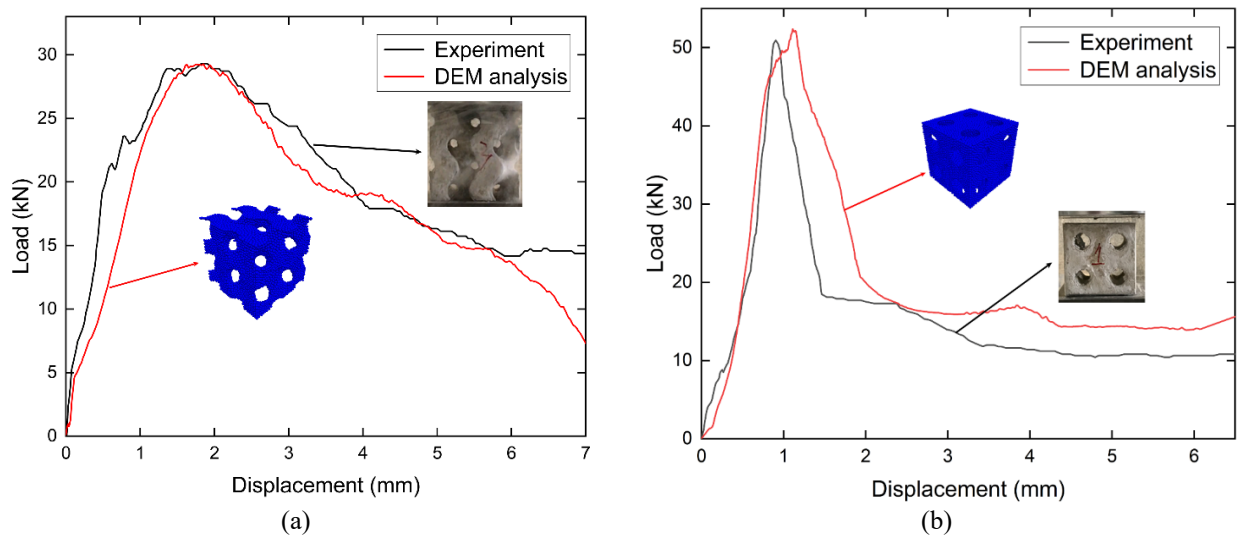


Figure 8.7 Load-displacement curves for concrete TPMS structures under compressive loads from tests (rest results from [197]) and numerical simulation for (a) main Gyroid variant and (b) secondary Primitive variant.

Figure 8.8 elucidates the fracturing patterns of the concrete main Gyroid and secondary Primitive

structures from laboratory test in [197] and DEM simulations. The images for numerical simulations are obtained at a displacement of 6.5 mm. The models after failure are represented using spheres and cylinder contacts. The image illustrated via spheres depict fragmentation into various segments, each assigned a distinct colour to signify bond fractures between adjacent ball units, indicative of cracking. Red markers highlight regions where cracking parallels the experimental findings from [53] and DEM simulations. Models employing contact elements visually map the distribution of compressive and tensile contacts, with areas dominated by tensile contacts being particularly susceptible to cracking due to concrete's brittle nature under tension. The resemblance of cracking zones in DEM models to those in experimental results under compressive stress suggests the efficacy of the DEM approaches, with assigned proper material properties, in forecasting the load-bearing capacity and fracture behaviour of concrete TPMS structures.

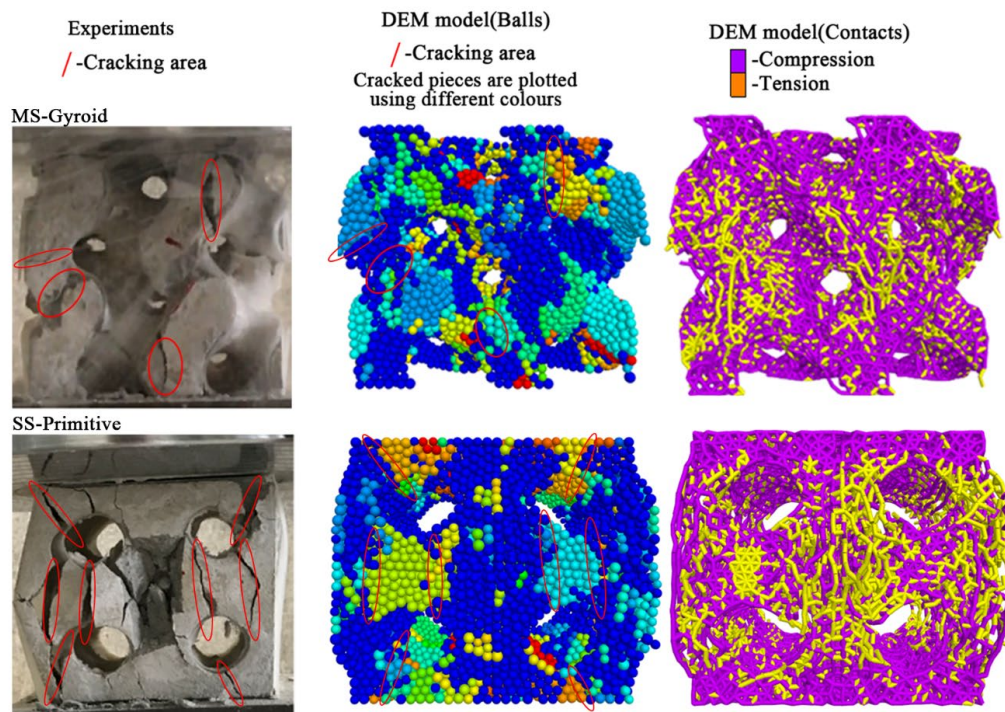


Figure 8.8 Cracked concrete TPMS structures. Images are from test and DEM numerical simulations.

8.2.5 Modelling procedures for varied loads

This segment delineates the methodologies employed to model the responses of Gyroid and Primitive structures under coupled compression and torsion forces. The research encompasses an examination of four distinct TPMS designs, namely, including the main and secondary Gyroid and Primitive structures. Initially, bonded cellular units in periodic condition (Bricks) corresponding to these TPMS variants, fabricated following the procedure outlined in section 8.2.2, are loaded and duplicated and arranged in a X2Y2Z2 array. These cellular units are then cohesively connected through the soft-bonded contacts, incorporating previously verified material characteristics. Subsequently, the models are resolved to a point where the mean unbalanced force ratio of the models, referred to as the ratio-average, attains a value of 1×10^{-4} , thereby ensuring the stresses inside the models are negligible. To facilitate the application of load, two rigid end caps, each comprising ten triangular facets, are constructed at the structure's extremities. As illustrated in Figure 8.9, compressive forces are applied through the imposition of antithetical motion velocities to the Wall elements at the upper and lower of the TPMS specimens. The torsion is introduced by imparting rotational velocity to the two wall caps. The magnitude of the compression force is ascertained by counting the z-directional forces in the linear contacts between the upper cap and the TPMS specimen, whereas the torsion is quantified through the measurement of contact moments exerted on the upper cap in the z-direction. Notably, for the main Primitive design, spheres proximal to the upper and lower walls are affixed to the wall elements via unbreakable bonded contact elements, ensuring structural integrity during load application.

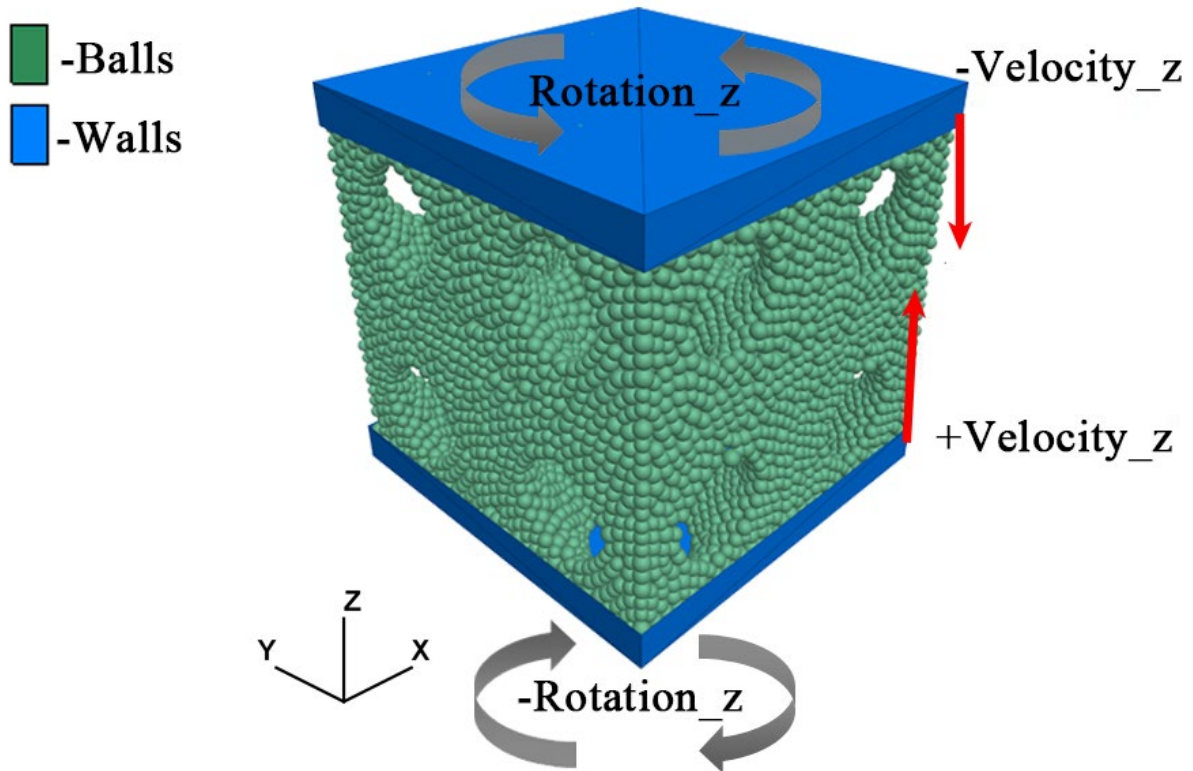


Figure 8.9 Illustration of applying compression and torsion loads in DEM modelling for concrete TPMS structures subjected, secondary Primitive design as an example.

8.3 DISCUSS OF SIMULATION RESULTS

8.3.1 Result under compressive load only

Figure 8.10 presents a comparative analysis of the compressive load-displacement curves for the main and secondary Gyroid and Primitive structures, each configured in a $2 \times 2 \times 2$ unit cell layout, under exclusive compressive loading. It is discernible that structures founded on the Primitive design manifest significantly superior ultimate compressive strengths in contrast to their Gyroid counterparts. Specifically, the maximum compressive loads determined for the main and secondary Gyroid and Primitive structures are recorded at 56.6 kN, 52.4 kN, 29.3 kN, and 35.9 kN, respectively. The variation in compressive strength between the main and secondary Primitive designs is noted at 7.5%, whereas the Gyroid-based structures exhibit a more pronounced discrepancy of 18.6%.

This variation is attributed to the inherent design of main skeletal TPMS structures, which periodically replicate the one eighth of cellular unit characteristic of secondary skeletal TPMS configurations, albeit with a mere half unit cell size phase shift in each axial direction. The equivalence of the nodal mathematical expressions, where $\Phi_{TPMS}(x + \pi, y + \pi, z + \pi) = -\Phi_{TPMS}(x, y, z)$, implies that regions where $\Phi_{TPMS}(x, y, z) \geq 0$ counterbalance those where $\Phi_{TPMS}(x + \pi, y + \pi, z + \pi) \leq 0$. As such, with an increase in the number of unit cells per axial direction, the geometries of primary and secondary TPMS structures will become increasingly similar, which could explain the tendency of the closer compressive strengths of the primary and secondary TPMS structures.

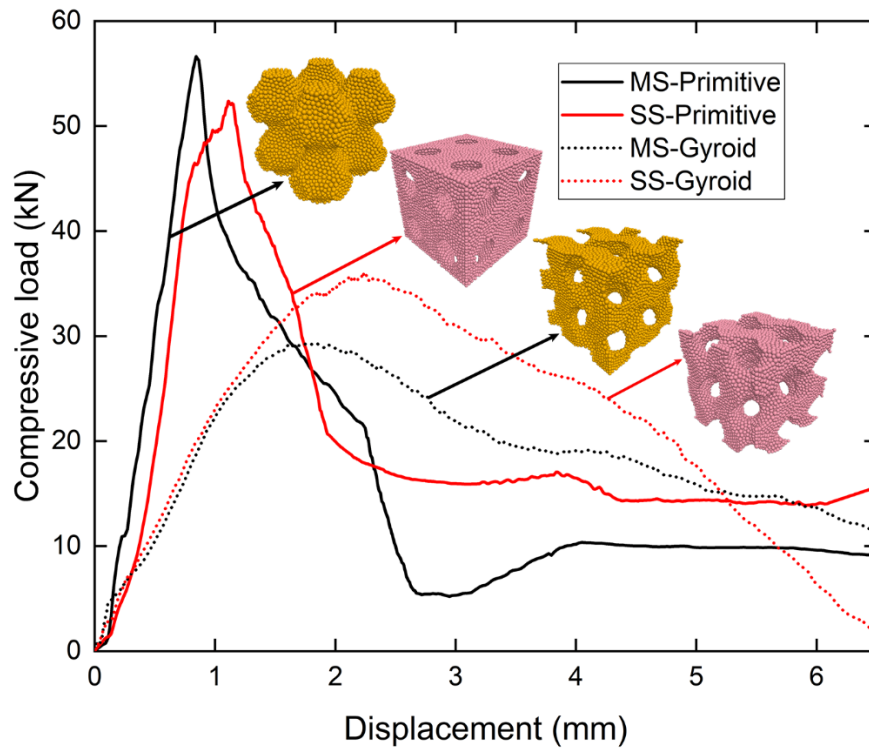


Figure 8.10 load-displacement response to only compression load for Gyroid and Primitive-based structures.

Figure 8.11 illustrates the TPMS models post-failure under compression, depicted through sphere elements delineating fractures and contact elements, with red disks marking the points of contact

bond failures, Observations reveal that the two Primitive specimens predominantly fracture in vertical orientation, fragmenting into a few big segments, whereas the Gyroid specimens disintegrate into a multitude of smaller shards.

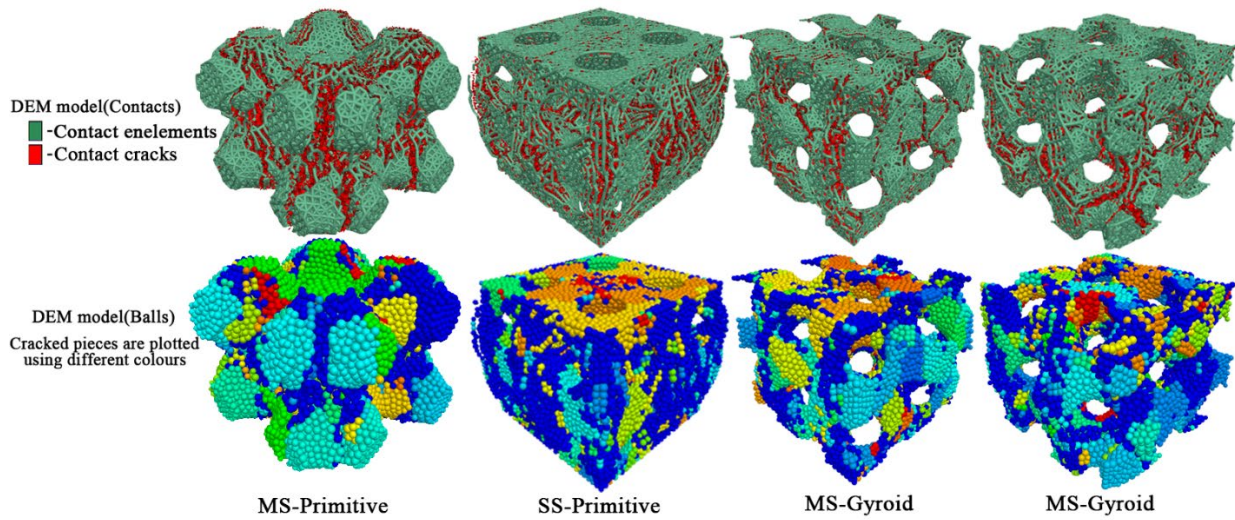


Figure 8.11 Cracking patterns in TPMS specimens subjected to compressive load only.

8.3.2 Result under torsion load only

Figure 8.12 delineates the correlation between torsion moment and rotation angle at upper surfaces of the modelled specimens, as determined through DEM simulations under torsional stress. The investigation varies rotation speeds of the upper cap from five degrees per minute to thirty degrees per minute in a five degrees per minute gradient, revealing an escalation in ultimate torsional loads with increased loading rates across all TPMS configurations. Specifically, at the highest rotation speed of thirty degrees per minute, the maximum torsion forces for the main and secondary Primitive and Gyroid designs are found to be 1.34, 1.62, 1.72, and 1.28 times greater, respectively, than those observed at rotation speed of five degrees per minute. Analysis of the two main Primitive designs and the secondary Gyroid variant under torsional loads unveiled a three-phase response

pattern, as illustrated in Figure 8.12 (a) and (b).

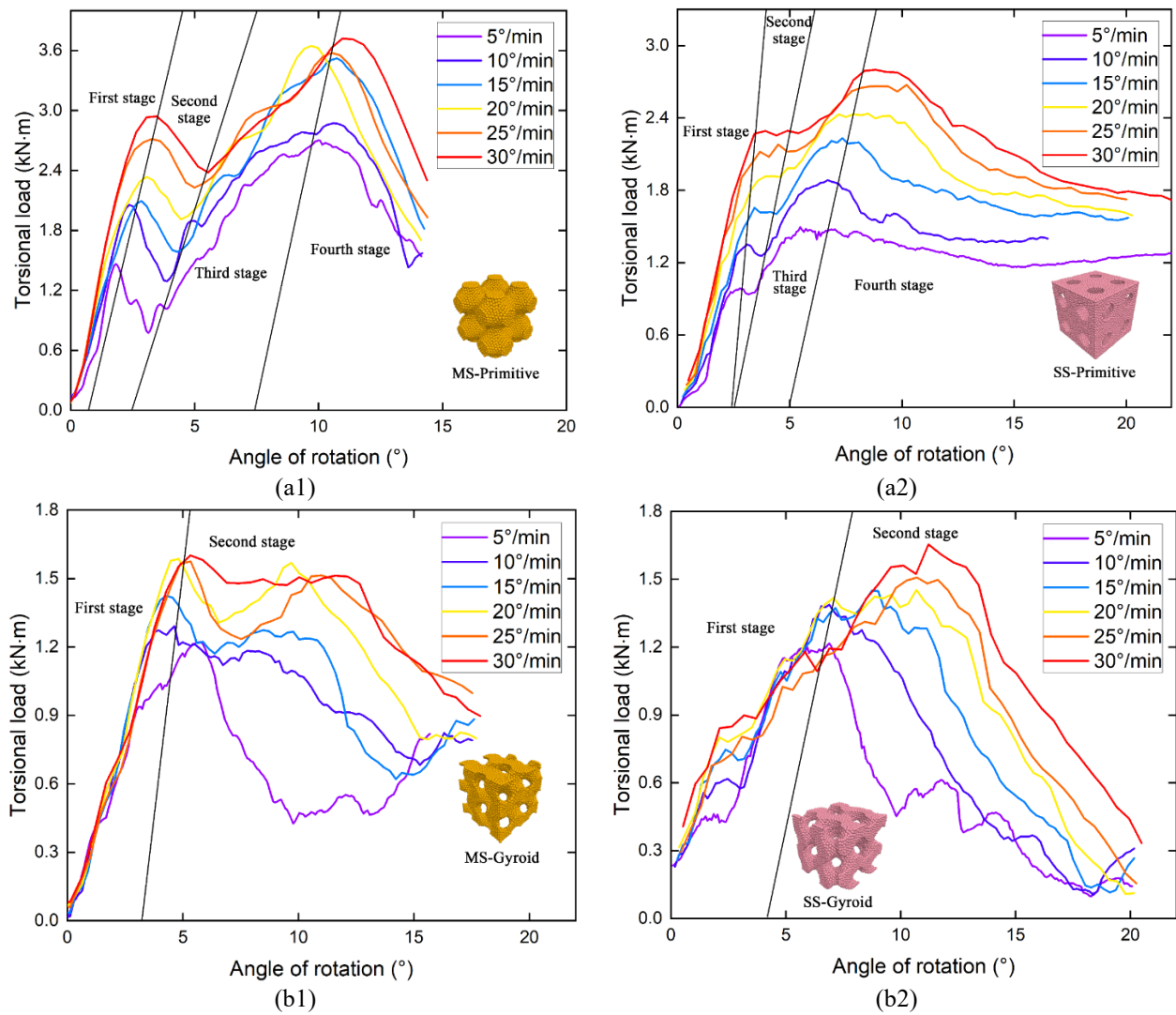


Figure 8.12 Torsion moment versus rotation angle curves under torsion condition of upper cap for main (1) and secondary (2) TPMS designs. (a) Primitive and (d) Gyroid.

Initially, torsional load escalates with an increase in rotation angle. The second phase sees a deceleration in torsional load augmentation, potentially even a slight reduction, attributed to cracking, although a gradual increase in load is still observed. Upon surpassing the peak load, the third phase is characterised by a diminishing torsional bearing capacity, where minor torsional stresses induce considerable twisting. Conversely, the MS-Gyroid structure's response under torsion is delineated by two distinct phases, with a continuous rise to peak load, devoid of a significant plateau at maximum torsion. This variation in torsion behaviour between two Gyroid designs can

be ascribed to their rotational symmetry ($\Phi(-\mathbf{r}) = -\Phi(\mathbf{r})$), despite sharing identical TPMS surfaces, with the direction of torsion further influencing their mechanical response. The simulation outcomes underscore that Primitive configurations offer superior torsional resistance compared to Gyroid structures at equivalent rotation speed, evidenced by the augmented peel torsion force and the bearing capacity (strength) during the plastic phase.

Figure 8.13 investigate the fractures of main and secondary Primitive and Gyroid designs post-torsional loads at a rotation speed of twenty degrees per minute. It is observed that Primitive-based structures predominantly fracture along vertical axes, whereas Gyroid-based structures exhibit cracks along transverse axes, with most fractures occurring within the vertical struts of the TPMS frameworks.

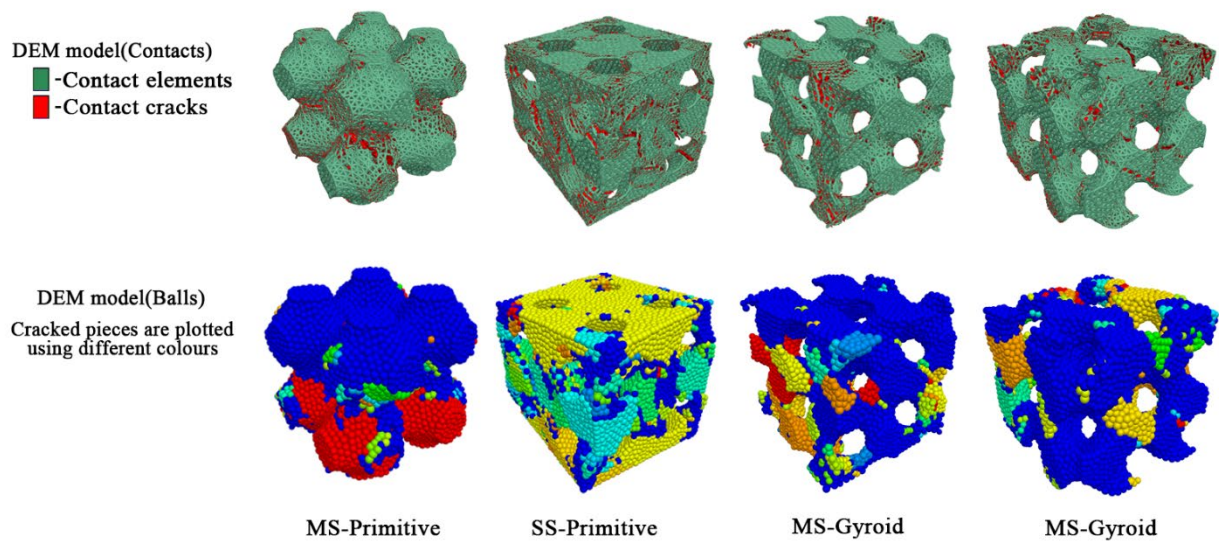


Figure 8.13 Cracking patterns in the four Gyroid and Primitive designs under a rotation speed of twenty degrees per minute.

8.3.3 Result under coupled compressive and torsional load

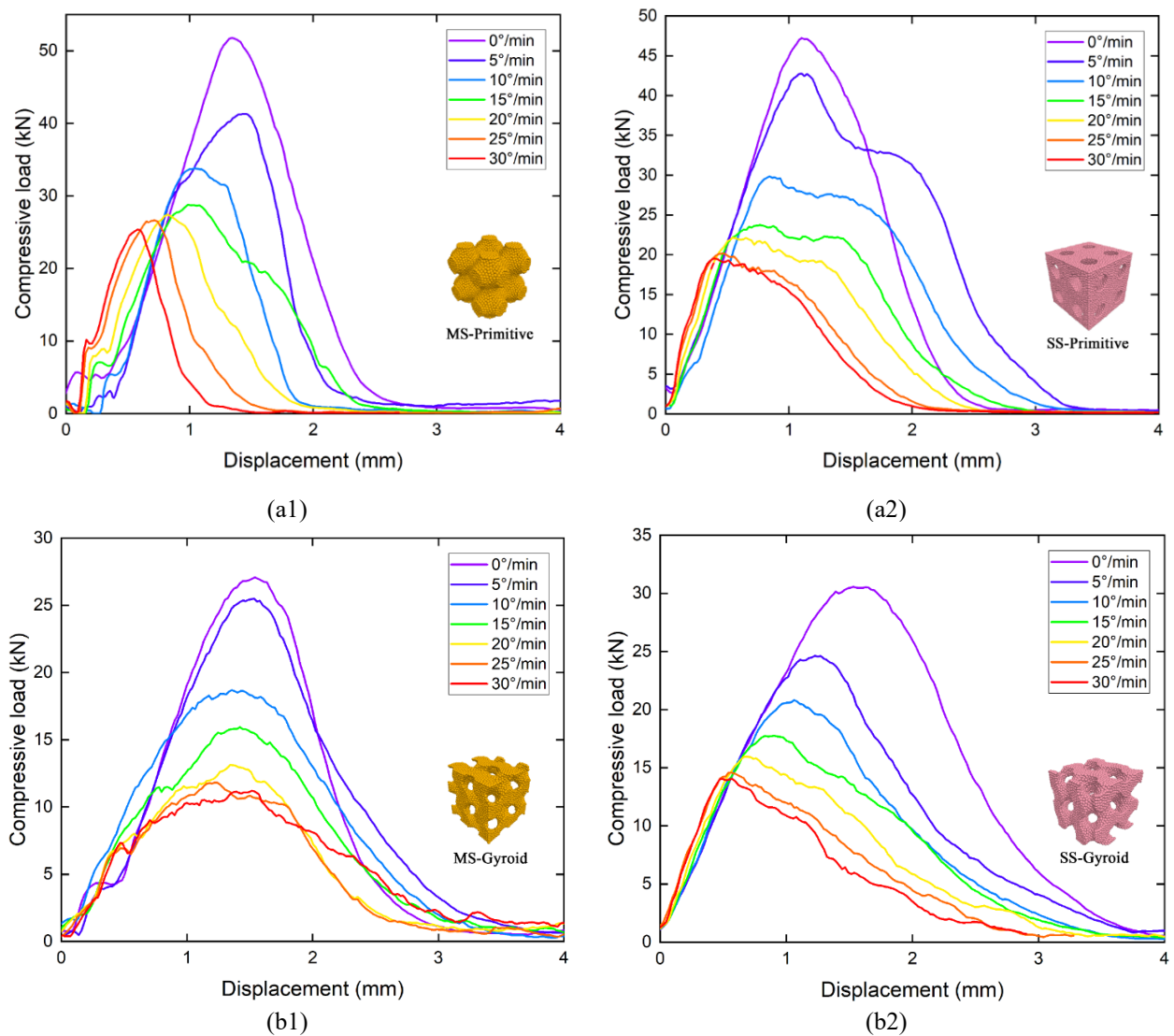


Figure 8.14 Compressive load-displacement response under mixed loading conditions for main (1) and secondary (2) TPMS designs. (a) Primitive and (d) Gyroid.

Figure 8.14 delineates the load-displacement graphs in compression for main and secondary Primitive and Gyroid designs under the influence of varying torsional rates, alongside coupled compression and torsion loads. It has been observed that as the rate of torsion application escalates, there is a discernible decrease in the maximum compression force across all the Primitive and Gyroid designs. Notably, at a rotation speed of twenty-five degrees per minute, all the Primitive and Gyroid designs approximate their minimal compression bearing capacity, with the gradient of the

graphs indicating the structure's rigidity in compression direction. The two main Primitive designs and the secondary Gyroid variant, in particular, manifest enhanced compressive modulus under higher torsional rates within the coupled loading scenario. At a torsional rate of $30^\circ/\text{min}$, the ultimate peak loads in compression for the main and secondary skeletal Primitive and Gyroid variants stand at 25.4 kN, 19.5 kN, 11.2 kN, and 14 kN, respectively. Compared to solely compressive loading, these values represent reductions of 51.0%, 58.9%, 58.7%, and 53.4%, illustrating a loss exceeding 50% of their ability to withstand compression when subjected to mixed loading scenarios.

Additionally, Figure 8.15 displays the torsion moment against rotation angle graphs derived from numerical simulations under mixed loading scenarios across varied rotation speeds. A comparative analysis with Figure 8.12 reveals that the torsion application rate exerts a reduced effect on the peak torsional capacities of the main and secondary skeletal Primitive and Gyroid variants when under mixed loading conditions than when solely subjected to torsional stress. The application of compressive loads significantly bolsters the torsion strength of the main and secondary skeletal Primitive and Gyroid variants. Furthermore, under dual loading conditions, these structures demonstrate failure at greater rotational angles and possess higher remaining torsional forces in the plastic phase, indicative of enhanced torsional ductility due to compressive stress. The two Primitive designs, in particular, features superior torsion resistance compared to their Gyroid-based counterparts.

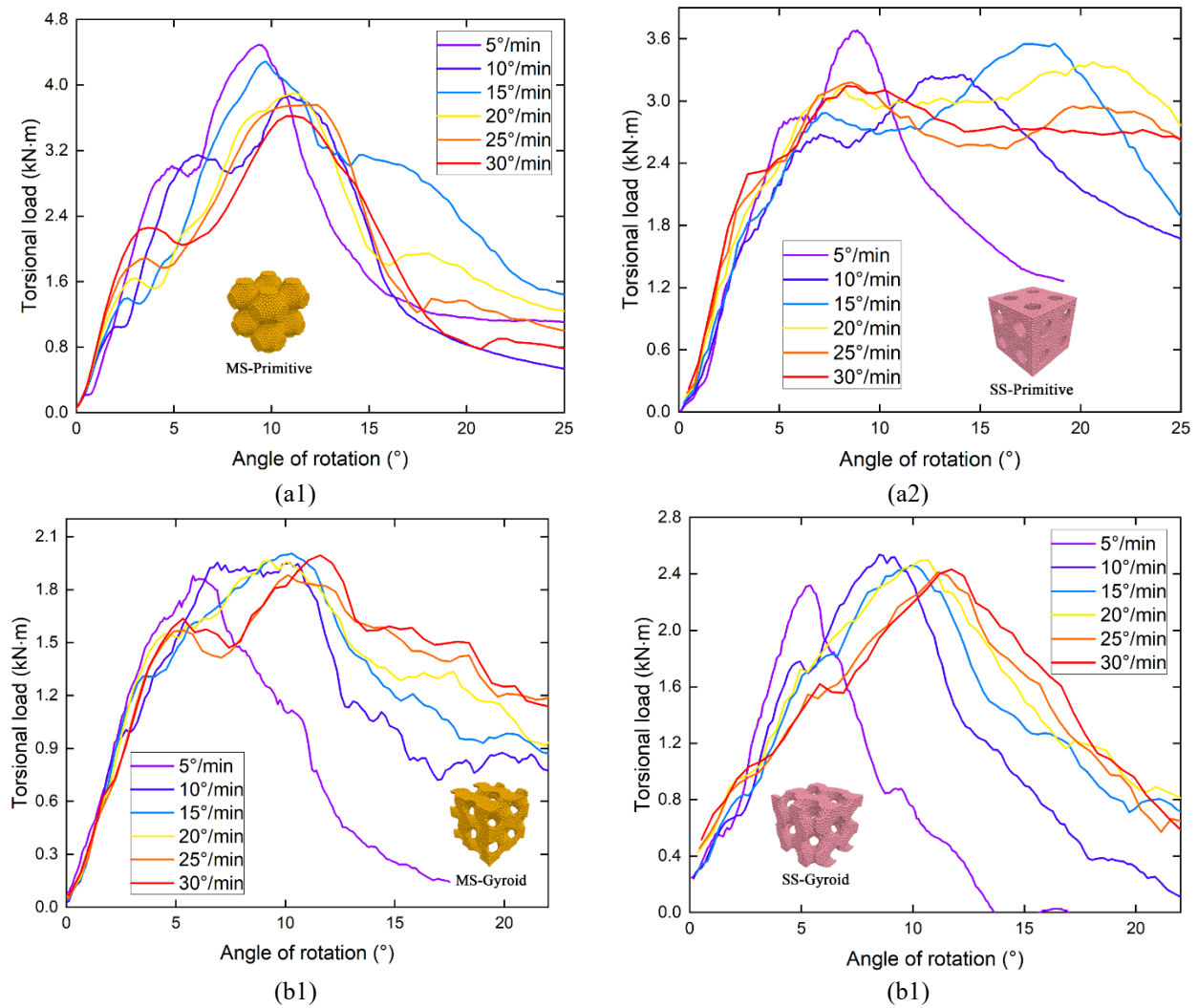


Figure 8.15 Torsion-load against rotation-angle graphs under mixed loading conditions for main (1) and secondary (2) TPMS designs. (a) Primitive and (d) Gyroid.

Figure 8.16 contrasts the peak compression forces and torsion moments between main and secondary skeletal Primitive and Gyroid variants under mixed loading conditions, revealing a clear superiority of the main and secondary Primitive designs in both compression and torsion than Gyroid variants. Under identical loading parameters, the peak compression force and torsion moments of the main and secondary Primitive designs are significantly greater, surpassing those of the main and secondary Gyroid designs by over fifty percent. Figure 8.17 examines the fracture images of the four TPMS variants post mixedly loaded simulations, highlighting that the distribution of cracking regions remains relatively consistent across the structures. The analysis,

in conjunction with Figure 8.11, Figure 8.13 and Figure 8.17, reveals that while the two Primitive variants predominantly crack along vertical and lateral axes, the two Gyroid variants exhibit oblique cracking patterns.

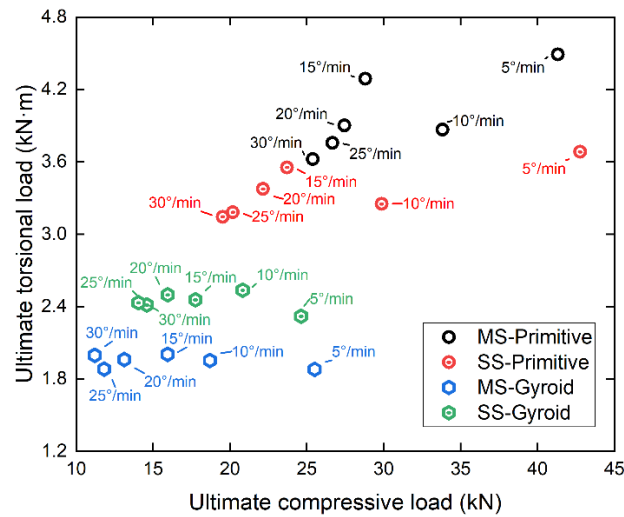


Figure 8.16 Peak compression forces and torsion moments for the main and secondary skeletal Primitive and Gyroid variants under various mixed loading conditions.

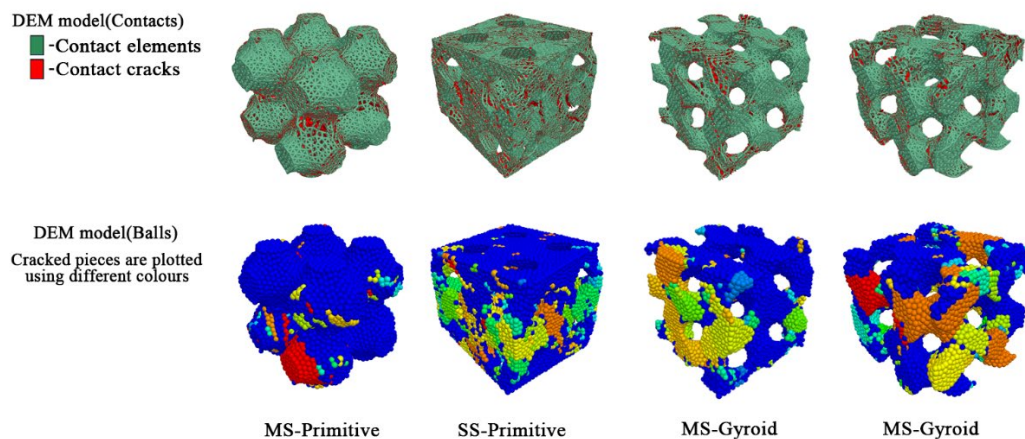


Figure 8.17 Cracking patterns in the main and secondary skeletal Primitive and Gyroid variants under mixed loading condition at 20°/min rotation speed.

8.4 CONCLUSION

In the present investigation, attention is directed towards the mechanical characterisation of concrete constructs modelled on two archetypal TPMS architectures: namely, the Gyroid and Primitive surfaces. This research endeavours to modelling four distinct TPMS designs, each with a designated relative density of 0.5 and dimensions encapsulating 10 cm by 10 cm by 10 cm, specifically encompassing the main and secondary skeletal Primitive and Gyroid variants. Employing the DEM approach, this chapter pioneers an innovative modelling approach for the simulation of concrete structures possessing complex geometries. The methodology integrates ball elements alongside nonlinear soft-bond contacts to model the TPMS specimens under the duress of simultaneous compression force and torsion moment, with the material properties informed by experimental investigations into concrete TPMS samples as obtained from [197]. Upon the empirical validation of the numerical simulations using compressive test outcomes, the investigation proceeds to scrutinise the structures under a spectrum of rotation speeds, thereby instituting a novel comparative discourse on the compressive and torsional resilience, in conjunction with the fracture dispersion, of concrete TPMS variants subjected to mixed loading conditions. The salient findings of this research are summarised. Firstly, the two Primitive constructs exhibited a pronounced superiority in both compression and torsion resistances relative to the two Gyroid designs, with numerical simulations revealing that structures based on the Primitive configuration sustain greater ultimate loads when subjected to identical loading paradigms. Secondly, the imposition of combined axial forces and torsion moments culminates in a significant diminution of the ultimate compressive loads across the four TPMS variants, with an enlargement in torsion rates correlating to a reduction in compressive capacity in excess of 50% at

a rotation speed of thirty degrees per minute, as opposed to scenarios characterised by purely compressive loading. Conversely, the ultimate torsional loads discern a slight augmentation under the regime of combined loading compared to conditions of exclusive torsional stress. Thirdly, the predilection towards particular cracking patterns amongst the main and secondary variants demonstrated a remarkable consistency irrespective of the loading conditions imposed, with Primitive-based designs manifesting fractures predominantly in the horizontal and vertical directions orientations, whilst the two Gyroid configurations when exposed to all types of loads exhibited a propensity for oblique fracturing.

TPMS structures, distinguished by their complex and repetitive geometric forms, exhibit promising potential within the ambit of civil constructions, courtesy of their exceptional structural properties and fascinating architectural geometry. Potential applications envisage the incorporation of TPMS constructs in load-bearing edifices, energy dissipation mechanisms, acoustic barriers, decorative architectural elements, and lightweight construction endeavours. Notwithstanding the promising prospects of TPMS structures, it is incumbent upon the academic and professional communities to engage in further research and developmental pursuits to unravel and optimise the performance attributes of TPMS constructs for pragmatic application. This scholarly endeavour contributes to the corpus of knowledge requisite for the informed selection of TPMS designs in engineering ventures confronted with the exigencies of combined compressive and torsional loads.

CHAPTER 9

CONCLUSION

9.1 INTRODUCTION

In this thesis, we introduce several novel contributions to the field of civil and railway engineering through the comprehensive investigation of TPMS structures. Primarily, we developed a simplified method to represent TPMS surfaces, which converts complex geometrical configurations into more manageable polygonal forms. This innovation not only facilitates the practical application of TPMS in large-scale infrastructures but also enhances the computational efficiency of our simulations. We have investigated the large-scale TPMS unit cells under various loads using FEM. Furthermore, this thesis marks the first application of the DEM to analyze the mechanical properties of TPMS structures. The thesis explores the impact of unit cell arrangements on the performance of TPMS structures, a critical aspect that has not been thoroughly investigated previously. This examination reveals how slight variations in the configuration can significantly influence the mechanical efficacy and resilience of the structures, providing crucial data that could influence design and implementation strategies in civil engineering projects. By integrating DEM with FEM, we have ventured into uncharted territory by evaluating the potential of TPMS structures to serve as railway support layers. This application-oriented exploration is aimed at addressing the specific needs of railway infrastructure, proposing TPMS as a viable solution to enhance the durability and stability of railway tracks. The rigor of the research work is underpinned by meticulous experimental designs and detailed simulations that underlie the findings presented. The methodological approach combines cutting-edge 3D printing technology with comprehensive mechanical testing and advanced computational models, ensuring that the conclusions drawn are both robust and replicable.

The pivotal research presented in this thesis is conducted at the Birmingham Centre for Railway Research and Education (BCRRE) at the University of Birmingham, having been generously supported by the China Scholarship Council. Heartfelt gratitude is extended towards the European Commission for the H2020-MSCA-RISE Project No. 691135 and the European Union's Horizon 2020 research and innovation programme under grant agreement No 730849. This chapter encapsulates the primary research findings and forecasts future directions in this field.

9.2 RESEARCH FINDINGS

This thesis presents an extensive investigation into the mechanical properties and potential applications of TPMS structures in civil engineering, within civil engineering, with a particular emphasis on their utility in railway systems and concrete structures under diverse loading conditions. By incorporating experimental analyses alongside FEM and DEM simulations, this research provides a detailed insight into the static and dynamic behaviours of TPMS structures. The following summarises the pivotal findings and discusses their implications for industry practices and potential standardisation.

Design and Performance of New Hybrid TPMS Structures: The research introduces innovative hybrid TPMS designs, engineered to optimise specific mechanical properties through nodal adjustments of existing TPMS configurations. Notably, these hybrid structures exhibit enhanced resistance to compressive, shear, and torsional loads, making them highly suitable for various civil engineering applications. Such adaptability and strength improvements may encourage the development of new industry standards for the design and implementation of TPMS in structural applications.

Axial Load Behaviours of IWP and SP Structures: The thesis provides a comprehensive analysis of IWP and SP structures subjected to axial loads, demonstrating how unit cell configurations significantly influence their compressive strength and energy absorption capabilities. The SP (Primitive) structures, in particular, offer superior compressive strength and more effective load distribution, underscoring their potential for enhancing mechanical resilience in practical applications.

Dynamic Performance of TPMS Structures: This research segment is pioneering in its examination of the damping characteristics of TPMS structures. The findings indicate that geometric configurations critically impact their dynamic responses, with certain designs achieving superior vibration damping capabilities. These insights into non-linear stiffness and damping ratios are crucial for the development of TPMS applications in environments subject to dynamic loads, such as transportation infrastructure.

TPMS Structures as Railway Support Layers: TPMS support layers utilising the Primitive configuration demonstrate superior reinforcement capabilities against vertical loads compared to the IWP and Gyroid structures. Specifically, the MS-Primitive variant achieves the highest track stiffness, underscoring the pivotal role that structural design plays in augmenting the mechanical resilience and overall performance of railway tracks. This finding highlights the potential for targeted design enhancements in TPMS configurations to significantly improve infrastructure durability and effectiveness in real-world applications.

Mechanical Characterisation of Concrete TPMS Constructs: Concrete constructs utilising TPMS designs show distinct advantages in compressive and torsional resistance, with the Primitive

configuration notably surpassing the Gyroid in ultimate load-bearing capacity. Additionally, this analysis illuminates specific cracking patterns associated with different TPMS configurations under combined loading conditions, offering valuable insights for the optimisation of concrete reinforcements.

The outcomes of this thesis are highly pertinent to the civil engineering industry, particularly in enhancing infrastructure resilience and optimising material use. The advanced understanding of TPMS structures' mechanical properties supports the argument for their broader adoption and could inform future updates to building codes and standards. For TPMS structures with large-scale unit cells, the compressive strength varies with different unit cell arrangements so a proper unit cell configuration should be determined when applying TPMS structures in civil engineering. As the number of unit cells increases, the average compressive strength also increases. When arranged in a $4 \times 4 \times 4$ configuration, it can achieve 90% or more of the compressive strength attained by a $7 \times 7 \times 7$ arrangement. TPMS structures based on the Schwarz P surface (SP) exhibit superior axial load-bearing capacity and intermediate dynamic energy absorption performance. They also demonstrate optimal support efficacy when utilised as railway supporting layers. Furthermore, the demonstrated benefits of TPMS in railway and concrete applications provide a compelling case for their integration into upcoming infrastructural projects, potentially setting new benchmarks for durability and design flexibility in the sector.

9.3 RECOMMENDATIONS FOR FUTURE RESEARCH

This thesis provides a comprehensive investigation into the mechanical properties and potential applications of TPMS in civil engineering, paving the way for innovative infrastructure solutions.

However, it identifies specific areas where future research could enhance understanding and application:

Material Diversity: The research predominantly utilises photosensitive resin and concretes. Future studies should broaden the material spectrum to include metals and composites to assess TPMS structures' material-dependent properties more comprehensively.

Scale of Models: The focus on DEM models limits the applicability of findings to real-scale structures. Subsequent research should scale up TPMS models to better evaluate their real-world performance under practical load conditions.

Dynamic Loading Conditions: The initial exploration of TPMS structures' dynamic properties, while pioneering, is limited. Future work should extend these studies to multiple degrees of freedom and diverse dynamic loading scenarios, such as seismic, wind, and vehicular impacts.

Complex Loading Scenarios: Although the study advances understanding of TPMS under standard loading conditions, real-world applications often involve complex, variable loads. Future research should explore TPMS performance under cyclic and fatigue loading to determine long-term durability.

Economic and Environmental Considerations: The focus has been largely mechanical, with less attention to the economic and environmental impacts of TPMS deployment in civil engineering. Comprehensive analyses of cost-effectiveness, sustainability, and environmental impact are recommended.

Experimental Validation of Computational Models: There is a need for further empirical research

to validate the FEM and DEM simulations, especially for new hybrid TPMS designs under varied complex loading conditions.

References

1. Debrezion, G., E. Pels, and P. Rietveld, *The Impact of Railway Stations on Residential and Commercial Property Value: A Meta-analysis*. The Journal of Real Estate Finance and Economics, 2007. **35**(2): p. 161-180.
2. Zhong, W., et al., *Experimental investigation between rolling contact fatigue and wear of high-speed and heavy-haul railway and selection of rail material*. Wear, 2011. **271**(9): p. 2485-2493.
3. Kaewunruen, S. and A.M. Remennikov, *Dynamic properties of railway track and its components: a state-of-the-art review*. New research on acoustics, 2008. **28**: p. 197-220.
4. Michas, G., *Slab track systems for high-speed railways*. 2012.
5. Remennikov, A.M. and S. Kaewunruen, *A review of loading conditions for railway track structures due to train and track vertical interaction*. Structural Control and Health Monitoring, 2008. **15**(2): p. 207-234.
6. Kaewunruen, S. and A.M. Remennikov, *Current state of practice in railway track vibration isolation: an Australian overview*. Australian Journal of Civil Engineering, 2016. **14**(1): p. 63-71.
7. Kianian, B., *Wohlers Report 2017: 3D Printing and Additive Manufacturing State of the Industry, Annual Worldwide Progress Report*. Chapters titles: The Middle East, and other countries. 2017, FORT COLLINS, COLORADO, USA: Wohlers Associates, Inc.
8. Attaran, M., *The rise of 3-D printing: The advantages of additive manufacturing over traditional manufacturing*. Business Horizons, 2017. **60**(5): p. 677-688.
9. Lipson, H. and M. Kurman, *Fabricated: The new world of 3D printing*. 2013: John Wiley & Sons.
10. Guo, H.-m., et al., *Investigation on wear and damage performance of laser cladding Co-based alloy on single wheel or rail material*. Wear, 2015. **328-329**: p. 329-337.
11. Biazon, L., et al., *Correlations between rail grease formulation and friction, wear and RCF of a wheel/rail tribological pair*. Tribology International, 2021. **153**: p. 106566.
12. Ringsberg, J.W., et al., *Rolling contact fatigue of rails—finite element modelling of residual stresses, strains and crack initiation*. Proceedings of the Institution of Mechanical Engineers, Part F: Journal of Rail and Rapid Transit, 2000. **214**(1): p. 7-19.
13. Wang, X., L. Lei, and H. Yu, *A Review on Microstructural Features and Mechanical Properties of Wheels/Rails Cladded by Laser Cladding*. Micromachines, 2021. **12**(2).
14. Wang, X., D. Deng, and H. Zhang, *Effects of mass energy and line mass on characteristics*

- of the direct laser fabrication parts*. Rapid Prototyping Journal, 2018. **24**(2): p. 270-275.
15. Wang, X., et al., *Overhang structure and accuracy in laser engineered net shaping of Fe-Cr steel*. Optics & Laser Technology, 2018. **106**: p. 357-365.
 16. Hiensch, M., et al. *Two-material rail development to prevent rolling contact fatigue and reduce noise levels in curved rail track*. 2001. Newcastle University.
 17. Hiensch, M., et al., *Two-material rail development: field test results regarding rolling contact fatigue and squeal noise behaviour*. Wear, 2005. **258**(7): p. 964-972.
 18. Franklin, F.J., et al., *Rolling contact fatigue and wear behaviour of the infrastar two-material rail*. Wear, 2005. **258**(7): p. 1048-1054.
 19. Hiensch, E.J.M., et al., *Prevention of RCF damage in curved track through development of the INFRA-STAR two-material rail*. Fatigue & Fracture of Engineering Materials & Structures, 2003. **26**(10): p. 1007-1017.
 20. Vilar, R., *Laser cladding*. Journal of Laser Applications, 1999. **11**(2): p. 64-79.
 21. Thawari, N., et al., *Influence of laser cladding parameters on distortion, thermal history and melt pool behaviour in multi-layer deposition of stellite 6: In-situ measurement*. Journal of Alloys and Compounds, 2021. **860**: p. 157894.
 22. Shamsaei, N., et al., *An overview of Direct Laser Deposition for additive manufacturing; Part II: Mechanical behavior, process parameter optimization and control*. Additive Manufacturing, 2015. **8**: p. 12-35.
 23. Chen, S.-E., et al., *Prototyping rail track for micro-people movers using additive manufacturing: Failure topology characterization*. Construction and Building Materials, 2021. **281**: p. 122623.
 24. Zhu, G., et al., *The influence of laser and powder defocusing characteristics on the surface quality in laser direct metal deposition*. Optics & Laser Technology, 2012. **44**(2): p. 349-356.
 25. Lai, Q., et al., *Influences of depositing materials, processing parameters and heating conditions on material characteristics of laser-cladded hypereutectoid rails*. Journal of Materials Processing Technology, 2019. **263**: p. 1-20.
 26. Hemmati, I., V. Ocelík, and J.T.M. De Hosson, *The effect of cladding speed on phase constitution and properties of AISI 431 stainless steel laser deposited coatings*. Surface and Coatings Technology, 2011. **205**(21): p. 5235-5239.
 27. Hemmati, I., V. Ocelík, and J.T.M. De Hosson, *Microstructural characterization of AISI 431 martensitic stainless steel laser-deposited coatings*. Journal of Materials Science, 2011. **46**(10): p. 3405-3414.
 28. Fu, Z.K., et al., *Investigation on microstructure and wear characteristic of laser cladding Fe-based alloy on wheel/rail materials*. Wear, 2015. **330-331**: p. 592-599.

29. Clare, A., et al., *Laser cladding for railway repair and preventative maintenance*. Journal of Laser Applications, 2012. **24**(3): p. 032004.
30. Niederhauser, S. and B. Karlsson, *Fatigue behaviour of Co–Cr laser cladded steel plates for railway applications*. Wear, 2005. **258**(7): p. 1156-1164.
31. Wang, W.J., et al., *Effect of laser cladding on wear and damage behaviors of heavy-haul wheel/rail materials*. Wear, 2014. **311**(1): p. 130-136.
32. Jin, Y., M. Ishida, and A. Namura, *Experimental simulation and prediction of wear of wheel flange and rail gauge corner*. Wear, 2011. **271**(1): p. 259-267.
33. Lewis, S.R., R. Lewis, and D.I. Fletcher, *Assessment of laser cladding as an option for repairing/enhancing rails*. Wear, 2015. **330-331**: p. 581-591.
34. Wang, X., et al., *Influences of pulse laser parameters on properties of AISI316L stainless steel thin-walled part by laser material deposition*. Optics & Laser Technology, 2017. **92**: p. 5-14.
35. Wang, K., et al., *Effect of Cobalt on Microstructure and Wear Resistance of Ni-Based Alloy Coating Fabricated by Laser Cladding*. Metals, 2017. **7**(12).
36. Roy, T., et al., *Residual stress in laser cladded heavy-haul rails investigated by neutron diffraction*. Journal of Materials Processing Technology, 2020. **278**: p. 116511.
37. Cantini, S. and S. Cervello, *The competitive role of wear and RCF: Full scale experimental assessment of artificial and natural defects in railway wheel treads*. Wear, 2016. **366-367**: p. 325-337.
38. Ocelík, V., et al., *Thick Co-based coating on cast iron by side laser cladding: Analysis of processing conditions and coating properties*. Surface and Coatings Technology, 2007. **201**(12): p. 5875-5883.
39. de Oliveira, U., V. Ocelík, and J.T.M. De Hosson, *Residual stress analysis in Co-based laser clad layers by laboratory X-rays and synchrotron diffraction techniques*. Surface and Coatings Technology, 2006. **201**(3): p. 533-542.
40. Duarte, V.R., et al., *Hot forging wire and arc additive manufacturing (HF-WAAM)*. Additive Manufacturing, 2020. **35**: p. 101193.
41. Donoghue, J., et al., *The effectiveness of combining rolling deformation with Wire–Arc Additive Manufacture on β -grain refinement and texture modification in Ti–6Al–4V*. Materials Characterization, 2016. **114**: p. 103-114.
42. Hongxi, L., et al., *Microstructure and Property of Fe60 Composite Coatings by Rotating Magnetic Field Auxiliary Laser Cladding*. Chinese Journal of Lasers, 2013. **40**: p. 0103007.
43. Hu, Y., et al., *Effects of electromagnetic compound field on the escape behavior of pores in molten pool during laser cladding*. Surface and Coatings Technology, 2020. **383**: p. 125198.
44. Lu, P., et al., *Laser cladding of rail; the effects of depositing material on lower rail grades*.

- Wear, 2019. **438-439**: p. 203045.
45. Roy, T., et al., *Effect of deposition material and heat treatment on wear and rolling contact fatigue of laser cladded rails*. Wear, 2018. **412-413**: p. 69-81.
 46. Roy, T., et al., *Evaluation of the mechanical properties of laser cladded hypereutectoid steel rails*. Wear, 2019. **432-433**: p. 202930.
 47. Zhu, Y., et al., *Study on wear and RCF performance of repaired damage railway wheels: Assessing laser cladding to repair local defects on wheels*. Wear, 2019. **430-431**: p. 126-136.
 48. Lewis, S.R., et al., *Improving rail wear and RCF performance using laser cladding*. Wear, 2016. **366-367**: p. 268-278.
 49. Lewis, S.R., et al., *Full-scale testing of laser clad railway track; Case study – Testing for wear, bend fatigue and insulated block joint lipping integrity*. Wear, 2017. **376-377**: p. 1930-1937.
 50. Narayanan, A., et al., *Residual stress in laser cladded rail*. Tribology International, 2019. **140**: p. 105844.
 51. Meng, L., et al., *Effect of laser cladding and laser-induction hybrid cladding coatings on the bending properties and fracture behavior of rails*. Surface and Coatings Technology, 2019. **374**: p. 1038-1050.
 52. Meng, L., et al., *A comparison of microstructure and mechanical properties of laser cladding and laser-induction hybrid cladding coatings on full-scale rail*. Materials Science and Engineering: A, 2019. **748**: p. 1-15.
 53. Seo, J.-W., et al., *Effects of Laser Cladding for Repairing and Improving Wear of Rails*. International Journal of Precision Engineering and Manufacturing, 2019. **20**(7): p. 1207-1217.
 54. Aladesanmi, V.I., O.S. Fatoba, and E.T. Akinlabi, *Laser cladded Ti+TiB₂ on Steel Rail Microstructural Effect*. Procedia Manufacturing, 2019. **33**: p. 709-716.
 55. Zheng, Z., X. Hongchao, and Y. Liang, *Exploring on Application of 3D Printing Technology in Field of Track Structure*. Railway Engineering, 2017(1): p. 44-47.
 56. Thomas, T. and G. Tiwari, *Crushing behavior of honeycomb structure: a review*. International Journal of Crashworthiness, 2019. **24**(5): p. 555-579.
 57. Qi, C., F. Jiang, and S. Yang, *Advanced honeycomb designs for improving mechanical properties: A review*. Composites Part B: Engineering, 2021. **227**: p. 109393.
 58. Shen, X., et al., *Dynamic mechanical response prediction model of honeycomb structure based on machine learning method and finite element method*. International Journal of Impact Engineering, 2024. **184**: p. 104825.
 59. Wang, J., et al., *On the performance of truss panels with Kagomé cores*. International Journal

- of Solids and Structures, 2003. **40**(25): p. 6981-6988.
60. Deshpande, V.S., N.A. Fleck, and M.F. Ashby, *Effective properties of the octet-truss lattice material*. Journal of the Mechanics and Physics of Solids, 2001. **49**(8): p. 1747-1769.
 61. Helou, M. and S. Kara, *Design, analysis and manufacturing of lattice structures: an overview*. International Journal of Computer Integrated Manufacturing, 2018. **31**(3): p. 243-261.
 62. Saranathan, V., et al., *Structure, function, and self-assembly of single network gyroid (I4132) photonic crystals in butterfly wing scales*. Proc Natl Acad Sci U S A, 2010. **107**(26): p. 11676-81.
 63. Al-Ketan, O., et al., *Nature-Inspired Lightweight Cellular Co-Continuous Composites with Architected Periodic Gyroidal Structures*. Advanced Engineering Materials, 2018. **20**(2): p. 1700549.
 64. Lei, H., et al., *Evaluation of compressive properties of SLM-fabricated multi-layer lattice structures by experimental test and μ -CT-based finite element analysis*. Materials & Design, 2019. **169**: p. 107685.
 65. SA, F.A., *D4.1 Novel materials and additive manufacturing processes, including opportunities to improve logistics and installation*, in *Switch and Crossing Optimal Design and Evaluation*. 2018.
 66. Ferdous, W., et al. *Composite railway sleepers: New developments and opportunities*. 2015. International Heavy Haul Association.
 67. Guo, Y., et al., *Effect of sleeper bottom texture on lateral resistance with discrete element modelling*. Construction and Building Materials, 2020. **250**: p. 118770.
 68. Takahashi, R., et al., *Integrated risk of rail buckling in ballasted tracks at transition zones and its countermeasures*. Soils and Foundations, 2019. **59**(2): p. 517-531.
 69. Jing, G.Q., et al., *Numerical and experimental analysis of single tie push tests on different shapes of concrete sleepers in ballasted tracks*. Proceedings of the Institution of Mechanical Engineers, Part F: Journal of Rail and Rapid Transit, 2018. **233**(7): p. 666-677.
 70. Siddiqui, A.R., et al., *Laboratory assessment of rubber grid-reinforced ballast under impact testing*. Géotechnique Letters, 2023. **13**(2): p. 118-128.
 71. Wang, M., et al. *Characterizing Particle-Scale Acceleration of Mud-Pumping Ballast Bed of Heavy-Haul Railway Subjected to Maintenance Operations*. Sensors, 2022. **22**, DOI: 10.3390/s22166177.
 72. Stathas, D., J.P. Wang, and H.I. Ling, *Model geogrids and 3D printing*. Geotextiles and Geomembranes, 2017. **45**(6): p. 688-696.
 73. MiladShirdel and MasoodFarzam, *Preliminary study on tensile performance of 3D-printed geogrids- effects of various geometrical configurations*. Proceedings of the Institution of Civil Engineers - Geotechnical Engineering. **0**(0): p. 1-48.

74. Liu, S., et al., *Characterization of Ballast Particle Movement at Mud Spot*. Journal of Materials in Civil Engineering, 2019. **31**(1): p. 04018339.
75. Liu, S., et al., *Simulations of large-scale triaxial shear tests on ballast aggregates using sensing mechanism and real-time (SMART) computing*. Computers and Geotechnics, 2019. **110**: p. 184-198.
76. Arab, M.G., et al., *Bio-Inspired 3D-Printed Honeycomb for Soil Reinforcement*, in *Geo-Congress 2020*. 2020. p. 262-271.
77. Amurane, I., et al., *Optimization of 3D printed geocells based on numerical simulation and experimental investigation*. IOP Conference Series: Earth and Environmental Science, 2019. **233**: p. 032043.
78. Tezel, A. and L. Koskela, *Off-site construction in highways projects: management, technical, and technology perspectives from the United Kingdom*. Construction Management and Economics, 2023. **41**(6): p. 475-499.
79. Al-Ketan, O., R. Rowshan, and R.K. Abu Al-Rub, *Topology-mechanical property relationship of 3D printed strut, skeletal, and sheet based periodic metallic cellular materials*. Additive Manufacturing, 2018. **19**: p. 167-183.
80. Yin, H., et al., *Crushing behavior and optimization of sheet-based 3D periodic cellular structures*. Composites Part B: Engineering, 2020. **182**: p. 107565.
81. Gibson, L.J., *Cellular Solids*. MRS Bulletin, 2003. **28**(4): p. 270-274.
82. Evans, A.G., et al., *The topological design of multifunctional cellular metals*. Progress in Materials Science, 2001. **46**(3): p. 309-327.
83. Hu, J., et al., *A lightweight methodology of 3D printed objects utilizing multi-scale porous structures*. The Visual Computer, 2019. **35**(6): p. 949-959.
84. Yu, S., J. Sun, and J. Bai, *Investigation of functionally graded TPMS structures fabricated by additive manufacturing*. Materials & Design, 2019. **182**: p. 108021.
85. Al-Ketan, O., M. Adel Assad, and R.K. Abu Al-Rub, *Mechanical properties of periodic interpenetrating phase composites with novel architected microstructures*. Composite Structures, 2017. **176**: p. 9-19.
86. Wu, L., et al., *Optical Performance Study of Gyroid-Structured TiO₂ Photonic Crystals Replicated from Natural Templates Using a Sol-Gel Method*. Advanced Optical Materials, 2018. **6**(21): p. 1800064.
87. Schroder-Turk, G.E., et al., *The chiral structure of porous chitin within the wing-scales of *Callophrys rubi**. J Struct Biol, 2011. **174**(2): p. 290-5.
88. Lai, M., et al., *Profiting from nature: macroporous copper with superior mechanical properties*. Chem Commun (Camb), 2007(34): p. 3547-9.
89. Zheng, X., et al., *Minimal surface designs for porous materials: from microstructures to*

- mechanical properties*. Journal of Materials Science, 2018. **53**(14): p. 10194-10208.
90. Dalaq, A.S., et al., *Finite element prediction of effective elastic properties of interpenetrating phase composites with architected 3D sheet reinforcements*. International Journal of Solids and Structures, 2016. **83**: p. 169-182.
 91. Abueidda, D.W., et al., *Effective conductivities and elastic moduli of novel foams with triply periodic minimal surfaces*. Mechanics of Materials, 2016. **95**: p. 102-115.
 92. Alhammadi, A., et al., *Microstructural characterization and thermomechanical behavior of additively manufactured AlSi10Mg sheet cellular materials*. Materials Science and Engineering: A, 2020. **791**: p. 139714.
 93. Deng, B. and G.J. Cheng, *Soap film inspired mechanical metamaterials approaching theoretical bound of stiffness across full density range*. Materials Horizons, 2021. **8**(3): p. 987-996.
 94. Khan, K.A. and R.K. Abu Al-Rub, *Viscoelastic properties of architected foams based on the Schoen IWP triply periodic minimal surface*. Mechanics of Advanced Materials and Structures, 2020. **27**(10): p. 775-788.
 95. Novak, N., et al., *Quasi-static and dynamic compressive behaviour of sheet TPMS cellular structures*. Composite Structures, 2021. **266**: p. 113801.
 96. Ouda, M., et al., *Novel static mixers based on triply periodic minimal surface (TPMS) architectures*. Journal of Environmental Chemical Engineering, 2020. **8**(5): p. 104289.
 97. Qureshi, Z.A., et al., *Using triply periodic minimal surfaces (TPMS)-based metal foams structures as skeleton for metal-foam-PCM composites for thermal energy storage and energy management applications*. International Communications in Heat and Mass Transfer, 2021. **124**: p. 105265.
 98. Shen, M., et al., *Mechanical properties of 3D printed ceramic cellular materials with triply periodic minimal surface architectures*. Journal of the European Ceramic Society, 2021. **41**(2): p. 1481-1489.
 99. Shi, X., et al., *Design optimization of multimorphology surface-based lattice structures with density gradients*. The International Journal of Advanced Manufacturing Technology, 2021.
 100. Simsek, U., et al., *Modal characterization of additively manufactured TPMS structures: comparison between different modeling methods*. The International Journal of Advanced Manufacturing Technology, 2021. **115**(3): p. 657-674.
 101. Altintas, G., *Vibration Properties of TPMS Based Structures*. 2018. **4**: p. 27-42.
 102. Elmadih, W., et al., *Mechanical vibration bandgaps in surface-based lattices*. Additive Manufacturing, 2019. **25**: p. 421-429.
 103. Simsek, U., et al., *Parametric studies on vibration characteristics of triply periodic minimum surface sandwich lattice structures*. The International Journal of Advanced Manufacturing Technology, 2021. **115**(3): p. 675-690.

104. Viet, N.V. and W. Zaki, *Free vibration and buckling characteristics of functionally graded beams with triply periodic minimal surface architecture*. Composite Structures, 2021. **274**: p. 114342.
105. Winter, B., et al., *Coexistence of both gyroid chiralities in individual butterfly wing scales of *Callophrys rubi**. Proceedings of the National Academy of Sciences, 2015. **112**(42): p. 12911-12916.
106. Han, L. and S. Che, *An Overview of Materials with Triply Periodic Minimal Surfaces and Related Geometry: From Biological Structures to Self-Assembled Systems*. Advanced Materials, 2018. **30**(17): p. 1705708.
107. Qiu, N., et al., *Experimental and numerical studies on mechanical properties of TPMS structures*. International Journal of Mechanical Sciences, 2024. **261**: p. 108657.
108. Li, Z., et al., *Design and evaluation of TPMS-inspired 3D-printed scaffolds for bone tissue engineering: Enabling tailored mechanical and mass transport properties*. Composite Structures, 2024. **327**: p. 117638.
109. Araya, M., et al., *Assessing the compressive and tensile properties of TPMS-Gyroid and stochastic Ti64 lattice structures: A study on laser powder bed fusion manufacturing for biomedical implants*. Journal of Science: Advanced Materials and Devices, 2024. **9**(1): p. 100663.
110. Zhang, T., et al., *Analysis of thermal storage behavior of composite phase change materials embedded with gradient-designed TPMS thermal conductivity enhancers: A numerical and experimental study*. Applied Energy, 2024. **358**: p. 122630.
111. Gado, M.G., et al., *Triply Periodic Minimal Surface Structures: Design, Fabrication, 3D Printing Techniques, State-of-the-Art Studies, and Prospective Thermal Applications for Efficient Energy Utilization*. Energy Technology, 2024. **n/a**(n/a): p. 2301287.
112. Lu, J.-Y., et al., *Insights into acoustic properties of seven selected triply periodic minimal surfaces-based structures: A numerical study*. Journal of Low Frequency Noise, Vibration and Active Control, 2023. **43**(1): p. 208-219.
113. Li, Z., et al., *Sound absorption performance of a micro-perforated plate sandwich structure based on selective laser melting*. Virtual and Physical Prototyping, 2024. **19**(1): p. e2321607.
114. Li, X., et al., *3D-Printed Lattice Structures for Sound Absorption: Current Progress, Mechanisms and Models, Structural-Property Relationships, and Future Outlook*. Advanced Science, 2024. **11**(4): p. 2305232.
115. Lei, M., et al., *Novel conformal sandwich lattice structures: Design concept, fabrication and mechanical properties*. Thin-Walled Structures, 2024: p. 111806.
116. Almesmari, A., I. Barsoum, and R.K. Abu Al-Rub, *Modelling, optimization, and testing of novel cuboidal spherical plate lattice structures*. Virtual and Physical Prototyping, 2024. **19**(1): p. e2308514.
117. Singh, A., O. Al-Ketan, and N. Karathanasopoulos, *Highly strain-rate sensitive and ductile*

- composite materials combining soft with stiff TPMS polymer-based interpenetrating phases*. Composite Structures, 2024. **328**: p. 117646.
118. Liu, Y., et al., *Mechanical properties of homogeneous and functionally graded spinodal structures*. International Journal of Mechanical Sciences, 2024. **269**: p. 109043.
 119. Gandy, P.J.F. and J. Klinowski, *Exact computation of the triply periodic Schwarz P minimal surface*. Chemical Physics Letters, 2000. **322**(6): p. 579-586.
 120. Fogden, A., *Parametrization of triply periodic minimal surfaces. III. General algorithm and specific examples for the irregular class*. Acta Crystallographica Section A, 1993. **49**(3): p. 409-421.
 121. Pinkall, U. and K. Polthier, *Computing Discrete Minimal Surfaces and Their Conjugates*. Experimental Mathematics, 1993. **2**(1): p. 15-36.
 122. Jones, A., et al., *Parametric design and evaluation of TPMS-like cellular solids*. Materials & Design, 2022. **221**: p. 110908.
 123. Reynolds, B.W., et al., *Characterisation of Heat Transfer within 3D Printed TPMS Heat Exchangers*. International Journal of Heat and Mass Transfer, 2023. **212**: p. 124264.
 124. Günther, F., et al., *Design procedure for triply periodic minimal surface based biomimetic scaffolds*. Journal of the Mechanical Behavior of Biomedical Materials, 2022. **126**: p. 104871.
 125. Wohlgemuth, M., et al., *Tripoly Periodic Bicontinuous Cubic Microdomain Morphologies by Symmetries*. Macromolecules, 2001. **34**(17): p. 6083-6089.
 126. Sathishkumar, N., et al., *Mechanical Properties of Tripoly Periodic Minimal Surface based lattices made by Polyjet Printing*. Materials Today: Proceedings, 2020. **22**: p. 2934-2940.
 127. Oudot, S., L. Rineau, and M. Yvinec, *Meshing volumes with curved boundaries*. Engineering with Computers, 2010. **26**(3): p. 265-279.
 128. Nguyen-Hoang, S., et al., *A combined scheme of edge-based and node-based smoothed finite element methods for Reissner–Mindlin flat shells*. Engineering with Computers, 2016. **32**(2): p. 267-284.
 129. Witten, A., *A MATLAB-based three-dimensional viewer*. Computers & Geosciences, 2004. **30**(7): p. 693-703.
 130. Li, C.M., et al., *Methodology for generating a 3D computerized breast phantom from empirical data*. Medical Physics, 2009. **36**(7): p. 3122-3131.
 131. Bentounsi, A., et al., *Computer-Aided Teaching Using MATLAB/Simulink for Enhancing an IM Course With Laboratory Tests*. IEEE Transactions on Education, 2011. **54**(3): p. 479-491.
 132. Ibadode, O., et al., *IbIPP for topology optimization—An Image-based Initialization and Post-Processing code written in MATLAB*. SoftwareX, 2021. **14**: p. 100701.

133. Kumar, J., et al., *Mechanical Property Analysis of Triply Periodic Minimal Surface Inspired Porous Scaffold for Bone Applications: A Compromise between Desired Mechanical Strength and Additive Manufacturability*. Journal of Materials Engineering and Performance, 2023. **32**(7): p. 3335-3347.
134. Chatzigeorgiou, C., et al., *Numerical investigation of the effective mechanical properties and local stress distributions of TPMS-based and strut-based lattices for biomedical applications*. Journal of the Mechanical Behavior of Biomedical Materials, 2022. **126**: p. 105025.
135. Cai, Z., et al., *The effect of porosity on the mechanical properties of 3D-printed triply periodic minimal surface (TPMS) bioscaffold*. Bio-Design and Manufacturing, 2019. **2**(4): p. 242-255.
136. Isaacson, A., S. Swioklo, and C.J. Connon, *3D bioprinting of a corneal stroma equivalent*. Experimental Eye Research, 2018. **173**: p. 188-193.
137. Wang, M., et al., *Linear and nonlinear elastic buckling of stereolithography resin egg-shaped shells subjected to external pressure*. Thin-Walled Structures, 2018. **127**: p. 516-522.
138. Deshmane, S., et al., *Stereolithography 3D printing technology in pharmaceuticals: a review*. Drug Development and Industrial Pharmacy, 2021. **47**(9): p. 1362-1372.
139. Mukhtarkhanov, M., A. Perveen, and D. Talamona *Application of Stereolithography Based 3D Printing Technology in Investment Casting*. Micromachines, 2020. **11**, DOI: 10.3390/mi11100946.
140. Wang, X., et al., *Effect of geometric configuration on compression behavior of 3D-printed polymeric triply periodic minimal surface sheets*. Mechanics of Advanced Materials and Structures, 2022: p. 1-11.
141. Li, Z., et al., *Additively manufactured dual-functional metamaterials with customisable mechanical and sound-absorbing properties*. Virtual and Physical Prototyping, 2022. **17**(4): p. 864-880.
142. Brischetto, S. and R.J.J.o.C.S. Torre, *Tensile and Compressive Behavior in the Experimental Tests for PLA Specimens Produced via Fused Deposition Modelling Technique*. 2020. **4**(3): p. 140.
143. Li, Z., et al., *Experimental investigation of compression properties of composites with printed braiding structure*. 2018. **11**(9): p. 1767.
144. Madenci, E. and I. Guven, *The finite element method and applications in engineering using ANSYS®*. 2015: Springer.
145. Chen, X. and Y. Liu, *Finite element modeling and simulation with ANSYS Workbench*. 2018: CRC press.
146. Louche, H., et al., *An experimental and modeling study of the thermomechanical behavior of an ABS polymer structural component during an impact test*. 2009. **36**(6): p. 847-861.

147. Dean, G. and L.J.P.t. Wright, *An evaluation of the use of finite element analysis for predicting the deformation of plastics under impact loading*. 2003. **22**(6): p. 625-631.
148. Wang, W., et al., *Tensile behavior of bio-inspired hierarchical suture joint with uniform fractal interlocking design*. 2020. **113**: p. 104137.
149. Al-Ketan, O. and R.K.J.A.E.M. Abu Al-Rub, *Multifunctional mechanical metamaterials based on triply periodic minimal surface lattices*. 2019. **21**(10): p. 1900524.
150. Ruiz De Galarreta, S., J.R.T. Jeffers, and S. Ghouse, *A validated finite element analysis procedure for porous structures*. Materials & Design, 2020. **189**: p. 108546.
151. Jing, G.Q., et al., *Numerical and Experimental Analysis of Lateral Resistance of Biblock Sleeper on Ballasted Tracks*. International Journal of Geomechanics, 2020. **20**(6): p. 04020051.
152. Li, J., et al., *Three-Dimensional Simulation of Aggregate and Asphalt Mixture Using Parameterized Shape and Size Gradation*. Journal of Materials in Civil Engineering, 2019. **31**(3): p. 04019004.
153. Suhr, B. and K. Six, *Simple particle shapes for DEM simulations of railway ballast: influence of shape descriptors on packing behaviour*. Granular Matter, 2020. **22**(2): p. 43.
154. Orefice, L. and J.G. Khinast, *Deformable and breakable DEM particle clusters for modelling compression of plastic and brittle porous materials — Model and structure properties*. Powder Technology, 2020. **368**: p. 90-104.
155. Itasca, C.G., *PFC (particle flow code in 2 and 3 dimensions), version 5.0 [user's manual]*. Int. J. Numer. Anal. Met., 2014. **32**(6): p. 189-213.
156. Kaewunruen, S., et al., *Enhancement of Dynamic Damping in Eco-Friendly Railway Concrete Sleepers Using Waste-Tyre Crumb Rubber*. Materials, 2018. **11**(7).
157. Kaewunruen, S., R. Meesit, and P. Mondal, *Early-age dynamic moduli of crumbed rubber concrete for compliant railway structures*. Journal of Sustainable Cement-Based Materials, 2017. **6**(5): p. 281-292.
158. Kaewunruen, S. and A.M. Remennikov, *Field trials for dynamic characteristics of railway track and its components using impact excitation technique*. NDT & E International, 2007. **40**(7): p. 510-519.
159. Li, Y., et al., *Analysis of fatigue crack propagation in rails under combined action of wheel load and residual stress*. Engineering Failure Analysis, 2020. **115**: p. 104689.
160. Li, D., et al., *Fatigue life modelling of railway prestressed concrete sleepers*. Structures, 2022. **41**: p. 643-656.
161. Liu, G., et al., *Study on vertical vibration and transmission characteristics of railway ballast using impact hammer test*. Construction and Building Materials, 2022. **316**: p. 125898.
162. Fu, H., Y. Yang, and S. Kaewunruen, *Multi-Hazard Effects of Crosswinds on Cascading*

- Failures of Conventional and Interspersed Railway Tracks Exposed to Ballast Washaway and Moving Train Loads*. Sensors, 2023. **23**(4): p. 1786.
163. Wang, J. and B. Du, *Sound Insulation Performance of Foam Rubber Damping Pad and Polyurethane Foam Board in Floating Floors*. Experimental Techniques, 2023. **47**(4): p. 839-850.
 164. Stefani, G., M. De Angelis, and U. Andreaus, *Influence of the gap size on the response of a single-degree-of-freedom vibro-impact system with two-sided constraints: Experimental tests and numerical modeling*. International Journal of Mechanical Sciences, 2021. **206**: p. 106617.
 165. Love, J.S. and M.J. Tait, *Estimating the added effective damping of SDOF systems incorporating multiple dynamic vibration absorbers with nonlinear damping*. Engineering Structures, 2017. **130**: p. 154-161.
 166. Andreaus, U. and M. De Angelis, *Nonlinear dynamic response of a base-excited SDOF oscillator with double-side unilateral constraints*. Nonlinear Dynamics, 2016. **84**(3): p. 1447-1467.
 167. Meesit, R. and S. Kaewunruen, *Vibration Characteristics of Micro-Engineered Crumb Rubber Concrete for Railway Sleeper Applications*. Journal of Advanced Concrete Technology, 2017. **15**(2): p. 55-66.
 168. Tao, S., et al., *Estimation of design sea ice thickness with maximum entropy distribution by particle swarm optimization method*. Journal of Ocean University of China, 2016. **15**(3): p. 423-428.
 169. Tweten, D.J., Z. Ballard, and B.P. Mann, *Minimizing error in the logarithmic decrement method through uncertainty propagation*. Journal of Sound and Vibration, 2014. **333**(13): p. 2804-2811.
 170. Hans, S., et al., *DAMPING IDENTIFICATION IN MULTI-DEGREE-OF-FREEDOM SYSTEM VIA A WAVELET-LOGARITHMIC DECREMENT—PART 2: STUDY OF A CIVIL ENGINEERING BUILDING*. Journal of Sound and Vibration, 2000. **235**(3): p. 375-403.
 171. Byeon, J.H. and S.H. Kim, *Extraction of the damping ratio of a beat wave using envelope logarithmic decrement*. Journal of Mechanical Science and Technology, 2022. **36**(6): p. 2729-2737.
 172. Sarantsev, M.I., *Determination of the Logarithmic Decrement of Damping of Natural Frequency Oscillations of the Sayano-Shushenskaya Hydropower Plant Dam Based on Engineering Seismometric Observations*. Power Technology and Engineering, 2021. **55**(1): p. 45-57.
 173. Vergassola, G., D. Boote, and A. Tonelli, *On the damping loss factor of viscoelastic materials for naval applications*. Ships and Offshore Structures, 2018. **13**(5): p. 466-475.
 174. Davis, W.O., *Measuring Quality Factor From a Nonlinear Frequency Response With Jump Discontinuities*. Journal of Microelectromechanical Systems, 2011. **20**(4): p. 968-975.

175. Zai, B.A., et al., *Effect of moisture absorption on damping and dynamic stiffness of carbon fiber/epoxy composites*. Journal of Mechanical Science and Technology, 2009. **23**(11): p. 2998-3004.
176. Daoud, H., et al., *Numerical and Experimental Characterization of the Dynamic Properties of Flax Fiber Reinforced Composites*. International Journal of Applied Mechanics, 2016. **08**(05): p. 1650068.
177. Banerjee, J.R., *Dynamic stiffness formulation for structural elements: A general approach*. Computers & Structures, 1997. **63**(1): p. 101-103.
178. Czech, K.R. and W. Gardziejczyk *Dynamic Stiffness of Bituminous Mixtures for the Wearing Course of the Road Pavement—A Proposed Method of Measurement*. Materials, 2020. **13**, DOI: 10.3390/ma13081973.
179. Hopkins, C., R. Wilson, and R.J.M. Craik, *Dynamic stiffness as an acoustic specification parameter for wall ties used in masonry cavity walls*. Applied Acoustics, 1999. **58**(1): p. 51-68.
180. Kaewunruen, S., A. Rachid, and K. Goto. *Damping effects on vibrations of railway prestressed concrete sleepers*. in *World Multidisciplinary Civil Engineering-Architecture-Urban Planning Symposium, IOP Conference Series: Material Science and Engineering (2018a, accepted)*. 2018.
181. Bala, A. and S. Gupta, *Thermal resistivity, sound absorption and vibration damping of concrete composite doped with waste tire Rubber: A review*. Construction and Building Materials, 2021. **299**: p. 123939.
182. Eltayeb, E., et al., *Dynamic performance of rubberised concrete and its structural applications – An overview*. Engineering Structures, 2021. **234**: p. 111990.
183. Lin, C.-Y., G.C. Yao, and C.-H. Lin, *A Study on the Damping Ratio of Rubber Concrete*. Journal of Asian Architecture and Building Engineering, 2010. **9**(2): p. 423-429.
184. Giner, I.G., et al., *Dynamic Modelling of High Speed Ballasted Railway Tracks: Analysis of the Behaviour*. Transportation Research Procedia, 2016. **18**: p. 357-365.
185. Ngamkhanong, C., S. Kaewunruen, and C. Baniotopoulos, *Nonlinear buckling instabilities of interspersed railway tracks*. Computers & Structures, 2021. **249**: p. 106516.
186. Li, X. and S.K. Vanapalli, *Simulation of progressive shear failure in railway foundation*. Transportation Geotechnics, 2021. **29**: p. 100550.
187. Chen, J. and Y. Zhou, *Dynamic responses of subgrade under double-line high-speed railway*. Soil Dynamics and Earthquake Engineering, 2018. **110**: p. 1-12.
188. Indraratna, B., M. Singh, and T.T. Nguyen, *The mechanism and effects of subgrade fluidisation under ballasted railway tracks*. Railway Engineering Science, 2020. **28**(2): p. 113-128.
189. Jing, G., et al., *Numerical investigation of the behavior of stone ballast mixed by steel slag*

- in ballasted railway track*. Construction and Building Materials, 2020. **262**: p. 120015.
190. Shi, Q. and B. Mishra, *Numerical Analysis of the Effect of Bedding Plane Strength on Laminated Roof Failure in Underground Entries Using Coupled FDM-DEM*. Mining, Metallurgy & Exploration, 2022. **39**(3): p. 1061-1071.
 191. Feng, K., et al. *Salt Cavern Thermal Damage Evolution Investigation Based on a Hybrid Continuum-Discrete Coupled Modeling*. Sustainability, 2023. **15**, DOI: 10.3390/su15118718.
 192. Luo, X., et al. *Mechanical Behaviour of Anchored Rock Containing Weak Interlayer under Uniaxial Compression: Laboratory Test and Coupled DEM-FEM Simulation*. Minerals, 2022. **12**, DOI: 10.3390/min12040492.
 193. Yin, Z.-Y., *Three-dimensional numerical modelling of progressive failure of caisson foundation in sand using a coupled FDM-DEM method*. Ocean Engineering, 2022. **253**: p. 111332.
 194. Nguyen, N.H.T., H.H. Bui, and G.D. Nguyen, *An approach to calculating large strain accumulation for discrete element simulations of granular media*. International Journal for Numerical and Analytical Methods in Geomechanics, 2020. **44**(11): p. 1525-1547.
 195. Cai, M., et al., *FLAC/PFC coupled numerical simulation of AE in large-scale underground excavations*. International Journal of Rock Mechanics and Mining Sciences, 2007. **44**(4): p. 550-564.
 196. Namura, A., Y. Kohata, and S. Miura, *Effect of Sleeper Size on Ballasted Track Settlement*. Quarterly Report of RTRI, 2004. **45**(3): p. 156-161.
 197. Nguyen-Van, V., et al., *Bioinspired cellular cementitious structures for prefabricated construction: Hybrid design & performance evaluations*. Automation in Construction, 2020. **119**: p. 103324.
 198. Jiang, M., Z. Shen, and J. Wang, *A novel three-dimensional contact model for granulates incorporating rolling and twisting resistances*. Computers and Geotechnics, 2015. **65**: p. 147-163.
 199. Gutiérrez-Ch, J.G., et al., *Distinct element method simulations of rock-concrete interfaces under different boundary conditions*. Engineering Geology, 2018. **240**: p. 123-139.
 200. Zhai, M., et al., *Microcracking behaviors and acoustic emission characteristics of granite subjected to direct shear based on a novel grain-based model*. Computers and Geotechnics, 2022. **151**: p. 104955.
 201. Brown, N.J., J.-F. Chen, and J.Y. Ooi, *A bond model for DEM simulation of cementitious materials and deformable structures*. Granular Matter, 2014. **16**(3): p. 299-311.
 202. Hentz, S., L. Daudeville, and V. Donzé Frédéric, *Identification and Validation of a Discrete Element Model for Concrete*. Journal of Engineering Mechanics, 2004. **130**(6): p. 709-719.